SISSA

SCUOLA INTERNAZIONALE SUPERIORE DI STUDI AVANZATI

PHYSICS AREA - ASTROPARTICLE PHYSICS COURSE

PROBING THE ΛCDM UNIVERSE AND BEYOND WITH PRESENT AND FUTURE 21CM INTENSITY MAPPING SURVEYS

PhD Candidate
MARIA BERTI

Referees
Prof. STEFANO CAMERA

Dr LAURA WOLZ

Supervisor
Prof. MATTEO VIEL
Co-Supervisor
Dr MARTA SPINELLI

Thesis submitted in fulfillment of the requirements
for the degree of Philosophiæ Doctor

MARIA BERTI

☞ mberti@sissa.it

☞ +39 334 531 6151

☞ Largo della Barriera Vecchia, 12, 34129 Trieste, Italy

Probing the ΛCDM Universe and beyond with present and future 21*cm intensity mapping surveys*, Philosophiae Doctor Degree Thesis © September 2023

ABSTRACT

The measurement of the large-scale distribution of neutral hydrogen in the late Universe, obtained with radio telescopes through the hydrogen 21cm line emission, has the potential to become a pivotal cosmological probe in the upcoming years. This thesis presents a comprehensive analysis focused on forecasting the constraining power of 21cm intensity mapping observations, exploring a wide set of cosmological models, from standard ΛCDM to modified gravity, dark energy, and massive neutrinos. We developed a pipeline to construct mock data sets for a variety of present and future 21cm observations, with an emphasis on the SKA Observatory and its precursor MeerKAT planned and ongoing surveys. We investigated the interplay between intensity mapping and other cosmological probes, such as the cosmic microwave background, galaxy clustering, and gravitational waves, providing valuable insights into the potential synergies between these different observables. To assess the constraining power of such observations we conducted a Bayesian analysis implementing a likelihood code to work with different 21cm probes and exploring the posterior with Monte Carlo Markov Chain methods. The numerical tools we develop are integrated with widely used codes and prepared to be exploited for upcoming observations and their cosmological analyses. As a proof of concept, the analysis pipeline is validated with the recent MeerKAT intensity mapping measurements in cross-correlation with galaxy clustering data, yielding encouraging results consistent with forecasted outcomes. The main findings of this thesis suggest a promising constraining power of 21cm observations when considered both alone and combined with other probes. The joint analysis with cosmic microwave background observations significantly narrows the parameter constraints, leading to precise estimates of pivotal cosmological parameters like $\Omega_c h^2$ and H_0. The tomographic nature of 21cm intensity mapping measurements further improves the estimated errors, potentially offering a powerful new probe to constrain beyond-ΛCDM scenarios. In conclusion, this thesis extensively tests the value of 21cm intensity mapping as a cosmological probe in the standard model scenario and beyond. It delivers tools for the preparation and analysis of current and future cosmological observations, taking part in the scientific community's effort to pave the way for future groundbreaking observations in cosmology that will potentially provide a deeper understanding of the fundamental properties of our Universe.

PUBLICATIONS

This thesis is based on the following publications:

[1] Maria Berti, Marta Spinelli, Balakrishna S. Haridasu, Matteo Viel, and Alessandra Silvestri. «Constraining beyond ΛCDM models with 21cm intensity mapping forecasted observations combined with latest CMB data.» In: *JCAP* 01.01 (2022), p. 018. DOI: 10.1088/1475-7516/2022/01/018. arXiv: 2109.03256 [astro-ph.CO].

[2] Giulio Scelfo, Maria Berti, Alessandra Silvestri, and Matteo Viel. «Testing gravity with gravitational waves × electromagnetic probes cross-correlations.» In: *JCAP* 02 (2023), p. 010. DOI: 10.1088/1475-7516/2023/02/010. arXiv: 2210.02460 [astro-ph.CO].

[3] Maria Berti, Marta Spinelli, and Matteo Viel. «Multipole expansion for 21 cm intensity mapping power spectrum: Forecasted cosmological parameters estimation for the SKA Observatory.» In: *Mon. Not. Roy. Astron. Soc.* 521.3 (2023), pp. 3221–3236. DOI: 10.1093/mnras/stad685. arXiv: 2209.07595 [astro-ph.CO].

[4] Jiamin Hou, Julian Bautista, Maria Berti, Carolina Cuesta-Lazaro, César Hernández-Aguayo, Tilman Tröster, and Jinglan Zheng. «Cosmological Probes of Structure Growth and Tests of Gravity.» In: *Universe* 9.7 (2023). ISSN: 2218-1997. DOI: 10.3390/universe9070302. URL: https://www.mdpi.com/2218-1997/9/7/302.

[5] Maria Berti, Marta Spinelli, and Matteo Viel. «21cm Intensity Mapping cross-correlation with galaxy surveys: current cosmological parameters estimation for MeerKAT and forecasts for the SKA Observatory.» In: 2023.

[6] Maria Berti, Marta Spinelli, Balakrishna S. Haridasu, and Matteo Viel. «Latest perspectives on weighing the neutrinos with the SKAO 21cm Intensity Mapping.» In: 2023.

[7] Balakrishna S. Haridasu, Maria Berti, and Matteo Viel. «Easing the CMB tension with Effective Field Theory models of Dark Energy.» In: 2023.

LIST OF SYMBOLS

SYMBOL	DESCRIPTION
a	Expansion scale factor in FLRW metric
η	Conformal time
z	Cosmological redshift
H	Hubble parameter
H_0	Hubble constant
h	Reduced Hubble constant
$\mathcal{H}$	Hubble parameter in conformal time
Ω_i	Density parameter relative to the species i
τ	Optical depth at reionization
Λ	Cosmological Constant
δ_r	Density contrast of the species r
Ω_r	Today's density parameter of the species r
A_s	Curvature perturbation amplitude
n_s	Spectral index
A_s	Amplitude of scalar perturbations
w	Equation of state parameter
w_0	Dark Energy equation of state parameter
$\Sigma_\nu m_\nu$	Total neutrino mass
$P(k)$	Matter power Spectrum
C_ℓ^{TT}	Temperature Power Spectrum
Ω^{EFT}	First order in perturbation EFT function

ACRONYMS

CDM   Cold Dark Matter

DM   Dark Matter

GR   General Relativity

EFT   Effective Field Theory

MG   Modified Gravity

CMB   Cosmic Microwave Background

DE   Dark Energy

BAO   Baryonic Acoustic Oscillations

LSS   Large Scale Structure

MCMC   Monte Carlo Markov Chain

CAMB   Code for Anisotropies in the Microwave Background

EFTCAMB   Effective Field Theory - CAMB

CosmoMC   Cosmological Monte Carlo

EFTCosmoMC   Effective Field Theory - CosmoMC

CL   Confidence Level

LIM   Line Intensity mapping

IM   Intensity mapping

HI   Neutral Hydrogen

SKAO   SKA Observatory

AP   Alcock-Paczyński

CONTENTS

INTRODUCTION

T HE ΛCDM MODEL stands as the cornerstone of modern cosmology, providing a robust framework to describe the evolution and the large-scale structure (LSS) of the expanding Universe. It is founded on the principles of general relativity (GR) and requires the existence of puzzling dark constituents: dark matter (DM) and dark energy (DE). The latter, which is responsible for the late-time cosmic acceleration [1, 2], constitutes almost 70% of the total content of the Universe today and it can be modeled as a cosmological constant (Λ) term in the Einstein's equations (see, e.g., [3]).

The standard cosmological model

The standard model has been extensively tested against a plethora of cosmological observations, ranging from the cosmic microwave background (CMB), to supernovae observations and measurements from the large-scale structure [4–7]. It has, up to now, demonstrated to be in remarkable agreement with observational data, although it leaves fundamental open questions and challenges. The nature of dark energy and cold dark matter remains unknown and tensions persist on the values of key cosmological parameters measured by different observations [8–11]. This motivated an extensive theoretical effort to provide extensions to the standard ΛCDM scenario, in the quest for new physics.

Alternative beyond-ΛCDM models include, among others, non-standard DE equations of state, modifications to gravity to model the cosmic acceleration, and non-standard massive neutrinos cosmologies. As for cosmic acceleration and DE, in the last decades, several alternative models have been proposed and studied [12–14], ranging from dynamical DE to modified gravity (MG). In the former, an additional field, typically a scalar, is added to the matter content. In the latter, the gravity sector of the action is modified, normally resulting in additional gravitational degrees of freedom. In practice, the distinction between DE and MG models is not always a strict one. Rather, one can focus on the additional propagating degrees of freedom and employ a unifying framework to study deviations from ΛCDM. One such framework is offered by the phenomenological parametrizations of gravity, in which all the modifications are cast into the evolution of two additional functions of time and scale [15–19]. Another alternative is the effective field theory (EFT) of DE [20, 21], which allows surveying large samples of DE-MG models for optimal exploitation of the wealth of upcoming high-precision data.

The beyond-ΛCDM Universe

Future cosmological observations hold great promise in advancing the understanding of the Universe. The first detection of a binary black hole merger by the LIGO/Virgo scientific collaboration [22, 23], and the plethora of new detections [24, 25] that came after that, led to the birth of the so-called gravitational waves (GWs) astronomy. With forthcoming experiments, such as the Einstein Telescope (ET) [26], Cosmic Explorer [27], LISA [28], KAGRA [29], and LIGO-India [30]), investigation of the Universe through GWs will soon play a major role in the investigation of the Universe. Moreover, the latest generation of galaxy surveys, like the Dark Energy Spectroscopic Instrument (DESI) [31, 32] and the Euclid mission [33, 34], will help to shed light on DE through high-precision measurements of baryon acoustic oscillations (BAO), galaxy

New frontiers of cosmological observations

clustering, growth of structures, and weak lensing. Along with cutting-edge observations, new probes are currently being pursued. A promising new probe is 21cm intensity mapping, one of the main cosmological probes studied in this thesis.

Neutral hydrogen as a cosmological probe

Neutral hydrogen (HI) is a fundamental element in the Universe and its late-time distribution traces the underlying matter field, making it an innovative key probe of the large-scale structure (LSS) [35–37]. The measurement of the large-scale distribution of HI and its evolution with time can thus play an important role in the upcoming years, providing a complementary probe to traditional galaxy surveys [38]. The 21cm signal, originating from the spin-flip transition in the hyperfine structure of the hydrogen ground state (see e.g. [39]), is redshifted by the expansion of the Universe, and, thus, it is detectable on Earth at radio frequencies. Several planned and ongoing experiments, either purpose-built compact interferometers such as CHIME [40, 41], CHORD or HIRAX [42], or single-dish telescopes such as GBT [43, 44] or FAST [45] aim to measure it with line intensity mapping (LIM or IM) techniques [46–52]. At the state of the art, only a few detections of the HI signal were achieved in cross-correlation with galaxy surveys [43, 44, 53–56].

Planned SKAO 21cm IM surveys

Radio cosmology is also one of the main scientific goals of the SKA Observatory (SKAO), which will be composed by the SKA-Low and SKA-Mid telescopes located in Australia and South Africa, respectively. Using the SKA-Mid telescope array as a collection of single-dishes [e.g. 37, 57] it will be possible to perform 21cm IM observations at the large scales relevant for cosmology up to redshift 3. The SKAO is currently under construction, and MeerKAT, the SKA-Mid precursor, has been conducting an IM survey for cosmology (MeerK-LASS, [58]). Preliminary data analysis has provided promising results [59, 60] and a first detection of the HI signal in cross-correlation with the WiggleZ galaxies [61]. However, the level of foreground residuals is still preventing a direct detection and this issue has triggered extensive simulation work on foreground cleaning performances [62–71]. In parallel with the effort in improving the data analysis and the foreground separation, it is of key importance to refine the forecast for the constraining power of the 21cm IM alone and in combination with other probes in order to make a better case for radio cosmology with the SKAO or optimize the survey design.

Synergies with complementary probes

The different experiments, targeting different observables, are and are expected to produce a large amount of data, which will significantly grow in the relatively near future. Given this variety, it is reasonable to explore the scientific opportunities that arise from combining together different data sets, thus studying the cross-correlation of different tracers of the LSS. Indeed, in several published works cross-correlations between the LSS and the CMB (e.g. [72–81]), neutrinos (e.g. [82]), different LSS tracers (e.g. [83–86]), IM (e.g. [63, 87–97]) or GWs (e.g. [98–114]) have been studied.

This thesis

In this thesis, we aim at studying the impact of future 21cm IM observations on cosmological parameter constraints, exploring both the ΛCDM Universe and beyond. The discussion, based on the works listed in Publications, is organized in three parts, as follows.

PART I The main aim of this opening part is to provide the theoretical and observational framework of this thesis. The discussion is to be intended as a handbook and a reference pointer to make this thesis accessible to not experts

and students. The author assumes that the expert reader could safely fast-forward to the subsequent part, using this first mainly as a convention and formalism reference.

The standard cosmological model is described in Chapter 1. We review the main features of the expanding Universe, recalling the basic principles of Einstein's general relativity and listing the known matter energy components. After presenting the perturbed Universe, we introduce the concept of power spectra and illustrate theoretical predictions for the matter one. A description of the parameters describing ΛCDM and its simplest extensions, with current constraints, concludes this chapter.

State-of-the-art techniques to probe the Universe are presented in Chapter 2. We gather here the cosmological observables and observations relevant to this thesis work, providing the theoretical modeling of the cosmological probes and the context in which experiments are inserted. We conclude by delineating the numerical tools we adopt to conduct our analysis.

Chapter 3, based on [14], issues a review on the most popular modifications to gravity and dark energy models. In this section, we give an overview of the parametrized frameworks of gravity, listing the latest constraints and forecasts in the literature from cosmological observations considered in this work.

PART II In this second part, the original work that constitutes this thesis is presented. We forecast 21cm observations and test its potential constraining power on the full set of ΛCDM cosmological parameters in combination with other cosmological probes.

In Chapter 4 we describe the modeling of the 21cm signal power spectrum multipoles and present the results of the forecast MCMC analysis we conduct for the SKAO. We construct mock observations within multiple bins in the redshift range $z = 0 - 3$ and investigate the effects of combining forecasted 21cm observations with the latest Planck CMB data. This chapter is based on [115].

The interplay between neutral hydrogen intensity mapping and galaxy clustering is explored in Chapter 5. We focus on the data sets that will be provided by the SKAO for the 21cm signal, while we consider DESI and Euclid for galaxy clustering. As a proof-of-concept, we test the full pipeline on the real data provided by the MeerKAT collaboration [55] presenting first constraints on cosmological parameters. This chapter is based on a publication prepared for submission [116].

PART III Having investigated the constraining power of 21cm probes on the ΛCDM Universe, we explore the impact of neutral hydrogen observations on a variety of beyond ΛCDM scenarios.

We explore constraints on dark energy and modified gravity with forecasted 21cm intensity mapping measurements using the effective field theory approach in Chapter 6. We construct a realistic mock data set of a low redshift, single-bin 21cm signal power spectrum measurement from the MeerKAT radio telescope. We compute constraints on cosmological and model parameters through, testing both the constraining power of 21cm observations alone and its effect when combined with the latest CMB data. We complement our analysis by testing the effects of tomography from a MeerKAT mock data set of observations in multiple redshift bins. This chapter is based on [117].

In Chapter 7 we present a forecast study that constrains the phenomenological MG function evolution. We consider cross-correlation of resolved GW events, from compact objects mergers detected by the Einstein Telescope, either assuming or excluding the detection of an electromagnetic counterpart, and electromagnetic signals, coming both from the IM of the neutral hydrogen distribution and resolved galaxies from the SKAO, considering weak lensing, the angular clustering and their cross term as observable probes. This chapter is based on [118].

Lastly, in Chapter 8 we present preliminary results on the neutrino mass constraints with the SKAO. This chapter is part of an ongoing project [119].

We summarize the main findings of this thesis and define the roadmap for future developments in the Conclusions.

Part I

A CHART THROUGH MODERN COSMOLOGY TO
NAVIGATE THIS THESIS

A STANDARD MODEL TO RULE THEM ALL (OUT)

WITH THE BIRTH of modern cosmology, marked by first measurements of the cosmic microwave background (CMB) and the large-scale structure (LSS), a widely accepted cosmological paradigm took hold. Today, it converged to the standard model of cosmology.

At the very beginning, the Universe, which is 13.7 Gyr old, goes through a phase of accelerated expansion called inflation. At the end of inflation, the initial perturbations that will evolve to form all the structures already exist. When the Universe is only 3 minutes old, the first light element nuclei are formed and, at this stage, it is dominated by radiation, mainly in the form of photons. As the temperature falls off due to the expansion, the radiation-to-matter transition occurs and non-relativistic components become more relevant. The Universe now, at approximately 40 000 yr of age, consists of cold dark matter (CDM) and a hot plasma of photons, protons, neutrons, electrons, light elements nuclei, and a small relic of neutrinos. At 380 000 yr old, recombination occurs and atomic hydrogen is formed for the first time. Radiation is now free to propagate and the Universe becomes transparent. The relic radiation from recombination is observable today as the CMB. From now on, matter perturbations can grow due to gravitational instability to form the rich large-scale structure observed today. As expansion continues, matter density is increasingly diluted until the equivalence between matter and dark energy (DE) occurs, 10 Gyr after the beginning. This relatively recent event marks the beginning of the DE era, a phase of accelerated expansion. According to general relativity (GR), dark energy can be modeled as a cosmological constant (Λ) term in Einstein's equations.

The standard model of cosmology, i.e. the ΛCDM model, has been extensively tested in the last decades and it proved to be in exquisite agreement with a variety of observations. However, given its phenomenological nature, it does not explain crucial fundamental physics open questions, such as what is the nature of the dark components. Nevertheless, although a plethora of beyond-ΛCDM scenarios was explored, ΛCDM is the most favored model by state-of-the-art measurements.

This chapter is an overview of the main elements that constitute the standard model of cosmology, mainly based on [120]. We present the expanding Universe in Section 1.1, describe the LSS of the Universe in Section 1.2, and summarize the ΛCDM model in Section 1.3. Being exhaustive is beyond the scope of this thesis, and for a detailed discussion, we refer the reader to the extensive literature on the subject [120–124].

1.1 THE EXPANDING UNIVERSE

Modern cosmology assumes that the Universe is homogeneous, isotropic, and perpetually expanding. Cosmic homogeneity and isotropy were assumed by the cosmological principle way before observational evidence. As a matter

of fact, the cosmological principle can be thought of as a generalization of the prior Copernican principle: our location in the Universe is not peculiar, preferred, or fundamental. Indeed, the visible Universe appears to be the same everywhere. More precisely, at sufficiently large scales observations confirm that it is in good approximation spatially homogeneous and isotropic. The expansion of the Universe is a well-tested phenomenon too. First observational evidence date back to the renowned Hubble discovery [125]. Having defined the fundamental properties of the observed Universe, in the following we introduce the mathematical formulation adopted to model it.

Gravity is the most relevant force in cosmology. According to the theory of general relativity, gravitation can be described by a metric tensor. The following four-dimensional spacetime metric $g_{\mu\nu}$ is the well-known Friedmann-Lemaître-Robertson-Walker (FLRW) metric:

$$
\begin{aligned}
ds^2 &\equiv g_{\mu\nu}\,dx^\mu dx^\nu \\
&= -dt^2 + a(t)^2 \left[\frac{dr^2}{1 - Kr^2} + r^2 \left(d\theta^2 + \sin^2\theta d\phi^2 \right) \right],
\end{aligned}
\tag{1.1}
$$

where r, θ, and ϕ are the spherical tridimensional coordinates. The FLRW metric describes an expanding, homogeneous, and isotropic Universe. Here and in the following, we adopt a system of units in which $c = 1$. Moreover, x^μ represents the four spacetime coordinates: x^0 stands for the cosmic time t, while x^i are three-dimensional spherical coordinates. The function $a(t)$, the scale factor, is a time-dependent parameter that characterizes the expansion. K is a constant that defines the spatial curvature. Up to r-rescaling, it is non-restrictive to only consider three values of K: $K = 0$ for a flat geometry of the spatial section, $K = 1$ for a closed geometry, and $K = -1$ for an open one. Current observations point toward a flat Universe [126, 127], so it is reasonable to assume $K = 0$.

For a spatially flat geometry, the FLRW metric is reduced to

$$
ds^2 = -dt^2 + a(t)^2 \left[dr^2 + r^2 \left(d\theta^2 + \sin^2\theta d\phi^2 \right) \right].
\tag{1.2}
$$

Defining the conformal time η

$$
\eta(t) \equiv \int_0^t \frac{d\tilde{t}}{a(\tilde{t})},
\tag{1.3}
$$

one can also rewrite the metric as

$$
ds^2 = a(t)^2 \left[-d\eta^2 + dr^2 + r^2 \left(d\theta^2 + \sin^2\theta d\phi^2 \right) \right].
\tag{1.4}
$$

To avoid confusion, we will address the total derivative with respect to the cosmic time t with the prime symbol $' \equiv \frac{d}{dt}$. Instead, for the total derivative with respect to the conformal time η we will use the dot symbol $\dot{} \equiv \frac{d}{d\eta}$.

To quantify how rapidly the scale factor changes in time, we introduce the Hubble parameter

$$
H(t) = \frac{1}{a}\frac{da}{dt}.
\tag{1.5}
$$

The Hubble parameter today, i.e. the Hubble constant H_0, is a fundamental parameter of the standard model of cosmology. The value of H_0 is currently the topic of heated discussions among the scientific community. Constraints on the

value of H_0 from different observations are not compatible and it is not clear if these tensions hide new physics or unresolved systematics (see e.g. [11]). According to the latest constraints from the CMB [4], the Hubble constant value is

$$H_0 = 67.32 \pm 0.42 \text{ km s}^{-1} \text{ Mpc}^{-1}. \tag{1.6}$$

It is common practice to rewrite H_0 as

$$H_0 = 100\,h \text{ km s}^{-1} \text{ Mpc}^{-1} \tag{1.7}$$

and expressing all the physical quantities that depend on the Hubble constant in terms of h.

The expansion of the Universe also affects light that travels through space. The wavelength of a light ray emitted by an object that is receding from the observer is stretched in the travel between the source and the observer. Therefore, observed wavelengths will be larger than the emitted ones due to cosmological expansion. We can have a measure of the stretching factor through the cosmological redshift, defined as

$$1 + z = \frac{\lambda_{obs}}{\lambda_{em}} = \frac{a_{obs}}{a_{em}}, \tag{1.8}$$

or simply

$$1 + z = \frac{a_0}{a}, \qquad a_0 = a(t_0), \tag{1.9}$$

if we consider the present time t_0 as the observer's time.

Cosmological redshift is a powerful tool to measure distances on cosmological scales. Let us picture the spatial part of the coordinate system defined above as a grid of points fixed in time. We define the comoving distance d_C as the constant distance between two points on the grid. For the flat FLRW metric (see Equation 1.2) the comoving distance is simply

$$d_C(r) = r. \tag{1.10}$$

The actual physical distance between the same two points on the grid, the proper distance d_P, depends on the expansion and is a function of time. For a spatially flat geometry, the proper distance at time t is simply the comoving distance stretched or shortened by the scale factor at that time

$$d_P(t) = a(t)\,d_C. \tag{1.11}$$

As customary, we fix $a_0 = 1$ and thus we consider $d_C = d_P(t_0)$. I.e., we choose the comoving distances to be the proper distances measured today.

Unfortunately, proper and comoving distances are not accessible with cosmological observations. Let us consider, instead, an observer at a fixed point in the tridimensional spherical coordinate system. An object with extension D that appears to the observer subtended by an angle θ is away from the observer by a distance

$$d_A = \frac{D}{\theta}, \tag{1.12}$$

where d_A is a radial distance, i.e. along the line-of-sight. For standard rulers, which are objects whose physical size D is known, e.g. as the baryon acoustic oscillations (BAO), d_A can be computed by measuring the angle θ. In an ex-

panding Universe, we can express D as a proper distance from the line element $a\,r d\theta$ in the FLRW metric. For a flat geometry, this implies that

$$d_A = a\,d_C = \frac{d_C}{1+z}. \tag{1.13}$$

Another observable quantity is the luminosity distance d_L. Let us recall that in a laboratory environment, the measured flux F from a luminous object at distance d is

$$F = \frac{L}{4\pi d^2}, \tag{1.14}$$

where L is the luminosity of the object, i. e. the energy per unit of time emitted by the source. As before, expansion modifies this definition. The rate and the energy of emitted photons will be reduced due to expansion. It can be shown that for a flat geometry

$$F = \frac{L\,a^2}{4\pi d_C^2}, \tag{1.15}$$

and thus

$$d_L = \frac{d_C}{a} = (1+z)\,d_C = (1+z)^2\,d_A. \tag{1.16}$$

We can calculate d_L by measuring F, once the luminosity is given. Objects with a known luminosity are called standard candles. A notable example of a standard candle is a supernova.

1.1.1 The Friedmann equations

The matter-energy content of the Universe can be described as a barotropic fluid, i. e. its density is a function of its pressure only. Therefore, energy and matter obey an equation of state

$$\mathrm{p} = w\rho, \tag{1.17}$$

where p is the pressure, ρ the density, and w is the equation of state parameter. The stress-energy tensor of such a fluid is

$$T_{\mu\nu} = (\rho + \mathrm{p})\,U_\mu U_\nu + \mathrm{p}\,g_{\mu\nu}, \tag{1.18}$$

where U^μ is the fluid four-velocity.

GR couples the spacetime geometry to the matter and energy content of the Universe. Given a metric and a stress-energy tensor $T_{\mu\nu}$, Einstein's equation describes how geometry, i.e. the Einstein's tensor $G_{\mu\nu} = R_{\mu\nu} - \frac{1}{2}g_{\mu\nu}R$, is related to the matter and energy content

$$G_{\mu\nu} = 8\pi G\,T_{\mu\nu}, \tag{1.19}$$

where $R_{\mu\nu}$ is the Ricci tensor and R its trace. Einstein's equation can be derived from a least action principle, as understood in Chapter 3.

Once FLRW metric is assumed as an *ansatz*, Equation 1.19 can be solved to find $\rho(t)$ and $a(t)$. With the chosen metric, Einstein's equation results in the well-known Friedmann equations

$$\frac{1}{a}\frac{d^2 a}{dt^2} = -\frac{4\pi G}{3}(\rho + 3p),\tag{1.20}$$

$$\left(\frac{1}{a}\frac{da}{dt}\right)^2 = H^2(t) = \frac{8\pi G}{3}\rho.\tag{1.21}$$

The two Friedmann equations Equation 1.20 and Equation 1.21 are consistent with the the energy-momentum conservation

$$\frac{d\rho}{dt} = -3\frac{da}{dt}(\rho + p),\tag{1.22}$$

i.e. the continuity equation.

It is sometimes useful to rewrite Friedmann equations in conformal time (Equation 1.3)

$$\dot{\mathcal{H}}(\eta) = -\frac{4\pi G}{3}a^2\rho,\tag{1.23}$$

$$\mathcal{H}^2(\eta) = \frac{8\pi G}{3}a^2\rho,\tag{1.24}$$

where $\mathcal{H} = aH$ is the conformal Hubble parameter.

1.1.2 *Cosmic inventory*

The complete cosmic inventory includes different species. We can classify them and predict their evolution according to the equation of state (Equation 1.17) they satisfy. Radiation and relativistic matter are described by an equation of state with a constant $w = \frac{1}{3}$. Using the continuity equation (Equation 1.22), the time-dependent dilution of the radiation density can be computed to be

$$p_r = \frac{1}{3}\rho_r \quad \Rightarrow \quad \rho_r(t) = \rho_{r,0}\,a(t)^{-4},\tag{1.25}$$

where the subscript $_0$ labels the present time value. Non-relativistic matter, instead, obeys a pressureless equation of state, i.e. $w = 0$. Thus, matter density decreases with the expansion as

$$p_m = 0 \quad \Rightarrow \quad \rho_m(t) = \rho_{m,0}\,a(0)^{-3}.\tag{1.26}$$

Besides ordinary matter, radiation, and particles described by the standard model of particle physics [128], current cosmological observations agree with the presence of two other different constituents: cold dark matter (CDM), a non-baryonic,[1] pressureless fluid that interacts only through gravitation, and dark energy (DE). How to model DE is one of the subjects of this thesis and it will be discussed later in Chapter 3.

---

[1] In cosmology it is customary to address as baryonic all the known standard model matter. Usually, in the early Universe context baryonic matter stands for protons, neutrons, and electrons.

It is useful to define a dimensionless parameter to compare the amount of different constituents. From Equation 1.21, we can define the critical density as

$$\rho_{\mathrm{cr}}(t) = \frac{3H(t)^2}{8\pi G},$$

(1.27)

which depends on time and discriminates between spatial geometries. For a flat Universe $\rho(t) = \rho_{\mathrm{cr}}(t)$. From the critical density, we can define the density parameter of the species s as

$$\Omega_s(t) = \frac{\rho_s(t)}{\rho_{\mathrm{cr}}(t)}.$$

(1.28)

Different conventions are used in the literature and sometimes it is not clear if Ω_s is actually $\Omega_s(t)$ or $\Omega_s(t = t_0)$. In this work, we adopt the latter convention unless explicitly stated. Notice that $\Omega = 1$ for zero curvature. In the following table we concisely summarize the constituents of the Universe and the notation we use for each of them:

RADIATION Ω_r	Ω_γ photons
$\Omega_r = \Omega_\gamma + \Omega_\nu$	Ω_ν neutrinos
MATTER Ω_m	Ω_b baryons
$\Omega_m = \Omega_b + \Omega_c$	Ω_c cold dark matter
DARK ENERGY Ω_{DE} or Ω_Λ	Ω_{DE} generic dark energy
	Ω_Λ cosmological constant
CURVATURE Ω_{K} (= 0 for K = 0)	
$\Omega_{\mathrm{K}} = 1 - \Omega_r - \Omega_m - \Omega_{\mathrm{DE}}$	
TOTAL Ω	
$\Omega = \Omega_r + \Omega_m + \Omega_{\mathrm{DE}} + \Omega_{\mathrm{K}}$	

Given the definition of critical density in Equation 1.27 and the lack of knowledge on H_0 parametrized through h,[2] a measure of Ω_s really constraints the quantity $\omega_s \equiv \Omega_s h^2$, that is commonly used in the literature. A picture of the matter-energy budget distribution according to the standard model of cosmology and current constraints is presented in Figure 1.1.

1.2   THE LARGE-SCALE STRUCTURE OF THE UNIVERSE

At sufficiently large scales, the background Universe appears to be homogeneous and isotropic, as discussed above. However, the measured distribution of galaxies clearly shows that this is not the case at all cosmological scales. At scales larger than galaxies, inhomogeneities in the distribution of matter, or structures, are organized in identifiable patterns that form the LSS of the Universe (Figure 1.2).

In the current picture, structures formed from small initial density perturbations that developed at early times. A measure of the initial instabilities can be found in today's observations of the CMB (Figure 1.3), where relative fluctuations of the order of 10^{-5} are detected. One can introduce inhomogeneities

---

[2]This little-h matter is known for causing headaches to the unexperienced cosmologist (and sometimes to the seasoned one too).
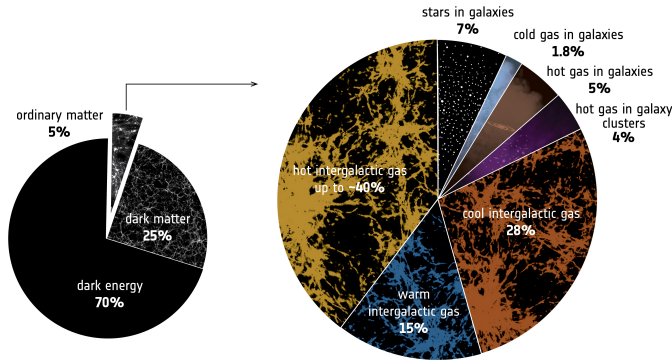
Figure 1.1: A schematic representation of the matter-energy content of the Universe. Credit: European Space Agency (https://www.esa.int/ESA_Multimedia/Images/2018/06/The_cosmic_budget_of_ordinary_matter).

perturbing the metric, the densities, and temperatures, splitting the background from the evolution of structures, and studying them separately.

In what follows, we review basic concepts of perturbation theory and the summary statistics used to describe LSS.

1.2.1 *The perturbed Universe*

Let us consider perturbations on a spatially flat background spacetime. The flat FLRW metric $\overline{g}_{\mu\nu}$ in conformal time is

$$
\begin{aligned}
\mathrm{d}s^2 &= \overline{g}_{\mu\nu}\,\mathrm{d}x^\mu \mathrm{d}x^\nu \\
&= a^2(\eta)\left[-\mathrm{d}\eta^2 + \delta_{ij}\,\mathrm{d}x^i \mathrm{d}x^j\right],
\end{aligned}
\tag{1.29}
$$

where δ_{ij} is the usual Kronecker delta. If we wish to describe a spacetime that is not perfectly homogeneous and isotropic, we can perturb the metric and consider up to the first order in the perturbations. The perturbed metric $g_{\mu\nu}$ is written as

$$
g_{\mu\nu} = \overline{g}_{\mu\nu} + \delta g_{\mu\nu},
\tag{1.30}
$$

where $\overline{g}_{\mu\nu}$ is the flat FLRW background and $\delta g_{\mu\nu}$ are the perturbations around this background. All $\delta g_{\mu\nu}$ components have to be small with respect to the background ones. Here and in the following we mark with an over-bar symbol "–" all background quantities.

In addition to metric perturbations, we also define the perturbed density of each matter-energy component

$$
\delta(\eta, \mathbf{x}) \equiv \frac{\rho(\eta, \mathbf{x}) - \overline{\rho}(\eta)}{\overline{\rho}(\eta)},
\tag{1.31}
$$
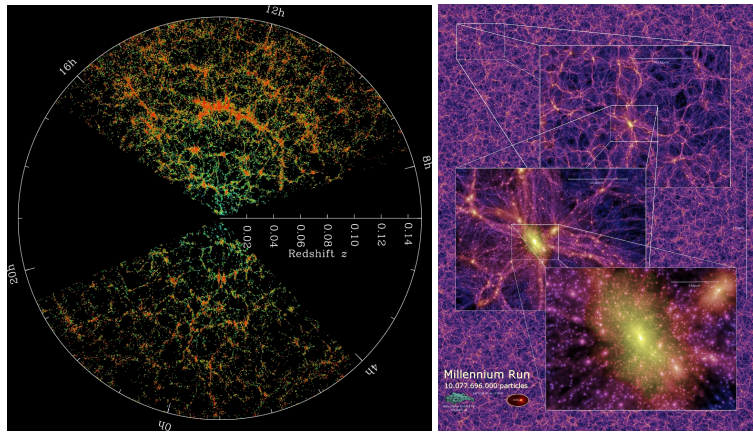
Figure 1.2: Measured (left panel) and simulated (right panel) large scale structure of the Universe, from SDSS observations (https://classic.sdss.org/home.php) and the Millennium simulation [129] respectively.

where $\delta(\eta, \mathbf{x})$ is called density contrast. In this way, we define perturbations as the difference between quantities in the physical spacetime and quantities of the background. As it is well-known, in GR field equations are invariant under a general coordinate transformation, and are, thus, left unchanged by the perturbation expansion.

The choice of the splitting between background and perturbations is not unique, i. e. there exists a gauge freedom. Perturbations in different gauges can be quite dissimilar, although all gauges are physically equivalent, i.e. observable quantities computed in different gauges are equivalent. In the literature, several gauge choices are studied. For instance, in the Newtonian or longitudinal gauge we consider an observer attached to the flat background. Following sign conventions of [120], the metric tensor in Newtonian gauge is

$$ds^2 = a^2(\eta) \left[-(1 + 2\Psi)d\eta^2 + (1 + 2\Phi)\delta_{ij}\, dx^i dx^j \right],\tag{1.32}$$

where Ψ and Φ are two scalar functions, the gravitational potentials. Connection to the Newtonian limit is straightforward in this gauge. In the following, we will work in the Newtonian gauge, the most intuitive and simple, and consider only scalar perturbations at the linear level.

The interaction between matter-energy components and spacetime properties is described by Einstein's equation. As for the metric, one can relate the perturbed Einstein's tensor to the perturbed energy-momentum tensor. At the linear level, perturbation evolution does not influence the background dynamics. Therefore, background and perturbations will follow the system of equations

$$\begin{aligned}\overline{G}_{\mu\nu} &= 8\pi G\, \overline{T}_{\mu\nu}, \\ \delta G_{\mu\nu} &= 8\pi G\, \delta T_{\mu\nu}.\end{aligned}\tag{1.33}$$
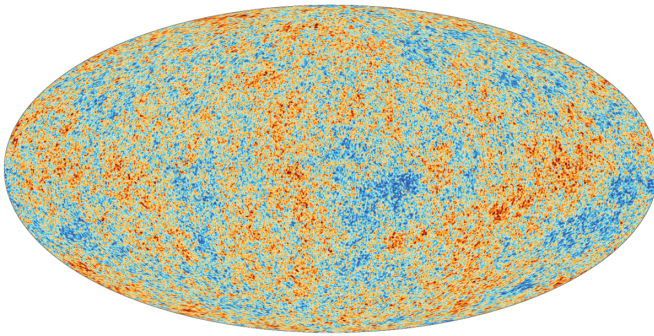
Figure 1.3: CMB temperature anisotropies map from Planck 2018 [4] observations.

Using the metric in Equation 1.32 and working in the Fourier space, from different components the following system can be derived from Equation 1.33

$$(00) \qquad k^2\Phi + 3\mathcal{H}\left(\dot{\Phi} - \mathcal{H}\Psi\right) = -4\pi G\, a^2\, \delta T^0{}_0, \tag{1.34}$$

$$(0j) \qquad k^2\left(\dot{\Phi} - \mathcal{H}\Psi\right) = -4\pi G\, ik_j\, \delta T^0{}_j, \tag{1.35}$$

$$(ii) \qquad \ddot{\Phi} + \mathcal{H}\left(2\dot{\Phi} - \dot{\Psi}\right) - \left(2\dot{\mathcal{H}} + \mathcal{H}^2\right)\Psi - \frac{k^2}{3}\left(\Phi + \Psi\right) = -\frac{4\pi G}{3}a^2\, \delta T^i{}_i, \tag{1.36}$$

$$(ij) \qquad k^2\left(\Phi + \Psi\right) = 8\pi G\, a^2\, \delta T^i{}_j. \tag{1.37}$$

Notice that these four equations are not independent: the stress-energy tensor perturbations are strictly bounded to the evolution of the gravitational potentials.

To fully describe our Universe we have to take into account the coupled evolution of all matter-energy components, i.e. baryons, radiation, CDM and DE. Matter constituents can be described as a perfect fluid. The equations that govern evolution are thus the Euler, continuity, and Poisson equations. The perturbed stress-energy tensor for a single perfect fluid, neglecting anisotropic stress, is

$$\begin{aligned}
\delta T^0{}_0 &= -\bar{\rho}\,\delta, \\
\delta T^0{}_j &= (\bar{\rho} + \bar{p})v_j, \\
\delta T^i{}_j &= \delta p\,\delta^i{}_j,
\end{aligned} \tag{1.38}$$

where δ is the density contrast previously defined, and v_j is the j component of the fluid velocity. With this stress-energy tensor definition, Equation 1.34 and Equation 1.35 can be combined to give the Poisson equation. From the perturbed stress-energy tensor conservation law one can derive the evolution equations for δ and v in Fourier space. It can be shown that, in the linear regime, these are

$$\dot{\delta} = -(1+w)(ikv + 3\Phi') - 3\mathcal{H}\left(c_s^2 - w\right)\delta, \tag{1.39}$$

$$\dot{v} = -\mathcal{H}(1+3w)v - \frac{w'}{1+w}v - \frac{c_s^2}{1+w}ik\,\delta - ik\Psi, \tag{1.40}$$

where w is the equation of state parameter, and $c_s^2 = \delta p/\delta\rho$ is the adiabatic sound speed. These equations can then be solved together with the set of per-

turbed Einstein equations to find the complete evolution. The system reduces to a second-order differential equation for the density contrast δ. The solutions to this equation describe the growth of matter structures (see Chapter 8 in [120]).

To describe photons or neutrinos we must know the evolution of the distribution function in conformal time $f(\mathbf{x}, \mathbf{p}, \eta)$, where $\mathbf{p}$ is the momentum. The distribution function evolves according to the Boltzmann equation

$$\frac{\mathrm{d}f}{\mathrm{d}\eta} = \frac{\partial f}{\partial \eta} + \frac{\mathrm{d}x^i}{\mathrm{d}\eta}\frac{\partial f}{\partial x^i} + \frac{\mathrm{d}p}{\mathrm{d}\eta}\frac{\partial f}{\partial p} + \frac{\mathrm{d}\hat{p}^i}{\mathrm{d}\eta}\frac{\partial f}{\partial \hat{p}^i} = C[f], \tag{1.41}$$

where $C[f]$ is called the collisional term and it takes into account variations of f due to collisions and interactions. For relativistic particles, f is the Fermi-Dirac distribution function for fermions or the Bose-Einstein one for bosons. In both cases, f is a function of the temperature T, which is a perturbed quantity. We can define the perturbed temperature Θ as

$$\Theta(\mathbf{x}, \hat{\mathbf{p}}, \eta) \equiv \frac{T(\mathbf{x}, \hat{\mathbf{p}}, \eta) - \overline{T}(\eta)}{\overline{T}(\eta)}. \tag{1.42}$$

In Fourier space, $\Theta(\mathbf{x}, \hat{\mathbf{p}}, \eta)$ becomes $\Theta(k, \mu, \eta)$, where $\mu \equiv \hat{k} \cdot \hat{p}$. By perturbing the Boltzmann equation (Equation 1.41) one finds the evolution equation for Θ, once the distribution function is given. Again, the equation for Θ can then be solved coupled to the perturbed Einstein equations (see Chapter 6 in [120]).

The Boltzmann formalism can be used to describe also the evolution of perturbations of different interacting species, and all non-gravitational interactions can be included in the collisional term. This leads to a set of coupled Boltzmann equations that describe the evolution of perturbation of each species involved. For instance, the photon-baryon plasma before recombination can be described by the Boltzmann equation. Here, Thomson scattering interactions source the collisional term. Let us define the optical depth τ via its conformal time derivative

$$\dot{\tau} \equiv -n_e \sigma_T a, \tag{1.43}$$

where n_e is the electron number density and σ_T is the Thomson cross section. The optical depth evaluates the tightness of the Thomson coupling. In the limit $\tau \to 0$, photons and baryons are completely decoupled. When electron density is instead high enough, baryons and photons will be tightly coupled and $\tau \gg 1$. The complete set of equations for the perturbation of a photon-baryon fluid at the linear level in the Fourier space can be computed to be

$$\dot{\Theta} = -\dot{\Phi} - ik\mu(\Theta + \Psi) - \dot{\tau}(\Theta_0 - \Theta + \mu v_b), \tag{1.44}$$

$$\dot{\delta}_b = -ikv_b - 3\dot{\Phi}, \tag{1.45}$$

$$\dot{v}_b = -\mathcal{H}v_b - ik\Psi + \frac{\dot{\tau}}{R}\left(v_b + 3i\Theta_1\right), \tag{1.46}$$

where $R \equiv 3\rho_b/4\rho_\gamma$ is the baryon to photon density ratio. Θ_0 and Θ_1 are, respectively, the monopole and the dipole term of the Legendre polynomials expansion of Θ. In a more realistic model, one should consider also effects due to the small fraction of neutrinos and non-electromagnetically interacting CDM

and DE components. Equations for neutrinos temperature perturbations, $\mathcal{N}$, and for CDM density perturbations are:

$$\dot{\mathcal{N}} = -\dot{\Phi} - ik\mu(\mathcal{N} + \Psi), \tag{1.47}$$

$$\dot{\delta}_c = -ikv_c - 3\dot{\Phi}, \tag{1.48}$$

$$\dot{v}_c = -\mathcal{H}v_c - ik\Psi, \tag{1.49}$$

where we highlight that Equation 1.48, Equation 1.49 are nothing but Equation 1.39, Equation 1.40 for a pressureless fluid ($w = 0$ and $c_s^2 = 0$). We discuss DE influence on perturbations in Chapter 3.

Once the initial conditions are given, it is possible to solve the system of coupled Boltzmann and Einstein equations in order to find the linear time evolution of the perturbations. According to the ΛCDM paradigm, perturbations arise during the inflationary period. Therefore, initial conditions must be set at very early times in the radiation-dominated era.

1.2.2 *Two point statistics and power spectra*

Cosmological observations are very different from experimental measures in other fields of physics. Due to the fact that we can access only one Universe, we cannot really *make* experiments. We cannot reproduce in our laboratories the feature of the Universe. We can try to test our theoretical model only via observations of what already exists. Let us consider the density contrast, predicting the value that $\delta(\eta, \mathbf{x})$ will assume at each point $\mathbf{x}$ is challenging. However, statistics offers us a more feasible alternative. The Universe is actually only one particular realization among the *ensamble* of all random possible outcomes of evolution. In this sense, we can only predict and compare average statistical properties. Due to homogeneity and isotropy, the cosmological principle implies that independent regions of the Universe, i.e. widely separated, must have the same average properties. Therefore, averaging over the *ensamble* realizations is equivalent to averaging over a large enough volume of our unique observable realization. Consequently, the portion of the Universe that we observe is a statistically fair representative sample. In conclusion, we can test theoretical predictions through the statistical properties of the observables. In particular, we consider random fields, i.e. fields that assume random values at each point according to a probability distribution function.

In general, a random field $\phi(\mathbf{x})$ is fully described by all its correlation functions $\langle \phi(\mathbf{x}_1) \dots \phi(\mathbf{x}_N) \rangle$, i.e. the n-point statistics, where we average over volume. Due to homogeneity, we will usually consider $\langle \phi(\mathbf{x}) \rangle = 0$. Of particular interest is the two-point correlation function $\xi(x)$

$$\xi(x) \equiv \langle \phi(\mathbf{x}_1)\phi(\mathbf{x}_2) \rangle, \quad \text{with} \quad x = |\mathbf{x}_1 - \mathbf{x}_2|. \tag{1.50}$$

Notice that ξ is a function only of the separation x due to isotropy. We can then derive the variance of the field as

$$\sigma^2 = \xi(0) = \langle \phi^2(\mathbf{x}) \rangle. \tag{1.51}$$

It is often useful to go to Fourier Space. In general $\phi_{\mathbf{k}}$, the Fourier transform of $\phi(\mathbf{x})$, will be a complex number. Then we can define the power spectrum $P(k)$ as

$$\langle \phi_{\mathbf{k}}^* \phi_{\mathbf{k}'} \rangle = (2\pi)^3 P(k) \, \delta(\mathbf{k} - \mathbf{k}'), \tag{1.52}$$

where $\delta(\dots)$ is the Dirac delta function. The power spectrum is related to the two-point correlation function through

$$\xi(x) = \frac{1}{(2\pi)^3} \int \mathrm{d}^3 k \, P(k) \, e^{i\,\mathbf{k}\cdot\mathbf{x}}. \tag{1.53}$$

Thus, they are the Fourier transform one of the other. $P(k)$ and $\xi(x)$ carry the same amount of information and are used in the study of random fields. They quantify how the given field is distributed in the tridimensional space. E. g., if the random field is the density contrast, the power spectrum or the two-point correlation function describes how matter structures are organized in the Universe.

We call a Gaussian random field a field whose probability distribution is Gaussian. Gaussian random fields are of particular interest in cosmology. We consider to good approximation all perturbation fields as Gaussian. As a matter of fact, Gaussian fields are easy to handle analytically and they are fully described by the two-point correlation function or the power spectrum. Moreover, in Fourier space, different modes are mutually independent. For Gaussian fields, phases of different modes follow a random distribution. Therefore, at the linear level, Gaussian fields remain Gaussian during evolution. Inflationary models usually predict Gaussian or almost Gaussian initial fluctuations [130], although non-gaussianities and higher point statistics are currently objects of study [131, 132].

1.2.3 *The linear matter power spectrum*

The LSS of the Universe at a given redshift is well described by the matter power spectrum. Perturbations are not always allowed to grow freely and they are subjected to very different phenomena during Universe evolution. To predict the form of the matter power spectrum today, one needs to know the effect on perturbations of all the processes that took place from the early Universe until today. In the following, we are going to give a qualitative picture of how today's matter power spectrum is computed.

According to the current paradigm, initial perturbations originate from inflation. Fluctuations of the gravitational potential at the end of inflation are nowadays parametrized by means of the power spectrum of the curvature perturbations $\mathcal{R}$, a gauge invariant quantity. This can be computed to be

$$P_{\mathcal{R}}(k) = 2\pi^2 A_s k^{-3} \left(\frac{k}{k_{\mathrm{p}}} \right)^{n_s - 1}. \tag{1.54}$$

A_s is the variance of curvature perturbations at the given pivot scale k_{p}.[3] The parameter n_s is the scalar spectral index. The spectrum is said scale-invariant

---

[3] Note that the value of k_{p} is arbitrary and it is usually taken to be the scale at which a given experiment is most sensitive.

if $n_s = 1$. Nearly scale-invariant spectra are usually predicted by inflationary models.

During inflation, perturbations at different scales exit the Hubble horizon due to the accelerated expansion. When decelerated expansion begins, all perturbations slowly enter back inside the horizon during the radiation-dominated era or later during the matter-dominated one. A perturbation is defined to be inside (outside) the horizon if its mode k is $k \geq 1/d_H$ ($k \leq 1/d_H$). Therefore, we can identify two regimes:

(i) perturbations that entered the horizon in the radiation-dominated era and thus have $k \gg k_{eq}$, where k_{eq} is the wavelength that corresponds to the size of the horizon at the equality between matter and radiation;

(ii) perturbations that entered the horizon after equality and thus have $k \ll k_{eq}$.

In order to compute the matter power spectrum at the present time, one has to find the evolution of the gravitational potential Φ from the radiation-dominated era until today. All changes in Φ are embedded in the transfer function $T(k)$, defined as

$$T(k) \equiv \frac{\Phi(k, a_T)}{\Phi_{LS}(k, a_T)}, \tag{1.55}$$

where the large-scale potential is

$$\Phi_{LS}(k, a_T) = \frac{9}{10}\Phi(k, a_i). \tag{1.56}$$

The value of a_T is usually taken to be $a_T \sim 0.03$ and marks the epoch after which Φ stops to be dependent on k. Here, a_i is the initial time, at the end of inflation. The exact dependence of T on k during the Universe evolution results from the perturbation equations (see Section 1.2.1). It is possible to see that

$$\text{(i) for } k \gg k_{eq}, \qquad T(k) \propto \frac{\ln k}{k^2}, \tag{1.57}$$

$$\text{(ii) for } k \ll k_{eq}, \qquad T(k) \simeq 1, \tag{1.58}$$

i.e., perturbations are free to grow on large scales while they are suppressed on small scales inside the horizon. For $a \geq a_T$ the gravitational potential Φ is constant in k, but when cosmic acceleration begins Φ may vary again. To take this effect into account, the growth factor function $D(a)$ is introduced as

$$\frac{\Phi(a)}{\Phi(a_T)} = \frac{D(a)}{a} \quad \text{with} \quad a \geq a_T. \tag{1.59}$$

The exact form of $D(a)$ depends on the expansion model considered.

Finally, all these factors sum up to give

$$\Phi(k, a_0) = \frac{9}{10}\Phi(k, a_i)T(k)D(a_0). \tag{1.60}$$

Since matter perturbations are related to the gravitational potential through

$$\delta_m(k, a_0) \propto k^2 \Phi(k, a_0), \tag{1.61}$$
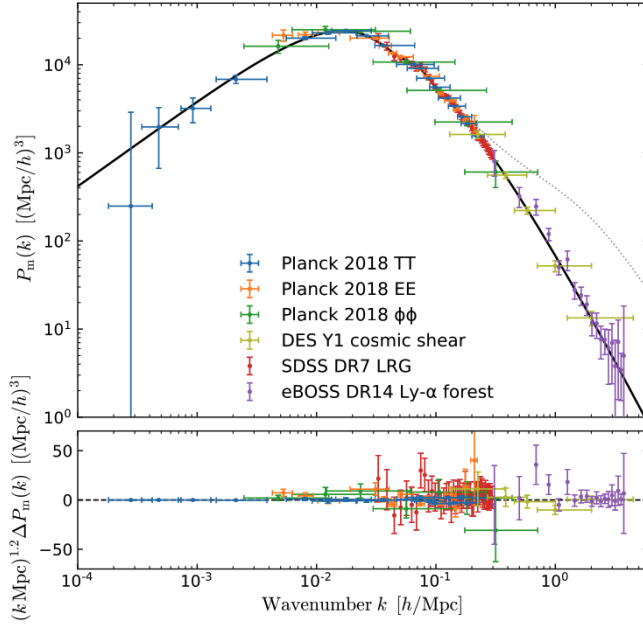
Figure 1.4: The theoretical and measured linear matter power spectrum. Plot reproduced from[133].

the linear matter power spectrum $P_m(k)$ calculated at the present time is

$$
\begin{aligned}
P_m(k) &= \langle |\delta_m(k, a_0)|^2 \rangle \\
&\propto A_s k^{n_s} T^2(k) D^2(a_0).
\end{aligned}
\tag{1.62}
$$

It is possible to see that

(I) for $k \gg k_{eq}$, $P_m(k) \propto k^{n_s-4}(\ln k)^2$,   (1.63)

(II) for $k \ll k_{eq}$, $P_m(k) \propto k^{n_s}$.   (1.64)

Thus, the linear matter power spectrum increases at large scales and decreases at small ones. The maximum of $P_m(k)$ will depend on k_{eq}, on the matter-energy content of the Universe, and on the expansion history. The theoretical and measured linear matter power spectrum is shown in Figure 1.4.

1.3   ΛcDM SIX PARAMETERS TO DESCRIBE THE UNIVERSE

The accepted concordance model of cosmology is the ΛCDM model. Indeed, cosmological observations point to a flat Universe dominated today by dark constituents. The standard model of cosmology relies on:

- the existence of a CDM component ($w = 0$), that must drive the growth of baryonic perturbations after recombination;

- the existence of a DE component, responsible for today's accelerated expansion compatible with the effects of a cosmological constant Λ ($w = -1$);

- an inflation paradigm, i.e. a mechanism that generates the primordial perturbations, that will later grow into the late-time LSS.

The ΛCDM model is in agreement with a variety of observations, such as CMB, supernovae, and geometrical and dynamical measurements from the LSS [4–7]. In the following, we describe the technical aspects of the ΛCDM model, useful to understand the results presented in this work.

When talking about ΛCDM, what the cosmologist has in mind, besides the paradigm presented above, is the set of values assumed by six fundamental parameters. These six are the least number of cosmological parameters needed to describe the shape of the matter and CMB power spectrum, the expansion, and the matter-energy content of the Universe. Cosmological observations aim at getting better and better constraints on these parameters. At the state of the art, Planck 2018 [4] and LSS (see e.g. [134]) observations are usually recognized as the standard reference for a ΛCDM cosmology. Here is a list of the parameters, their meaning, and their assumed value (according to [4]).

PARAMETER	VALUE	DESCRIPTION
$\Omega_b h^2$	0.022383	Ω_b and Ω_c are dimensionless quantities that describe the fractional content of baryonic and cold matter today, defined in Equation 1.28. Here, it is understood that $\Omega_{TOT} = \Omega_\Lambda + \Omega_b + \Omega_c + \Omega_\nu = 1$, where Ω_ν is fixed and encompass the contribution from one massive neutrino. Given that we deal with real observations, the actual measured quantities are $\Omega_b h^2$ and $\Omega_c h^2$. A Planck 2018 cosmology ($h = 67.32$), implies that $\Omega_b = 0.049$ and $\Omega_c = 0.265$, i.e. 5% and 26% of the total matter-energy budget respectively, as depicted in Figure 1.1.
$\Omega_c h^2$	0.12011	
$100\theta_{MC}$	1.040909	θ_{MC} is a numerical approximation of the angular size of the sound horizon, based on [135]. It is implemented in a widely used code: CosmoMC [136] (and from here the subscript MC). If θ_{MC} is fixed among the other parameters, then H_0 can be derived and, thus, one can equivalently choose to use either θ_{MC} or H_0. However, when dealing with CMB observations the size of the sound horizon is a more natural choice, given that the position of the peaks is a direct measure of θ_{MC}. Furthermore, variations in θ_{MC} prompt milder modifications to the observables with respect to H_0. It is, thus, easier to handle θ_{MC} from a numerical point of view. For these reasons, θ_{MC} is used in seminal papers in literature (e.g. [137]) and in this thesis too.
τ	0.0543	τ is the optical depth defined in Equation 1.43 due to reionization, i.e. integrated from now to the end of the epoch of reionization. It can provide constraints on the redshift at which reionization occurs besides on galaxy evolution models. The parameter is sometimes dubbed as τ_{reio}, to avoid confusion.

$\ln(10^{10}A_s)$	3.0448	A_s and n_s are the amplitude of the primordial curvature perturbations and the scalar spectral index as defined in Equation 1.54, at the pivot scale $k_p = 0.05$ Mpc^{-1}. They set the features of the initial conditions. The effects of varying them can be seen in later time probes too, e.g. in the matter power spectrum. The measured spectral index point towards an almost scale-invariant primordial power spectrum (i.e. $n_s \sim 1$).
n_s	0.96605	

From these six cosmological parameters, several others can be derived. Here, we gather the most used ones and relevant for this work:

PARAMETER	VALUE	DESCRIPTION
H_0	67.32 km s^{-1} Mpc^{-1}	The current value of the expansion rate, i.e. the Hubble constant (Equation 1.6). The measured value of H_0 is a hot topic in today's cosmology circles. Indeed, the value presented here is the CMB measurement, however, some later times probes prefer higher values of H_0, greater than 70 km s^{-1} Mpc^{-1}. If this discrepancy hides new physics is still to be understood (see e.g. [11]).
Ω_m	0.3158	Today's matter density parameter, comprehensive of massive neutrinos. The measured value implies that $\Omega_\Lambda = 0.6842$ for a flat cosmology.
σ_8	0.8120	Today's matter power spectrum normalization at linear scales, including baryons, CDM and massive neutrinos. This parameter is an alternative to the power spectrum amplitude A_s and it is mostly used in LSS studies. It is defined as the root mean square of the matter fluctuations field δ, filtered at the scale $R = 8 h^{-1}$Mpc, the approximate scale at which growth of structure becomes non-linear. Lower values of σ_8 imply smoother matter distribution. The value of σ_8 inferred by Early Universe probes differs from the one from LSS. This results in a second milder tension, that could lead to new physics [138].

Despite the indisputable success of the standard cosmological model, some major questions still remain unanswered. From the theory side, the unknown

nature of dark matter and dark energy required an intense effort to propose alternative models [13, 139]. Discrepancies in different cosmological observations, seen in the tensions on the H_0 and $\sigma_8 - \Omega_m$ constraints, also motivated an extensive quest for new physics [8–11]. However, although an impressive number of alternative models has been tested, at the state-of-the-art the observational data seem to have no clear preference for a specific beyond ΛCDM model.

In the final analysis, the standard model of cosmology withstands and it is still the theory most supported by observations. Upcoming observations, such as the Euclid mission [34] and the SKAO[4], will allow unprecedented high-precision tests of gravity on large cosmological scales, allowing for yet a new trial for the ΛCDM model.

1.3.1   *Going beyond ΛCDM*

When going beyond the standard model of cosmology, one can study the effect of adding some additional parameters that govern beyond ΛCDM effects. The most common modifications involve the following parameters, where we indicate the fiducial value they assume in a ΛCDM cosmology.

| PARAMETER	ΛCDM VALUE	DESCRIPTION
w or w_0 w_a	-1 0	The w parameter, or sometimes w_0, is the equation of state parameter that relate DE pressure to density. In a ΛCDM scenario it is fixed to the negative value of -1. However, several alternatives have been proposed and studied. The simplest DE modification is changing w to a non-standard value. This scenario is usually referred to as the wCDM model. Among other more complex and time-dependent modifications, we mention the Chevallier-Polarski-Linder (CPL) parametrization. Here, w is a linear function of the scale factor a [140] $w = w_0 + (1-a)\,w_a$.
A_L	1	Although it is not a physical extension of ΛCDM, the A_L issue puzzles cosmologists since first CMB detections [141]. A_L is an overall factor that rescales the lensing potential CMB power spectrum as $\mathcal{C}^{\Phi\Phi} \to A_\mathrm{L}\mathcal{C}^{\Phi\Phi}$. It affects the temperature power spectrum by smoothing the peaks. It does not carry any physical meaning and it was introduced to assess deviations of the measured power spectra to theoretical predictions. The GR predicted value is $A_\mathrm{L} = 1$, however, CMB data show a mild preference for $A_\mathrm{L} > 1$, with a significance of $\sim 2\sigma$ [4]. It remains unclear if $A_\mathrm{L} = 1$ hides not understood systematic or new physics. Although it is the mildest among the three cosmological tensions, it has been seen that A_L is strictly intertwined with H_0 and σ_8. The current challenge is to propose a model that reconciles all the tensions at the same time [138].

---

[4] See https://www.skao.int/.
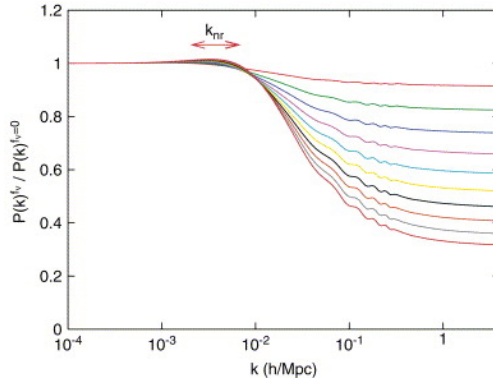
Figure 1.5: Modifications induced by massive neutrinos on the matter power spectrum. Defining the density fraction as $f_\nu = \Omega_\nu / \Omega_m$, the figure shows the ratio between the matter power spectrum with f_ν between 0.01 and 0.1 and the matter power spectrum for massless neutrinos. Image reproduced from [142].

Varying the fiducial ΛCDM value of these parameters is already considered an alternative theory. If one wants to study more specific models beyond ΛCDM, e.g. alternative theories of DE, additional parameters describing the modified model must be considered, as discussed in Chapter 3.

1.3.1.1 *Massive neutrinos*

Cosmological observations can probe fundamental physics. A distinguished example is the constraints cosmology can provide on the neutrino mass. In the following, we review key concepts in the theory of cosmological neutrinos. For a complete review, we refer to [142].

Neutrinos can modify cosmological observables mainly due to the total mass. Indeed, the neutrino mass affects the evolution of the total energy density. At higher energies, neutrinos are relativistic and follow radiation evolution. When they become non-relativistic their velocity decays and they contribute to the matter density. This in turn modifies the expansion through the Friedmann equations.

Neutrino perturbations are, instead, affected by the neutrino mass through the neutrino free-streaming. Due to their high velocities, neutrinos stream out of higher-density regions towards lower-density ones. This results in a damping of the structures smaller than the neutrino mean free path, i.e. the free-streaming length. The minimum free-streaming scale is computed to be

$$k_{fs} \simeq 0.018 \sqrt{\Omega_m \frac{m}{1\,\text{eV}}} h\,\text{Mpc}^{-1}, \tag{1.65}$$

where m is the mass of the involved neutrinos. Scales larger than k_{fs} ($k < k_{fs}$) are not affected by free streaming.

Through measurements of the CMB and matter power spectra it is possible to infer bounds on the neutrino mass. The CMB temperature power spectrum is affected by the neutrino mass mainly through the neutrino density Ω_ν. The effect on the matter power spectrum is ascribable to the free-streaming. Higher

neutrino masses would result in a stronger suppression of the small-scale power, as shown in Figure 1.5.

Some of the relevant parameters that describe cosmological neutrinos are the following:

PARAMETER	ΛCDM VALUE	DESCRIPTION
Σm_ν	0.06 eV	It is the total neutrino mass, summed over the three neutrino species. It can be linked to the neutrino density parameter as $\Omega_\nu h^2 = \Sigma m_\nu / 94$ eV. Current constraints from particle physics are $\Sigma m_\nu \geq 0.06$ eV [143] and $\Sigma m_\nu < 0.8$ eV [144].
N_{eff}	3.046	Effective number of neutrino species. It includes the three neutrino species and the contribution from relativistic neutrino relics. N_{eff} enters in the total radiation density as $\rho_r = (1 + \frac{7}{8} \left(\frac{4}{11}\right)^{4/3} N_{eff})\rho_\gamma$. Detecting any variation from this value would be proof of non-standard neutrino physics.

In this work, we focus on the effect of massive neutrinos, i.e. of constraining Σm_ν that we discuss in Chapter 8.

2

PROBING THE UNIVERSE

I N CHAPTER 1, we summarized the main features of an expanding Universe from a theoretical point of view. Here, we focus on the matter of constraining the cosmological parameters that describe the ΛCDM model and beyond.

We introduce the cosmological observables relevant to this thesis in Section 2.1. An overview of the state-of-the-art of cosmological surveys is given in Section 2.2. We conclude by presenting the statistical analysis techniques that we use in Section 2.3. The content of this chapter is mainly based on [14, 120].

2.1 COSMOLOGICAL OBSERVABLES

We review the cosmological observables considered in this thesis: the cosmic microwave background, which probes the Universe at recombination, galaxy clustering, and line intensity mapping, which allows probing large volumes of the late-time Universe.

2.1.1 *Cosmic microwave background anisotropies*

The cosmic microwave background (CMB) is the relic radiation from recombination, which occurred almost 380 000 years after the Universe's birth, corresponding to the redshift $z \simeq 1100$. Before recombination, the Universe consists of a hot plasma of baryonic matter and radiation tightly coupled by Thomson scattering processes. When radiation decouples from baryonic matter, the Universe becomes transparent and photons are free to stream. During the decoupling process photons are scattered by electrons for the last time. This takes place in an interval $\Delta z \simeq 100$ at the so-called last scattering surface. Electrons are now free to combine with protons and neutrons to form atomic neutral hydrogen for the first time. Photons from the last scattering surface are what we observe as the CMB radiation today. First discovered in 1963 [145], the CMB is a microwave radiation uniform in all directions of the sky. It presents an almost perfect black body spectrum centered on the temperature $\bar{T} = 2.725\,\mathrm{K}$ [146].

Although the CMB temperature distribution is close to homogeneous, COBE [147] experiment first, WMAP [148] and Planck [137] later, detected fluctuations in the temperature distribution. The most updated temperature map shows relative anisotropies of the order of 10^{-5} (see Figure 1.3). Properties of temperature inhomogeneities can be derived by perturbation theory, making the statistics of CMB anisotropies today an important probe to test cosmological models.

We call anisotropies the fluctuations that we observe today, due to the fact that CMB temperature varies among the direction of observation. At recombination,

temperature fluctuations were actually isotropic, but not homogeneous. Inhomogeneities at recombination are seen as anisotropies today. Let us consider temperature fluctuations Θ as defined in Equation 1.42. We fix the observer on Earth at the present time, thus Θ will be a function only of the direction of observation in the sky $\hat{\mathbf{n}}$. It is useful to expand fluctuations in spherical harmonics

$$\Theta(\hat{\mathbf{n}}) = \sum_{\ell m} \Theta_{\ell m} Y_{\ell m}(\hat{\mathbf{n}}). \tag{2.1}$$

The temperature power spectrum[1] C_ℓ is defined by the spherical harmonics coefficients as

$$\langle \Theta_{\ell m}^* \Theta_{\ell' m'} \rangle = \delta_{\ell\ell'} \delta_{mm'} C_\ell. \tag{2.2}$$

It is possible to see that the spatial temperature power spectrum $P^T(k)$ of inhomogeneities is related to the angular power spectrum C_ℓ of anisotropies via

$$\frac{\ell(\ell+1)}{2\pi} C_\ell \simeq \frac{k^3}{2\pi} P^T(k). \tag{2.3}$$

It is then custom to study the quantity $\frac{\ell(\ell+1)}{2\pi} C_\ell \equiv \mathcal{D}_\ell$ instead of C_ℓ only.

The CMB temperature (TT) power spectrum has a well-understood and rich structure (see e.g. [149]). It presents a fixed number of peaks, i.e. the acoustic peaks, and troughs, each of them resulting from all the physical processes that take place at recombination. Variations in the cosmological parameters affect the structure of the power spectrum. Although the intricate relations between the numerous cosmological parameters make it sometimes difficult to detangle each separate effect, we summarize the impact of each parameter presented in Section 1.3 as follows:

- changing the matter content, i.e. $\Omega_b h^2$ and $\Omega_c h^2$, affect both the relative position and the amplitude of the peaks. Indeed, $\Omega_b h^2$ modifies the structure of the peaks due to its relation to the sound horizon. $\Omega_c h^2$, instead, drives the BAO (see Section 2.1.2 below). Current CMB observational errors allow for a precise measure of both $\Omega_b h^2$ and $\Omega_c h^2$;

- varying the initial conditions, i.e. A_s and n_s change the temperature angular power spectrum in a more obvious way. A_s affects the overall amplitude, while a shift $n_s \to n_s + \alpha$ induce a $(\ell/\ell_p)^\alpha$ scaling at small scales, with ℓ_p being the scale corresponding to the pivot one;

- the effects of reionization on the CMB is modulated by τ. Higher values of τ suppress anisotropies at small scales. It is more difficult to measure A_s and n_s and τ with the CMB due to the fact that changing τ can mimic the effect of varying A_s and n_s, introducing a correlation between these parameters and, thus, higher uncertainties;[2]

- DE influences the position of the peaks in the power spectrum, leaving unchanged the global structure and the number of peaks. However, the main effect of DE is on the behavior of C_ℓ at very large scales, through the Integrated Sachs-Wolfe (ISW) effect (see e.g. [151]). The best constraints

---

[1] We highlight that although C_ℓ is dimensionless it is usually shown in plots with $(\mu K)^2$ units, where C_ℓ is implicitly multiplied by $\bar{T}^2$.

[2] As it is well-known, polarization measurements can break this degeneracy, improving the constraints [150].

on DE, whose strongest effects appear at late times, are obtained by combining CMB observations to other LSS probes.

Although photons at decoupling are initially not polarized, inhomogeneities can lead to linearly polarized relic radiation. In analogy to electromagnetism, it is possible to parametrize polarization through E-modes and B-modes. E-modes arise naturally from Thomson scattering occurring through the last scattering surface. B-modes, instead, are connected to the gravitational waves relic predicted by inflation. Detection of B-modes is still an open challenge. The polarization field can then be treated similarly to the temperature field. Therefore, polarization power spectra are defined as

$$
\begin{aligned}
\langle E_{\ell m}^* E_{\ell m} \rangle &= \delta_{\ell\ell'}\delta_{mm'}C_l^{EE} \\
\langle B_{\ell m}^* B_{\ell m} \rangle &= \delta_{\ell\ell'}\delta_{mm'}C_l^{BB},
\end{aligned}
\tag{2.4}
$$

where $E_{\ell m}$ and $B_{\ell m}$ are the coefficients of the spherical harmonics decomposition of the polarization field.

Besides the polarization power spectra Equation 2.4, it is possible to study also the lensing potential power spectrum $C_\ell^{\phi\phi}$ [152].

2.1.2 *Galaxy clustering*

The matter power spectrum introduced in Equation 1.62 has a rich structure that carries key cosmological information. Unfortunately, there is no direct probe of the matter field, making a direct measure of P_m impossible. However, through measurements of baryonic matter tracers, such as the distribution of galaxies, properties of the matter power spectrum can be inferred indirectly.

Observing the tri-dimensional distribution of galaxies (see Figure 1.2) allows for a measure of the galaxy power spectrum P_g. The dependence of P_g on P_m can be exploited by taking into account two main effects. Galaxies are only a fraction of the matter content of the Universe and, thus, their distribution does not follow precisely the full matter distribution. One can correct this effect by introducing a scale-independent bias factor b_g

$$
P_g(k,z) = b_g(z)^2 P_m(k,z)
\tag{2.5}
$$

at linear order. On top of that, galaxies usually have peculiar velocities which can induce distortions in the observed power spectrum and redshift. In the redshift space, at large scales, these distortions can be cast in an additional term according to the Kaiser effect [153]. The power spectrum can thus be modeled as

$$
P_g(k,z,\mu) = [b_g(z) + f(z)\mu^2]^2 P_m(k,z),
\tag{2.6}
$$

where $f \equiv \mathrm{d}\ln D(a)/\mathrm{d}\ln a$ is the growth rate[3] and $\mu = \hat{z} \cdot \hat{k}$ is the cosine between the line of sight and the wavevector **k**. The distortion term models the effect of peculiar velocities in two ways: given that $f\mu^2$ is a positive quantity it enhances apparent overdensities with respect to the real space ones; the maximum enhancement appears only along the line of sight, i.e. for wavevectors parallel to the line of sight (and with $\mu = 1$), while the Kaiser effect is not present for perturbations along the transverse direction ($\mu = 0$).

---

[3]For a ΛCDM cosmology it can be computed that $f(a) \sim \Omega_m(a)^{0.55}$.

Assuming a Poissonian sampling of the galaxy distribution, it is possible to associate a white noise, called shot noise, with the measured power spectrum. It can be seen that

$$P_{\mathrm{SN}} = \frac{1}{\bar{n}_{\mathrm{g}}}, \tag{2.7}$$

where $\bar{n}_{\mathrm{g}}$ is the mean number density of galaxies, which in general would depend on the considered redshift. The full expression of the galaxy power spectrum is then

$$P_{\mathrm{g}}(k, z, \mu) = [b_{\mathrm{g}}(z) + f\mu^2]^2 P_{\mathrm{m}}(k, z) + P_{\mathrm{SN}}(z). \tag{2.8}$$

This model can be extended to include more complex LSS features such as the finger of God effect (see e.g. [154]).

Varying the cosmological parameters modifies $P_{\mathrm{g}}(k, z, \mu)$ mainly through its dependence on the matter power spectrum. Measuring $P_{\mathrm{g}}(k, z, \mu)$ cannot provide direct measurements of the cosmological parameters. However, it can provide constraints on the combination of parameters $b_{\mathrm{g}}\sigma_8$ and $f\sigma_8$, where σ_8 is defined in Section 1.3. This latter is a valuable probe, in particular, to constrain DE theories.

As discussed earlier, soon before recombination the Universe consists mainly of a baryon-photon plasma. DM is already decoupled, while photons and baryons are tightly coupled to each other via Thomson scattering interactions. Perturbations already formed, but only DM ones are free to grow. Instead, baryon and photon perturbations are forced to evolve together as a single two-component fluid. Due to the large number of photons, the high pressure of the fluid acts against the gravitational collapse of baryons, causing the baryon-photon fluid to escape the over-density regions. In this way, spherical sound waves are created. This process will result in oscillations in the baryon-photon plasma, namely baryon acoustic oscillations (BAO). Sound waves are free to travel through the plasma with a speed equal to a significant fraction of the speed of light. As baryons and photons start to decouple, the sound waves progressively slow down until they stop at recombination. After recombination, photons and baryonic matter evolve separately: photons stream freely, while baryons perturbations grow via gravitational instability. Yet acoustic oscillations leave a trace in both photon's and baryons' subsequent evolution. Therefore, we can observe the BAO imprints in the power spectrum and in today's galaxy distribution.

Acoustic oscillations follow theoretically from perturbation theory (see Equation 1.44-Equation 1.46 and Equation 1.34-Equation 1.37). In the tight coupling approximation, perturbations are described by a second-order differential equation, that has an oscillating solution with a period that depends on the baryon density. A fundamental parameter is the sound horizon r_s

$$r_s(\eta) \equiv \int_0^{\eta} \mathrm{d}\tilde{\eta}\, c_s(\tilde{\eta}), \tag{2.9}$$

where $c_s(\eta)$ is the adiabatic sound speed of the coupled photon-baryon fluid. The sound horizon estimates the distance traveled by a sound wave until time η. The size of the sound horizon at recombination $r_s^* = r_s(\eta_{\mathrm{rec}})$ is a fundamental scale that can be used as a standard ruler. The sound horizon at recombination sets the location of the first peak in the CMB power spectrum. The BAO feature

appears in the large-scale structure as an enhancement in the two-point galaxy correlation function. The BAO imprint in the galaxy distribution was first measured at a scale of around 150 Mpc [155]. The value of r_s^* strongly depends on the DE amount. Therefore, the measure of the BAO scale is a fundamental probe to test expansion history and DE theories.

2.1.3 *Line intensity mapping*

Line intensity mapping (LIM or IM) [52] has recently become a promising cosmological probe. It has the potential to fill the gap between the epoch of recombination, probed by the CMB, and late-time Universe properties, seen through galaxy clustering observations. LIM measures the integrated emission of the spectral line of interest from multiple galaxies and the intergalactic medium. It samples the sky with low angular resolution, allowing for fast surveys of exceptionally large 3D volumes. Given that the emission frequency of the targeted line is usually well-known, with LIM it is possible to precisely estimate the redshift of the source and construct tomographic, i.e. within multiple bins, observations. Therefore, LIM surveys may be able to explore the Universe at unprecedented redshifts hardly accessible by other LSS probes.

The post-reionization LIM signal is a biased tracer of the underlying matter distribution at different redshifts. The observable is the power spectrum of the brightness temperature (T_b) perturbations and it can be modeled similarly to the galaxy power spectrum (Equation 2.8). At a given redshift, the power spectrum for a given line L can be expressed as

$$P_{\mathrm{L}}(k, z, \mu) = \bar{T}_b^2(z)[b_{\mathrm{L}}(z) + f\mu^2]^2 P_{\mathrm{m}}(k, z) + P_{\mathrm{SN}}(z), \qquad (2.10)$$

where $\bar{T}_b$ is the mean brightness temperature of the line [39], b_{L} is the bias of the considered probe, P_{m} and P_{SN} are the matter and shot noise power spectra respectively. Both the bias and the shot-noise term are dependent on the line luminosity function. In literature, both the angular power spectrum and the power spectrum multipoles are widely used. We refer to [156] for a review on how to model the LIM signal.

One of the most studied lines is the 21cm signal arising from the spin-flip transition in the neutral hydrogen HI ground state [35, 36, 39, 157, 158]. Studying the 21cm cosmology offers a possibility of probing MG effects at high redshifts [159, 160]. At lower redshifts, neutral hydrogen HI-dominated galaxies also emit 21cm [161], providing a key cosmological probe of LSS properties.

Rotational lines of carbon monoxide (CO) [162–164], fine structure line of ionized carbon (CII) [165, 166], as well as Lyman-α, Hα, and Hβ lines [167–170] are also interesting spectral features that complement the 21cm line.

Overall, LIM is suited to probe gravity and LSS in a wide redshift range. It additionally allows to constrain the BAO features evolution and, thus, constrains the background evolution [52].

2.1.4 *Numerical predictions of cosmological observables*

Analytic solutions to the coupled Einstein and Boltzmann equations cannot always be easily found. However, numerical techniques can be used to find the full solutions. An Einstein-Boltzmann solver is a numerical code that solves the

linearized set of all the coupled Einstein and Boltzmann equations introduced before. Einstein-Boltzmann solvers appeared first in the eighties in the seminal works [171] and [172]. Computations are in general numerically expensive and a turning point was the CMBFAST code, which with the line-of-sight integration techniques reduced the calculation time by orders of magnitude. This led to the birth of modern Einstein-Boltzmann solvers, such as the most widely used CAMB [173] and CLASS [174], or DASh [175] and CMBEASY [176]. In this thesis, we mainly use the code CAMB, *Code for Anisotropies in the Microwave Background*,[4] and its extensions. Given a specific cosmological model, CAMB numerically solves the coupled Einstein-Boltzmann equations during the evolution. The outcome of CAMB consists mainly of the CMB and matter power spectra. Implementing in CAMB the computation of the late-time 21cm intensity mapping power spectrum is an integral part of this thesis.

Numerically computed observables can be then compared with experimental data to constrain the cosmological parameters. We are going to review observations and analysis techniques in the next sections.

2.2   COSMOLOGICAL OBSERVATIONS

In the era of precision Cosmology, a variety of observational campaignes has been carried out. Moreover, ongoing and planned cosmological surveys are expected to change or confirm the current standard model with unprecedented sensitivity.

2.2.1   *CMB surveys*

CMB experiments measure the temperature and polarization fluctuations of photons emitted from the last scattering surface. The main parameters defining a CMB survey are the sky area, the angular resolution set by the telescope beam, the frequency coverage and resolution, the sensitivity to the fluctuations, and the noise level at different frequency channels. CMB experiments provide insights into the early Universe and complement LSS probes.

The first main CMB experiment was the Cosmic Background Explorer (COBE) [177] satellite, which conducted a full sky survey with an angular resolution of $7°$. Its two full-sky successors were the Wilkinson Microwave Anisotropy Probe (WMAP) [178], with a resolution of $0.3°$, and the Planck satellite [137], with a resolution of 10 arcmin. Ground-based surveys include the Atacama Cosmology Telescope (ACT) [179, 180], which covers area of 1 000 deg^2 with resolution of ~ 1 arcmin, the South Pole Telescope (SPT) [181, 182], which covers 500 deg^2 with resolution ~ 1 arcmin, BICEP/Keck [183], and the Cosmology Large Angular Scale Surveyor (CLASS) [184]. In the future, the Stage 4 CMB observatory CMB-S4 [185] will cover 8 000 deg^2 and achieve a resolution < 3 arcmin, while the Simons Observatory [186] will cover 15 000 deg^2 with a resolution of ~ 1.5 arcmin.

In this thesis, we constrain cosmological parameters using the following data sets from the most updated Planck 2018 results [4]. The CMB likelihood includes the high-ℓ TT, TE, EE lite likelihood in the interval of multipoles $30 \leq \ell \leq 2508$ for TT and $30 \leq \ell \leq 19696$ for TE, EE. Lite likelihoods are calculated with the

---

[4]See https://camb.info/.

Plik lite likelihood [187]. Instead, for the low-ℓ TT power spectrum, we use data from the Commander component-separation algorithm in the range $2 \leq \ell \leq 29$. We adopt also the Planck CMB lensing likelihood and the low EE polarization power spectrum, referred to as lowE, in the range $2 \leq \ell \leq 29$, calculated from the likelihood code SimAll [188].

2.2.2 *Galaxy surveys*

Another powerful cosmological probe is galaxy clustering. Galaxy surveys divide into photometric and spectroscopic and allow the sampling of the three-dimensional galaxy distribution to measure galaxy clustering, which we focus on in this thesis, BAO, and weak lensing. Photometric surveys are the traditional method to observe the 3D LSS systematically and provide valuable insights into the intrinsic physical properties of galaxies and their evolutionary processes. They are also commonly used for the purpose of identifying objects of interest that warrant further spectroscopic investigation (see e.g. [189]). Additionally, these surveys contribute to constraining cosmological models via e.g. weak gravitational lensing measurements. The study of large-scale structures with galaxies can be done with the angular information provided by the galaxy positions, while radial information is limited due to the number of available photometric bands. Photometric redshift estimates have uncertainties of the order of a few percent, typically ~ 0.05. Upcoming photometric surveys are expected to have a better redshift uncertainty of ≤ 0.01. Among the numerous ongoing and planned photometric surveys we mention the Euclid satellite mission [190], which will conduct a photometric survey covering 15 000 deg^2 with 10^9 galaxies in the redshift range $0 < z < 2$.

Contrary to photometric, spectroscopic surveys allow us to map the distribution of galaxies in three dimensions, since the radial information is coming from precise redshift measurements. A spectroscopic survey is usually equipped with a spectrometer, decomposing the light of objects into thin wavelength bands. Target lists for such spectroscopic surveys are defined based on the angular positions, fluxes, and colors, which are processed to obtain the spectra. Emission and/or absorption features are easily seen in observed spectra and they are used to obtain precise redshift estimates. Spectroscopic surveys typically have redshift uncertainties of $\sim 10^{-3}$. A large variety of cosmological spectroscopic surveys have been and will be explored, including deep surveys on small areas, interesting for galaxy population studies, to shallower surveys on large areas, ideal for statistical measurements of the density field of tracers. Pioneer galaxy spectroscopic surveys include the 2dF Galaxy Survey (2dFGS) [191], 6dF Galaxy Survey (6dFGS) [192], WiggleZ Dark Energy Survey (WiggleZ) [193]. Cosmological programs with Sloan Digital Sky Surveys (SDSS) [194, 195], the Baryon Oscillation Spectroscopic Survey (BOSS) [196] and the extended BOSS (eBOSS) [197] have provided the largest 3D map up to date. BOSS covered 10 000 deg^2 with $\sim 1.5 \times 10^6$ objects within $0 < z < 0.7$, and eBOSS covered the 7 500 deg^2 with $\sim 10^6$ objects for an extended redshift range $0.6 < z < 3.5$ and more types of tracers. The Dark Energy Spectroscopic Survey (DESI) [198] is a currently ongoing 5-year survey. By the end of the survey it will deliver $\sim 30 \times 10^6$ spectra and cover 14 000 deg^2 area. In the near future, both Euclid and Roman satellite experiments will deliver spectroscopic data in
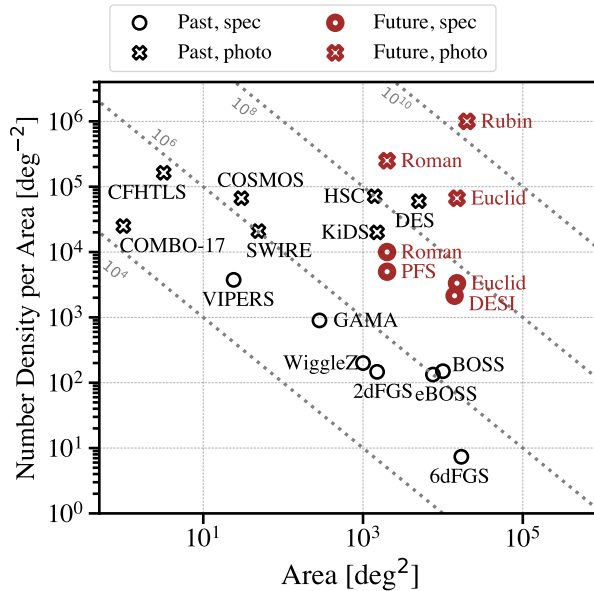
Figure 2.1: Landscape of past (black) and current/future galaxy surveys (red) for galaxy number density per area as a function of the survey area. Photometric surveys are represented with a cross and spectroscopic surveys are with open circles. Grey dotted lines corresponds to 10^4, 10^6, 10^8, and 10^{10} galaxies. Overall, current/future surveys cover a larger area and with a higher number density per area. Image taken from [14].

addition to imaging data. Euclid will provide $\sim 5 \times 10^7$ spectra at $0.7 < z < 1.8$ and Roman will provide $\sim 2 \times 10^7$ spectra at $1 < z < 3$.

Figure 2.1 shows the landscape of the galaxies surveys with photometric redshifts (cross) and spectroscopic surveys (circle) for galaxy number density per area as a function of the survey area. Overall, the future surveys (red) occupy the upper right corner, which covers a larger survey area with higher galaxy number density per area relative to the past surveys (black).

In this thesis, we use several galaxy clustering observations. We constrain cosmological parameters from both the BAO signal and galaxy clustering in cross-correlation with 21cm signal measurements.

2.2.3 *Cosmological surveys in the radio band*

Radio surveys, in particular radio continuum and HI intensity mapping, are a promising tool to test the Universe at unexplored redshifts. A radio continuum survey provides a high angular resolution of radio galaxies but a low resolution in redshifts. As discussed in Section 2.1.3, the HI intensity mapping offers, instead, a high radial resolution but a low resolution in the angular direction. Radio continuum and intensity mapping are, thus, commensal surveys, i.e. they will provide complementary information from the same cosmological probe. In addition, the HI galaxy redshift surveys in the local Universe, up to $z \sim 0.4$, are similar to what we can obtain from an optical spectroscopic survey where galaxy 3D coordinates can be provided.
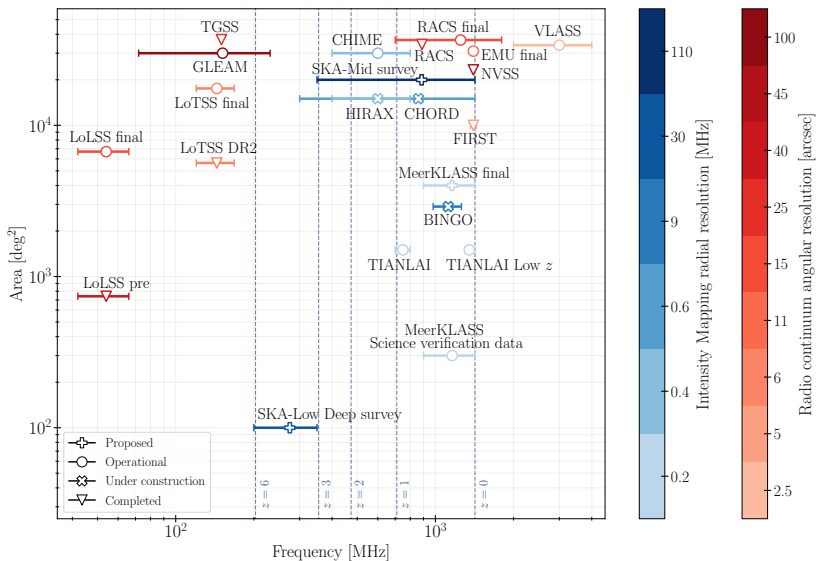
Figure 2.2: A summary of radio surveys. The warm red colors denote the radio contin-
uum maps while the cold blue colors represent the 21cm intensity mapping.
The error bars show the frequency ranges for each of the instruments or
surveys. While the advantage of radio surveys is their high angular resolu-
tions, the surveys that measure the 21cm signal are good at their high radial
resolution, i.e the frequency and its corresponding redshifts (dashed blue
vertical lines). We mark the two kinds of resolutions as different gradients of
colors. Image reproduced from [14].

The main parameters defining a radio survey are the frequency range and
resolution, which translates into the accessible volume and redshift binning.
We can further categorize them mainly by covered area, angular resolution,
and observational technique, e.g. interferometry [52] or single-dish [51]. There
will be a large amount of radio data available in the following decades. Several
instruments are either currently taking data, under construction, or being
planned. Indeed, a plethora of experiments targeting IM is currently running,
under construction, or being proposed. We summarize the main surveys in
radio continuum and HI intensity mapping in Figure 2.2.

For 21cm IM, the main instruments are CHIME [40, 41], HIRAX [42], LOFAR [199],
GBT [43, 44], FAST [45], BINGO [200, 201], CHORD [202], TIANLAI [203, 204]. For
a review of the state of the art of the ongoing and proposed IM surveys, we
refer to [52]. A first detection of the HI signal has been achieved around 10
years ago [53] in cross-correlation with galaxy surveys. Few other studies
have claimed detection of the signal, always in cross-correlation with galaxy
clustering[43, 44, 54]. Preliminary auto power spectrum detections are, instead,
available only at small scales [56]. Indeed, observationally IM suffers from
strong continuum foreground contamination, including diffuse galactic syn-
chrotron emission, bright point sources, and atmospheric turbulence, which
can potentially degrade the predicted constraining power. Several foreground
removal techniques are currently being proposed and tested [62–71, 205, 206].

In this thesis, we focus on modeling forecasted observations for the SKA Ob-
servatory (SKAO) [57] and its precursor MeerKAT [58, 59, 61]. Radio cosmology

is indeed one of the main key science projects of the SKAO, which will be composed of the SKA-Low and SKA-Mid telescopes, in Australia and South Africa respectively. Using the SKA-Mid telescope array as a collection of single-dishes (see e.g. [37, 57]) it will be possible to perform 21cm IM observations at the large scales relevant for cosmology up to redshift $z = 3$. The SKAO is currently under construction, and MeerKAT, the SKA-Mid precursor, has been conducting a IM survey for cosmology [58]. Preliminary data analysis has provided promising results [59, 60] and a first detection of the HI signal in cross-correlation with the WiggleZ galaxies [61]. However, the level of foreground residuals is still a non-negligible issue.

Parallel to the effort in improving the data analysis and the foreground separation, it is of key importance to refine the forecast for the constraining power of the 21cm IM alone and in combination with other probes in order to make a better case for radio cosmology with the SKAO and optimize the survey design. This thesis contributed in this regard by forecasting mock observations for both MeerKAT [117] and the SKAO [115] (see Chapter 6 and Chapter 4 respectively).

2.3 CONSTRAINING THE COSMOLOGICAL PARAMETERS

In the last few decades, the intensely improved quality of observations and data allowed for better and better measurements of cosmological observables. At the same time, a plethora of models beyond ΛCDM (see Chapter 3 below), described by an increasing number of parameters, required to be tested against experimental evidence. To address these needs, statistics became a central tool in cosmology to constrain the parameters, discriminate among models, and deal with the increasing amount of data. Following [120, 207, 208], here we review the basic concepts of statistics for cosmology, necessary for the analysis that we perform in this thesis.

2.3.1 *Bayesian analysis for cosmology*

Being x a real and continuous random variable, the probability density $\mathcal{P}(x)$ is the function that describes the expectation of the occurrence of x. From $\mathcal{P}(x)$ we can calculate the probability P of x to assume a value in the interval (a, b) as

$$\mathrm{P}\left(x \in (a, b)\right) = \int_a^b \mathrm{d}x\, \mathcal{P}(x), \tag{2.11}$$

where $\mathcal{P}(x)$ is a non-negative normalized function. As common use in literature, we refer to $\mathcal{P}(x)$ as probability density, probability distribution or simply distribution.

In general, a data analysis procedure must provide: the best-fit values for the set of parameters describing the model; the confidence levels or limits, i.e. the error estimates on the best-fit values; a statistical way to measure the goodness of the fit. A classical procedure to estimate these quantities is to use the chi-square statistic. Minimizing the chi-square χ^2 one can obtain the best-fit value of the parameters and the uncertainties on them. An estimate of the goodness of fit, instead, can be obtained through the χ^2 hypothesis test, related to the χ^2 distribution.

Historically, cosmologists usually adopt, instead, a Bayesian approach to statistics. In general, if H is a hypothesis, in our case a theory, and D is an event, a measured set of data, the conditional probability distribution $\mathcal{P}(H|D)$ of H being true given the event D occurred, i.e. the data were measured, is defined via the Bayes theorem

$$\mathcal{P}(H|D) = \frac{\mathcal{P}(D|H)\,\mathcal{P}(H)}{\mathcal{P}(D)}. \tag{2.12}$$

We define:

- $\mathcal{P}(H|D)$ is the posterior distribution, that describes the probability that the model H, described by a specific set of parameters, is true given the observed data D. From the posterior distribution parameter constraints can be computed, and, thus, estimating the posterior is the goal of the analysis;

- $\mathcal{P}(D|H)$ is the likelihood, i.e. the probability distribution to have measured a specific set of data D, given the model H;

- $\mathcal{P}(H)$ is called the prior distribution, or simply prior, on the considered model, in which prior knowledge on the theory is cast.

Through the Bayes theorem, we can infer the most likely posterior distribution for the studied theory by knowing or guessing the prior distribution and calculating or sampling the likelihood.

Let us consider a model described by a set $\boldsymbol{\alpha}$ of m parameters α_i, where $\boldsymbol{\alpha} = (\alpha_1, \ldots, \alpha_m)$ is a vector in an m-dimensional parameter space. If the set $D_1, \ldots, D_n$ is the outcome of an observation and $y_1^{\alpha}, \ldots, y_n^{\alpha}$ are the values expected from the theory, the likelihood function is usually well approximated by a multivariate Gaussian distribution

$$\mathcal{L}(D|\boldsymbol{\alpha}) = \frac{1}{\sqrt{(2\pi)^n \,|\det(C)|}} \exp\left[-\frac{1}{2} \sum_{i,j} (D_i - y_i^{\alpha})\, C_{ij}^{-1} \,(D_j - y_j^{\alpha}) \right], \tag{2.13}$$

where $C_{ij} = \langle (D_i - y_i^{\alpha})(D_j - y_j^{\alpha}) \rangle$ is the covariance matrix of the data set. In a Bayesian approach, we find the posterior distribution to be

$$\mathcal{P}(\boldsymbol{\alpha}|D) \propto \mathcal{L}(D|\boldsymbol{\alpha})\mathcal{P}(\boldsymbol{\alpha}). \tag{2.14}$$

Thus, $\mathcal{P}(\boldsymbol{\alpha}|D)$ can be computed from the likelihood function, and the best-fit values of the set $\boldsymbol{\alpha}$ are the ones that maximize the likelihood function.

Usually, in cosmology one has to deal with a rather large number of parameters. Therefore, as we further discuss in the following, one deals with two-dimensional, or higher-dimensional, confidence regions, in addition to confidence levels. The Bayesian method is particularly suited to easily calculate confidence regions from the posterior distribution. In fact, as in equation Equation 2.11 we can calculate probability via the multidimensional integral $\int d\boldsymbol{\alpha}\, \mathcal{P}(\boldsymbol{\alpha}|D)$ in the parameter space. However, we would like to obtain confidence levels for each of the parameters α_i. This can be simply achieved by computing the marginalized posterior distribution, which we obtain by in-

tegrating the full posterior distribution over the unwanted parameters, i. e. with

$$\mathcal{P}(\alpha_j|D) = \int d\alpha_1 \ldots d\alpha_{j-1} d\alpha_{j+1} \ldots d\alpha_m \mathcal{P}(\boldsymbol{\alpha}|D) \tag{2.15}$$

one computes the confidence levels on the parameter α_j. In this way, we can either calculate single confidence levels for each of them or obtain the joint constraints, i. e. the two-dimensional confidence regions, for a subset of parameters. In this thesis, we will show 1D and 2D marginalized posterior distributions.

As we will see below, the Bayesian likelihood method is extensively employed in numerical data analysis for cosmology.

2.3.2 *The Monte Carlo Markov Chain method*

Cosmological theories are described by several parameters, e. g. as discussed above the standard ΛCDM model needs from six to eleven or more parameters. For each set of parameters, observables can take a relatively long time to be numerically computed, e.g. up to the order of a few minutes in the worst-case scenario with the standard Einstein-Boltzmann codes. To fully explore the parameter space in order to compute the likelihood and to perform Bayesian integrations would require a prohibitive amount of computational time. To avoid this difficulty, Monte Carlo Markov Chain (MCMC) methods [209, 210] are regularly employed.

A Markov chain is a randomized walk in which each further step depends only on the current state of the system and not on the previous history. The basic idea of MCMC numerical techniques is to explore the parameter space via Markov chains that move towards the highest probability region. In the Bayesian approach, this allows us to sample properly the posterior distribution function. MCMC methods have been widely studied and state-of-the-art codes offer an extremely high level of accuracy and sophistication. In order to picture a general idea rather than to be exhaustive, here we consider only the most renowned technique, that is the Metropolis-Hastings algorithm [211].

Let us consider a target distribution function $\mathcal{P}(\boldsymbol{\alpha})$, which is proportional to a known function $\mathcal{L}(\boldsymbol{\alpha})$. Assuming to work in the Bayes theorem framework, these could be the posterior distribution and the likelihood respectively. Having chosen a starting point $\boldsymbol{\alpha}_0$, we sample the parameter space with a Markov chain that moves towards the maximum of $\mathcal{L}(\boldsymbol{\alpha})$. The Metropolis-Hastings algorithm establishes the rule according to which we decide whether to accept or not the next step $\boldsymbol{\alpha}_{n+1}$ at each point $\boldsymbol{\alpha}_n$. The procedure is the following:

- first, a proposal density $q(\boldsymbol{\alpha}_n, \boldsymbol{\alpha}_{n+1})$ is chosen, usually a Gaussian that proposes the subsequent point in the parameter space $\boldsymbol{\alpha}_{n+1}$;

- then the acceptance ratio

$$\alpha = \mathcal{L}(\boldsymbol{\alpha}_{n+1})/\mathcal{L}(\boldsymbol{\alpha}_n) = \mathcal{P}(\boldsymbol{\alpha}_{n+1})/\mathcal{P}(\boldsymbol{\alpha}_n) \tag{2.16}$$

is computed for the proposed new point;

- a random number $x \in [0,1]$ from a uniform distribution is drawn and if $\alpha \geq x$ the proposed step $\boldsymbol{\alpha}_{n+1}$ is accepted, otherwise it is rejected and $\boldsymbol{\alpha}_{n+1} = \boldsymbol{\alpha}_n$ is set.

In other words, if the subsequent step brings the chain to a higher probability region ($\alpha > 1 \Leftrightarrow \mathcal{P}(\boldsymbol{\alpha}_{n+1}) > \mathcal{P}(\boldsymbol{\alpha}_n)$) it is always accepted. If not, steps for which $\mathcal{P}(\boldsymbol{\alpha}_{n+1})$ is slightly greater than $\mathcal{P}(\boldsymbol{\alpha}_n)$ are more likely to be accepted, in order not to escape towards lower probabilities domains. After a first burn-in phase in which the walk still depends on the initial position, the chain then provides a fair sample of the target distribution in a reasonable amount of computational time. Once we have the sampling of $\mathcal{P}(\boldsymbol{\alpha})$, we can compute all the relevant quantities that we are interested in, such as the marginalized distributions and the confidence levels. We are going to illustrate how a MCMC run works in practice for cosmology in the next section.

2.3.2.1 *MCMC samplers for cosmology*

At the state of the art, several codes to conduct MCMC analysis for cosmology are available. The basic idea of their working principle is the following:

1. the model to be studied, the set of cosmological parameters $\boldsymbol{\alpha}$ to constrain, and the data sets to be used are defined;

2. the MCMC routine begins with choosing an almost random starting point $\boldsymbol{\alpha}_0$, according to the prior distribution, for the chain in the multidimensional parameter space;

3. the sampler calls an Einstein-Boltzmann solver and computes at the point $\boldsymbol{\alpha}_0$ the theoretical predictions on the observables, such as the CMB power spectra $\mathcal{C}_\ell^{XY}|_{\boldsymbol{\alpha}_0}$, the matter power spectrum $P(k)|_{\boldsymbol{\alpha}_0}$ and so on;

4. with the computed theoretical observables the code calculates the likelihood function $\mathcal{L}\left(\mathcal{C}_\ell^{XY}|_{obs}, P(k)|_{obs}, \ldots \,\middle|\, \mathcal{C}_\ell^{XY}|_{\boldsymbol{\alpha}_0}, P(k)|_{\boldsymbol{\alpha}_0}, \ldots\right)$ using the selected observational data sets;

5. once the likelihood is computed, a new point $\boldsymbol{\alpha}_1$ is proposed and the MCMC routine considers whether or not to accept it, either way, the chain goes one step further;

6. the points from 3 to 5 are repeated recursively for each new step of the chain until a certain convergence criterion is satisfied (see Section 2.3.3.1).

In the Bayesian approach, the output is then a sampling of the total posterior distribution function. Notice that different choices are available for the MCMC routine, e.g. one can use a generalized version of the Metropolis-Hastings algorithm or a fast algorithm optimized for Planck data sets [212].

CosmoMC is a parallelized Monte Carlo code that samples high dimensional parameter spaces. For technical details, we refer to the CosmoMC website[5] and the GitHub repository.[6] The CosmoMC code can be used both for constraining cosmological parameters and also as a generic MCMC sampler. In this work, we extend the CosmoMC code by implementing the likelihood for 21cm intensity mapping observations.

In conclusion, the MCMC method allows for efficient numerical sampling of the likelihood function, which results in cosmological parameter constraints in the Bayesian approach. Despite the undisputed potential of these techniques, a

---

[5]See https://cosmologist.info/cosmomc/.
[6]See https://github.com/cmbant/CosmoMC.

few issues must be treated with care. Among all, how to choose the prior and how this choice influences the results is a central problem (see e.g. [207]).

2.3.3   *Posterior distribution and parameter constraints*

In this section, we describe which is the output of a MCMC run and the tools to analyze it. First, let us clarify what we are looking to compute from the output of a MCMC simulation:

- constraints on every parameter that describes the studied model, i. e. we need the best-fit values and confidence levels (CL); we will usually compute the 68% or sometimes 95% CL, which correspond to constraints within one and two σ respectively;

- the full form of the marginalized posterior distribution for each parameter;

- joint marginalized constraints on couples, sometimes triplets, of relevant parameters, i. e. 2D or 3D contour plots.

All these quantities can be calculated from the MCMC sampling of the global posterior distribution.

Notice that one usually identifies different types of parameters: cosmological, that are the ΛCDM parameter plus the ones specific for the beyond ΛCDM model considered; nuisance, parameters relative to the likelihood implementation that are forced to vary for each specifically used data set; derived, parameters that do not vary but that are computed from actually varying parameters.

The strength of the MCMC approach is that the full posterior is proportional to the number density of points in the parameter space. Marginalized distributions are simply the histograms of the MCMC sampled points, projected onto sub-spaces of the complete parameter space. With MCMC simulations, no further computationally expansive integration is needed to compute marginalized quantities. To perform this analysis, CosmoMC is already provided with the tool GetDist,[7] a Python package optimized for the CosmoMC output. In this thesis, we use GetDist to compute confidence levels, plot the marginalized posterior distributions, and get the contour plots. We refer to the online documentation and to the GetDist notes[8] for technical details and tutorials. However, in the following, we focus only on one of the analysis tools that GetDist offers.

2.3.3.1   *Convergence tests*

In order to get accurate and correct constraints, it is necessary to check somehow if the MCMC chains properly sampled the parameter space, i. e. if they are long enough to produce statistically good results. Therefore, it is necessary to perform on the output a convergence analysis. GetDist provides several different criteria to check the convergence status. Here we focus on the Gelman-Rubin method [213], also called the R-diagnostic. Let us consider m different chains, each formed by n elements, where we already discarded the burn-in phase. Elements in the chains are vectors in the parameter space, but we restrict ourselves to only one parameter $\alpha_{i,j}$ in all chains, where the index $i = 1, \ldots, m$

---

[7] See https://getdist.readthedocs.io/en/latest/index.html.
[8] See https://cosmologist.info/notes/GetDist.pdf.

runs over different chains and $j = 1, \ldots, n$ over elements in a single chain. Following [207], the mean value of the chosen parameter within the chain is

$$\bar{\alpha}_i = \frac{1}{n} \sum_{j=1}^{n} \alpha_{i,j}, \tag{2.17}$$

while the associated variance is

$$\sigma_i^2 = \frac{1}{n-1} \sum_{j=1}^{n} \left(\alpha_{i,j} - \bar{\alpha}_i \right)^2. \tag{2.18}$$

From σ_i we can define W to be the mean value of the variances over chains

$$W = \frac{1}{m} \sum_{i=1}^{m} \sigma_i^2 = \frac{1}{m(n-1)} \sum_{i,j=1}^{m,n} \left(\alpha_{i,j} - \bar{\alpha}_i \right)^2. \tag{2.19}$$

The average between chains, i. e. the average of averages, is instead

$$\bar{\alpha} = \frac{1}{m} \sum_{i=1}^{m} \bar{\alpha}_i = \frac{1}{m \cdot n} \sum_{i,j=1}^{m,n} \alpha_{i,j} \tag{2.20}$$

with variance

$$B = \frac{1}{m-1} \sum_{i=1}^{m} \left(\bar{\alpha}_i - \bar{\alpha} \right)^2, \tag{2.21}$$

that we label as B in order to be consistent with the notation in the literature. Finally, from W and B we can define the parameter R as

$$R = \frac{\left(1 - \frac{1}{n}\right) W + \left(1 + \frac{1}{m}\right) B}{W}, \tag{2.22}$$

that depends on the ratio B/W of the variance between chains and within chains. In the limit in which all chains have more or less the same mean value $\bar{\alpha}_i$, we have that $W \sim B$ and, thus, we expect that $R \to \left(1 + \frac{1}{m}\right) \simeq 1$ for $n \to \infty$. Therefore, we consider the chains converged for the given parameter if the quantity $R - 1$ is sufficiently small. This computation has to be done for each varying parameter. For an estimate of the global convergence on the MCMC run we consider the worst R value, i. e. the highest, among all the parameters.

In this thesis, we consider a convergence threshold of $R - 1 < 0.02$.

3

DARK ENERGY AND MODIFIED GRAVITY

I N THIS CHAPTER, we briefly overview the most popular modified gravity (MG) and dark energy (DE) models. Although the cosmological constant provides an excellent explanation for the accelerated cosmic expansion, more natural choices can be classified into two categories: 1) modifications of the stress-energy tensor on the right-hand side of the Einstein's field equation, which leads to DE models; 2) modifications of e.g. the Einstein-Hilbert action on the left-hand side of the field equation, which leads to MG models. In practice, there are no clear boundaries between DE or MG models (for a review see e.g. [214]). Nevertheless, it is possible to make certain distinctions based on the strong equivalence principle and observe whether ordinary matter experiences additional forces beyond gravity. E.g., Figure 3.1 presents a flowchart in distinguishing MG *vs* DE following [214].

As discussed in Section 1.2.1, in the conformal Newtonian gauge, the line element is given by Equation 1.32, where the gauge invariant Newtonian potential Ψ and curvature potential Φ appear. In the case of GR, the difference between the two potentials is negligible, and the 00 component of the Einstein equation on sub-horizon scales leads to the Poisson equation

$$\nabla^2 \Psi = 4\pi G a^2 \delta\rho_{\rm m}, \qquad (3.1)$$

where $\delta\rho_{\rm m} \equiv \rho_{\rm m} - \bar{\rho}_{\rm m}$ is the fluctuation of the matter density. In the presence of a fifth force, Equation 3.1 is modified and structure formation deviates from the one predicted by GR. There are different ways to "modify gravity", among which scalar-tensor theories (e.g. [215]) are probably the most well-studied models. One of the most general scalar-tensor theories with second-order field equations in four dimensions is the Horndeski theory [216], whose action is constructed as

$$S = \int {\rm d}^4 x \sqrt{-g} \left\{ \sum_{i=2}^{5} \mathcal{L}_i \left[\phi, g_{\mu\nu} \right] + \mathcal{L}_{\rm m}(g_{\mu\nu}, \psi) \right\}. \qquad (3.2)$$

Each of the four Lagrangian densities in the summation is a function of four parameters $\{\mathcal{L}_2[K], \mathcal{L}_3[G_3], \mathcal{L}_4[G_4], \mathcal{L}_5[G_5]\}$, where $\{K, G_3, G_4, G_5\}$ are arbitrary functions of (ϕ, X), with ϕ a scalar field and $X \equiv -\nabla^\nu \phi \nabla_\nu \phi / 2$. $\mathcal{L}_{\rm m}$ is the matter Lagrangian density, with ψ the matter field.

In Section 3.1, we will review two MG models, the $f(R)$ model and the braneworld model, which can be linked to Horndeski theory by properly choosing the four Horndeski functions. These two models are the most representative and have been widely tested using different astrophysical probes and implemented in cosmological simulations (see e.g. the discussion in [14]). We then present several parametrized, model-independent frameworks of gravity in Section 3.2, and review the state-of-the-art constraints on DE relevant for this thesis in Section 3.3.
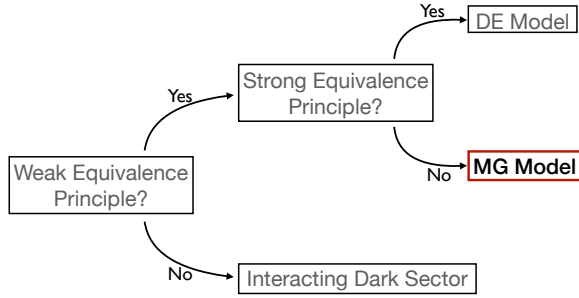
Figure 3.1: A flowchart for distinguishing DE model and modified gravity models (based on Joyce, Lombriser, and Schmidt [214]). The weak equivalence principle (WEP) states that there exists a Jordan frame metric to which matter species are minimally coupled, independent of their composition or structure. Taking scalar-tensor theory as an example, all matter species couple universally to the metric in the presence of a scalar field. The strong equivalence principle (SEP) further restricts the WEP such that the equivalence principle also applies to objects that exert a self-gravitational force. If the coupling between matter fields and the metric does not involve any scalar fields, it's a DE model. Whereas if the matter fields couple to the metric non-trivially via the scalar field, it is a MG model to be considered in this paper. Image reproduced from [14].

3.1   EXAMPLES OF ALTERNATIVE MODELS

3.1.1   *Conformal coupling models: $f(R)$ gravity*

$f(R)$ gravity [217, 218] is a very popular class of modified gravity models, which can be described by the following gravitational action

$$S = \frac{1}{16\pi G} \int d^4x \sqrt{-g} \left[R + f(R) \right] + S_{\mathrm{m}}[g_{\mu\nu}, \psi], \tag{3.3}$$

where the cosmological constant Λ is replaced by an algebraic function of the Ricci scalar, $f(R)$, and S_{m} is the action for the matter field ψ. Various functional forms for $f(R)$ were proposed in early works to explain the cosmic acceleration [219–221]. However, they do not pass Solar System tests of gravity [222, 223]. The work in [224] suggested a functional form of $f(R)$ compatible with local gravity test

$$f(R) = -m^2 \frac{c_1 \left(\frac{R}{m^2} \right)^n}{c_2 \left(\frac{R}{m^2} \right)^n + 1} \approx \rho_{\Lambda,\mathrm{eff}} + f_{R0} \left(\frac{R}{\bar{R}_0} \right)^{-n}, \tag{3.4}$$

where $\bar{R}_0$ is the background Ricci scalar today. This functional form is chosen such that in the small curvature limit at high redshifts we recover ΛCDM and in the large curvature limit at low redshifts it mimics cosmic acceleration. To satisfy cosmological and local observations, the condition $R/m^2 \ll 1$ is required, with m being a free parameter representing a mass scale. The two free parameters c_1 and c_2 are adjusted accordingly such that the effective DE density $\rho_{\Lambda,eff}$ gives rise to a cosmological constant that matches observation. $f_{R0} \equiv f_R(z=0)$ is the present-day value of the background field, with the scalar field

being $f_R \equiv df(R)/dR$. This scalar field f_R is of particular importance, and the impact of $f(R)$ gravity can be viewed in terms of the dynamics of f_R. The larger the amplitude of the scalar field $|f_R|$, the stronger the deviation from GR.

Varying the action in Equation 3.3 with respect to the metric we can derive the modified Einstein equations, whose trace can be interpreted as the equation of motion for f_R

$$\Box f_R = \frac{\partial V_{eff}}{\partial f_R}, \qquad V_{\text{eff}}(f_R) = V(f_R) + A(f_R)\bar{\rho}_{\text{m}}, \tag{3.5}$$

where $\Box \equiv \nabla_\mu \nabla^\mu$ is the d'Alembert operator. The effective potential V_{eff} consists of two parts: one is a bare function that depends on the scalar field itself; the other one also knows about the external matter field density $\bar{\rho}_{\text{m}}$ (see equation 20 in [224] for the exact form of V_{eff}). The density-dependent term of the effective potential in Equation 3.5 explains why this functional form of $f(R)$ can pass the local gravity tests as its dynamics associate high-density regions with high curvature of spacetime.

The interaction range of the scalar field is determined by the Compton wavelength λ_c

$$\lambda_c \equiv m_{f_R}^{-1} \qquad \text{with} \qquad m_{f_R}^2 \equiv \frac{\partial^2 V_{\text{eff}}}{\partial f_R^2}. \tag{3.6}$$

The more massive the scalar field, the shorter the Compton wavelength, and the shorter range the fifth force can mediate its interaction. The presence of the fifth force leads to a different structure formation history, embodied in the modified Poisson equation. Under the quasi-static[1] and weak field[2] approximations, the Poisson equation takes the following modified form

$$\begin{aligned}\nabla^2 \Psi &\approx \frac{16\pi G}{3} a^2 \delta\rho_{\text{m}} - \frac{1}{6} a^2 \delta R \\ &= 4\pi G a^2 \delta\rho_{\text{m}} - \frac{1}{2}\nabla^2 f_R,\end{aligned} \tag{3.7}$$

where the first term is the standard Poisson equation, and the second term represents the fifth force, $F_{5th} \propto \nabla f_R$, generated by the scalar field f_R. Under the static limit, Equation 3.5 can be rewritten as

$$\nabla^2 f_R = -\frac{a^2}{3}\left[\delta R - 8\pi G \delta\rho_{\text{m}}\right], \tag{3.8}$$

where $\delta R = R(f_R) - \bar{R}$.

The $f(R)$ model can be shown to be equivalent to a scalar-tensor theory in which the scalar field has a universal coupling to different matter species by a conformal transformation [222, 225]. At the same time, the connection between the $f(R)$ gravity and Horndeski can be seen by setting [226]

$$G_4 = \phi = f_R, \quad K = f(R) - Rf_R, \quad G_3 = 0. \tag{3.9}$$

---

[1] The quasi-static limit assumes that the time derivative of the scalar field perturbation is negligible compared to the spatial gradient of the scalar field.

[2] Weak field approximation assumes that the amplitudes of the scalar field perturbations and gravitational potentials are much smaller than the speed of light squared.

3.1.2 *Derivative coupling models: DGP gravity*

In the DGP model [227], the Universe is a four-dimensional *brane* embedded in a five-dimensional spacetime or bulk. The total action of the model is

$$S = \int_{\text{brane}} \mathrm{d}^4 x \sqrt{-g} \frac{R}{16\pi G} + \int \mathrm{d}^5 x \sqrt{-g^{(5)}} \frac{R^{(5)}}{16\pi G^{(5)}} + S_{\text{m}}(g_{\mu\nu}, \psi_i), \quad (3.10)$$

where $g_{\mu\nu}$, g, R, and G are the metric tensor, the determinant of the metric, the Ricci scalar and the gravitational constant in the 4-D brane respectively, and $g^{(5)}$, $R^{(5)}$ and $G^{(5)}$ are their equivalents in the 5-D bulk. S_{m} is the action of the matter fields ψ_i which are assumed to be confined on the brane. The transition from 4D to 5D is governed by the crossover scale $r_{\text{c}} \equiv G^{(5)}/(2G)$.

There are two branches of solutions for the DGP model. The self-accelerating branch [228] can lead to cosmic acceleration purely gravitationally, without introducing a cosmological constant. However, this branch of the solution is theoretically unstable [229] and the observed expansion history does not seem to align with the predictions of the self-accelerating DGP model [230]. The *normal branch* is theoretically stable, but it cannot lead to an accelerated Hubble expansion. A most trivial negative pressure energy stress component [231] or extra DE component must be added to match observational data [232]. Nevertheless, DGP models remain attractive as benchmark models and in the following, we will only discuss the normal branch of the DGP model (nDGP).

The structure formation in the nDGP model is governed by the modified Poisson and scalar equations in the quasi-static and weak field limits [233]

$$\nabla^2 \Psi = 4\pi G a^2 \delta\rho_{\text{m}} + \frac{1}{2}\nabla^2 \phi, \quad (3.11)$$

$$\nabla^2 \phi + \frac{r_{\text{c}}^2}{3\beta_{\text{dgp}}a^2 c^2}\left[(\nabla^2\phi)^2 - \left(\nabla_i\nabla_j\phi\right)^2\right] = \frac{8\pi G a^2}{3\beta_{\text{dgp}}}\delta\rho_m, \quad (3.12)$$

where ϕ is a scalar degree of freedom related to the bending modes of the brane, i.e. it describes the position of the brane in the fifth dimension. The total modified gravitational potential Ψ is given by $\Psi = \Psi_{\text{N}} + \phi/2$, with Ψ_{N} being the standard Newtonian potential. Again, the fifth force is proportional to the field's gradient and is given by $F_{5th} = \nabla\phi/2$. The parameter $\beta_{\text{dgp}}(a)$ is a time-dependent function that depends on the crossover scale r_{c} (see equation 2.25 in [233]).

The DGP model gives rise to a cubic interaction $\sim (\partial\phi)^2 \Box \phi$ in its four-dimensional effective theory [229], with ϕ being the Galileon [234]. The Galileon is a scalar field with a shift symmetry (in analogy to Galilei transformation in classical mechanics). The generalized Galileon [235] can be mapped to the Horndeski theory [236]. The cubic Galileon model can be reduced to a Horndeski model with the mapping

$$G_4 = 1, \quad K = -c_2 X, \quad G_3 = c_3 X/M^3, \quad (3.13)$$

where c_3 and M are free parameters in the Galileon model. Note that it is common to fix $c_2 = -1$.

Above, we gave two examples of specific models of DE/MG. When approaching cosmological observations, it might be useful first to assess in which direction the data constrain gravity by adopting a phenomenological approach. Indeed, working with parameterized frameworks of gravity is a powerful and efficient way to test general relativity with no preference for a given model. In the following, we present the most popular parameterized frameworks.

While the parametrization approach allows one to assess more general classes of models, connections back to physics models can become ambiguous as the phenomenological behavior of the models can be non-unique. This approach can nevertheless provide a null test of the standard model of cosmology and a general test of gravity.

An interesting alternative model-independent approach that does not rely on fixing a parametrization is gravity reconstruction [237–241]. Latest results [242] show how it is possible to restrict the theory space directly from cosmological observations, reconstructing the redshift evolution of the MG functions via numerical interpolation. In [242] the authors develop a sophisticated machinery, prompt to be used with future high-precision observations.

3.2.1 *MG phenomenological functions*

Let us consider a Universe described by the metric of Equation 1.32, where perturbations are determined by the potentials Ψ and Φ. A straightforward approach to MG-DE theories is to cast all the modifications to the perturbation evolution into two parameterized functions. One can refer to these as modified growth or MG phenomenological parameters. Usually, one describes how the coupling between gravity and matter density is modified, i.e. how changes the Poisson equation. The other accounts for the variation among Ψ and Φ. In the past decade, various choices of parametrization have been explored. We review some of the most popular ones.

Following the notation of [243], possible MG parameters can be introduced by modifying the standard equations in the sub-horizon quasi-static approximation

$$(i)\ Q(a,k): \qquad -k^2\Phi \equiv 4\pi Ga^2 Q(a,k)\rho\Delta, \qquad (3.14)$$

$$(ii)\ \mu(a,k): \qquad -k^2\Psi \equiv 4\pi Ga^2 \mu(a,k)\rho\Delta, \qquad (3.15)$$

$$(iii)\ \Sigma(a,k): \qquad -k^2(\Phi+\Psi) \equiv 8\pi Ga^2\Sigma(a,k), \qquad (3.16)$$

$$(iv)\ \eta(a,k): \qquad \eta(a,k) \equiv \Phi/\Psi, \qquad (3.17)$$

with $\Delta \equiv \delta + 3aHv/k$ being the Gauge-invariant comoving density perturbation, ρ the energy density, and v the irrotational component of the peculiar velocity. Q and μ modify the Poisson equation for Φ and Ψ, respectively. Σ parametrizes the change in the lensing response to the massless particle to a given matter field, and η, the so-called gravitational slip parameter, reflects the non-zero anisotropic tensor. It is sufficient to choose two from the equations $(i-iv)$ given that they are obviously not independent. For $Q=\mu=\Sigma=\eta=1$ we recover the GR limit. For clustering DE models (e.g. k-essence [244, 245]), there is no gravitational slip, but the Poisson equations can be modified (see

Table 3.1: Connection between well-known models of DE-MG and the EFT formalism (from Bloomfield et al. [21] and Frusciante and Perenon [250]). Here, 0 means that the EFT function is identically equal to 0, ✓ indicates that the function is present, – indicates that the function is not present, while ⋆ indicates that the function is related to other EFT functions.

EFT functions	Ω	Λ	c	M_2^4	$\bar{M}_1^3$	$\bar{M}_2^2$	$\bar{M}_3^2$	$\hat{M}^2$	m_2^2
ΛCDM	0	✓	–	–	–	–	–	–	–
$f(R)$	✓	✓	–	–	–	–	–	–	–
Brans-Dicke	✓	✓	✓	–	–	–	–	–	–
Quintessence	0	✓	✓	–	–	–	–	–	–
k-essence	0	✓	✓	✓	–	–	–	–	–
DGP	✓	✓	✓	✓⋆	✓	–	–	–	–
Horndeski	✓	✓	✓	✓	✓	✓	✓⋆	✓⋆	–

e.g. the review [13]).[3] In general, modified gravity models can introduce modifications to the Poisson equation and incorporate anisotropic stress terms with slip parameters that deviate from unity (e.g. Brans-Dicke, $f(R)$, and DGP theories). However, it is important to note that there can be exceptions within specific subclasses of models, such as the generalized cubic covariant Galileon model, which exhibits an equal potential $\Psi = \Phi$ [248]. Nevertheless, it is worth mentioning that opposite signs of $\mu - 1$ and $\Sigma - 1$ would tend to disfavor all Horndeski models [249]. Moving forward, our focus will center on (μ, Σ) due to their observational significance. Specifically, μ holds a connection to the Newtonian potential and can be constrained through galaxy clustering via redshift space distortions. On the other hand, Σ is linked to the Weyl potential and can be probed by the lensing and ISW effects. While the slip parameter η often possesses a simple functional form in many models, it tends to have weaker constraints from data [18].

3.2.2   *Effective field theory of dark energy*

Effective field theory (EFT) is a general theoretical technique, which was first employed in a cosmological scenario to the describe inflation [251–253]. It was later applied to describe DE by means of a unifying and model-independent framework [20, 21]. Indeed, the idea behind EFT of DE is to construct the most general, single scalar field action to be *effective*, i.e. to be easily interfaced with observations, and *unifying*, in the sense that it aims to include the highest possible number of DE-MG models as special cases.

The recipe to construct the EFT action can be summarized as follows:

1. Usually, the validity of the weak equivalence principle is assumed *a priori*. This makes the Jordan frame, where the metric is universally coupled to the matter fields, the best-suited framework. We refer to [20] for details on the Jordan frame and the alternative formulation in the Einstein frame;

---

[3]Strictly speaking, $\Psi - \Phi$ can be sourced by an anisotropic pressure and a short-wave correction term. [246, 247] in the k-essence model. However, the absolute difference in the two potentials is shown to be small and can be safely neglected [247].

2. The action is constructed within the unitary gauge [251, 252]. In practice, this means that the perturbation of the extra scalar degree of freedom ϕ representing the DE-MG framework is vanishing. This corresponds to foliate the 4-dimensional spacetime in 3-dimensional hypersurfaces by breaking the time-translation symmetry and fixing a preferred time slicing;

3. The chosen foliation is characterised through the unit vector n_μ perpendicular to the time slicing

$$n_\mu \equiv -\frac{\partial_\mu \phi}{\sqrt{-\hat{g}^{\mu\nu}\partial_\mu\phi\partial_\nu\phi}} = -\frac{\delta_\mu^0}{\sqrt{-\hat{g}^{00}}}, \tag{3.18}$$

where $\hat{g}_{\mu\nu}$ is the Jordan frame metric. From the unit vector, we can define the extrinsic curvature $K_{\mu\nu}$ as $K_\mu{}^\nu = \nabla_\mu n^\nu$;

4. We construct the action from all the perturbed operators invariant under the residual symmetry of spatial diffeomorphisms, such as the upper time-time component of the metric $\delta\hat{g}^{00}$, the Riemann tensor $\delta R_{\mu\nu\alpha\beta}$, the Ricci tensor $\delta R_{\mu\nu}$ and scalar δR, the extrinsic curvature δK_ν^μ and its trace δK;

5. Due to the broken time-translation symmetry, the coefficients of the operators in the action are allowed to be time-dependent functions. We call these parameters EFT functions.

The resulting EFT of DE action in conformal time up to the second order in perturbations is

$$
\begin{aligned}
S_{\text{EFT}} = \int \mathrm{d}^4x \sqrt{-g} \bigg\{ &\frac{M_{\text{Pl}}^2}{2} \left[1 + \Omega(\tau)\right] R + \Lambda(\tau) - c(\tau)a^2\delta g^{00} \\
&+ \frac{M_2^4(\tau)}{2} \left(a^2\delta g^{00}\right)^2 - \frac{\bar{M}_1^3(\tau)}{2} a^2\delta g^{00}\delta K - \frac{\bar{M}_2^2(\tau)}{2}\left(\delta K\right)^2 \\
&- \frac{\bar{M}_3^2(\tau)}{2} \delta K_\nu^\mu \delta K_\mu^\nu + \frac{\hat{M}^2(\tau)}{2} a^2\delta g^{00}\delta R^{(3)} \\
&+ m_2^2(\tau)(g^{\mu\nu} + n^\mu n^\nu)\partial_\mu\left(a^2 g^{00}\right)\partial_\nu\left(a^2 g^{00}\right) \\
&+ \dots \bigg\} + S_m\left[\psi_m, g_{\mu\nu}\right],
\end{aligned}
\tag{3.19}
$$

where S_m is the matter action. There are nine time-dependent EFT functions: $\{\Omega, \Lambda, c\}$ that multiply first-order operators and affect both the background and the perturbation evolution, and $\{M_2^4, \bar{M}_1^3, \bar{M}_2^2, \bar{M}_3^2, \hat{M}^2, m_2^2\}$ for second order operators that enter only in the evolution of the perturbations. We recover the GR limit when all the EFT functions vanish, with the exception of Λ, and the EFT action reduces to the standard Einstein-Hilbert one.

The EFT of DE framework allows for exploring a wide range of models. Within the so-called *pure* EFT approach, one can test the bare effect of each operator in the action, by parameterizing the evolution of the EFT function. Otherwise, one can link the EFT parameters to well-known DE-MG models, i.e. *mapping*

approach. For example, $f(R)$ theories of gravity are simply connected to the EFT formalism as follows [20]

$$\Omega = f_R, \quad \Lambda = \frac{M_{Pl}^2}{2}(f - Rf_R), \quad c = 0, \tag{3.20}$$

with $M_2^4 = \bar{M}_1^3 = \bar{M}_2^2 = \bar{M}_3^2 = \hat{M}^2 = m_2^2 = 0$. The corresponding relations can be found also for the other models considered in this paper. In Table 3.1 we gather a summary of how the EFT formalism is linked to specific models of DE.

The EFT formalism offers a powerful parameterized framework derived from solid theoretical assumptions. It is widely used in literature and numerical tools to work within the EFT frameworks are the Einstein-Boltzmann solver EFTCAMB [254] and the MCMC sampler EFTCosmoMC[4] [255]. For a complete review of EFT of DE and a summary of the most recent constraints, we refer the interested reader to [250].

3.2.3 *The α-basis parameterisation*

Although the EFT of DE framework allows to explore a very wide parameter space, it is not always straightforward how to connect each EFT function to a specific physical interpretation. An alternative parameterization that offers a clearer physical meaning is the α-basis. First introduced by [256], with the α-basis all the modifications of gravity described by Horndeski theories are cast into four independent functions of time: $\alpha_K(t)$, $\alpha_B(t)$, $\alpha_M(t)$ and $\alpha_T(t)$. In the following, we summarize the physical meaning attached to each of these functions [256]:

- α_K, dubbed as *kineticity*, is connected to the kinetic energy term in the Horndeski lagrangian (see Equation 3.2) and depends on the functions K, G_3, G_4 and G_5;

- α_B quantifies the *braiding*, i.e. the mixing between the kinetic terms of the scalar field and the metric. It depends on the G_3, G_4 and G_5 functions;

- α_M describes the running of the effective Planck mass and can be easily expressed in terms of Horndeski functions as

$$HM_{Pl}^2\alpha_M \equiv \frac{dM_{Pl}}{dt}, \tag{3.21}$$

with H being the Hubble parameter and $M_{Pl}^2 \equiv 2\Big(G_4 - 2XG_{4,X} + XG_{5,\phi} - \dot{\phi}HXG_{5,X}\Big)$;

- α_T is the *tensor speed excess*, that quantifies the excess of speed of gravitational waves with respect to the speed of light. It depends on the Horndeski functions as

$$\alpha_T \equiv \frac{2X}{M_{Pl}^2}\left[2G_{4,X} - 2G_{5,\phi} - (\ddot{\phi} - \dot{\phi}H)G_{5,X}\right]. \tag{3.22}$$

---

[4]See http://eftcamb.org/

The α-basis parametrization is widely used and it is implemented in the public-available Einstein-Boltzmann solver hi-class[5] [257, 258]. For further discussion on this parametrization, including its connection to the EFT formalism, we refer to [250, 256].

3.3 OVERVIEW OF RECENT CONSTRAINTS ON DE-MG MODELS

We may now ask ourselves this question: *why would we further study $f(R)$ and DGP gravity models given that we still need a cosmological constant Λ or DE component to explain the cosmic acceleration?* One of the motivations for studying the MG theories was to explain accelerated expansion by replacing the cosmological constant with a more natural model. Now that a large class of self-accelerated models is being ruled out by constraints from large-scale structure and gravitational waves [259, 260], MG theories result less attractive from a cosmological perspective. These two benchmark models remain nevertheless meaningful in certain ways. First, they are the few survivors from various tests at different astrophysical scales. At small scales, they can successfully incorporate screening mechanisms to recover Newtonian gravity; at large scales, the enhancement in structure growth they predict can be allowed by astrophysical probes when choosing corresponding parameters properly. Second, we need to bridge observations and theory. These two models, with well-developed simulations and analytic templates, are illustrative examples of what MG signals could possibly look like for a given observable, especially when MG-induced features are dominated by systematics of instrumental and astrophysical origin. Finally, the cosmological constant is a phenomenological model that empirically describes cosmic acceleration. It is not surprising that there is room to introduce further parameters in this model and in the meantime, keep this model valid, while numerous attempts in the MG models teach us what is the room left.

As an alternative to the model-specific approach, the parametrization framework is another way of searching for deviations from GR and is highly complementary, especially given that there are many MG models and it is hard to study all models exhaustively.

3.3.1 *Survivors from gravitational wave detections*

In GR, the gravitational waves (GW) travel at the speed of light. Many modified gravity models alter this prediction. Therefore, GW can put constraints on the modified gravity models. A simple model-independent parametrization of the speed of the gravitational wave is

$$c_T^2 = c^2 \left(1 + \alpha_T(t)\right), \tag{3.23}$$

where c_T^2 is the speed of tensor modes, t is the physical time, α_T is given in Equation 3.22. The difference in the arrival time of the photons and the gravitational waves results in a bound of the property function $\alpha_T(t)$. The property function α_T can be related to G_4 and G_5 functions defined in Equation 3.2 [236, 256]. Applying the condition $\alpha_T = 0$ we have the speed of GW being the speed of light $c_T = c$, and at the same time, eliminating part of $\mathcal{L}_4$ and the entire $\mathcal{L}_5$ in the Horndeski Lagrangian given by Equation 3.2. Hence, models that

---

[5] See http://miguelzuma.github.io/hi_class_public/

involve quartic and quintic galileons are ruled out as they invoke the full $\mathcal{L}_4$ and $\mathcal{L}_5$, while the cubic galileons can still survive.

In the same way, we can ask ourselves which EFT functions do survive the GW170817 event [261]. Being careful with the adopted notation and formalism, it is possible to map α_T into EFT functions. In the formalism of this paper this relation would be [21, 250, 256]

$$\alpha_T = -\frac{\bar{M}_2^2/M_{\text{Pl}}^2}{1 + \Omega + \bar{M}_2^2/M_{\text{Pl}}^2}. \qquad (3.24)$$

If α_T is suppressed by the GW detection, this implies that the $\bar{M}_2$ function is vanishing.[6] This rather simple condition on the EFT theories allows for a better understanding of the implications of GW detection on the surviving theories. In the $f(R)$ case, $\bar{M}_2$ is zero (see Equation 3.20), therefore, GW does not constrain $f(R)$ model.

Another impact of modified gravity is through the running Planck mass α_M, linked to the Ω parameter in the EFT formalism. In the tensor sector, it acts as a friction term in the equation of motion of GW. A running Planck mass can thus change the GW amplitude and lead to a difference in the luminosity distance by GW and its electromagnetic counterpart [262]; at the same time, it can also move around the amplitude of the primordial peak of the B-mode spectrum [263]. As the tensor-to-scalar ratio r also shifts the peak amplitude, there is a degeneracy between the r and α_M. This degeneracy can be lifted by combining with probes sensitive to the scalar sector since a running Planck mass can affect background evolution and structure growth [263]. [264] studied the GW luminosity distance in $f(R)$ gravity with simulated mock data for Einstein telescope (ET) [26]. They found that the ET-like data in the first running decade could only provide constraints for $|f_{R0}| < 10^{-2}$ and not be very helpful in constraining the $f(R)$ gravity. In the case of DGP models, the GW amplitude could "leak" into higher dimensions. The leakage can cause additional GW damping during its propagation. Therefore constraints can also be obtained by comparing GW and electromagnetic luminosity distances. [265] performed the study on the DGP model and found that the model is very poorly constrained by GW170817 event, where only wavelengths comparable to the cosmic horizon (very low frequency) can leak into extra dimensions.

3.3.2 *Constraints from galaxy surveys and CMB*

Since modified gravity can affect the growth of cosmic structure, the combination $f(z)\sigma_8(z)$, inferred from the anisotropic clustering of the galaxy auto-correlation (see Section 2.1.2), can be used test for potential deviation from GR (see e.g. the parametrization of $f\sigma_8$ employed in [266]). Figure 16 in [14], shows compiled measurements from past galaxy spectroscopic surveys, compared to the ΛCDM cosmology using the best fitting value from Planck data [150] with a 5% errorbar. The precision on current constraints of growth rate in terms of $f\sigma_8(z)$ is up to 8%. Future surveys with increased volume and the number of galaxies will largely improve upon the statistical precision.

---

[6]Of course one could try to force $\alpha_T = 0$ also with very large Ω. However, this would lead to exotic theories incompatible with the Universe we observe.
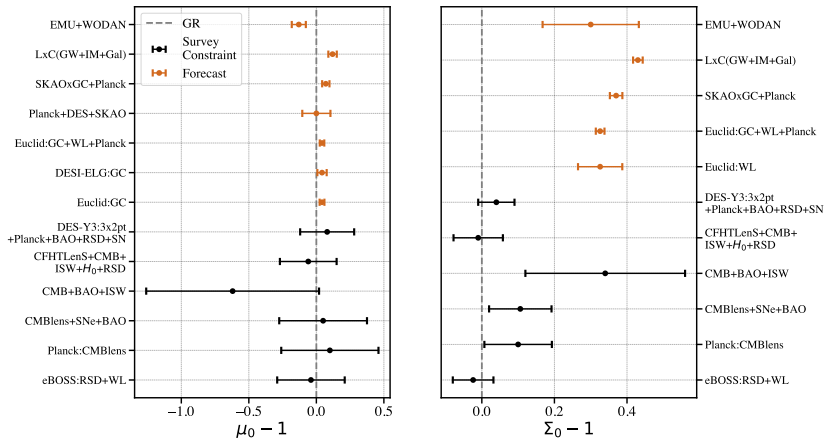
Figure 3.2: Constraints (black) and forecasts (orange) for $\mu_0 = \mu|_{z=0}$ and $\Sigma_0 = \Sigma|_{z=0}$. Plot reproduced from [14].

While the constraints on the product of $f(z)$ and $\sigma_8(z)$ are consistent with the standard GR scenario, there is a potential tension in $\sigma_8(z)$ [5, 8], in particular on the derived parameter $S_8 \equiv \sigma_8 \left(\Omega_m/0.3\right)^{0.5}$, as breafly discussed in Chapter 1. Extensive research has been conducted on systematics related to various probes, aiming to understand the possible systematics-induced tensions between the early-time and multiple late-time measurements (see e.g. [138]). For example, the CMB estimates are reliant on models via parameters related to amplitude, such as the sum of neutrino mass and the optical depth. They can impact the derived value of S_8 [267]. Additionally, there is also an anomaly in Planck lensing amplitude A_L [182, 267–270]. The presence of an intriguing $\sim 2\sigma$ tension between CMB measurements and several late-time measurements could potentially indicate deviations from the standard ΛCDM model, provided that systematic errors can be entirely ruled out. Tentative candidates are: axion monodromy inflation [271–273], sterile neutrinos [274, 275], alternative DE models [276–279], and modified gravity models [243, 280–282]. However, if this discrepancy is attributed to exotic physics, the proposed model must reconcile the effects at both early and late times and successfully pass the scrutiny from cosmological probes.

Figure 3.2 shows the constraints from the current survey (black) and the forecast (brown) on the $\mu_0 = \mu|_{z=0}$ and $\Sigma_0 = \Sigma_0|_{z=0}$ functions (see Equation 3.16 and Equation 3.17). In the case of GR, we expect $\mu_0 - 1 = 0$ and $\Sigma_0 - 1 = 0$. The current constraints [4, 5, 283, 284] are all consistent with GR. Future surveys on galaxy clustering, weak lensing, line intensity mapping, cosmic microwave background, and gravitational wave will greatly improve upon the constraints [118, 239, 285, 286].

Finally, we summarize the current constraints on the $f(R)$ gravity parameter as a function of scale for different probes. While the current surveys can only establish a lower limit for the present-day value of f_{R0} at approximately 10^{-4}, future galaxy surveys and CMB experiments (Section 2.2) hold promising potential for enhancing the constraints. Moreover, probes such as 21cm (see

next section) and underdense regions [287] can be harnessed to offer further promising avenues.

3.3.3 *Constraints from line intensity mapping*

Studies in the literature mostly focused on forecasting the constraining power of future observations since there have been no LIM auto power spectrum detection yet, as discussed in Section 2.2.3. For 21cm intensity mapping a variety of scenarios were taken into account. Some of them focused on the EoR epoch [49, 289–291]. For the late-time Universe, 21cm IM is expected to improve the constraints on the background evolution [292–294], but also the perturbations [295]. Several models were studied, from phenomenological parametrizations to specific theories. Some studies tried to forecast the constraints on the μ, Σ and η MG functions, e.g. [285], while other focused on EFT of DE [117]. Specific studied models are $f(R)$ [159, 160], generalised scalar-tensor theories [296], early DE [297, 298], interacting DE [299, 300], and others [91, 301]. Recently, several studies focused on the cross-correlation between IM and other LSS probes, such as weak lensing, gravitational waves, and galaxy clustering [118, 286, 302, 303]. The constraining power on DE of other lines, instead, is still mostly uncharted [304, 305].

The main take-home message of this intense work carried out by the community is that LIM observations are expected to improve significantly the constraining power on beyond-ΛCDM models, due to their ability to sample wide ranges of redshift, i.e. its tomographic nature. To support this statement we refer again to Figure 3.2.

This work contributed to the scientific discussion by studying the constraining power of 21cm observations on EFT models of DE [117] and forecasting cross-correlation observations between 21cm IM and GW [118]. We refer to Chapter 6 and Chapter 7 respectively for a detailed discussion.

---

[6]Ref. [288] found the f_{R0} is unconstrained in the cosmic shear analysis after marginalizing over nuisance or cosmological parameters.

Part II

HYDROGEN AS A COSMOLOGICAL PROBE

THE 21CM SIGNAL POWER SPECTRUM MULTIPOLES

T HE 21CM SIGNAL measurements, obtained with radio telescopes through the 21cm signal emission, have the potential to become a key cosmological probe in the upcoming years, as discussed in Section 2.1. In this chapter, we explore the constraining power of 21cm intensity mapping observations on the full set of cosmological parameters that describe the ΛCDM model. We focus on the first two detectable multipoles of the 21cm power spectrum.

We find that 21cm multipole observations alone are enough to obtain constraints on the cosmological parameters comparable with other probes. Combining the 21cm data set with CMB observations significantly reduces the estimated errors. The strongest effect is on $\Omega_c h^2$ and H_0, for which the error is reduced by almost a factor of four. We conclude that 21cm SKAO observations will provide a competitive cosmological probe, complementary to CMB and, thus, pivotal for gaining statistical significance on the cosmological parameters constraints, allowing a stress test for the current cosmological model.

The discussion is organized as follows. The modeling of the 21cm power spectrum and power spectrum multipoles is discussed in Section 4.1, while Section 4.2 is devoted to the construction of the mock data set and the likelihood implementation. Results are presented in Section 4.3. The constraining power of the mock 21cm power spectrum multipoles is evaluated in Section 4.3.1. We investigate how 21cm observations affect the constraining power of other probes, i.e. CMB measurements, in Section 4.3.2. A discussion on the impact of opening the parameter space to the brightness temperature, the HI bias, and the growth rate is given in Section 4.3.3. We also investigate the impact of extending our mock data set to non-linear scales in Section 4.3.4. A summary of the results and our conclusions are outlined in Section 4.4.

Through all this work we assume a Universe described by a Planck 2018 [4] fiducial cosmology (see Section 1.3).

This chapter is based on the publication «Multipole expansion for 21cm intensity mapping power spectrum: Forecasted cosmological parameters estimation for the SKA Observatory.», by M. BERTI, M. Spinelli, and M. Viel, in Mon. Not. Roy. Astron. Soc. 521.3 (2023) [115].

4.1 MODELLING THE 21CM SIGNAL

In this section, we outline the formalism used throughout this work. We describe the theoretical 21cm linear power spectrum in Section 4.1.1, how the telescope effects impact the theoretical model in Section 4.1.2, and define the final observables in Section 4.1.3.

4.1.1 *The theoretical 21cm signal linear power spectrum*

The 21cm power spectrum conveys rich cosmological information: it is a biased, redshift-dependent tracer of the matter distribution and thus an interesting probe of the three-dimensional LSS of the Universe.

As discussed in Section 2.1, we model the 21cm linear power spectrum as [57, 153, 158]

$$P_{21}(z, k, \mu) = \bar{T}_b^2(z) \left[b_{HI}(z) + f(z) \, \mu^2 \right]^2 P_m(z, k), \qquad (4.1)$$

where $\bar{T}_b$ is the HI mean brightness temperature, b_{HI} is the HI bias, f is the growth rate, $\mu = \hat{k} \cdot \hat{z}$ is the cosine of the angle between the wave number and the line-of-sight, and $P_m(z, k)$ is the linear matter power spectrum. We neglect in Equation 4.1 the shot noise term, which is believed to be negligible at linear scales [93, 158, 306, 307]. We refer to section Section 4.3.4 for a discussion on non-linear scales and the shot noise term.

We use the parametrization of the brightness temperature from [51]

$$\bar{T}_b(z) = 180 \, \Omega_{HI}(z) \frac{h \, H_0}{H(z)} (1 + z)^2 \text{mK}, \qquad (4.2)$$

where we consider the HI density parameter to evolve mildly in redshift as $\Omega_{HI}(z) = 4. \times 10^{-4}(1 + z)^{0.6}$ (see [308]). Given that we lack an analytical model, $b_{HI}(z)$ at fixed redshift is computed by interpolating numerical results from hydro-dynamical simulations [158, 309].

The growth rate $f(z)$ and the linear matter power spectrum $P_m(z, k)$ are, instead, computed numerically by means of the Einstein-Boltzmann solver CAMB[1] [173].

4.1.2 *The effect of the telescope on the theoretical 21cm signal power spectrum*

One of the main instrumental effects on the theoretical 21cm power spectrum is the telescope response that we model as a Gaussian beam which suppresses the power spectrum on scales smaller than the beam's full width at half maximum [51, 55, 68, 310, 311].

This effect can be written in terms of R_{beam}, the beam physical dimension

$$\begin{aligned} R_{beam}(z) &= \sigma_\theta r(z) \\ &= \frac{\theta_{FWHM}}{2\sqrt{2 \ln 2}} r(z), \end{aligned} \qquad (4.3)$$

where $r(z)$ is the comoving distance, $\theta_{FWHM} = \frac{1.22\lambda_{21}}{D_{dish}}(1 + z)$ is the full width at half maximum, and D_{dish} is the diameter of the dish.

The beam damping factor in Fourier space $\tilde{B}(z, k, \mu)$ can thus be written as

$$\tilde{B}(z, k, \mu) = \exp\left[\frac{-k^2 R_{beam}^2(z)(1 - \mu^2)}{2} \right]. \qquad (4.4)$$

Note that the factor $(1 - \mu)$ model the smoothing only along the transverse direction since the damping along the radial direction is negligible due to the high-frequency resolution of 21cm observation [310].

The observed, i.e. beam convolved, 21cm power spectrum is then

$$\hat{P}_{21}(z, k, \mu) = \tilde{B}^2(z, k, \mu) P_{21}(z, k, \mu), \qquad (4.5)$$

where $P_{21}(z, k, \mu)$ is defined in Equation 4.1.

---

[1] See https://camb.info/.

4.1.3 *Multipole expansion*

The non-isotropic redshift space 21cm power spectrum can be decomposed using Legendre polynomials $\mathcal{L}_\ell(\mu)$ as

$$\hat{P}_{21}(z,k,\mu) = \sum_\ell \hat{P}_\ell(z,k)\mathcal{L}_\ell(\mu). \tag{4.6}$$

The first Legendre polynomials are the following functions of μ

$$\mathcal{L}_0(\mu) = 1, \qquad \mathcal{L}_2(\mu) = \frac{3\mu^2}{2} - \frac{1}{2}. \tag{4.7}$$

The coefficients of the expansion, i.e. the multipoles of the 21cm power spectrum, are then given by

$$\hat{P}_\ell(z,k) = \frac{(2\ell+1)}{2} \int_{-1}^{1} \mathrm{d}\mu \, \mathcal{L}_\ell(\mu)\hat{P}_{21}(z,k,\mu), \tag{4.8}$$

where the expression for $\hat{P}_{21}(z,k,\mu)$ can be found in Equation 4.5.

In our analysis, we construct mock observations for the monopole $\hat{P}_0(z,k)$ and the quadrupole $\hat{P}_2(z,k)$, i.e. $\ell = 0$ and $\ell = 2$ respectively. We refer to Appendix a for the explicit analytical expression of these quantities.

4.2 FORECASTING THE SKAO CONSTRAINING POWER

In this section we focus on the SKA-Mid telescope and its proposed cosmological surveys describing our methodology to obtain realistic forecasts on their constraining power on the cosmological parameters. In Section 4.2.1 and Section 4.2.2 we construct the mock tomographic data set of SKA-Mid observations. The description of the likelihood function and the parameter estimation method are reported in Section 4.2.3.

4.2.1 *SKA-Mid telescope specifications*

We construct mock single-dish 21cm power spectrum observations of the SKA-Mid telescope, modeling the 21cm IM survey as in [57]. The telescope specifications relevant to our work are reported in Table 4.1.

We assume a combination of two surveys: a Medium-Deep Band 2 survey that covers a sky area of 5,000 deg^2 in the frequency range $0.95 - 1.75$ GHz (i.e. the redshift range $0 - 0.5$); a Wide Band 1 survey that covers a sky area of 20,000 deg^2 in the frequency range $0.35 - 1.05$ GHz (i.e. the redshift range $0.35 - 3$). We forecast observations for six equi-spaced, non-overlapping redshift bins, in the range $z = 0 - 3$ with $\Delta z = 0.5$. The six bins are centered at redshifts $z_c = \{0.25, 0.75, 1.25, 1.75, 2.25, 2.75\}$. We assume the Band 2 survey specification for the mock 21cm power spectrum at redshift 0.25 and the Band 1 survey specification for all the others. Note that in our analysis each bin is regarded as independent.

The survey sky coverage and the redshift range define the volume for the mock observations thus fixing the range of accessible scales for our analysis. In Fourier space, the largest scale available at each central redshift is $k_{\min}(z_c) =$

Table 4.1: Assumed specifications for SKA-Mid survey [57].

Parameter		Value
D_{dish} [m]	SKAO dish diameter	15
N_{dish}	SKAO dishes	133
t_{obs} [h]	observing time	10000
T_{sys} [K]	system temperature	25
$\delta\nu$ [MHz]	frequency resolution	1
Δz	width of the redshift bins	0.5
	Medium-Deep Band 2	
	band frequency range	0.95 - 1.75 GHz
	corresponding redshift range	0 - 0.5
A_2 [deg^2]	survey area	5000
$\Omega_{sur,2}$ [sr]	survey area	1.5
$f_{sky,2}$	covered sky area	0.12
	Wide Band 1	
	band frequency range	0.35 - 1.05 GHz
	corresponding redshift range	0.35 - 3
A_1 [deg^2]	survey area	20000
$\Omega_{sur,1}$ [sr]	survey area	6.1
$f_{sky,1}$	covered sky area	0.48

$2\pi/\sqrt[3]{V_{bin}(z_c)}$, where $V_{bin}(z_c)$ is the volume of each redshift bin, defined in Equation 4.10 in Section 4.2.2.1.

The smallest scale is, instead, imposed by the size of the telescope beam and it can be estimated as $k_{max}(z_c) = 2\pi/R_{beam}(z_c)$. At scales smaller than k_{max}, the signal is dominated by the beam providing no relevant information on cosmology. Although we do not show results here, we tested pushing the k_{max} limit beyond the beam scale. We found no significant impact on the cosmological parameters constraints. If not already provided by the cut-off given by the size of the telescope beam, we impose a $k_{max} = 0.2\,h\text{Mpc}^{-1}$ to avoid entering the non-linear regime for the power spectrum.

Finally, we choose a fixed k-bin width as a function of redshift $\Delta k(z_c)$ in order to be large enough for modes to be independent, assuming $\Delta k(z_c) \sim 2k_{min}(z_c)$.

4.2.2 *Mock data set*

In the following, we discuss the sources of errors considered in this work and present the final mock data set used to forecast the constraining power of the 21cm observations.

Table 4.2: Computed values of redshift dependent quantities at each central redshift z_c. For the first redshift bin ($z = 0.25$) we assume SKA-Mid Band 2 specifications, while we use SKA-Mid Band 1 parameters for the other five bins. We refer to Table 4.1 for a list of used SKA-Mid specifications.

z_c	central redshift	0.25	0.75	1.25	1.75	2.25	2.75	
$\bar{T}_b$	mean brightness temperature	0.78×10^{-1}	1.3×10^{-1}	1.9×10^{-1}	2.5×10^{-1}	3.0×10^{-1}	3.6×10^{-1}	[mK]
b_{HI}	HI bias	1.03	1.33	1.62	1.89	2.17	2.45	
V_{bin}	volume of the bin	0.11×10^{10}	1.98×10^{10}	3.14×10^{10}	3.71×10^{10}	3.90×10^{10}	3.88×10^{10}	[h^{-3}Mpc^3]
R_{beam}	beam size	6.38	23.36	43.74	66.13	89.83	114.5	[h^{-1} Mpc]
P_N	noise power spectrum	0.6	10	16	19	20	20	[mK^2 h^{-3}Mpc^3]
k_{max}	minimum scale	0.2	0.2	0.14	0.09	0.07	0.05	[h Mpc^{-1}]
k_{min}	maximum scale	6.00×10^{-3}	2.32×10^{-3}	1.99×10^{-3}	1.88×10^{-3}	1.85×10^{-3}	1.85×10^{-3}	[h Mpc^{-1}]
Δk	k-bin width	12×10^{-3}	5×10^{-3}	4×10^{-3}	4×10^{-3}	4×10^{-3}	4×10^{-3}	[hMpc^{-1}]
N	number of data points	16	43	36	25	18	14	

4.2.2.1   Instrumental noise

For a single-dish intensity mapping SKAO-like experiment, the noise power spectrum can be modeled as [37, 156]

$$
P_{\mathrm{N}}(z) = \frac{T_{\mathrm{sys}}^2 4\pi f_{\mathrm{sky}}}{N_{\mathrm{dish}} t_{\mathrm{obs}} \delta\nu} \frac{V_{\mathrm{bin}}(z)}{\Omega_{\mathrm{sur}}}. \tag{4.9}
$$

Here, given a redshift bin centered at z and of width Δz, the volume of the redshift bin $V_{\mathrm{bin}}(z)$ can be computed as

$$
\begin{aligned}
V_{\mathrm{bin}}(z) &= \Omega_{\mathrm{sur}} \int_{z-\Delta z/2}^{z+\Delta z/2} \mathrm{d}z' \, \frac{\mathrm{d}V}{\mathrm{d}z'\mathrm{d}\Omega} \\
&= \Omega_{\mathrm{sur}} \int_{z-\Delta z/2}^{z+\Delta z/2} \mathrm{d}z' \, \frac{cr(z')^2}{H(z')}.
\end{aligned} \tag{4.10}
$$

with $r(z)$ being the comoving distance. A description of all the other parameters that appear in Equation 4.9 and their assumed values can be found in Table 4.1.

4.2.2.2   Variance

To construct mock observations we need an estimate of the errors on the power spectrum. Following e.g. [156] we write the variance per k and μ bin $\sigma(z, k, \mu)$ as

$$
\sigma^2(z, k, \mu) = \frac{\left(\hat{P}_{21}(z, k, \mu) + P_{\mathrm{N}}(z)\right)^2}{N_{\mathrm{modes}}(z, k, \mu)}, \tag{4.11}
$$

where $\hat{P}_{21}(z, k, \mu)$ is the 21cm signal power spectrum, defined in Equation 4.5, and $P_{\mathrm{N}}(z)$ is the noise power spectrum of Equation 4.9. $N_{\mathrm{modes}}(z, k, \mu)$ is the number of modes per k and μ bins in the observed sky volume. We can compute it as

$$
N_{\mathrm{modes}}(z, k, \mu) = \frac{k^2 \Delta k(z) \Delta\mu(z)}{8\pi^2} V_{\mathrm{bin}}(z). \tag{4.12}
$$

Here, $V_{\mathrm{bin}}(z)$ is the volume of the redshift bin centered at z, while $\Delta k(z)$ and $\Delta\mu(z)$ are the k and μ bin width respectively. In our analysis, however, we integrate over all the possible values of μ in the interval $\mu \in (-1, 1)$, as we will discuss in more detail in the next section. Thus, computing the number of μ modes, Equation 4.12 reduces to

$$
N_{\mathrm{modes}}(z, k) = \frac{k^2 \Delta k(z)}{4\pi^2} V_{\mathrm{bin}}(z). \tag{4.13}
$$

4.2.2.3   Multiple covariance

Another source of error is the covariance between different multipoles. We define the covariance between the multipoles ℓ and ℓ' as a function of k and z [see 50, 51, 312–314]

$$
C_{\ell\ell'}(z, k) = \frac{(2\ell + 1)(2\ell' + 1)}{2} \int_{-1}^{1} \mathrm{d}\mu \, \mathcal{L}_\ell(\mu) \, \mathcal{L}_{\ell'}(\mu) \, \sigma^2(z, k, \mu), \tag{4.14}
$$

where we neglect mode coupling. Here, $\sigma^2(z, k, \mu)$ is the variance per k and μ bin at redshift z, as defined in Equation 4.11. In our analysis we focus on the

monopole $\hat{P}_0$ and the quadrupole $\hat{P}_2$ and assume a set of N measurements of the 21cm multipoles at scales $\{k_1, \ldots, k_N\}$

The multipole covariance defined in Equation 4.14 allows us to estimate both the covariance for a given multipole and between different multipoles. Thus, the most general covariance matrix for $\hat{P}_0$ and $\hat{P}_2$ combined is a $2N \times 2N$ symmetric block matrix. At fixed redshift, it is constructed as

$$\mathbf{C}(z) = \begin{pmatrix} \mathbf{C}_{00}(z) & \mathbf{C}_{02}(z) \\ \mathbf{C}_{02}(z) & \mathbf{C}_{22}(z) \end{pmatrix}. \tag{4.15}$$

Each block $\mathbf{C}_{\ell\ell'}$ is a diagonal matrix of dimensions $N \times N$, defined as $\mathbf{C}_{\ell\ell'}(z) = \mathrm{diag}(C_{\ell\ell'}(z, k_1), \ldots, C_{\ell\ell'}(z, k_N))$, where the elements $C_{\ell\ell'}(z, k_i)$ are computed as in Equation 4.14 at each $\{k_1, \ldots, k_N\}$.

The blocks along the diagonal, i.e. $\mathbf{C}_{00}(z)$ and $\mathbf{C}_{22}(z)$, are the covariance matrices for the monopole and the quadrupole alone. The off-diagonal block $\mathbf{C}_{02}(z)$, instead, describes the covariance between $\hat{P}_0$ and $\hat{P}_2$.

In the simplified case where the monopole $\hat{P}_0$ and the quadrupole $\hat{P}_2$ are uncorrelated, we can neglect the off-diagonal terms in $\mathbf{C}(z)$ and assume the block-diagonal covariance matrix

$$\mathbf{C}_{\mathrm{diag}}(z) = \begin{pmatrix} \mathbf{C}_{00}(z) & 0 \\ 0 & \mathbf{C}_{22}(z) \end{pmatrix}. \tag{4.16}$$

In our work, we compute the covariance matrices $\mathbf{C}_{00}(z)$, $\mathbf{C}_{02}(z)$, $\mathbf{C}_{22}(z)$, $\mathbf{C}_{\mathrm{diag}}(z)$, and $\mathbf{C}(z)$ numerically, from the analytical expression for the monopole and the quadrupole (see Appendix a).

4.2.2.4 *Mock data set errors*

Taking into account the sources of errors described above, we can compute the errors on our mock data points assuming the SKA-Mid observations.

Assuming a set of N measurements of the 21cm multipole $\hat{P}_\ell$ at scales $\{k_1, \ldots, k_N\}$, the computed error on each point of the data set is

$$\sigma_{\hat{P}_\ell}(z, k_i) = \sqrt{C_{\ell\ell}(z, k_i)}$$
$$= \sqrt{\frac{(2\ell+1)^2}{2} \int_{-1}^{1} \mathrm{d}\mu \, \mathcal{L}_\ell^2(\mu) \, \sigma^2(z, k_i, \mu)}, \tag{4.17}$$

for each k_i in $\{k_1, \ldots, k_N\}$.

At each central redshift z_c and data point k we compute the monopole $\hat{P}_0(z_c, k)$, the quadrupole $\hat{P}_2(z_c, k)$ and the errors, as discussed above. In table Table 4.2, we gather some of the used redshift-dependent quantities for the interested reader. The resulting forecasted data sets for the monopole and the quadrupole are shown in Figure 4.1.

4.2.3 *Constraining the cosmological parameters*

In order to exploit the constraining power of the mock data set presented in Section 4.2.2, we define a likelihood function (Section 4.2.3.1) and then
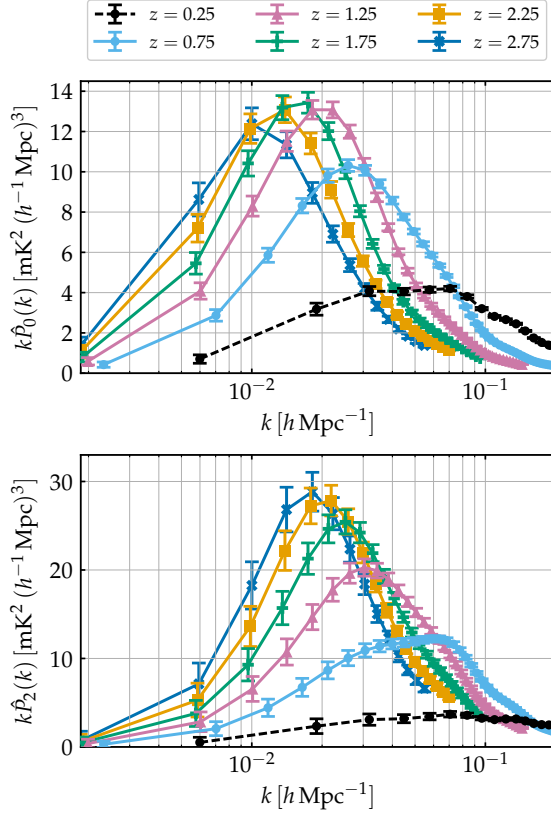
Figure 4.1: Tomographic mock data set for 21cm linear power spectrum monopole (upper panel) and quadrupole (lower panel) observations. The considered six redshift bins are centered at redshifts {0.25, 0.75, 1.25, 1.75, 2.25, 2.75}. For the first redshift bin (black dashed line) we assume a SKA-Mid Band 2 survey. The data sets for the other five bins, instead, assume a SKA-Mid Band 1 survey (see Table 4.1). We refer to Section 4.2.2 for further details on how the signal and the errors are computed.

set up the framework to constrain the cosmological parameters adopting a Bayesian approach (Section 4.2.3.2). Given a set of observations and a theory that depends on that set of parameters, the Bayes theorem links the posterior distribution to the likelihood function. The high-dimensional posterior can then be sampled using MCMC methods (see Section 2.1).

4.2.3.1   *Likelihood function and signal-to-noise*

Given a set of measurements at scales $\{k_1, \dots, k_N\}$ and redshift z_c, to compute the likelihood function we define the vector

$$\Theta(z_c) = \left(\hat{\mathbf{P}}_0(z_c), \hat{\mathbf{P}}_2(z_c) \right), \tag{4.18}$$
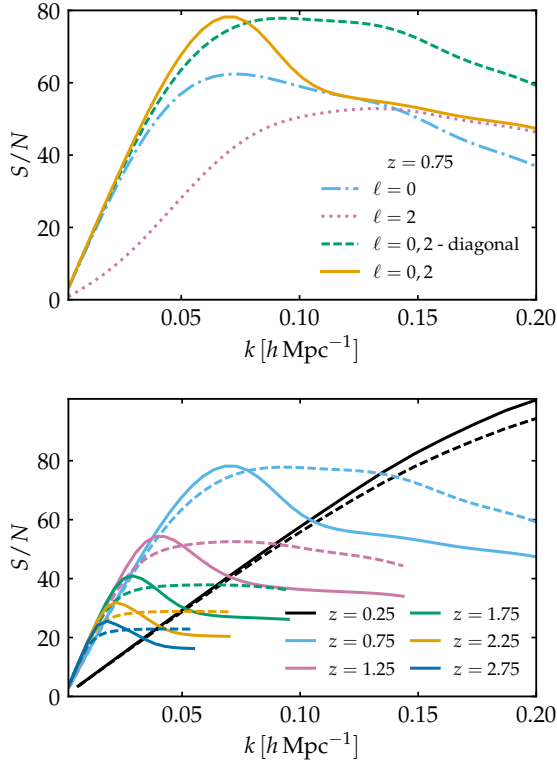
Figure 4.2: Signal-to-noise ratio as a function of k (see Equation 4.20). In the upper panel, we show the signal-to-noise at given redshift $z = 0.75$, for different combinations of multipoles: the monopole alone (blue dashed-dotted line), the quadrupole alone (pink dotted line), the two combined (green dashed line) and the two combined considering the full non-diagonal covariance matrix (yellow solid line). In the lower panel, we show the signal-to-noise redshift dependence for the monopole and the quadrupole combined, considering a diagonal covariance matrix (dashed lines) and the full non-diagonal one (solid lines).

with $\hat{\mathbf{P}}_\ell(z_c) = (\hat{P}_\ell(z_c, k_1), \ldots, \hat{P}_\ell(z_c, k_N))$. When we use both the monopole and the quadrupole, the logarithmic likelihood is computed as

$$-\ln[\mathcal{L}] = \sum_{z_c} \frac{1}{2} \Delta\mathbf{\Theta}(z_c)^{\mathrm{T}} \mathbf{C}^{-1}(z_c) \Delta\mathbf{\Theta}(z_c), \qquad (4.19)$$

where we define $\Delta\mathbf{\Theta}(z_c) = \mathbf{\Theta}^{th}(z_c) - \mathbf{\Theta}^{obs}(z_c)$, the difference between the values of $\mathbf{\Theta}(z_c)$ predicted from theory and observed. Here, $\mathbf{C}(z_c)$ is the covariance matrix defined in Equation 4.15, which becomes $\mathbf{C}_{\mathrm{diag}}(z_c)$, i.e. Equation 4.16, when we neglect multipole covariance. We consider independent redshift bins, i.e. we simply sum over the contribution from each central redshift. When studying $\hat{P}_0$ and $\hat{P}_2$ separately we use only the relevant blocks of the covariance matrix $\mathbf{C}(z_c)$, thus using a simplified version of Equation 4.19.

Using a similar formalism, we can compute the signal-to-noise at a specific k for each central redshift as

$$[\text{S/N}]^2(z_c, k) = \boldsymbol{\Theta}_k(z_c)^{\text{T}} \, \mathbf{C}_k^{-1}(z_c) \, \boldsymbol{\Theta}_k(z_c) \qquad (4.20)$$

where $\boldsymbol{\Theta}_k(z_c) = (\hat{P}_0(z_c, k), \hat{P}_2(z_c, k))$ and $\mathbf{C}_k(z_c)$ is a matrix defined as

$$\mathbf{C}_k(z_c) = \begin{pmatrix} C_{00}(z_c, k) & C_{02}(z_c, k) \\ C_{02}(z_c, k) & C_{22}(z_c, k) \end{pmatrix}. \qquad (4.21)$$

The expression of the signal-to-noise when we neglect the multipole covariance or when we use only $\hat{P}_0$ or $\hat{P}_2$ is modified accordingly, as described for the likelihood function above.

The resulting signal-to-noise as a function of k is shown in Figure 4.2. We recall that the maximum scale explored is the minimum scale between the maximum scale imposed by the beam width and the linear regime cut-off of $k_{\max} = 0.2 \, h\text{Mpc}^{-1}$ (see Section 4.2.2.4).

At fixed redshift (upper panel of Figure 4.2), we observe that, when the monopole and the quadrupole are used together ($\ell = 0, 2$), we get a higher signal-to-noise with respect to the monopole ($\ell = 0$) and the quadrupole ($\ell = 2$) alone. For the $\ell = 0, 2$ case, we observe that when we consider multipole covariance (yellow solid line) we get an enhancement of the signal-to-noise at higher scales and a suppression at lower ones. As discussed in [68], this effect is caused by the beam smoothing factor in the model for $\hat{P}_{21}$ (see Section 4.1.2). We examine the implications of using different combinations of multipoles on the parameters constraints in Section 4.3.1.

We show how the signal-to-noise decreases as a function of redshift in the lower panel of Figure 4.2. Its shape is consistent at all redshifts (the full signal-to-noise for the mock measurements in Band 2 ($z = 0.25$), can be found in Figure 4.8). In our analysis, we will always consider the cumulative contribution from all the redshift bins.

4.2.3.2   *Numerical analysis*

To perform the MCMC analysis we use an expanded version of the MCMC sampler CosmoMC[2] [136, 212]. We modify it in order to include the computation of the theoretical expectations for the monopole and the quadrupole (see Appendix a) and of the likelihood function defined above (see Equation 4.19).

The analysis of the MCMC samples to compute the marginalized constraints is performed with the Python package GetDist[3] [315].

We conduct an MCMC analysis varying the six parameters describing the ΛCDM model, i.e. we vary $\{\Omega_b h^2, \Omega_c h^2, n_s, \ln(10^{10} A_s), \tau, 100\theta_{\text{MC}}\}$. Results on other parameters, such as H_0 and σ_8, are derived from results on this set. We list the fiducial values and the flat prior we use in Table 4.3.

---

[2]See https://cosmologist.info/cosmomc.
[3]See https://getdist.readthedocs.io.

Table 4.3: Assumed fiducial cosmology [4] and used flat priors.

Parameter	Fiducial value	Prior
$\Omega_b h^2$	0.022383	$[0.005, 0.1]$
$\Omega_c h^2$	0.12011	$[0.001, 0.99]$
n_s	0.96605	$[0.8, 1.2]$
$\ln(10^{10} A_s)$	3.0448	$[1.61, 3.91]$
τ	0.0543	$[0.01, 0.8]$
$100\theta_{\text{MC}}$	1.040909	$[0.5, 10]$

4.3 RESULTS

We present in this section the results of our analysis. We first explore the constraining power of the mock 21cm data set, using different combinations of multipoles (Section 4.3.1); we then combine the mock data set with Planck CMB data (Section 4.3.2); we study the effect of nuisance parameters describing the neutral hydrogen astrophysics in Section 4.3.3; finally, we discuss the impact of non-linear scales in Section 4.3.4.

We show the marginalized 1D and 2D posteriors for the studied set of parameters. Note that 68% confidence level constraints are presented as percentages with respect to the marginalized mean value. We recall that with the label "Planck 2018" we refer to the combination TT, TE, EE + low-ℓ + lowE + lensing (see Section 2.2.1).

4.3.1 *Probing the constraining power of 21cm signal observations*

In Figure 4.3 and Table 4.4, we show the marginalized contours and constraints[4] that we obtain using our SKA-Mid tomographic data set, i.e. with observations at different redshifts, for different combinations of multipoles. Note that we show only some of the model parameters for brevity.

As one could expect from the signal-to-noise predictions of Figure 4.2, using only the quadrupole leads to the broadest constraints, while the most constraining results are obtained for the monopole and the quadrupole combined. The off-diagonal terms of the multipole covariance do not affect much the constraints. The marginalized percentage constraints for the baseline case ($\hat{P}_0 + \hat{P}_2$ considering the full covariance) for the complete set of cosmological parameters can be found in Figure 4.6 and Table 4.6.

Our results show, as expected, that the constraining power on the cosmological parameters of the SKA-Mid mock data set is greater than what one could obtain with MeerKAT alone [117]. The data set we constructed is enough to constrain five out of six of the cosmological parameters. This is because 21cm observations are not sensitive to variations on τ, which remains unconstrained. The marginalized confidence levels are broad with respect to Planck constraints [4], but comparable with other probes. E.g., with tomographic ob-

---

[4]We specify that, when dealing with asymmetrical posterior distributions, we estimate the percentage constraint using the mean value between the left and right marginalized error. Given that this is a forecasts analysis, this approximation is enough for the purpose of this work.
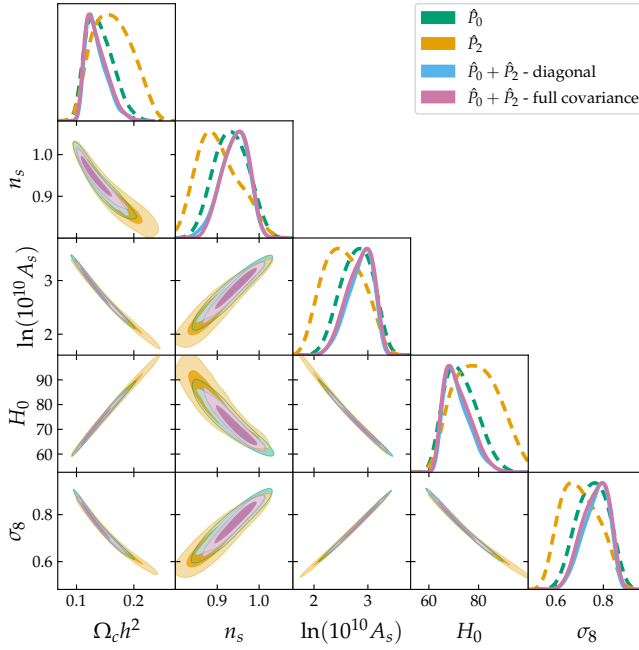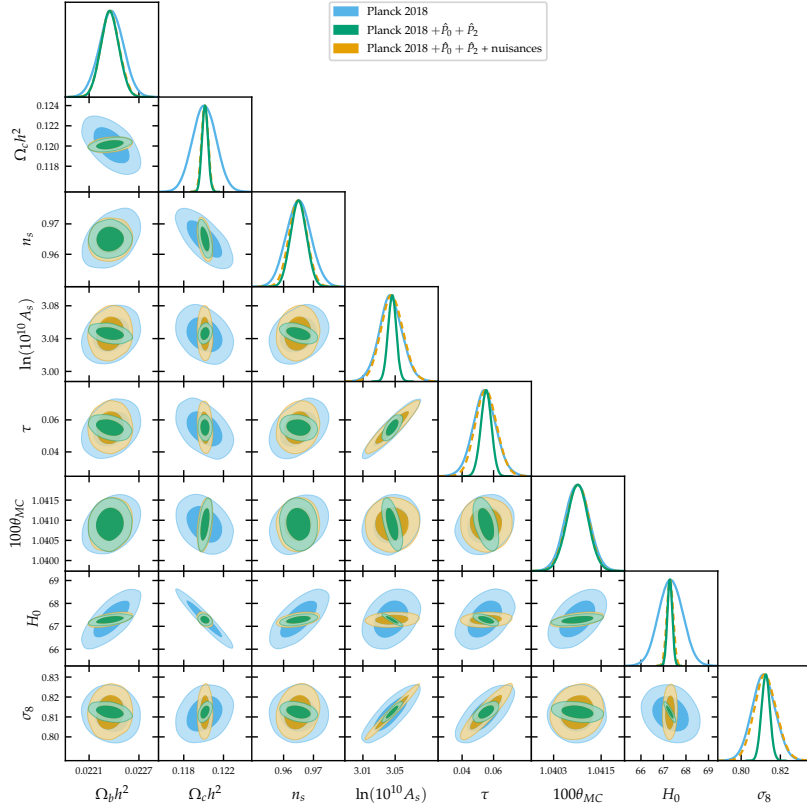
Figure 4.3: Joint constraints (68% and 95% confidence regions) and marginalized posterior distributions on a subset of the cosmological parameters. We show the constraints obtained using the mock tomographic data set for the monopole only ("$\hat{P}_0$"), the quadrupole only ("$\hat{P}_2$"), the two combined with ("$\hat{P}_0 + \hat{P}_2$ full covariance") and without ("$\hat{P}_0 + \hat{P}_2$ diagonal") considering multipole covariance. The relative constraints are listed in Table 4.4.

servations of the monopole and the quadrupole combined, we constrain H_0 with a relative error of $\sigma_{H_0} = 7.4\%$,

$$H_0 = 71.6^{+3.8}_{-6.8} \text{ km s}^{-1}\text{Mpc}^{-1} \quad \text{(68\%, } \hat{P}_0 + \hat{P}_2 \text{ - full covariance).} \tag{4.22}$$

We stress that when we state a constraint on a single parameter obtained using our mock 21cm data set, the central value does not have any physical meaning and it is driven by the input fiducial cosmology value.

Although not competitive with Planck, our tomographic measurements with six redshift bins and at linear scales provide an estimate of H_0 with an uncertainty comparable with others late Universe measurements [11], and, as we further discuss in Section 4.3.4, constraints on H_0 are improved if we extend our data set to non-linear scales. SKA-Mid 21cm observations will have thus the potential to provide new information for the discussion on the H_0 value [316].

Looking at the 2D contours, we observe that there is a marked degeneracy between the cosmological parameters. As already found for mock MeerKAT observations, 21cm measurements show a strong degeneracy in the H_0 - $\Omega_c h^2$ plane [117]. This feature is ascribable to the dependence on the matter power spectrum. At the considered scales the shape of $P_m(k)$ is found to be dependent on the combination of parameters $\Omega_m h$ [317]. A measure of the 21cm multipoles would fix up to some degree of confidence the shape of the matter power spec-

Table 4.4: Marginalized percentage constraints on cosmological parameters at the 68% confidence level. We show the results obtained using the mock tomographic data set for the monopole only ("$\hat{P}_0$"), the quadrupole only ("$\hat{P}_2$"), the two combined with ("$\hat{P}_0 + \hat{P}_2$ full covariance") and without ("$\hat{P}_0 + \hat{P}_2$ diagonal") considering multipole covariance. Confidence regions for the same set of results are shown in Figure 4.3.

Parameter	$\hat{P}_0$	$\hat{P}_0$	$\hat{P}_2 + \hat{P}_2$ diagonal	$\hat{P}_0 + \hat{P}_2$ full covariance
$\Omega_c h^2$	16.71%	21.57%	12.71%	13.36%
n_s	4.59%	5.59%	3.55%	3.44%
$\ln(10^{10} A_s)$	10.94%	15.26%	8.26%	8.83%
H_0	9.09%	12.01%	6.91%	7.39%
σ_8	9.56%	11.92%	7.11%	7.64%

trum and, in turn, the value of $\Omega_m h$. This implies that $\Omega_m h^2$, and consequently $\Omega_c h^2$, is correlated with h and H_0. This correlation is pivotal when combining intensity mapping data with CMB measurements, as we discuss in the following section.

4.3.2 *21cm signal observations combined with CMB data*

In the above section, we studied the constraining power of the 21cm multipoles. Here, we combine our baseline data set (the monopole $\hat{P}_0$ plus the quadrupole $\hat{P}_2$ considering the full covariance) with Planck CMB measurements. The rationale behind this is to investigate if and how 21cm observations can complement the detailed information on the cosmological parameters carried by the CMB.

We refer to Section 2.2.1 for a description of the used Planck 2018 [4] data sets and likelihoods. For consistency, we first run the Planck likelihood in our framework and reproduce constraints in agreement with the Planck 2018 results

$$
\begin{cases}
\Omega_c h^2 = 0.1201 \pm 0.0012 \\
H_0 = 67.32 \pm 0.53 \ \text{km s}^{-1}\text{Mpc}^{-1} \\
\ln(10^{10} A_s) = 3.045 \pm 0.014 \\
\sigma_8 = 0.8115 \pm 0.0060
\end{cases}
\quad \text{(68\%, Planck 2018).} \quad (4.23)
$$

Our results for the combination of the CMB data and our mock 21cm observation are presented in Table 4.5 and in Figure 4.4. Adding the 21cm power spectrum multipoles to the CMB significantly improves the constraining power on the majority of the cosmological parameters. The effect is particularly pronounced on $\Omega_c h^2$ and H_0, for which the error is reduced by approximately a fourth. This gain in constraining power is due to the combination of opposite degeneracy directions between the CMB and the 21cm power spectrum on these cosmological parameters. This effect is particularly strong in the H_0 - $\Omega_c h^2$ plane, where the degeneracy is completely removed. In the A_s - σ_8 plane, the effect is milder but still significant.
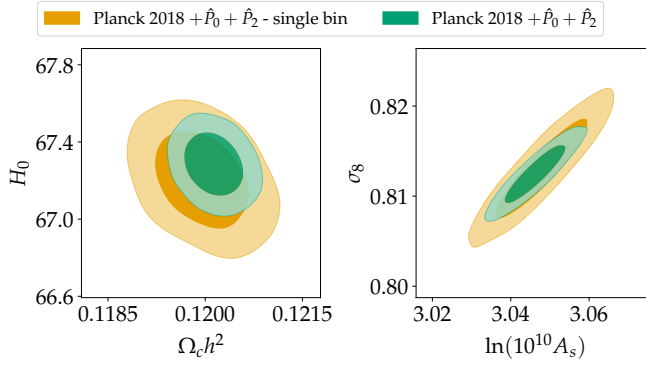
Figure 4.4: Joint constraints (68% and 95% confidence regions) and marginalized posterior distributions on cosmological parameters. The label "Planck 2018" stands for TT, TE, EE + lowE + lensing, while the label "$\hat{P}_0 + \hat{P}_2$" stands for the baseline tomographic data set for the monopole and the quadrupole combined and with multipole covariance taken into account. The label "nuisances" (dashed line) indicates that we vary the nuisances parameters along with the cosmological ones. The relative constraints are listed in Table 4.5.

In more detail, we find

$$
\begin{cases}
\Omega_c h^2 = 0.12014 \pm 0.00030 \\
H_0 = 67.28 \pm 0.11 \ \text{km s}^{-1}\text{Mpc}^{-1} \\
\ln(10^{10} A_s) = 3.0463 \pm 0.0052 \\
\sigma_8 = 0.8125 \pm 0.0021
\end{cases}
\quad (68\%, \ \text{Planck 2018} + \hat{P}_0 + \hat{P}_2). \qquad (4.24)
$$

We recall that the central value of the obtained constraints does not have a physical meaning and it is driven by the input fiducial cosmology we use for our mock 21cm observations. However, these values are useful to properly visualize the constraining power of our mock observations.

More important from a quantitative point of view is, instead, the relative error. We find $\sigma_{\Omega_c h^2} = 0.25\%$ and $\sigma_{H_0} = 0.16\%$, to be compared with the Planck

Table 4.5: Marginalized percentage constraints on cosmological parameters at the 68%
confidence level. Here, the label "Planck 2018" stands for TT, TE, EE + lowE +
lensing, while the label "$\hat{P}_0 + \hat{P}_2$" stands for the baseline tomographic data set
for the monopole and the quadrupole combined and with multipole covariance
taken into account. The label "nuisances" indicates that we vary the nuisance
parameters along with the cosmological ones. The label "single bin" indicates
that use the mock observation of the 21cm multipoles in a single redshift bin
centered at $z = 0.82$. Confidence regions for the same set of results are shown
in Figure 4.4.

Parameter	Planck 2018	$+\hat{P}_0 + \hat{P}_2$	+ nuisances	single bin
$\Omega_b h^2$	0.64%	0.49%	0.49%	0.73%
$\Omega_c h^2$	0.99%	0.25%	0.27%	0.39%
n_s	0.42%	0.27%	0.31%	0.32%
$\ln(10^{10} A_s)$	0.46%	0.17%	0.45%	0.26%
τ	13.44%	6.09%	12.19%	7.69%
$100\theta_{MC}$	0.03%	0.03%	0.03%	0.04%
H_0	0.79%	0.16%	0.20%	0.25%
σ_8	0.73%	0.26%	0.70%	0.45%

only estimates of $\sigma_{\Omega_c h^2} = 0.99\%$ and $\sigma_{H_0} = 0.79\%$. The estimate of the error
on H_0 we obtain combining 21cm power spectrum multipoles with CMB is
competitive with other LSS probes, e.g. with Euclid[5] forecasts [34]. The errors
on A_s and σ_8 are significantly reduced too, by more than a factor two: the
relative errors are $\sigma_{\ln(10^{10} A_s)} = 0.17\%$ and $\sigma_{\sigma_8} = 0.26\%$ to be compared with
$\sigma_{\ln(10^{10} A_s)} = 0.46\%$ and $\sigma_{\sigma_8} = 0.73\%$ of the Planck only result. Moreover, it is
interesting to see how the improvement on the other cosmological parameters
induces a better estimate of τ, although the 21cm observable alone has not a
significant constraining power on it.

From our analysis, it is clear that combining the CMB, an early Universe probe,
with late-time LSS measures strengthens our knowledge of the ΛCDM model.
The strong improvement obtained on $\Omega_c h^2$ and H_0 is due to the dependence on
the matter power spectrum of the 21cm multipoles, which fixes the product $\Omega_m h$
as discussed above. CMB observations fix a different combination of parameters,
i.e. $\Omega_m h^3$ [318], resulting in $\Omega_c h^2$ and H_0 to be anti-correlated [137]. Providing
an independent measurement of $\Omega_m h$, e.g. with 21cm observations, removes
the degeneracy and improves the constraints on $\Omega_m h^2$ and h, which impacts
directly on $\Omega_c h^2$ and H_0. This is a well-known effect, found also in [38]. Our
analysis improves on previous works by using the latest available CMB data,
the SKAO survey specifications, and full MCMC computations.

The advantage of 21cm observations over galaxy clustering surveys lies in its
tomographic nature. Measuring the 21cm signal within the full frequency range
that will be accessible with SKAO will provide a view of the late-time Universe
with exquisite redshift resolution up to redshift 3. This will complement the
cosmological information carried by the CMB, which is a two-dimensional probe
of the early Universe. To prove the importance of observations within multiple
redshift bins, we compare in Figure 4.5 our tomographic results with a single
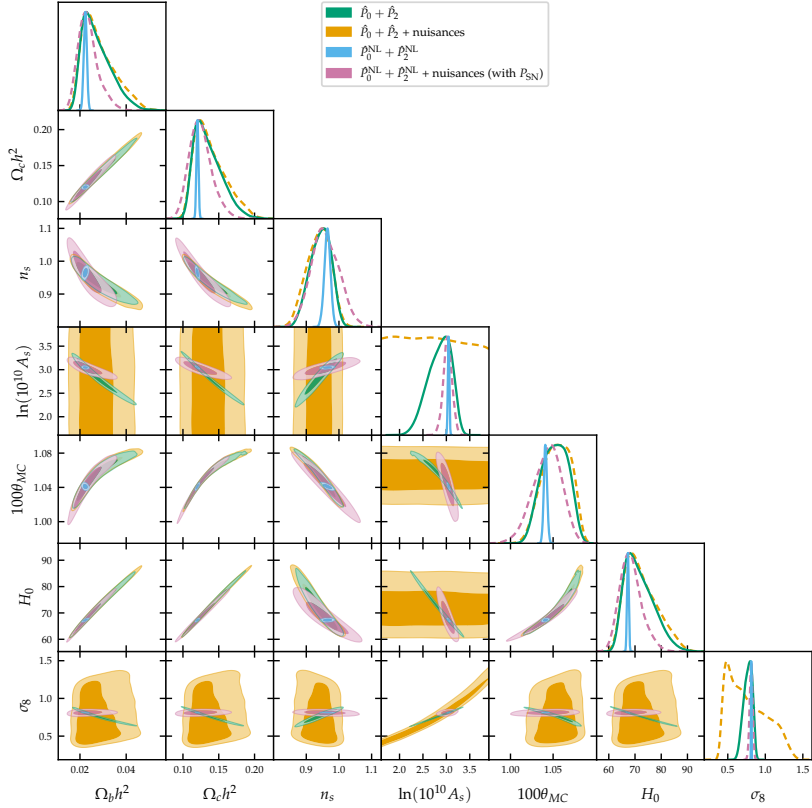
---

[5] https://sci.esa.int/web/euclid

Figure 4.5: Joint constraints (68% and 95% confidence regions) and marginalized posterior distributions on cosmological parameters. The label "Planck 2018" stands for TT, TE, EE + lowE + lensing, while the label "$\hat{P}_0 + \hat{P}_2$" stands for the baseline tomographic data set for the monopole and the quadrupole combined and with multipole covariance taken into account. The label "single bin" indicates that use the mock observation of the 21cm multipoles in a single redshift bin centered at $z = 0.82$. The relative constraints are listed in Table 4.5.

bin observation at redshift $z = 0.82$, that mimics the analysis carried out in [68], when both are combined with Planck data. We find that using multiple bins observations significantly improves the constraints, especially for $\Omega_c h^2$ and H_0. The error on H_0 shrinks from 0.25%, in the single bin case, to 0.16%, in the tomographic one, as shown in Table 4.5.

We conclude that tomographic 21cm observations provide complementary information to the CMB, allowing for a significantly improved estimation of the cosmological parameters.

Note that the improvement is stronger than the effect of adding BAO measurements to the CMB [4]. Although we do not show results here, we tested also the effect of using BAO [266, 319, 320] along with the multipoles and the CMB, finding no significant repercussion on the constraints.

4.3.3 Introducing astrophysical uncertainties

In the analysis discussed above, we assumed perfect knowledge of the astrophysics involved in the estimate of 21cm signal observations. In particular, we assumed to know the total HI density Ω_{HI} (that enters in Equation 4.2) and the HI bias b_{HI} as a function of redshift. However, these quantities depend on the detailed baryon physics at play and their connection with dark matter is not completely understood [e.g. 158, 307, 321, 322]. To take into account our ignorance on these parameters in our analysis, we follow [156] and rewrite the power spectrum of Equation 4.5 as

$$\hat{P}_{21}(z, k, \mu) = \tilde{B}^2(z, k, \mu)\left[\bar{T}_{\mathrm{b}}(z)b_{\mathrm{HI}}(z)\sigma_8(z)+ \right.$$
$$\left. + \bar{T}_{\mathrm{b}}(z)f(z)\sigma_8(z)\,\mu^2\right]^2 \frac{P_{\mathrm{m}}(z, k)}{\sigma_8(z)}. \tag{4.25}$$

Table 4.6: Marginalized percentage constraints on cosmological parameters at the 68% confidence level. Here, the label "$\hat{P}_0 + \hat{P}_2$" stands for the baseline tomographic data set for the monopole and the quadrupole combined and with multipole covariance taken into account. The label "$\hat{P}_0^{\mathrm{NL}} + \hat{P}_2^{\mathrm{NL}}$" indicates that the full non-linear data set has been used. The label "nuis." indicates that we vary the nuisance parameters along with the cosmological ones. The symbol "—" stands for unconstrained. Confidence regions for the same set of results are shown in Figure 4.6.

Parameter	$\hat{P}_0 + \hat{P}_2$	+ nuis.	$\hat{P}_0^{\mathrm{NL}} + \hat{P}_2^{\mathrm{NL}}$	+ nuis. ($\hat{P}_{\mathrm{SN}}$)
$\Omega_b h^2$	21.04%	22.81%	3.02%	17.30%
$\Omega_c h^2$	13.36%	14.66%	1.16%	12.27%
n_s	3.44%	3.94%	0.95%	4.45%
$\ln(10^{10} A_s)$	8.83%	—	0.49%	3.00%
$100\theta_{MC}$	1.53%	1.62%	0.18%	1.61%
H_0	7.39%	8.10%	0.49%	5.90%
σ_8	7.64%	—	0.37%	2.41%

The redshift dependent combinations of functions $\bar{T}_b b_{\mathrm{HI}} \sigma_8(z)$ and $\bar{T}_b f \sigma_8(z)$ can be added to the set of estimated parameters as nuisances. The most general parametrization for these nuisance parameters does not impose any specific redshift evolution. Given that we have six redshift bins, we need twelve new parameters: six $[\bar{T}_b b_{\mathrm{HI}} \sigma_8]_i$ and six $[\bar{T}_b f \sigma_8]_i$, one for each redshift, with i being $i = \{1, \ldots, 6\}$. However, the high dimensionality of this configuration impact significantly the required computational time for the convergence of the MCMC procedure for the exploration of the posterior.

Alternatively, one can lower the number of nuisance parameters by assuming a parametrization for the redshift evolution of $\bar{T}_b b_{\mathrm{HI}} \sigma_8(z)$ and $\bar{T}_b f \sigma_8(z)$ in agreement with their theoretical prediction. We use a 3rd-degree polynomial model

$$\bar{T}_b b_{\mathrm{HI}} \sigma_8(z), \ \bar{T}_b f \sigma_8(z) = az^3 + bz^2 + cz + d, \tag{4.26}$$

and reduce the nuisances from twelve to eight: four coefficients $[\bar{T}_b f \sigma_8]_q$, with $q = \{a, b, c, d\}$, and other four $[\bar{T}_b f \sigma_8]_q$. We find that assuming this redshift evolution gives the same results with respect to the twelve nuisances case while we achieve a better and faster convergence. Thus, we choose to work with this latter parametrization of the nuisances.

In Figure 4.7 we show the theoretical redshift evolution (under the assumption discussed in Section 4.1.1) and the fitted one for $\bar{T}_b b_{\mathrm{HI}} \sigma_8$ and $\bar{T}_b f \sigma_8$. In the following, we show the results we obtain varying the eight nuisance parameters. Note that we assume a very wide flat prior, centered at the theoretical expected value for each nuisance parameter.

We present the results for the multipoles alone in Table 4.6 and Figure 4.6.

When opening the parameter space to the nuisances, we see a complete loss of constraining power on A_s. This is expected, due to the fact that by varying the nuisances we lose information on the amplitude of the power spectrum. The deterioration of the constraint on A_s translates in a weakening of the constraining power on σ_8. This, in turn, widens the errors also on τ.

Figure 4.6: Joint constraints (68% and 95% confidence regions) and marginalized posterior distributions on cosmological parameters. Here, the label "$\hat{P}_0 + \hat{P}_2$" stands for the baseline tomographic data set for the monopole and the quadrupole combined and with multipole covariance taken into account. The label "$\hat{P}_0^{NL} + \hat{P}_2^{NL}$" indicates that the full non-linear data set has been used. The label "nuisances" (dashed lines) indicates that we vary the nuisance parameters along with the cosmological ones. The relative constraints are listed in Table 4.6.

Nevertheless, the impact of nuisance parameters is limited to these two parameters. The constraints on the other cosmological parameters remain unaffected showing the power of tomography: using the six redshift bins allows to include the evolution of the 21cm power spectrum multipoles and, thus, preserves their constraining power in particular on $\Omega_c h^2$ and H_0.

The same discussion applies when we combine the multipoles with CMB, as in Section 4.3.2 but also varying the nuisance parameters. Results are shown in Figure 4.4 and Table 4.5 from which it can be seen that the constraints on $\Omega_c h^2$ and H_0 remain essentially unvaried. Note, however, that the constrain on A_s and τ and, consequently, on σ_8 are driven just by the Planck data.

For completeness, 2D contours and the marginalized posteriors for the nuisance parameters themselves are shown in Figure b.2 and discussed in Appendix b.
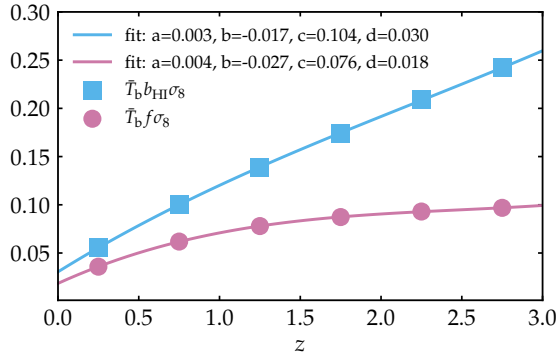
Figure 4.7: Redshift evolution for the nuisance parameters $\bar{T}_b b_{HI}\sigma_8(z)$ and $\bar{T}_b f\sigma_8(z)$. We show the theory predicted values for the six redshift bins we consider (circles and squares) and the best-fit redshift evolution (solid lines) modeled as a 3rd-degree polynomial (see Equation 4.26).

4.3.4 Extending to non-linear scales

Up to now, we investigated the constraining power on the cosmological parameters of 21cm observations at linear scales, which are the ones best sampled by the large beam of the single-dish intensity mapping. At the linear scales, it is also possible to explore beyond ΛCDM models [117], for which we often lack non-linear scale predictions. In a ΛCDM scenario and for the low-z bins, we can, however, push our analysis to larger k and study their constraining power.

For all redshift bins but the first two, the k_{max} cut-off due to the frequency-dependent beam (see Section 4.2.2.4) is much stronger than the linear-scale cut-off $k = 0.2\,h\,\mathrm{Mpc}^{-1}$. The two lowest redshift bins ($z = 0.25$ and $z = 0.75$) can instead be extended to larger k if we relax the linear-scale cut-off. We acquire 15 and 67 new points and we are able to reach $k \sim 0.27\,h\,\mathrm{Mpc}^{-1}$ and $k \sim 1\,h\,\mathrm{Mpc}^{-1}$ at redshifts $z = 0.75$ and $z = 0.25$, respectively. In this new k-range, the shot noise is non-negligible and it needs to be considered in the modeling.

We create the new mock non-linear data set as

$$\hat{P}_{21}^{NL}(z,\,k,\,\mu) = \tilde{B}^2(z,k,\mu)\big[P_{21}^{NL}(z,k) + P_{SN}(z)\big], \tag{4.27}$$

where P_{SN} is the shot noise level estimated at different redshift interpolating results from hydro-dynamical simulations [158]. The non-linear 21cm power spectrum $P_{21}^{NL}(z,k)$ is obtained as in Equation 4.1, but substituting the linear matter power spectrum with the non-linear one, computed numerically with CAMB[6]. The expressions for the 21cm multipoles are changed accordingly.

In Figure 4.8, we show the signal-to-noise for the new non-linear tomographic data set obtained with the model of Equation 4.27. For the scales larger than $k = 0.2\,h\,\mathrm{Mpc}^{-1}$, the results for the various redshifts are analogous to the ones of Figure 4.2.

With this non-linear data set, we perform an analysis similar to the one discussed in the previous sections. We study the constraining power of non-

---

[6]We use the HALOFIT [323] version from [324].

Table 4.7: Shot noise values used in the computation of the non-linear 21cm power spectrum, at each central redshift z_c. For the first redshift bin ($z = 0.25$) we assume SKA-Mid Band 2 specifications, while we use SKA-Mid Band 1 parameters for the other bin. We refer to Table 4.1 for more instrumental details.

z_c	central redshift	0.25	0.75	
P_{SN}	shot noise	0.72	2.4	$[\mathrm{mK}^2\,h^{-3}\mathrm{Mpc}^3]$
N	number of data points	83	58	
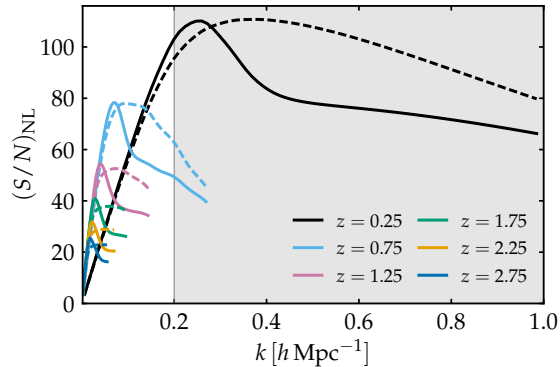
Figure 4.8: Computed signal-to-noise ratio as a function of k (see Equation 4.20). We show the signal-to-noise computed for the six redshift bins and for the monopole and the quadrupole combined, considering a diagonal covariance matrix (dashed lines) or the full non-diagonal one (solid lines). The shaded area highlights the new scales acquired extending the mock 21cm power spectrum to non-linear scales.

linear 21cm observations alone and combined with CMB. We first assume perfect knowledge of the quantities Ω_{HI} and b_{HI} linked to baryon physics. Note that, for this ideal case without any nuisance parameters, we assume also that the level of the shot noise is known.

Results are presented in Table 4.4 and Figure 4.6.

Even if only the first two bins are concerned, the extension of the data set to non-linear scales significantly improves on the constraining power of 21cm observations. We find

$$H_0 = 67.28 \pm 0.33 \ \mathrm{km \ s^{-1} Mpc^{-1}} \quad {\scriptstyle (68\%, \ \hat{P}_0^{\mathrm{NL}} + \hat{P}_2^{\mathrm{NL}}),} \qquad (4.28)$$

thus a relative error of $\sigma_{H_0} = 0.49\%$, competitive with the one from Planck 2018 data alone (i.e. $\sigma_{H_0} = 0.79\%$).

We then test the more realistic case where we vary the nuisance parameters. Along with the eight nuisances for the redshift evolution of $\bar{T}_b b_{\mathrm{HI}} \sigma_8(z)$ and $\bar{T}_b f \sigma_8(z)$ (see Section 4.3.3), we include six additional parameters $P_{\mathrm{SN},i}$, with $i = \{1,\ldots,6\}$, to model the shot noise in each redshift bin.

We get

$$H_0 = 68.3^{+3.4}_{-4.7} \ \mathrm{km \ s^{-1} Mpc^{-1}} \quad {\scriptstyle (68\%, \ \hat{P}_0^{\mathrm{NL}} + \hat{P}_2^{\mathrm{NL}} + \mathrm{nuis.} \ (P_{\mathrm{SN}})).} \qquad (4.29)$$

The relative error is $\sigma_{H_0} = 5.9\%$, better than the corresponding result for the linear-scale case discussed in Section 4.3.3 (i.e. $\sigma_{H_0} = 7.4\%$). When we open to nuisances with the non-linear data set, the presence of the shot noise terms helps to fix the height of the power spectrum and we do not lose all the constraining power on A_s and σ_8. We can thus constrain all the cosmological parameters, with the exception of τ. The posteriors for the shot noise parameters $P_{\mathrm{SN},i}$ and the other nuisances are shown in Figure b.3 and commented in Appendix b.

In summary, extending the data set to non-linear has an essential role in increasing the constraining power of the 21cm multipoles alone. Our results suggest that competitive constraints independent from other probes could be obtained with 21cm intensity mapping observations at lower redshifts and non-linear scales.

When combining the non-linear data set $\hat{P}_0^{\mathrm{NL}} + \hat{P}_2^{\mathrm{NL}}$ + nuisances with Planck data, instead, we do not observe substantial changes in the constraints with respect to the Planck + $\hat{P}_0 + \hat{P}_2$ + nuisances case (shown in Figure 4.4). As discussed in Section 4.3.2, the improvement in combining the two probes mainly comes from the interaction of opposite degeneracy direction for some of the cosmological parameters between the CMB and the 21cm power spectrum. These are unaffected by the extension to non-linear scales and thus when combined with the Planck data, this extended mock data set does not add much information with respect to the linear one.

4.4 CONCLUSIONS

In this work, we forecast the constraints on the ΛCDM cosmological parameters for a neutral hydrogen intensity mapping survey with the SKAO telescope, assuming the measurement of the first multipoles of the redshift-space 21cm power spectrum. We construct and analyze this mock data set as an alternative large-scale structure probe alone and in combination with Planck CMB data. We model monopole and quadrupole signal of the 21cm power spectrum at linear scales as in [68, 311, 314] and we include in our analysis the full non-diagonal covariance matrix between the multipoles.

We follow the SKAO Red Book [57] proposal and simulate single-dish observations with the SKA-Mid telescope both in Band 2 (frequency range $0.95 - 1.75$ GHz) and in Band 1 (frequency range $0.35 - 1.05$ GHz). Assuming a Planck 2018 fiducial cosmology, we construct a tomographic data set of observations within six different redshift bins. To test the constraining power on the cosmological parameters of the constructed data set, we implement the computation of the likelihood function for the monopole and the quadrupole, fully integrated with the MCMC sampler CosmoMC. We include a discussion on the impact of our lack of knowledge on the baryonic physics involved in the computation of the 21cm power spectrum, as nuisance parameters in the analysis.

We first focus on the 21cm power spectrum measurements at linear scales, which are the preferred target of single-dish intensity mapping observations with SKA-Mid, due to the large beam on the sky. However, for the lowest redshifts, the telescope beam is small enough to allow to probe also the non-linear scales. We thus extend our mock data set to non-linearities and we add the shot noise contribution to check if this could improve on the constraining power. The results of our analysis can be summarized as follows.

We find that the mock SKA-Mid 21cm observations have good constraining power on the cosmological parameters. The constraints we obtain are comparable with other probes. E.g., with the 21cm monopole and quadrupole combined, both H_0 and σ_8 are constrained at the $\sim 7\%$ level. The 2D contours present very marked degeneracies between the parameters, especially in the $\Omega_c h^2$ - H_0 and $\ln(10^{10} A_s)$ - σ_8 planes.

Adding the mock 21cm observations to Planck 2018 CMB data, it is possible to significantly narrow the constraints, with respect to Planck alone. Although the effect is observable on all the parameters, we get the most significant improvement on $\Omega_c h^2$ and H_0, for which the errors are lessened by a fourth. With 21cm multipoles + Planck, we estimate $\Omega_c h^2$ and H_0 at the 0.25% and 0.16% levels respectively, to be compared with 0.99% and 0.79%, obtained with Planck alone. For $\ln(10^{10} A_s)$ and σ_8 the errors are reduced by more than a factor two. We constrain $\ln(10^{10} A_s)$ at the 0.17% and σ_8 at the 0.26% level, to be compared with the 0.46% and 0.73% Planck estimates, respectively. Furthermore, we observe that combining the tomographic 21cm data set with CMB alleviates some of the degeneracies between the parameters, resulting in improved constraints. The strongest effect is visible in the $\Omega_c h^2$ - H_0 plane. Although 21cm observations are not sensitive to τ, we find that with Planck the improvement on the other parameters is reflected also on τ, reducing the error by a factor of two.

To take into account the lack of knowledge on the brightness temperature T_b (that depends on the total HI density Ω_{HI}) and the HI bias b_{HI}, we repeat our analysis including nuisance parameters. In particular, we consider the combinations $\bar{T}_b b_{\mathrm{HI}} \sigma_8$ and $\bar{T}_b f \sigma_8$, where f is the growth factor. We find that, when we open the parameter space to these nuisances, the constraining power of 21cm multipoles on A_s, and consequently on σ_8, is crucially reduced. However, the results obtained for $\Omega_c h^2$ and H_0 remain unaffected, for both the 21cm data set alone and combined with Planck. This result confirms the strength of 21cm tomographic measurements and motivates, even more, the current observational effort in this field.

When we extend the 21cm data set to non-linear scales we find a tightening in the constraints. The most noteworthy result is that the constraining power of 21cm multipole observations on A_s and σ_8 is remarkably improved, even when we open up the parameter space to the nuisance parameters. This is due to the fact the information at lower scales helps to fix the amplitude of the power spectrum.

We conclude that 21cm SKAO observations will provide a competitive cosmological probe, complementary to CMB and, thus, pivotal for gaining statistical significance on the cosmological parameters constraints.

The formalism presented in this work and the mock data set we construct can be straightforwardly adapted to forecast constraints on the neutrino mass and beyond ΛCDM models, as discussed in Chapter 8. Note that our modeling does not include possible residual foreground contamination. A discussion on how the constraints on the cosmological parameters could be biased by this systematic is left for future work.

THE 21CM SIGNAL CROSS-CORRELATION WITH GALAXY CLUSTERING

I N CHAPTER 4, we investigated the impact of future 21cm power spectrum multiple measurements, planned for the SKAO cosmological surveys, on our knowledge of the standard cosmological model. Intensity mapping is however a relatively young technique and, at the state of the art, the considered 21cm auto power spectrum detections are limited by systematics both due to residual foreground emission and calibration challenges. The cross-correlation of 21cm observations with galaxy clustering measurements is, instead, less prone to these systematics since they are uncorrelated with the ones from galaxy surveys and thus heavily reduced. As discussed in Chapter 2, cross-correlation detections have been available since 2010. It is, thus, of great importance to refine the cross-correlation forecasts for the 21cm and galaxy clustering, in order to optimize the IM survey design and maximally exploit the synergy with the upcoming cutting-edge galaxy surveys.

We focus, as before, on the planned SKAO surveys with SKA-Mid, for the 21cm intensity mapping, while for galaxy surveys we consider the pivotal clustering measurements that will be provided by key instruments in the next few years, i.e. the Dark Energy Spectroscopic Instrument (DESI) and the Euclid mission. We expand the formalism of Chapter 4 by implementing the cross-correlation power spectrum in the redshift range of overlap of the two types of probes.

The constraints that we forecast for the parameters of the ΛCDM model are promising. The predicted signal-to-noise ratio for the cross-correlation can reach ~ 50 for $z \sim 1$ and $k \sim 0.1h$ Mpc^{-1}. When the cross-correlation signal is combined with current CMB data from Planck, the error on $\Omega_c h^2$ and H_0 is reduced by a factor of 3 and 6, respectively, compared to CMB only data, due to the independent measurements of matter clustering provided by 21cm IM and galaxy clustering. The cross-correlation signal has a constraining power that is comparable to the auto-correlation one, presented in Chapter 4, and combining all the clustering measurements a sub-percent error of 0.33% on H_0 can be achieved, which is about a factor of 2 better than CMB only measurement. As a proof-of-concept, we test the full pipeline on the intensity mapping MeerKAT data published by the MeerKLASS collaboration and present some preliminary constraints on the cosmological parameters.

The structure of the chapter is as follows. The methodology is reviewed in Section 5.1. The building of the mock observations is detailed in Section 5.2. Results are summarized in Section 5.3 with the presentation of the constrained obtained. A summary of the results and our conclusions are outlined in Section 5.4.

5.1   MODELING THE CROSS-CORRELATION SIGNAL

The analysis presented here for the 21cm × galaxy clustering power spectrum is an extension of the one discussed in Chapter 4. Since we adopt analogous formalism and framework of the previous study, in the following, we review only the essential information while we refer the reader to Chapter 4 for more details. To be exhaustive, we discuss also the 21cm auto-power spectrum and the galaxy power spectra in Section 5.1.1 and Section 5.1.2, which enter the error estimation. The model for the cross-correlation power spectrum is presented in Section 5.1.3.

5.1.1   *Model for the observed 21cm signal power spectrum*

As seen in Equation 4.27, the 21cm non-linear power spectrum can be modeled as [57, 153, 158]

$$P_{21}(z, k, \mu) = \bar{T}_b^2(z) \left[\left(b_{\mathrm{HI}}(z) + f(z) \mu^2 \right)^2 P_{\mathrm{m}}(z, k) + P_{\mathrm{SN}} \right], \qquad (5.1)$$

where $\bar{T}_b$ is the HI mean brightness temperature, b_{HI} is the HI bias, f is the growth rate, $\mu = \hat{k} \cdot \hat{z}$ is the cosine of the angle between the wave number and the line-of-sight, $P_{\mathrm{m}}(z, k)$ is the non-linear matter power spectrum and P_{SN} is the shot noise term.

For the evolution in redshift of the brightness temperature, we use the parametrization defined in Equation 4.2. Given that we lack an analytical model, $b_{\mathrm{HI}}(z)$ and $P_{\mathrm{SN}}(z)$ at a given redshift are computed by interpolating numerical results from hydro-dynamical simulations [158, 309]. The growth rate $f(z)$ and the non-linear matter power spectrum $P_{\mathrm{m}}(z, k)$ are, instead, computed numerically by means of the Einstein-Boltzmann solver CAMB[1] [173].

To mimic a realistic observation, we introduce the effect of a Gaussian telescope beam, as a suppression of the power spectrum on scales smaller than the beam's full width at half maximum [51, 55, 68, 310, 311]. The corresponding dumping factor $\tilde{B}(z, k, \mu)$ can be written in terms of the beam's physical dimension R_{beam}, as in Equation 4.4.

Moreover, in a real-world scenario, one must consider the possibility of having chosen the wrong fiducial cosmology. This can be taken into account with the Alcock–Paczynski (AP) modifications [325]. Anisotropies along the radial and transverse direction can be modeled as[2]

$$\alpha_\perp(z) = \frac{D_A(z)}{D_A^{\mathrm{fid}}(z)} \qquad \text{and} \qquad \alpha_\parallel(z) = \frac{H^{\mathrm{fid}}(z)}{H(z)}. \qquad (5.2)$$

Here, $D_A^{\mathrm{fid}}(z)$ and $H^{\mathrm{fid}}(z)$ are the values of the angular diameter distance and the Hubble parameter at redshift z predicted by the fiducial cosmology. The AP parameters $\alpha_\perp$ and $\alpha_\parallel$ modify the overall amplitude of the power spectrum

---

[1]See https://CAMB.info/. Note that non-linear corrections to the matter power spectrum are computed with the HALOFIT [323] version from [324].

[2]In literature, several definitions of $\alpha_\perp$ and $\alpha_\parallel$ have been proposed, e.g. [134, 326, 327]. We follow the one of e.g. [34, 68].

and the wave vectors. The wave vector components along and transverse to the line of sight are then distorted as

$$q = \frac{k}{\alpha_\perp} \sqrt{1 + \mu^2 \left(\frac{\alpha_\perp^2}{\alpha_\parallel^2} - 1 \right)} \tag{5.3}$$

and

$$\nu = \frac{\alpha_\perp \mu}{\alpha_\parallel \sqrt{1 + \mu^2 \left(\frac{\alpha_\perp^2}{\alpha_\parallel^2} - 1 \right)}}, \tag{5.4}$$

where k and μ are the assumed fiducial values of the wave vectors.

The observed 21cm power spectrum, marked with the symbolˆ, including the beam smoothing and the AP effects, is then

$$\hat{P}_{21}(z, k, \mu) = \frac{1}{\alpha_\perp^2 \alpha_\parallel} \tilde{B}^2(z, q, \nu) P_{21}(z, q, \nu), \tag{5.5}$$

where $P_{21}(z, q, \nu)$ is defined in Equation 5.1, but computed on the new variables q and ν.

We note that, in this chapter, we expand the modeling of Chapter 4, where we neglected the AP contribution in first approximation. A discussion on the effect of the inclusion of the AP distortions on the cosmological parameter constraints is presented in Appendix c.

5.1.2 *Model for the galaxy power spectrum*

The simplest parametrization of the galaxy power spectrum at a given redshift can be written as

$$P_g(z, k, \mu) = \left(b_g(z) + f(z) \mu^2 \right)^2 P_m(z, k) + \frac{1}{\bar{n}_g(z)}, \tag{5.6}$$

where b_g is the galaxy bias and $\bar{n}_g$ is the galaxy number density. The term $1/\bar{n}_g$ is the shot noise term for the galaxy power spectrum. In this work, we use values of b_g and $\bar{n}_g$ in agreement with the official expected values for the planned galaxy surveys, as discussed in Section 5.2.2.

Note that for the galaxy power spectrum, due to the different observing techniques, there is no need to take into account the beam correction. The AP distortions, instead, are the ones described in the previous section for P_{21}. Therefore, the observed galaxy power spectrum we consider is

$$\hat{P}_g(z, k, \mu) = \frac{1}{\alpha_\perp^2 \alpha_\parallel} P_g(z, q, \nu). \tag{5.7}$$

5.1.3 *The cross-correlation signal power spectrum*

To predict the cross-correlation power spectrum between the 21cm signal and galaxy clustering, we use the following model (see e.g. [61, 286])

$$P_{21,g}(z, k, \mu) = \bar{T}_b \left(b_{HI} + f\mu^2 \right) \left(b_g + f\mu^2 \right) P_m(z, k, \mu), \tag{5.8}$$

where all the quantities appearing here are defined in the previous sections. In the expression above we do not make explicit the redshift dependence of the brightness temperature, the bias, and the growth rate for the sake of notation easiness. Moreover, it can be shown that the shot noise contribution for the cross-correlation power spectrum is negligible [158, 328].

Taking into account the intensity mapping beam effect and the AP distortions, the observed cross-correlation signal becomes

$$\hat{P}_{21,g}(z, k, \mu) = \frac{1}{\alpha_\perp^2 \alpha_\parallel} r \tilde{B}_\perp(z, q, \nu) P_{21,g}(z, q, \nu), \qquad (5.9)$$

with r being a cross-correlation coefficient.[3]

5.1.4 *Multipole expansion*

As discussed in Section 4.1.3, the non-isotropic power spectrum can be decomposed using Legendre polynomials $\mathcal{L}_\ell(\mu)$. The coefficients of the expansion, i.e. the multipoles of the power spectrum, are given by

$$\hat{P}_{X,\ell}(z, k) = \frac{(2\ell + 1)}{2} \int_{-1}^{1} d\mu\, \mathcal{L}_\ell(\mu) \hat{P}_X(z, k, \mu), \qquad (5.10)$$

for X being either the 21cm intensity mapping (X = 21), the galaxy clustering (X = g) or their cross-term (X = 21, g). In this work, we use the auto power spectrum and cross-correlation monopoles, for which $\ell = 0$ and $\mathcal{L}_0(\mu) = 1$. In particular, we focus on forecasting the cross-correlation power spectrum monopole $\hat{P}_{21,g,0}(z, k)$. In the following, for clarity of notation, we drop the subscript 0 and simply refer to the monopoles as $\hat{P}_{21,g}(z, k)$, $\hat{P}_g(z, k)$ and $\hat{P}_{21}(z, k)$.

5.2 CONSTRUCTING THE MOCK CROSS-CORRELATION DATA

The goal of this work is to forecast the constraining power of the cross-correlation between 21cm and galaxy clustering. To this end, we construct mock data sets of cross-correlation measurements from future surveys. In this section, we describe our methodology to obtain realistic forecasts of the cosmological parameter constraints. The 21cm and galaxy surveys we take into account are presented in Section 5.2.1. Details on the construction of the synthetic data set and the analysis framework are given in Section 5.2.2 and Section 5.2.3.

5.2.1 *Survey specifications*

5.2.1.1 *21cm intensity mapping*

The main focus of our analysis is the 21cm intensity mapping signal that can be measured with the SKAO telescope. We consider, in particular, a cosmological survey with the SKA-Mid telescope in single-dish mode, following SKA

---

[3] The definition of r is not unique (see e.g. the discussion in [61]). In this work, we consider it an overall constant for simplicity, given that r is considered as a nuisance parameter (Section 5.2.3.2).

Table 5.1: Assumed specifications for SKA-Mid Wide band 1 [57], DESI ELG [32, 286], and Euclid-like surveys [34]. For simplicity, we refer to SKA-Mid as SKAO, to DESI ELG as DESI, and to Euclid-like as Euclid. We collect the used effective redshifts z and bin widths Δz, the galaxy biases b_g and number densities $\bar{n}_\mathrm{g}$, that we express in units of $[10^{-4}h^3 \ \mathrm{Mpc}^{-3}]$, the 21cm intensity mapping bias b_HI, and the 21cm power spectrum shot noise P_SN, in units of $[(h^{-1} \ \mathrm{Mpc})^3]$.

SKAO				
Band frequency range				0.35 - 1.05 [GHz]
Corresponding redshift range				0.35 - 3
Dish diameter D_dish				15 [m]

SKAO × Euclid				
Observed redshift range				0.9 - 1.8
Overlapping survey area				10 000 $[\mathrm{deg}^2]$
Corresponding Ω_sur				3.0 [sr]
z	1.	1.2	1.4	1.65
Δz	0.2	0.2	0.2	0.3
b_g	1.46	1.61	1.75	1.9
$\bar{n}_\mathrm{g}$	6.86	5.58	4.21	2.61
b_HI	1.49	1.60	1.71	1.84
P_SN	124	114	101	85.0

SKAO × DESI										
Observed redshift range								0.7 - 1.7		
Overlapping survey area								5 000 $[\mathrm{deg}^2]$		
Corresponding Ω_sur								1.5 [sr]		
z	0.75	0.85	0.95	1.05	1.15	1.25	1.35	1.45	1.55	1.65
Δz	0.1	0.1	0.1	0.1	0.1	0.1	0.1	0.1	0.1	0.1
b_g	1.05	1.08	1.11	1.14	1.18	1.21	1.25	1.28	1.32	1.36
$\bar{n}_\mathrm{g}$	11.2	8.32	8.16	5.14	4.49	4.19	1.57	1.35	0.921	0.344
b_HI	1.35	1.40	1.46	1.52	1.57	1.63	1.68	1.73	1.78	1.84
P_SN	132	130	126	122	116	111	105	98	91	85

Cosmology SWG [57]. We assume a Wide Band 1 survey that covers a sky area of 20 000 deg^2 in the frequency range $0.35 - 1.05$ GHz (i.e. the redshift range $0.35 - 3$).

5.2.1.2 *Galaxy surveys*

We assume a Euclid-like spectroscopic galaxy survey, following what has been proposed in [34]. We consider observations within four different redshift bins in the range of 0.9 - 1.8. The assumed values of the galaxy bias and number density computed at each effective redshift are presented in Table 5.1.

To obtain a cross-correlation signal, one must take into account observations of the same portion of the sky. An indicative map of the planned sky coverage is shown in Figure 5.1. In agreement with other studies in literature, we assume a 10 000 deg^2 overlapping patch of the sky observed by the SKAO and a Euclid-like survey.
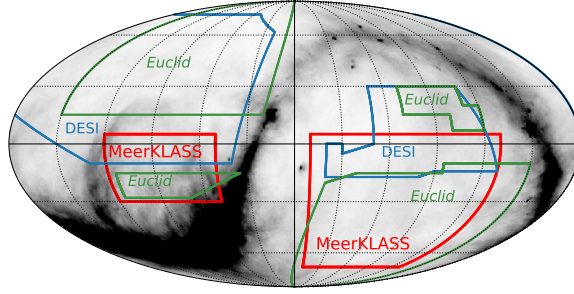
Figure 5.1: Estimaded sky coverage of future galaxy and intensity mapping surveys.

Hereafter, we simply refer to the Euclid survey, where is understood that a Euclid-like survey as the one described above is intended.

To construct cross-correlation measurements between the SKAO and DESI, we follow [286]. We focus on the DESI Emission Line Galaxies (ELG), as they probe a redshift range similar to the one covered by Euclid, i.e. 0.7 - 1.7, making easier a direct comparison between the two experiments. In Table 5.1, we report the assumed values of the galaxy bias and number density at each effective redshift and we consider an overlapping area between DESI ELG and SKAO of 5 000 deg^2. The smaller area overlap with respect to a Euclid-like survey is forced by the different hemisphere locations of the two telescopes and can be roughly visualized in Figure 5.1.

5.2.2   *Mock data sets*

We construct two different mock data sets for the 21cm and galaxy clustering cross-correlation power spectrum. One mimics SKAO × Euclid analysis and the other the SKAO×DESI one, for the redshift bins and survey specifications described in Section 5.2.1 and Table 5.1.

As discussed in Section 4.1.3, the scales that are accessible with the observations are fixed by the volume probed with the surveys in a given redshift bin. In Fourier space, the largest scale available at each effective redshift is $k_{\min}(z) = 2\pi / \sqrt[3]{V_{\mathrm{bin}}(z)}$, where $V_{\mathrm{bin}}(z)$ is the volume of each redshift bin, which we compute as

$$
\begin{aligned}
V_{\mathrm{bin}}(z) &= \Omega_{\mathrm{sur}} \int_{z-\Delta z/2}^{z+\Delta z/2} \mathrm{d}z' \, \frac{\mathrm{d}V}{\mathrm{d}z'\mathrm{d}\Omega} \\
&= \Omega_{\mathrm{sur}} \int_{z-\Delta z/2}^{z+\Delta z/2} \mathrm{d}z' \, \frac{cr(z')^2}{H(z')}.
\end{aligned}
\tag{5.11}
$$

with $r(z)$ being the comoving distance and Ω_{sur} the survey are in steradians (see Table 5.1). The smallest scale is, instead, imposed by the size of the SKAO telescope beam, due to the damping effect introduced in Equation 4.4. It can be estimated as $k_{\max}(z) = 2\pi / R_{\mathrm{beam}}(z)$. At scales smaller than $k_{\max}$, the signal is dominated by the beam providing no relevant information on cosmology. Finally, we choose a fixed k-bin width as a function of redshift $\Delta k(z)$ in order to be large enough for modes to be independent, i.e. $\Delta k(z) \sim 2k_{\min}(z)$.
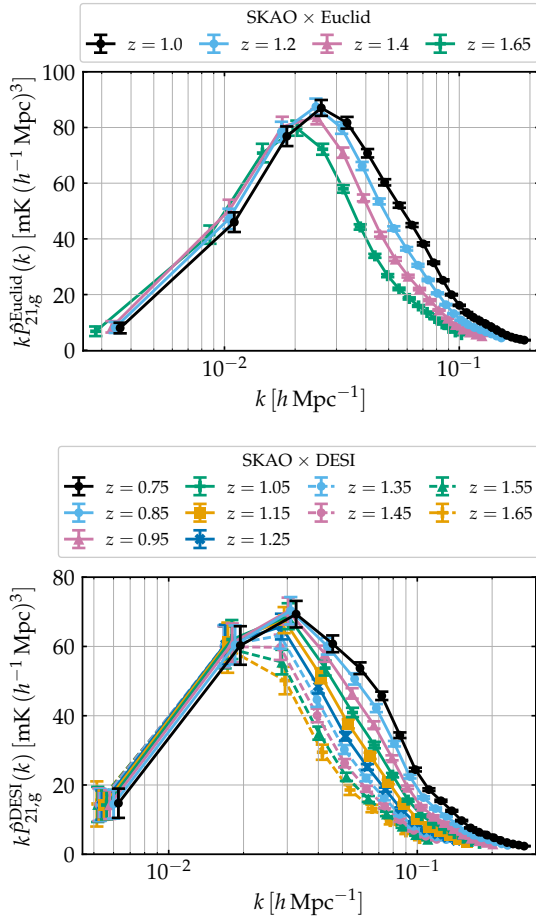
Figure 5.2: Mock data set for SKAO×Euclid (upper panel) and SKAO×DESI (lower panel) observations. The considered redshift bins are different for the two galaxy surveys. We refer to Section 5.2 for the extended discussion on how the signal and the errors are computed.

Assuming a set of N measurements at redshift z of the cross-correlation power spectrum $\hat{P}_{21,g}(k)$ at scales $\{k_1, \ldots, k_N\}$, we estimate the error on at each point as (see e.g. [61, 329])

$$\hat{\sigma}_{21,g}(k) = \frac{1}{\sqrt{2N_{\mathrm{modes}}(k)}} \sqrt{\hat{P}_{21,g}^2(k) + \hat{P}_{21}(k)\hat{P}_{g}(k)}, \qquad (5.12)$$

where $\hat{P}_{21,g}$ is the cross-correlation power spectrum defined in Equation 5.9, $\hat{P}_{21}$ and $\hat{P}_g$ are the 21cm and the galaxy power spectrum introduced in Equation 6.1 and Equation 5.7 respectively. Here, N_{modes} is the number of modes per k and μ bin, computed as

$$N_{\mathrm{modes}}(z,k) = \frac{k^2 \Delta k(z)}{4\pi^2} V_{\mathrm{bin}}(z). \qquad (5.13)$$

At each central redshift z and data point k we compute the cross-correlation power spectrum for SKAO×Euclid observations, labeled as $\hat{P}_{21,g}^{\text{Euclid}}(z,k)$, the one for SKAO×DESI, $\hat{P}_{21,g}^{\text{DESI}}(z,k)$, and the corresponding errors, as discussed above. In table Table 5.1, we gather some of the used redshift-dependent quantities. The resulting mock data sets are shown in Figure 5.2.

5.2.3 *Numerical analysis*

In order to exploit the constraining power of the mock data set presented in Section 5.2.2, we define a likelihood function and then set up the framework to constrain the cosmological parameters by adopting a Bayesian approach. Given a set of observations and a theory that depends on a set of parameters, the Bayes theorem links the posterior distribution to the likelihood function. The high-dimensional posterior can then be sampled using MCMC methods (see Section 2.1).

5.2.3.1 *Likelihood function for the 21cm multipoles*

Given a set of measurements at scales $\{k_1, \dots, k_N\}$ and redshift z, to compute the likelihood function we define the vector $\Theta(z) = \left(\hat{P}_{21,g}(z,k_1), \dots, \hat{P}_{21,g}(z,k_N) \right)$. The logarithmic likelihood is computed as

$$-\ln\left[\mathcal{L}\right] = \sum_z \frac{1}{2}\, \Delta\Theta(z)^{\mathsf{T}}\, \mathsf{C}^{-1}(z)\, \Delta\Theta(z), \tag{5.14}$$

where $\Delta\Theta(z) = \Theta^{\text{th}}(z) - \Theta^{\text{obs}}(z)$, the difference between the values of $\Theta(z)$ predicted from theory and observed. Here, $\mathsf{C}(z)$ is the covariance matrix computed as $\mathsf{C}(z) = \text{diag}(\hat{\sigma}_{21,g}^2(z,k_1), \dots, \hat{\sigma}_{21,g}^2(z,k_N))$. We consider independent redshift bins, i.e. we simply sum over the contribution from each central redshift.

Figure 5.3 shows the signal-to-noise ratios as a function of k in each redshift bin for both the constructed mock data sets. We observe that the signal-to-noise decreases at higher redshifts. The behavior and orders of magnitude found here are compatible with the results for the 21cm power spectrum multipoles in [68, 115].

We conduct an MCMC analysis varying the six parameters describing the ΛCDM model, i.e. we vary $\{\Omega_b h^2, \Omega_c h^2, n_s, \ln(10^{10}A_s), \tau, 100\theta_{\text{MC}}, \Sigma m_\nu, P_{\text{SN},i}\}$ assuming wide flat priors on each of the parameters. Results on other parameters, such as H_0 and σ_8, are derived from results on this set. The assumed fiducial cosmology is Planck 2018 [4] (see Section 1.3). To perform the study, we develop a likelihood code integrated with the MCMC sampler CosmoMC[4] [136, 212]. We further expand on the code we implemented and used in Chapter 4 including the computation of the theoretical expectations for the 21cm and galaxy clustering cross-correlation power spectrum and the relative likelihood function at different redshift. We recall that each redshift bin is considered independent, thus we consider a diagonal covariance matrix constructed with the

---

[4]See https://cosmologist.info/cosmomc.
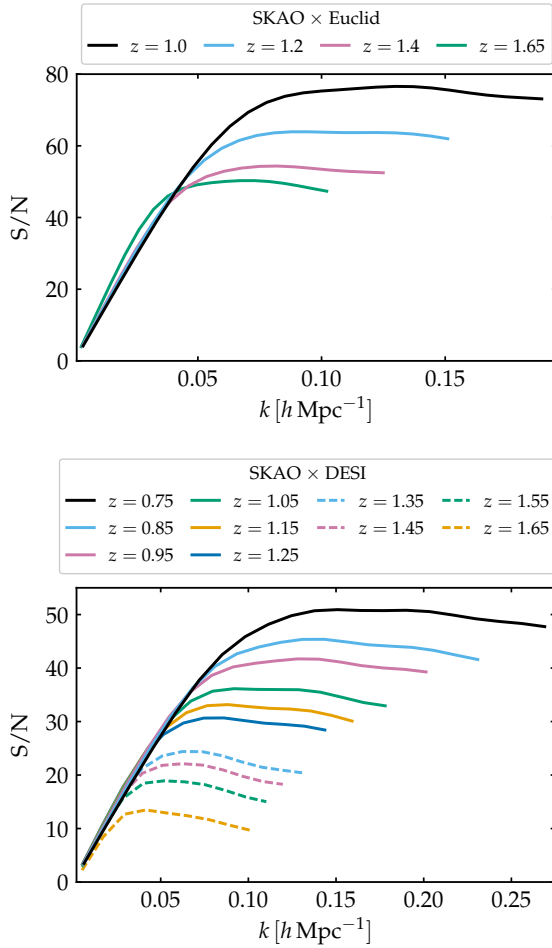
Figure 5.3: Predicted signal-to-noise ratio as a function of k for SKAO×Euclid (upper panel) and SKAO×DESI (lower panel) mock observations.

forecasted errors. The analysis of the MCMC samples to compute the marginalized constraints is performed with the Python package GetDist[5] [315].

5.2.3.2 *Nuisance parameters*

As discussed in Chapter 4, along with the cosmological parameters we implement different nuisances. Indeed, the access to the matter clustering is not direct as it appears in Equation 5.9 in combination with the brightness temperature and the HI bias and the galaxy bias. These quantities, although the scientific community hopes to obtain external measurements (e.g. the total neutral hydrogen density as a function of redshift, key unknown for the brightness temperature, is one of the scientific goals of the MeerKAT survey Laduma), may need to be treated as unconstrained quantities in a pessimistic scenario.

---

[5]See https://getdist.readthedocs.io.

To take into account this lack of knowledge, we allow for combinations of these parameters to vary in the MCMC run, thus leaving free the overall amplitude of the power spectrum. The contribution from the nuisances is then marginalized out in the final analysis.

To be completely agnostic, for the cross-correlation power spectrum we include in the nuisances also the correlation coefficient r and the galaxy bias. Thus, we consider the following three combinations of parameters $\sqrt{r}\bar{T}_b b_{\mathrm{HI}}\sigma_8$, $\sqrt{r}\bar{T}_b b_{\mathrm{g}}\sigma_8$, and $\sqrt{r}\bar{T}_b f\sigma_8$, where we re-normalized the matter power spectrum as $P_{\mathrm{m}}/\sigma_8^2$.

Given that all the parameters are redshift-dependent quantities, the actual number of nuisances is three times the number of redshift bins. This translates into 4×3 nuisance parameters for SKAO×Euclid and 10×3 for SKAO×DESI. Especially in the latter case, the high number of parameters to vary can impact the numerical efficiency of the MCMC computations. Following what is already done in Chapter 4, for SKAO×DESI only we reduce the number of nuisances by constraining their redshift evolution through a polynomial parametrization. Rewriting $N(z) = az^3 + bz^2 + cz + d$ for $N(z) = \sqrt{r}\bar{T}_b b_{\mathrm{HI}}\sigma_8$, $\sqrt{r}\bar{T}_b b_{\mathrm{g}}\sigma_8$, $\sqrt{r}\bar{T}_b f\sigma_8$, we implement as nuisances the coefficient of the polynomial a, b, c, and d, reducing the number of nuisance parameters from 30 to 12.

In the following, with the label "nuisances" or "nuis." we refer to the parameters described above. For each nuisance, we assume a wide flat prior.

5.3   RESULTS

We present in this section the results of our analysis. We first explore the constraining power of the mock cross-correlation data, with and without nuisances (Section 5.3.1). We then combine the mock data sets with Planck CMB data (Section 5.3.2). Finally, in section Section 5.3.3 we present the constraints we obtain on the cosmological parameters for the published measurement of the MeerKAT×WiggleZ cross-correlation power spectrum presented in [61].

Throughout this analysis, we compare results from the cross-correlation forecast with the best result obtained with the 21cm multipoles, i.e. the fully non-linear monopole and quadrupole data set that we label as "$\hat{P}_0 + \hat{P}_2$". Note that we expand on the results of Chapter 4 by introducing the AP, in order to be consistent with the modeling of the cross-correlation used in this chapter. Thus, "$\hat{P}_0 + \hat{P}_2$" here include AP effects. For a discussion on the impact of AP distortions, we refer to Appendix c.

We show the marginalized 1D and 2D posteriors for the studied set of parameters. Note that 68% confidence level constraints are presented as percentages with respect to the marginalized mean value. We recall that with the label "Planck 2018" we refer to the combination TT, TE, EE + low-ℓ + lowE + lensing (see Section 2.2.1).

5.3.1   *Probing the constraining power of future 21cm × galaxy clustering data*

In Figure 5.4 and Figure 5.5 we present the forecasted posterior distributions we obtain for the SKAO×DESI and SKAO×Euclid mock data sets we construct in this work. We show only some of the model parameters for brevity.

Table 5.2: Marginalized percentage constraints on cosmological parameters at the 68% confidence level. We show the results obtained using different combinations of forecasted data sets. The label "$\hat{P}_0 + \hat{P}_2$" stands for the forecasted 21cm power spectrum monopole and quadrupole observations (see Chapter 4). "$\hat{P}_{21,g}^{Euclid}$," and "$\hat{P}_{21,g}^{DESI}$" refer to the mock cross-correlation power spectrum data sets constructed above. The label "nuis." indicates that we vary the nuisance parameters along with the cosmological ones.

PAR.	$\hat{P}_0 + \hat{P}_2$	$\hat{P}_{21,g}^{DESI}$	$\hat{P}_{21,g}^{DESI}$ + nuis.	$\hat{P}_{21,g}^{Euclid}$	$\hat{P}_{21,g}^{Euclid}$ + nuis.	$\hat{P}_{21,g}^{DESI} + \hat{P}_{21,g}^{Euclid}$ + nuis.	$\hat{P}_0 + \hat{P}_2 + \hat{P}_{21,g}^{DESI} + \hat{P}_{21,g}^{Euclid}$ + nuis.
$\Omega_b h^2$	2.59%	6.43%	23.11%	5.78%	16.99%	12.52%	3.89%
$\Omega_c h^2$	0.99%	3.81%	16.63%	3.75%	11.87%	8.59%	2.67%
n_s	1.19%	2.43%	6.79%	1.82%	4.59%	3.56%	1.08%
$\ln(10^{10}A_s)$	0.37%	0.78%	8.08%	0.54%	7.62%	4.73%	0.81%
$100\theta_{MC}$	0.17%	0.39%	0.75%	0.30%	0.62%	0.54%	0.21%
H_0	0.25%	0.69%	1.96%	0.49%	1.07%	0.87%	0.33%
σ_8	0.29%	0.40%	9.41%	0.58%	10.03%	6.37%	1.11%

We obtain comparable results for both the SKAO×Euclid and the SKAO×DESI analysis. Looking at the 2D contours, we observe that the correlations between the cosmological parameters are similar and in line with the results obtained with the 21cm multipoles. The marked degeneracy in the $H_0 - \Omega_c h^2$ plane, found in previous work [115, 117], is present also for the cross-correlation power spectrum case. As discussed in [317], measuring cosmological observables that strongly depend on the matter power spectrum, as $\hat{P}_{21,g}$ does, fixes the shape of P_m. This translates into fixing the quantity $\Omega_m h$, which, in turn, induces the strong correlation $\Omega_c h^2 \propto H_0$. This feature is particularly relevant when combining 21cm observations with CMB data, as discussed in the next section.

As expected from the signal-to-noise estimates of Figure 5.3, better constraints are obtained for the SKAO×Euclid data set (Table 5.2). Although DESI probes the same redshift range of Euclid and even with a higher number of redshift bins, Euclid will have a larger sky area of overlap with SKAO, suggesting that a larger sky coverage increases the constraining power more than the number of redshift bins. As expected, the best constraints are the ones obtained with the 21cm multiples, in particular for $\Omega_c h^2$ and H_0. Indeed, the $\hat{P}_0 + \hat{P}_2$ is constructed to sample a wider redshift ($z = 0 - 3$) and scales range (up to $k \sim 1\,h/\mathrm{Mpc}$ at low redshifts). It is interesting, however, to see that, despite these differences, cross-correlation results are still able to deliver competitive constraints. This makes a strong case for cross-correlation studies, especially in light of the reduced challenges in terms of residual systematics from the 21cm intensity mapping observations. Adding the nuisance parameters, i.e. assuming no prior knowledge of the astrophysics at play, has the effect of varying the overall amplitude of the cross-correlation power spectrum. This translates into a broadening of the constraints, in particular on A_s. Moreover, the 2D contours are generally broader and show less clear correlations, except for the $H_0 - \Omega_c h^2$ and $H_0 - \Omega_b h^2$ planes. Although the shape is stretched, the $H_0 - \Omega_c h^2$ degeneracy is still marked.

Table 5.3: Marginalized percentage constraints on cosmological parameters at the 68% confidence level. We show the results obtained using different combinations of forecasted data sets. The label "Planck 2018" stands for TT, TE, EE + lowE + lensing, while the label "$\hat{P}_0 + \hat{P}_2$" refers to the forecasted 21cm power spectrum monopole and quadrupole observations (see Chapter 4). "$\hat{P}_{21,g}^{\mathrm{Euclid}}$" and "$\hat{P}_{21,g}^{\mathrm{DESI}}$" refer to the mock cross-correlation power spectrum data set constructed above. The label "nuis." indicates that we vary the nuisance parameters along with the cosmological ones.

PAR.	Planck 2018	$+\,\hat{P}_0 + \hat{P}_2$	$+\,\hat{P}_{21,g}^{\mathrm{DESI}}$	$+\,\hat{P}_{21,g}^{\mathrm{DESI}}$ + nuis.	$+\,\hat{P}_{21,g}^{\mathrm{Euclid}}$	$+\,\hat{P}_{21,g}^{\mathrm{Euclid}}$ + nuis.	$+\,\hat{P}_{21,g}^{\mathrm{DESI}} +\hat{P}_{21,g}^{\mathrm{Euclid}}$ + nuis.	$+\,\hat{P}_0 + \hat{P}_2$ $+\,\hat{P}_{21,g}^{\mathrm{DESI}} +\hat{P}_{21,g}^{\mathrm{Euclid}}$ +nuis
$\Omega_b h^2$	0.64%	0.45%	0.48%	0.52%	0.48%	0.50%	0.49%	0.46%
$\Omega_c h^2$	0.99%	0.28%	0.39%	0.55%	0.36%	0.48%	0.42%	0.31%
n_s	0.42%	0.27%	0.33%	0.34%	0.32%	0.32%	0.30%	
$\ln(10^{10} A_s)$	0.46%	0.18%	0.12%	0.44%	0.12%	0.45%	0.44%	0.43%
τ	13.44%	5.54%	5.39%	12.09%	5.50%	11.82%	11.89%	11.38%
$100\theta_{\mathrm{MC}}$	0.03%	0.02%	0.03%	0.03%	0.03%	0.02%	0.03%	0.03%
H_0	0.79%	0.11%	0.25%	0.41%	0.21%	0.33%	0.28%	0.14%
σ_8	0.73%	0.34%	0.24%	0.69%	0.24%	0.70%	0.69%	0.67%
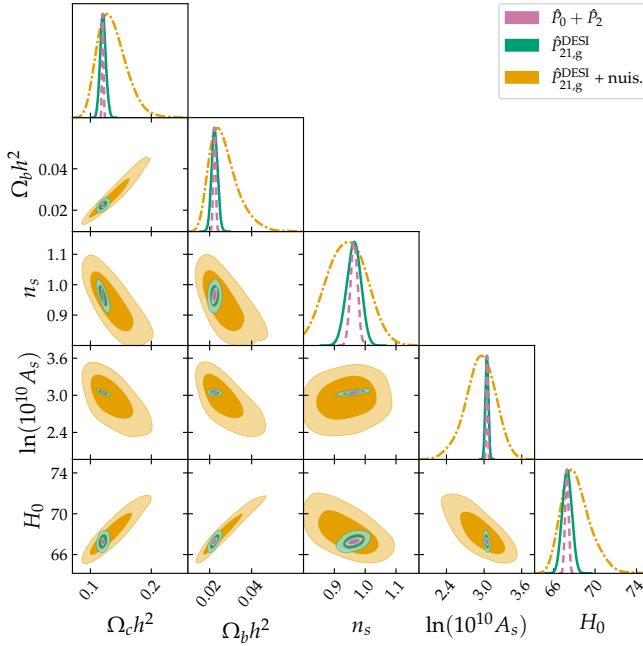
Figure 5.4: Result for SKAO×DESI cross-correlation. Joint constraints (68% and 95% confidence regions) and marginalized posterior distributions on a subset of the cosmological parameters. The label "$\hat{P}_0 + \hat{P}_2$" (dashed lines) stands for the forecasted 21cm power spectrum monopole and quadrupole observations (see Chapter 4). "$\hat{P}_{21,g}^{\text{DESI}}$" refers to the mock cross-correlation power spectrum data set constructed above. The label "nuis." (dashed-dotted lines) indicates that we vary the nuisance parameters along with the cosmological ones. The corresponding constraints are listed in Table 5.2.

In Figure 5.6 we show the results on the full set of cosmological parameters for the combination of the two cross-correlation data sets and the 21cm multipoles one. Note that we do not report the constraints on τ, due to the fact that the considered probes are not sensitive to this parameter. We compare the results with the ones for the 21cm multipoles and the $\hat{P}_{21,g}^{\text{DESI}}$ data set as a reference. In order to explore a more realistic scenario, we include the nuisance parameters. We observe that combining SKAO×DESI and SKAO×Euclid improves the constraints obtained with the two data sets separately. Including also the 21cm multipoles lead to the best result. With observations from 21cm probes only in the pessimistic case of including the nuisances, we are able to achieve constraints on the cosmological parameters comparable with Planck CMB observations.

We conclude that 21cm IM observations in cross-correlation with galaxy clustering seem to have a reduced constraining power with respect to 21cm auto-power spectrum measurements. However, when combined with the latter, they improve the constraints, showing that the cross-correlation signal carries complementary cosmological information.
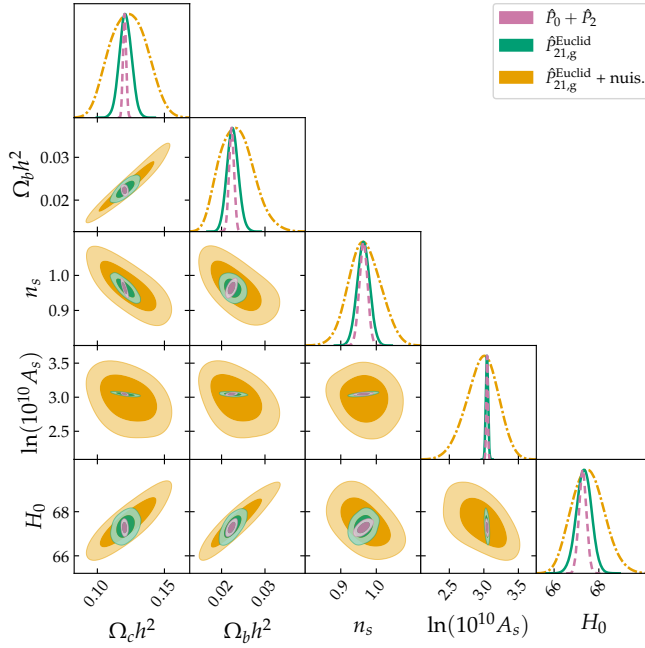
Figure 5.5: Results for SKAO×Euclid cross-correlation. Joint constraints (68% and 95% confidence regions) and marginalized posterior distributions on a subset of the cosmological parameters. The label "$\hat{P}_0 + \hat{P}_2$" (dashed lines) stands for the forecasted 21cm power spectrum monopole and quadrupole observations (see Chapter 4). "$\hat{P}_{21,g}^{\text{Euclid}}$" refers to the mock cross-correlation power spectrum data set constructed above. The label "nuis." (dashed-dotted lines) indicates that we vary the nuisance parameters along with the cosmological ones. The corresponding constraints are listed in Table 5.2.

5.3.2 *Combining 21cm × galaxy clustering with CMB observations*

Most recent forecast analyses find 21cm IM future observations to be a pivotal cosmological probe, highly complementary to CMB observations [57]. Indeed, in Chapter 4 we found that observations of the 21cm power spectrum multipoles contribute significantly to improving the constraints and reducing the degeneracies on the cosmological parameters. In this section, we investigate the effects of combining 21cm and galaxy clustering cross-correlations with CMB measurements.

For consistency, we first run the Planck likelihood in our framework and reproduce constraints in agreement with the Planck 2018 results. We then study the effect of adding the $\hat{P}_{21,g}^{\text{Euclid}}$ and $\hat{P}_{21,g}^{\text{DESI}}$ data sets and the two combined. As in Section 5.3.1, we compare the results we obtain with the constraints from the 21cm power spectrum multiples (see Chapter 4).

Table 5.3 shows the percentage constraints for this analysis. We observe that adding $\hat{P}_{21,g}^{\text{Euclid}}$ or $\hat{P}_{21,g}^{\text{DESI}}$ to Planck 2018 data reduces the estimated constraints with respect to the Planck alone results. The effect is prominent for $\Omega_c h^2$ and H_0, for which the error is reduced by a factor of ~ 3, and A_s, with a factor of
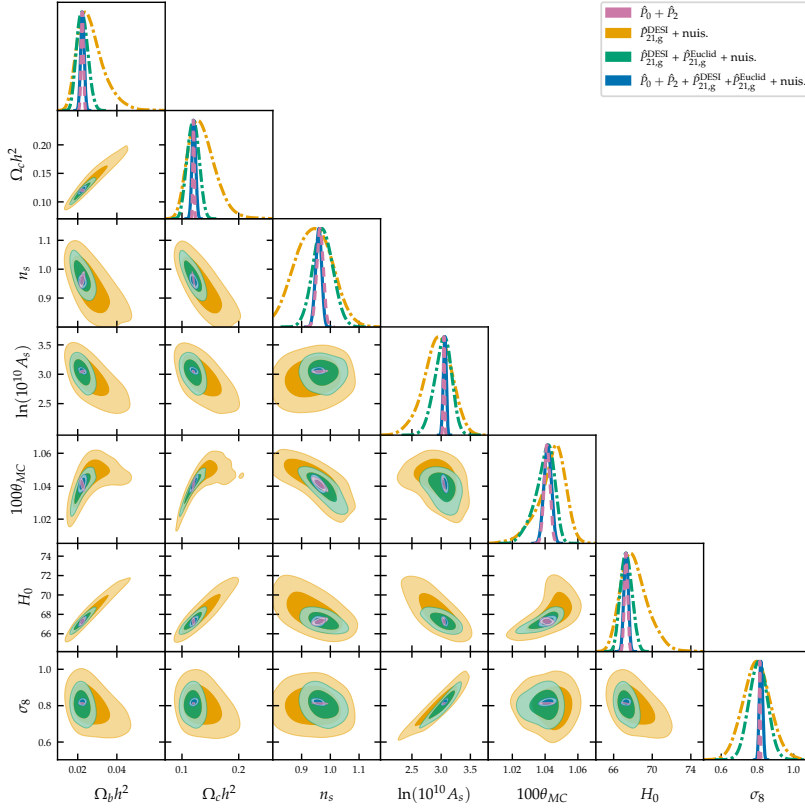
Figure 5.6: Joint constraints (68% and 95% confidence regions) and marginalized posterior distributions on a subset of the cosmological parameters. The label "$\hat{P}_0 + \hat{P}_2$" (dashed lines) stands for the forecasted 21cm power spectrum monopole and quadrupole observations (see Chapter 4). "$\hat{P}_{21,g}^{\text{Euclid}}$" and "$\hat{P}_{21,g}^{\text{DESI}}$" refer to the mock cross-correlation power spectrum data sets constructed above. The label "nuis." (dashed-dotted lines) indicates that we vary the nuisance parameters along with the cosmological ones. The relative constraints are listed in Table 5.2.
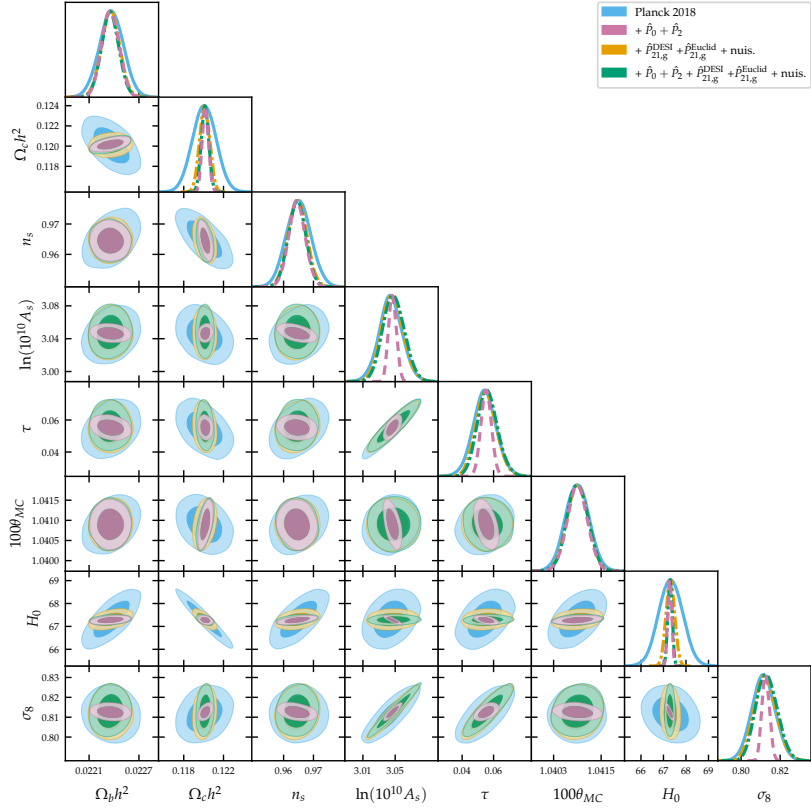
Figure 5.7: Joint constraints (68% and 95% confidence regions) and marginalized posterior distributions on a subset of the cosmological parameters. The label "Planck 2018" stands for TT, TE, EE + lowE + lensing, while the label "$\hat{P}_0 + \hat{P}_2$" (dashed lines) stands for the forecasted 21cm power spectrum monopole and quadrupole observations (see Chapter 4). "$\hat{P}_{21,g}^{\text{Euclid}}$" and "$\hat{P}_{21,g}^{\text{DESI}}$" refer to the mock cross-correlation power spectrum data sets constructed above. The label "nuis." (dashed-dotted lines) indicates that we vary the nuisance parameters along with the cosmological ones. The corresponding constraints are listed in Table 5.3.

~ 4 decrease. As one can see from Figure 5.7, in the $H_0 - \Omega_c h^2$ plane the effect is ascribable to the correlation directions. Indeed, with Planck observations H_0 and $\Omega_c h^2$ are anti-correlated, while they are positively correlated with $\hat{P}_{21,g}$. Combining the two removes the degeneracy and reduces errors. The effect is also particularly evident for A_s since the CMB probes the quantity $A_s \exp(-2\tau)$ and the matter power spectrum, which is constrained by 21cm data is sensitive to S_8, which is in turn degenerate with the optical depth to reionization as measured from the CMB. Thereby adding 21cm data effectively removes the degeneracies.

When nuisance parameters are taken into account, as expected the improvement on the constraints is softened. In particular for A_s, and consequently σ_8, the constraining power is lost when the parameter space is open to the nuisances. Varying the nuisances corresponds to effectively changing the amplitude of the power spectrum and, thus, it results in worsened constraints on A_s.

The effects observed for the cross-correlation data sets combined with CMB are qualitatively comparable to the results obtained for the 21cm power spectrum multipoles. This confirms that when combining different kinds of 21cm observations with CMB data the improvement in the constraints is always driven mainly by the breaking of the degeneracy in the $\Omega_c h^2 - H_0$ plane. Indeed, our analysis reveals that even a less constraining measurement, such as the 21cm and galaxy cross-correlation, is effective in improving the errors on $\Omega_c h^2$ and H_0 if it presents a sufficiently marked correlation among these parameters.

To better prove this point, in Figure 5.7 we compare the effect of combining Planck data with the 21cm multipoles, $\hat{P}_{21,g}^{\text{DESI}}$ and $\hat{P}_{21,g}^{\text{Euclid}}$, and the three combined. We find that even with the nuisances, results from $\hat{P}_{21,g}^{\text{DESI}} + \hat{P}_{21,g}^{\text{Euclid}}$ (orange contours) are similar to the constraints from the multiples, for which, instead, the nuisances are kept fixed as a best-result reference (pink contours). The main difference resides in the loss of constraining power on A_s and the related parameters, which is however ascribable to the inclusion of the nuisances. Further adding the 21cm multiples to $\hat{P}_{21,g}^{\text{DESI}} + \hat{P}_{21,g}^{\text{Euclid}}$ (green contours),[6] does not impact the constraining power or the shape of the correlations. This confirms that the 21cm probe is pivotal in breaking the CMB degeneracy in the $\Omega_c h^2 - H_0$ plane and the effect is relevant already at the level of cross-correlation or with SKAO precursor power spectrum measurements, as we will show in Chapter 6.

We conclude that cross-correlations measurements of 21cm IM and galaxy clustering are a key cosmological probe complementary to CMB observations and, in combination with Planck, their forecasted constraining power is compatible with the one from 21cm power spectrum multipole measurements with the SKAO.

5.3.3 *State-of-the-art cosmological parameters constraints from the MeerKAT $\times$ WiggleZ detection*

Cosmological 21cm observations with the SKAO will be possible in about 5 years when the Observatory will be fully operational. However, the SKA-Mid pathfinder, MeerKAT is already taking data and its first cosmological surveys are promising. Recently, a power spectrum detection with the MeerKLSS survey,

---

[6] Note that in this case also the 21cm power spectrum nuisances are varied as in Chapter 4.
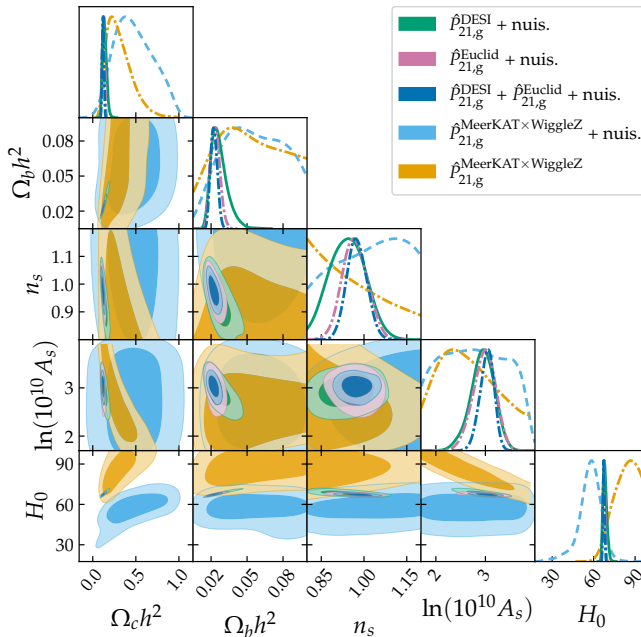
Figure 5.8: Joint constraints (68% and 95% confidence regions) and marginalized posterior distributions on a subset of the cosmological parameters. The labels "$\hat{P}_{21,g}^{\mathrm{Euclid}}$" and "$\hat{P}_{21,g}^{\mathrm{DESI}}$" refer to the mock cross-correlation power spectrum data sets constructed above. "$\hat{P}_{21,g}^{\mathrm{MeerKAT \times WiggleZ}}$" refers to the cross-correlation power spectrum detection. The label "nuis." (dashed-dotted lines) indicates that we vary the nuisance parameters along with the cosmological ones. The relative constraints are listed in Table 5.4.

the intensity mapping survey with MeerKAT, in cross-correlation with galaxy clustering data has been made at the 7.7σ level [61]. The analysis pipeline we develop in this work is constructed to be ready to use with real cross-correlation power spectrum measurements. Therefore, we decide to test our methodology on the published results available for MeerKLASS. In the following, we present the result we obtain on the cosmological parameters constraints. We refer the interested reader to Appendix d for the technical consistency checks we run on the adopted power spectrum model and the predicted signal-to-noise ratio.

We tune the parameters of the likelihood function to match the settings of the observed data. Instead of the SKAO specifications, we use the MeerKLASS survey parameters, i.e. we consider a 200 dg² survey area and dishes of a diameter of $D_{\mathrm{dish}} = 13.5$ m. The observed effective redshift is $z = 0.43$ with a bin width of $\Delta z = 0.059$. The signal is observed in cross-correlation with the WiggleZ 11h galaxy survey [193, 330]. When we do not include the nuisance parameters, we use the measured galaxy bias value $b_{\mathrm{g}} = 0.911$ [331] and cross-correlation factor $r = 0.9$ [332]. Other parameters and theoretical predictions are left unchanged.

We present the cosmological parameters constraints resulting from our MCMC analysis in Figure 5.8 and Table 5.4. We observe that the state-of-the-

Table 5.4: Marginalized percentage constraints on cosmological parameters at the 68% confidence level. We show the constraints on the cosmological parameters obtained with the MeerKAT×WiggleZ cross-correlation power spectrum detection. The label "nuis." indicates that we vary the nuisance parameters along with the cosmological ones. The symbol "—" stands for unconstrained, while "/" indicate that the parameter is not present.

Parameter	$\hat{P}_{21,g}^{\text{MeerKAT}\times\text{WiggleZ}}$	$\hat{P}_{21,g}^{\text{MeerKAT}\times\text{WiggleZ}}$ + nuis.
$\Omega_b h^2$	—	—
$\Omega_c h^2$	$0.314^{+0.079}_{-0.18}$	$0.48^{+0.19}_{-0.27}$
$100\theta_{MC}$	$1.090^{+0.061}_{-0.083}$	$1.051^{+0.085}_{-0.070}$
n_s	—	—
$\ln(10^{10} A_s)$	—	—
τ	—	—
H_0	84^{+10}_{-7}	57^{+8}_{-6}
σ_8	$0.974^{+0.068}_{-0.092}$	$1.04^{+0.30}_{-0.49}$

art constraining power is limited with respect to the results forecasted for SKAO×Euclid and SKAO×DESI, as expected due to the wider redshift ranges, probed scales, and survey area. Single bin MeerKAT observations are not yet able to constrain the complete set of cosmological parameters. However, the degeneracies between the parameters match the ones expected from our forecasts. In particular, the $H_0 - \Omega_c h^2$ correlation is clearly visible, although much less prominent. From these real measurements, we can infer new information on the marginalized mean value of the cosmological parameters. We find that all the constraints are compatible with the Planck results.

The most constrained parameters are $\Omega_c h^2$ and H_0, proving that 21cm observations will be most useful to constrain them and their derived parameters. When fixing the nuisances, we find a high central value for H_0, although with a large error. We believe that this is not a physical effect, but is rather coming from a mismatch between the assumed brightness temperature value in our analysis and the one that seems to describe the observed data (see Appendix d for a more in-depth discussion). The conservative result is then the one in which nuisances are taken into account. In this case, we find that MeerKAT × WiggleZ data prefer a lower value of H_0, although the significance is not high enough to draw firm conclusions.

From the constraints on the nuisances, one could estimate the value of Ω_{HI}. With our analysis we find the constraints on the nuisance parameters from real data to be too wide to infer a meaningful result.

Lastly, although we do not show here the results, we test the effect of combining MeerKAT × WiggleZ data with Planck 2018 observations. We find that the measured cross-correlation power spectrum does not increase significantly the constraining power of CMB observations, leaving the constraints and the 2D contours mostly unchanged.

Although the constraining power of real detection is not yet competitive with other probes, the quality of the current 21cm IM observations in cross-correlation with galaxy clustering will improve sharply in the upcoming years

and will soon become a useful independent cosmological probe. Moreover, the forecasted results for future surveys are very promising.

5.4 CONCLUSIONS

In this work, we forecast the constraints on the ΛCDM cosmological parameters for power spectrum measurements of 21cm intensity mapping in cross-correlation with galaxy clustering. Modeling the cross-power spectrum as in [61], we forecast mock observations of the SKAO cross-correlated with DESI and Euclid-like surveys. We test the constraining power of such probes alone and combined with the latest Planck CMB observations. Note that our modeling does not include possible residual foreground and systematics contamination.

We follow the SKAO Red Book [57] proposal and simulate single-dish observations with the SKA-Mid telescope in Band 1 (frequency range $0.35 - 1.05$ GHz). We cross-correlate this signal with a Euclid-like spectroscopic survey [34] and the DESI Emission Line Galaxies one [286, 333] in the redshift range 0.7 - 1.7. Assuming a Planck 2018 fiducial cosmology, we construct two data sets of observations within multipole redshift bins. To test the constraining power on the cosmological parameters of our mock observations, we implement a likelihood function for the cross-correlation power spectrum, fully integrated with the MCMC sampler CosmoMC. We include a discussion on the impact of our lack of knowledge on the baryonic physics involved in the computation of the 21cm power spectrum, as nuisance parameters in the analysis.

We first focus on assessing the constraining power of cross-correlation observations alone, compared to the results we obtain for the 21cm multipoles in Chapter 4. We, then, combine the two to investigate if they carry complementary information. The results of our analysis can be summarized as follows.

We find that SKAO power spectrum measurements in cross-correlation with galaxy clustering have a constraining power comparable to the 21cm auto-power spectrum, discussed in Chapter 4. The SKAO×DESI and SKAO×Euclid data sets we construct are able to constrain the cosmological parameters up to the sub-percent level. They seem to be particularly effective on H_0, on which we obtain constraints between the 0.49% and the 1.96% from 21cm and galaxy clustering cross-correlation alone. The tightest constraints are achieved when we combine 21cm power spectrum multipoles with the cross-correlation mock observations, for which we obtain a 0.33% constraint on H_0, a value that is competitive with Planck.

When combining the cross-correlation mock measurements with CMB data, we find that they are pivotal to reduce the errors on the cosmological parameters. The effect is particularly prominent for $\Omega_c h^2$ and H_0, for which the errors are reduced by a factor between 2.5 - 1.8 and 3.8 - 2 respectively. Again, the best result is obtained by combining all the 21cm probes together. In this case, the error with respect to Planck alone results is reduced by a factor of 3.2 for $\Omega_c h^2$ and 5.6 for H_0, with the nuisance parameters taken into account.

Lastly, we test our analysis pipeline on the recent data for the cross-power spectrum between MeerKAT, the SKA-Mid pathfinder, and WiggleZ galaxy clustering [61]. We find that state-of-the-art observations have limited constraining power on the complete set of cosmological parameters. However, the main

features of the marginalized constraints are compatible with the forecasted results of this work.

We conclude that 21cm SKAO observations in cross-correlation with galaxy clustering will provide a competitive cosmological probe, complementary to CMB and, thus, extremely important for gaining statistical significance on the cosmological parameters constraints. The working pipeline presented in this work is found to be compatible and easily employable with real observations. The analysis we carry out can be straightforwardly adapted to forecast constraints on the neutrino mass and beyond ΛCDM models. These extensions are currently under study.

Part III

HYDROGEN AS A TEST OF THE BEYOND ΛCDM
UNIVERSE

A MEERKAT FORECAST ON EFT OF DARK ENERGY MODELS

THE MEERKAT telescope, the SKAO precursor in South Africa, can be successfully exploited for 21cm intensity mapping. It is currently operational and has already attained encouraging results, as discussed in Chapter 2 and Chapter 5. In this work, we produce constraints on model parameters from forecasted 21cm power spectrum MeerKAT measurements. The analysis in this chapter differs from the one of Chapter 4 in the following aspects. While in Chapter 4 we rigorously construct a tomographic data set to test the ΛCDM model, in this work, we focus on single-bin observations and explore both a ΛCDM scenario and several DE-MG models within the effective field theory (EFT) framework (see Chapter 3). We build a realistic, single-bin mock data set for the 21cm power spectrum at the effective redshift currently being observed by MeerKAT, i.e. $z = 0.39$. To prove the importance of tomographic measurements on beyond-ΛCDM theories, we further extend the data set to mimic more ideal measurements within multiple redshift bins.

In agreement with results in Chapter 4, in this work we find that adding the 21cm likelihood to CMB data provides significantly tighter constraints on $\Omega_c h^2$ and H_0, with a reduction of the error with respect to Planck results at the level of more than 60%. For the parameters describing beyond-ΛCDM theories, we observe a milder reduction in the errors with respect to the Planck constraints at the level of $\leq 10\%$. The improvement increases up to $\sim 35\%$ when we constrain the parameters using tomographic mock observations. We conclude that the power spectrum of the 21cm signal is sensitive to variations of the parameters describing the examined beyond-ΛCDM models. The improvement in the constraining power induced by tomographic observations first motivated the analysis of Chapter 4.

The structure of this paper is the following. In Section 6.1, we delineate our methodology, describe the modeling of the 21cm signal power spectrum, and outline the theoretical framework. In Section 6.2 we discuss the results we obtain. Constraints on ΛCDM are presented Section 6.2.1. In Section 6.2.2, we discuss results for the considered EFT models. We investigate the effect of implementing the HI bias and the brightness temperature as nuisance parameters in Section 6.2.3. Results for a wCDM background are shown in Section 6.2.4. We explore the impact of more ideal tomographic observations in Section 6.2.5. We conclude by outlining the main results of this work in section Section 6.3.

6.1 METHODS

In Section 6.1.1 we describe the model for the 21cm power spectrum, while in Section 6.1.2 we provide details on the likelihood implementation. In Section 6.1.3, instead, we summarize the main aspects of EFT for cosmic acceleration, outline the theoretical models that we test, and list the most recent constraints available in the literature.

We adopt the Planck 2018 best-fit results [4] (see Section 1.3).

6.1.1   *Model for the 21cm signal as observed by MeerKAT*

As in Chapter 4, we consider the following model for the 21cm signal linear power spectrum [57, 153, 158]

$$P_{21}(z, k, \mu) = \bar{T}_b^2(z) \left[(b_{\mathrm{HI}}(z) + f(z)\,\mu)^2 P_{\mathrm{m}}(z, k) + P_{\mathrm{SN}} \right], \tag{6.1}$$

where $\bar{T}_b(z)$ is the mean brightness temperature, $b_{\mathrm{HI}}(z)$ is the HI linear bias, $f(z)$ is the linear growth rate, $\mu = \hat{k} \cdot \hat{z}$, $P_{\mathrm{m}}(z, k)$ is the total matter power spectrum and P_{SN} is the HI shot noise. For the time being, we restrict ourselves to the case $\mu = 1$ and neglect the effect of the shot noise term [93, 158], leaving the study of different values of μ and the introduction of the shot noise for future work. I.e., we use

$$P_{21}(z, k) = \bar{T}_b^2(z)(b_{\mathrm{HI}}(z) + f(z))^2 P_{\mathrm{m}}(z, k). \tag{6.2}$$

For the mean brightness temperature, we rely on the following parametrization from [39]

$$T_b(z) = 23.88 \left(\frac{\Omega_b h^2}{0.02} \right) \sqrt{ \frac{0.15}{\Omega_m h^2} \frac{(1+z)}{10} } \; x_{\mathrm{HI}} \; \mathrm{mK}, \tag{6.3}$$

where Ω_b and Ω_m are the baryon and total matter density parameters today and $x_{\mathrm{HI}} = \frac{\Omega_{\mathrm{HI}}}{\Omega_{\mathrm{H}}}$ is the fraction of neutral atomic hydrogen. Following results in literature we assume the hydrogen fraction to be $\Omega_{\mathrm{H}} = 0.74 \Omega_b$ [307] and consider a constant value of $\Omega_{\mathrm{HI}} \sim 10^{-3}$. This choice of Ω_{HI} is justified by observations [308] and has been already adopted in other works [57, 158].

We model the linear bias $b_{\mathrm{HI}}(z)$ from numerical simulation results. In [158] b_{HI} is estimated for a discrete set of redshifts $z = 0, 1, 2, 3, 4, 5$ in a ΛCDM framework. We interpolate linearly these points to estimate $b_{\mathrm{HI}}(z)$ also at intermediate redshift values. Notice that, at the scales we operate, we can safely consider the bias to be scale-independent.

The linear growth rate is computed as $f(z) = f\sigma_8(z)/\sigma_8(z)$, where $f\sigma_8(z)$ is numerically computed from the density-velocity correlation, i.e. $f\sigma_8(z) = \sigma_8^{(vd)}(z)^2/\sigma_8^{(dd)}(z)$, as defined in [150]. This way of obtaining the growth rate is model dependent and allows us to estimate it also for models beyond ΛCDM, where the $f(z)$ behavior may not be trivial. This method, on the other hand, cannot account for any possible scale dependence of the growth rate, a known feature of several MG models. However, the growth rate for the subset of models we study results to be scale-independent in the range of scales we investigate and, thus, we are allowed to use this method.

Finally, as well as $f\sigma_8(z)$ and $\sigma_8(z)$, the matter power spectrum $P_{\mathrm{m}}(z, k)$ is computed with the Einstein-Boltzmann solvers CAMB [173] and EFTCAMB [254, 334], the CAMB extension to test MG-DE models in an Effective Field Theory approach.[1] We highlight that in our construction of $P_{21}(z, k)$ model dependent quantities are the matter power spectrum $P_{\mathrm{m}}(z, k)$ and the growth rate f, which we are able to compute for ΛCDM and beyond ΛCDM models. The other factors

---

[1] See https://camb.info/ and http://eftcamb.org/.
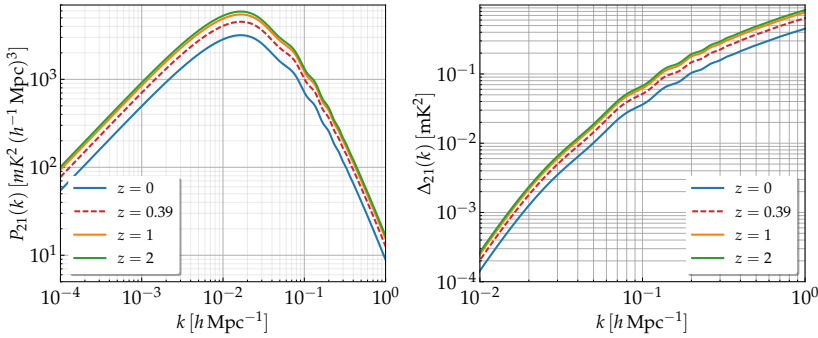
Figure 6.1: Linear power spectra for the 21cm signal at different redshifts. Results are computed with the model in Equation 6.2 for the ΛCDM fiducial cosmology, i.e. Planck 2018 best-fit results [4]. We show both the full power spectrum $P_{21}(k)$ (left) and the adimensional one $\Delta_{21}(k) \equiv k^3 P_{21}(k)/2\pi^2$ (right).

in Equation 6.2, i.e. the brightness temperature T_b and the bias b_{HI}, are fixed for different models. This is because it is not clear how to compute these quantities for models beyond ΛCDM. We further discuss this topic in Section 6.2.3. The theoretical predictions of $P_{21}(z, k)$ in the fiducial ΛCDM cosmology at different redshifts are shown in Figure 6.1.

6.1.2 *21cm signal likelihood implementation*

Given a set of observed $P_{21}(z, k)$ values, $\mathbf{P}_{21}^{obs}$, at a fixed redshift, we compute theoretical predictions of the 21cm signal, i.e. $\mathbf{P}_{21}^{th}$, at the same redshift and k. As described in Section 6.1.1, $P_{21}^{th}(z, k)$ is derived from the brightness temperature, the HI bias, the growth rate, and the matter power spectrum, as in Equation 6.2. At each MCMC step values of $P_m(k)$ and f are provided by CAMB/EFTCAMB, whereas T_b and b_{HI} are kept fixed to their values from the fiducial cosmology.

Thus, the $P_{21}(k)$ logarithmic likelihood function $\mathcal{L}$ is computed as

$$-\ln\left[\mathcal{L}\left(\mathbf{P}_{21}^{obs}|\mathbf{P}_{21}^{th}\right)\right] = \frac{1}{2}(\mathbf{P}_{21}^{th} - \mathbf{P}_{21}^{obs})^{\mathrm{T}}\,\mathbf{C}^{-1}\,(\mathbf{P}_{21}^{th} - \mathbf{P}_{21}^{obs}), \qquad (6.4)$$

where $\mathbf{C}$ is the covariance matrix, with dimensions $n \times n$, being n the number of data points. We assume $\mathbf{C}$ to be diagonal, given that we rely only on linear scales, and compute it from the observational errors $\vec{\sigma}_{P_{21}}$ as

$$\mathbf{C}_{ij} = \sigma_{P_{21},i}^2\,\delta_{ij}, \qquad (6.5)$$

with δ_{ij} being the usual Kronecker delta and $i, j = 1, \ldots, n$.

We consider also the possibility to compute the likelihood from different redshift bins. If that is the case, observations at each redshift are assumed independent. Each contribution to the logarithmic likelihood is calculated separately and then added together. Moreover, it is also possible to choose an alternative parametrization for the brightness temperature T_b. From the
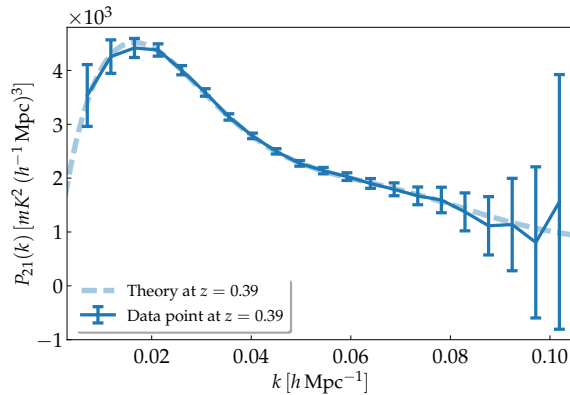
Figure 6.2: Mock data set observations and theory prediction at $z = 0.39$ for the 21cm signal power spectrum. Error bars are generated considering a realistic intensity mapping survey with the MeerKAT telescope. Central values are instead obtained from points predicted by the theory for ΛCDM and the fiducial cosmology we assume. Each point from the theory is then displaced randomly according to a Gaussian distribution with a fifth of the error on that point as standard deviation.

definition in Equation 6.3 we can extrapolate the redshift dependence and rewrite T_b in a more general way

$$T_b = a_{T_b} \sqrt{1 + z}, \tag{6.6}$$

where in this case all the contributions from cosmological parameters and Ω_{HI} absorbed in the value of the amplitude a_{T_b}.

It is then possible to treat a_{T_b}, along with the bias b_{HI}, as nuisance parameters of the $P_{21}(k)$ likelihood function, as we discuss in Section 6.2.3. We assume this to take into account the effect of possible variations in the brightness temperature and the bias, for which we lack a theoretical model, in particular for beyond ΛCDM theories.

We numerically compute the constraints by means of the latest publicly available version of the MCMC codes CosmoMC [136] and EFTCosmoMC [255], the CosmoMC extension for studying MG-DE models in an EFT framework.[2] CosmoMC/EFTCosmoMC allows the exploration of the parameter space by computing the likelihood from several different observational data. We expand this set by implementing the computation of the likelihood for $P_{21}(k)$ from upcoming intensity mapping observations as described above.[3]

6.1.2.1 A realistic mock data set

A central ingredient for the likelihood of Equation 6.4 is the measured 21cm power spectrum P_{21}^{obs} and its observational error $\sigma_{P_{21}}^2$ as a function of the k in each of the ith available bin. With the aim of obtaining realistic constraints for both the standard and non-standard models explored in this work, we adopt the following approach to generate mock data. We assume we are using

---

[2]See also https://cosmologist.info/cosmomc/.

[3]To this end we write a new module, twentyonepk.f90, to be added to the Fortran version of CosmoMC/EFTCosmoMC .

the MeerKAT telescope as a collection of 64 single 13.5 m dishes, as it is the preferred practice in intensity mapping analysis [37, 58, 59], scanning a total sky area of 2 000 deg^2. We consider L-band observations and thus a central redshift of $z = 0.39$. We assume for the signal the same modeling as for Section 6.1.1 and consider the effect of both the instrumental noise and the telescope beam. We consider a thermal noise level given by the radiometry equation with a system temperature taken directly from MeerKAT technical available documentation, a frequency resolution of 1 MHz, and 2 400 h of total observing time. The beam is assumed to be Gaussian and to scale proportionally to λ / D_{eff}, where λ is the observed frequency and D_{eff} is the effective dish size. We then compute the error as

$$\sigma_{P_{21},i}^2 = \frac{(2\pi)^3}{V_{\text{sur}}} \frac{1}{4\pi k_i^2 \Delta k} \left(P_{21}(k_i) + P_{\text{noise}} \right), \tag{6.7}$$

where V_{sur} is the survey total volume, $\Delta k = 2\pi / V_{\text{sur}}^{1/3}$ is the $k-$bin width, and P_{noise} encodes both the effect of the beam and the thermal noise. Note that we create our mock data only once, assuming a standard ΛCDM cosmology for $P_{21}(k)$. Given the fiducial cosmology and the errors of Equation 6.7 the final data set is constructed generating, for each $k-$bin, a new data point Gaussian distributed around the theory with a standard deviation of $\sigma_{P_{21},i}^2$, as depicted in Figure 6.2. Intensity mapping experiments have yet to completely solve additional challenges, such as the cleaning of the foreground emissions, e.g. see [335], beam modeling uncertainties [65, 336], and possible residual artifacts in the data [337, 338]. In this work, we do not model these and leave them to further studies.

6.1.2.2 *Additional external intensity mapping forecasts on background quantities*

We also test the efficacy of the $P_{21}(k)$ likelihood combined with additional intensity mapping information on background and growth of structure quantities provided by other experiments at higher redshift. As described in [339], 21cm intensity mapping observations in the redshift range $2.5 < z < 5$ are expected to provide powerful constraints on cosmological parameters. In [339], constraints on the quantities $f\sigma_8(z)$, the angular diameter distance $D_A(z)$, and the Hubble parameter $H(z)$ are computed for a hypothetical observation of the telescope HIRAX [42] in this redshift range. Our aim is to equip the $P_{21}(k)$ likelihood with additional information on the background evolution, coming from external 21cm intensity mapping observations. To do so we construct an additional likelihood and mock data sets for $f\sigma_8(z)$, $D_A(z)$, and $H(z)$. In the following, we refer to this likelihood as the *background* likelihood.

The mock data set build for $f\sigma_8(z)$, $D_A(z)$ and $H(z)$ at redshift $z = 0.39$, is shown in Table 6.1. To construct it, we start from the forecast relative errors on these quantities at redshift $z = 2.5$ [339]. Following the trend found in [339], we assume the relative errors on $f\sigma_8$, D_A and H to be increasing with the redshift. Then, in order to be conservative, we set the relative error at $z = 0.39$ to the upper limit given by the relative errors at $z = 2.5$. We compute absolute errors and central points from theoretical estimates of $f\sigma_8(z)$, $D_A(z)$, and $H(z)$, as explained in Table 6.1.

	$\sigma_x/x(z = 2.5)$	$x(z = 0.39)$	$\sigma_x(z = 0.39)$
$f\sigma_8$	0.075	0.478	0.036
H [km s^{-1} Mpc^{-1}]	0.014	83.3	1.2
D_A [Mpc]	0.053	1130	60

Table 6.1: Data points and errors on $f\sigma_8$, the angular diameter distance D_A and the Hubble parameter H at redshift $z = 0.39$. In the first column, we show the forecast relative errors on these quantities at $z = 2.5$ computed in [339]. In the second column, we show theoretical expectations for $f\sigma_8$, D_A, and H obtained with CAMB for our fiducial cosmology at redshift $z = 0.39$. In the third column, there are the absolute errors on each quantity, which we derived from the relative errors at redshift $z = 2.5$ as $\sigma_x(z = 0.39) = \sigma_x/x(z = 2.5) \cdot x(z = 0.39)$. I.e., we set $\sigma_x/x(z = 0.39) = \sigma_x/x(z = 2.5)$.

From this mock data set, we implement an additional likelihood term for each $x = f\sigma_8$, H, D_A at $z = 0.39$:

$$-\ln\left[\mathcal{L}\left(x^{obs}|x^{th}\right)\right] = \frac{1}{2}(x^{th} - x^{obs})\frac{1}{\sigma_x^2}(x^{th} - x^{obs}).$$

We then sum each piece to the $P_{21}(k)$ likelihood, defined in Equation 6.4. We stress that the 21cm power spectrum data and the background data obtained from 21cm measurements are considered to be independent. This is of course an assumption that deserves to be investigated with dedicated mock data sets.

6.1.3   *Theoretical framework*

In this section, we review general aspects of the beyond ΛCDM models that we consider for our analysis. As anticipated, we work within the Effective field theory (EFT) framework. In the following, we first review the basic aspects of EFT of DE. Then, we describe in more detail the set of EFT models that we consider, and, finally, we briefly summarize the latest available constraints. We stress that in our work we follow mainly the notation of [254, 334].

6.1.3.1   *Effective field theory formalism*

Upcoming, high-precision cosmological observations are expected to shed light on the nature of gravity on large scales and the physics of DE. Given the plethora of candidates for DE/MG, it is important to adopt a unifying framework that allows for an efficient comparison with data. To this extent, the EFT approach is a powerful tool that provides us with a general, unified description of the late-time DE/MG at the level of the action, as discussed in Chapter 3. The EFT framework has been originally introduced in Cosmology in the context of inflation [251–253]. Subsequently, it was applied to quintessence [340] and eventually to scalar-tensor models of DE/MG [20, 21]. The EFT of DE is formulated in terms of a unifying action that allows for efficient and broad sampling of the theory space under general conditions of stability. It can be used in an agnostic way, with a set of free functions of time parametrizing theoretically allowed deviations from ΛCDM; or in a model-specific way, where the functions are customized to specific models through a mapping procedure. For a

detailed description of this, as well as a complete review of the state-of-the-art constraints on EFT models we refer the reader to [250].

The EFT formalism allows sampling a large number of different theoretical scenarios, of increasing complexity. For a first thorough forecast of 21cm intensity mapping constraints on DE/MG, we start from the subset representing Generalized Brans Dicke (GBD) theories, which includes $f(R)$ and, more generally, chameleon-type theories. In the EFT language, this class of theories can be explored simply by varying two functions of time, which determine both background and dynamics of linear perturbations. In our analysis, we opt for the Hubble parameter, $H(a)$ and the conformal coupling $\Omega(a)$ (see [341] for further details on the mapping of these theories into EFT of DE and EFTCAMB.). Hereafter, we will use $\Omega^{\text{EFT}}(a)$ to indicate this function, in order to avoid confusion with matter parameters that we vary in our analysis. This corresponds to assuming a designer approach, in which we fix the expansion history and explore the space of non-minimally coupled DE/MG models reproducing it by means of varying the coupling $\Omega^{\text{EFT}}(a)$[4]. Let us recall that a non-zero conformal coupling implies a running of the Planck mass which can be alternatively explored with the function $\alpha_M \equiv H^{-1}\mathrm{d}\ln M_P^2/\mathrm{d}t$. Within the context of GBD , we simply have $\alpha_M = H^{-1}\mathrm{d}\ln(1+\Omega^{\text{EFT}})/\mathrm{d}t$. We will present constraints on both Ω^{EFT} and α_M.

GBD models represent a large set of DE/MG models that survive the latest constraints from the direct detection of gravitational waves, while still displaying an interesting phenomenology at the level of large-scale structure [342]. While being relatively simple, they are still subject to the so-called stability constraints, which ensure that the theory is free from pathologies, such as ghost and gradient instabilities [18, 343, 344]. Imposing such viability conditions correctly is of crucial importance when studying EFT models in an MCMC framework, in order to select the correct parameter space volume. In the EFTCAMB/EFTCosmoMC codes routines to check the stability of a model are already implemented. In the following, we refer to these as viability conditions [254, 334].

6.1.3.2 *Selected models and their latest constraints*

Let us outline the models that we consider for our analysis with the $P_{21}(k)$ likelihood while reviewing the most recent constraints on them. Our results relative to each scenario are discussed in Section 6.2.

We start by analyzing the ΛCDM case, for which theoretical predictions of the 21cm power spectrum at different redshifts are shown in Figure 6.1. We also consider the wCDM model, one of the simplest extensions to ΛCDM, where the DE equation of state parameter w is constant but different from -1, as it is the case for ΛCDM. No conformal coupling in this case. These two cosmologies are our starting point, on top of which we then turn on the conformal coupling, exploring different choices. Since we work in the designer approach, where we have fixed $H(a)$, we can focus on the effects of the coupling on perturbations.

We explore different choices for $\Omega^{\text{EFT}}(a)$, adopting parametrizations that have been already explored in the context of different observables. This allows

---

[4]In the sub-case of $f(R)$ gravity, $\Omega^{\text{EFT}} = \mathrm{d}f/\mathrm{d}R$ in our convention.
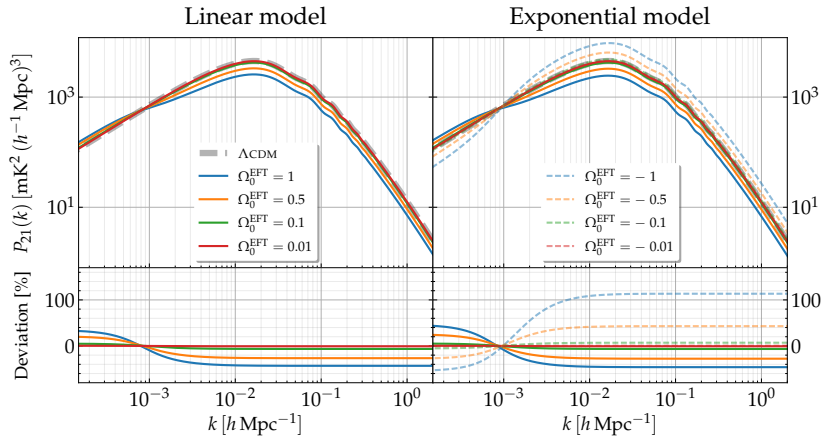
Figure 6.3: Upper panels: linear power spectra for the 21cm signal for ΛCDM and several *pure* EFT models, described by different values of the parameter Ω_0^{EFT}. Lower panels: percentage deviations from ΛCDM predictions, computed as $(P_{21}^{\text{EFT}} - P_{21}^{\Lambda\text{CDM}}) \times 100 / P_{21}^{\Lambda\text{CDM}}$. We show theoretical predictions at redshift $z = 0.39$ for a *pure* linear EFT model (left panel) and an exponential one with fixed $\beta = 1$ (right panel). For the linear case we consider $\Omega_0^{\text{EFT}} = 0.01, 0.1, 0.5, 1$, while for the exponential $\Omega_0^{\text{EFT}} = \pm 0.01, \pm 0.1, \pm 0.5, \pm 1$. The other cosmological parameters are set to the assumed fiducial cosmology values.

us to draw a more meaningful comparison of the constraining power of $P_{21}(k)$ with other probes. We start with the linear case, for which $\Omega^{\text{EFT}}(a)$ is

$$\Omega^{\text{EFT}}(a) = \Omega_0^{\text{EFT}} a, \tag{6.8}$$

where Ω_0^{EFT} is a constant and all other second-order EFT functions are set to zero. As it was shown in [255], the viability conditions require a non-negative Ω_0^{EFT}, i.e. $\Omega_0^{\text{EFT}} \geq 0$, both in the case of a ΛCDM and wCDM background. We recover the ΛCDM limit when $\Omega_0^{\text{EFT}} \to 0$. We refer to this model as *pure* linear EFT. The parameter Ω_0^{EFT} has been constrained to be $\Omega_0^{\text{EFT}} < 0.043$ (95% CL) on a ΛCDM background, from Planck 2015 TT, TE, EE power spectra combined with BAO, Supernovae and H_0 priors data sets [243]. On a wCDM background, instead, the constraint $\Omega_0^{\text{EFT}} < 0.058$ (95% CL) was found from Planck 2013 TT power spectrum and lensing data combined with BAO observations [255]. Both the matter power spectrum and the growth rate depend on Ω_0^{EFT}, thus the 21cm power spectrum is expected to be sensitive to this parameter as well.

Another interesting parametrization is the exponential one, i.e

$$\Omega^{\text{EFT}}(a) = \exp(\Omega_0^{\text{EFT}} a^\beta) - 1. \tag{6.9}$$

It is possible to see that this model has a simple mapping into the alternative parametrization referred to as the α-basis [256], of which we discussed the first function, α_M. Namely, it corresponds to a non-minimally coupled model in which the kinetic braiding and conformal coupling are related in a simple way,
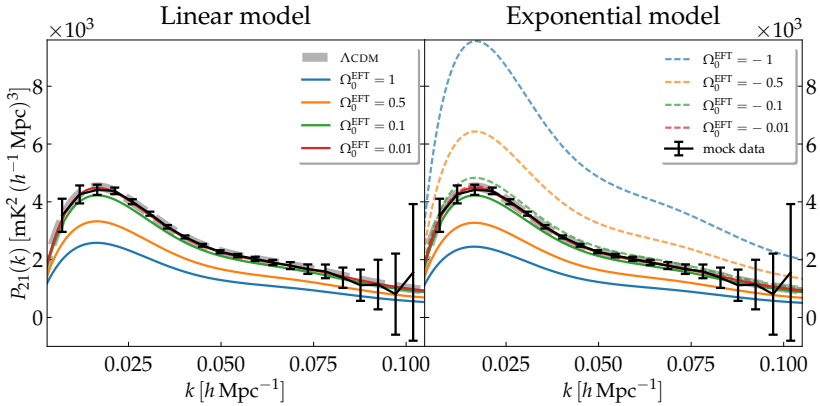
Figure 6.4: Linear power spectra for the 21cm signal for ΛCDM and several *pure* EFT models, described by different values of the parameter Ω_0^{EFT}. We show theoretical predictions at redshift $z = 0.39$ for a *pure* linear EFT model (left panel) and an exponential one with fixed $\beta = 1$ (right panel). For the linear case we consider $\Omega_0^{\text{EFT}} = 0.01, 0.1, 0.5, 1$, while for the exponential $\Omega_0^{\text{EFT}} = \pm 0.01, \pm 0.1, \pm 0.5, \pm 1$. The other cosmological parameters are set to the assumed fiducial cosmology values. Black points with errorbars are the mock data set we construct in this work, as described in Section 6.1.2.1.

i.e. $\alpha_B = -\alpha_M$, and α_K is determined by the background, i.e. it is a function of H and α_M [243]. The function α_M evolves as

$$\alpha_M = \alpha_M^0 a^\beta, \tag{6.10}$$

where we identify $\alpha_M^0 = \Omega_0^{\text{EFT}} \beta$. We refer to this model as *pure* exponential EFT.

The latest, most stringent constraints on the exponential model are $\alpha_M^0 < 0.062$ (95% CL), and $\beta = 0.92^{+0.53}_{-0.24}$ (68% CL), from Planck 2015 data combined with BAO and Supernovae datasets on a ΛCDM background [243]. From Planck 2018 data, instead, a mild (1.6 σ) preference for a negative running of the Planck mass has been observed [4].[5] Constraints computed from Planck 2018 TT, TE, EE power spectra, lensing, and low polarization CMB data are $\Omega_0^{\text{EFT}} = -0.049^{+0.037}_{-0.024}$ (68% CL), $\alpha_M^0 = -0.040^{+0.041}_{-0.016}$ (68% CL), $\beta = 0.72^{+0.38}_{-0.14}$ (68% CL).

Our predictions of $P_{21}(k)$ for a wide range of Ω_0^{EFT} values are shown in Figure 6.3, where we observe that the 21cm power spectrum is sensitive to variations in the EFT parameters. At small scales and redshift $z = 0.39$, the amplitude of $P_{21}(k)$ is rescaled for different values of Ω_0^{EFT}. This is the range of scales we investigate, as described in Section 6.1.2.1. Variations in this regime are at the level of $1 - 40\%$ (continuous lines), up to more than 100% for negative values of Ω_0^{EFT} (dashed lines). At large scales, instead, we observe a transfer of power, but it is not possible to probe this regime with current experiments. The behavior of $P_{21}(k)$ for EFT models is induced mainly by the matter power spectrum $P_m(z, k)$. In the $P_{21}(k)$ model of Equation 6.2, the only quantities sensitive to EFT modifications are $P_m(z, k)$ and $f(z)$, which origins an overall rescaling. Thus, if we have a good estimate for the astrophysical quantities that

---

[5] This preference is reduced to $< 1\sigma$, with the inclusion of the BAO and weak lensing datasets.
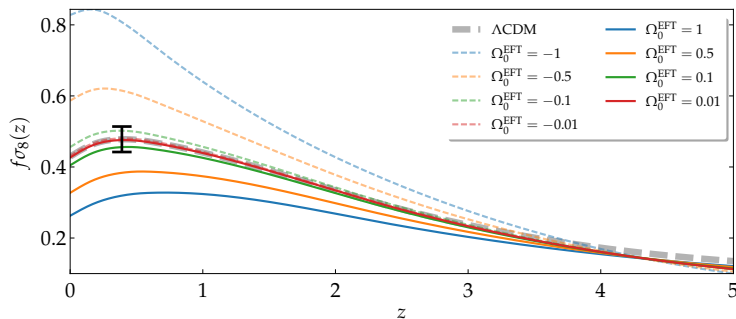
Figure 6.5: Theoretical predictions for the quantity $f\sigma_8$. We show the redshift evolution of $f\sigma_8$ for different models, i.e. ΛCDM, a *pure* linear EFT model described by $\Omega_0^{\mathrm{EFT}} = 0.01, 0.1, 0.5, 1$ (solid lines), a *pure* exponential EFT model with $\Omega_0^{\mathrm{EFT}} = -0.01, -0.1, -0.5, -1$ and $\beta = 1$. The black data point with error bars at $z = 0.39$ is the one given in Table 6.1. The other cosmological parameters are set to the assumed fiducial cosmology values.

Param.	Prior	Param.	Prior	Param.	Prior
$\Omega_b h^2$ ..	$[5 \times 10^{-3}, 0.1]$	τ	$[0.01, 0.8]$	w_0	$[-1.5, 0]$
$\Omega_c h^2$ ..	$[0.1 \times 10^{-3}, 0.99]$	$\ln(A_s)$	$[1.61, 3.91]$	Ω_0^{EFT} .	$[-1, 1]$
$100\theta_{MC}$	$[0.5, 100]$	n_s	$[0.8, 1.2]$	β	$[0, 3]$

Table 6.2: Adopted flat priors on cosmological and *pure* EFT parameters.

enter in the $P_{21}(k)$ model, e.g. the brightness temperature, we expect that the $P_{21}(k)$ may be useful to constrain these kinds of EFT models.

In figures Figure 6.4 and Figure 6.5, we compare EFT modifications to $P_{21}(k)$ and $f\sigma_8$ with the mock data sets we construct in sections Section 6.1.2.1 and Section 6.1.2.2 respectively. With the errorbars shown we expect the $P_{21}(k)$ likelihood to be sensitive to EFT modifications. We stress that the current constraints from CMB data on EFT parameters limit Ω_0^{EFT} to be $\Omega_0^{\mathrm{EFT}} \leq 0.1$ (green lines). EFT modifications for $\Omega_0^{\mathrm{EFT}} \leq 0.1$ fall within the errorbars of the mock data. We discuss the implications of this feature in Section 6.2.2.

When performing MCMC analyses for the models outlined above, we vary the six cosmological parameters $\{\Omega_b h^2, \Omega_c h^2, 100\theta_{MC}, \tau, A_s, n_s\}$ and the EFT parameters describing each EFT models. Results for all other quantities, such as H_0 and σ_8, are derived from constraints on the free parameters. If not explicitly stated, we consider the flat priors listed in Table 6.2.

6.2 RESULTS

In this section, we illustrate the results obtained for the models outlined in Section 6.1.3.2. We present constraints on cosmological and EFT parameters from several different data sets. On the one hand, we test the effect of 21cm data alone. On the other, we analyze the impact of adding $P_{21}(k)$ to CMB observations. We refer to [117] for tables showing the full results of our analyses, i.e. the complete sets of constraints on all the model parameters.
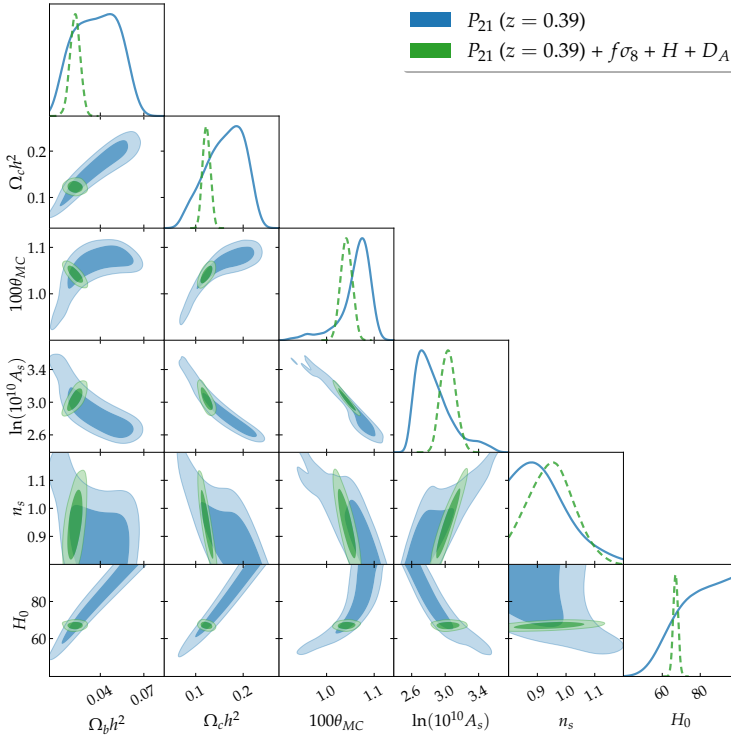
Figure 6.6: Joint constraints (68% and 95% confidence regions) and marginalized posterior distributions on cosmological parameters for a ΛCDM model. Here the label $P_{21}(z = 0.39)$ stands for the 21cm power spectrum likelihood at redshift $z = 0.39$, while $f\sigma_8 + H + D_A$ represents the additional *background* likelihood described in Section 6.1.2.2 and computed at the same redshift $z = 0.39$. We consider the parameter τ fixed to the fiducial cosmology value, i.e. $\tau = 0.0543$.

We recall that with the label "Planck 2018" we refer to the combination TT, TE, EE + low-ℓ + lowE + lensing (see Section 2.2.1).

6.2.1 *ΛCDM reference results*

We begin by testing the constraining power of the mock data set we constructed. We constrain cosmological parameters for ΛCDM using the $P_{21}(k)$ likelihood alone and combined with the *background* likelihood (see Section 6.1.2.2). Results of this first analysis are shown in Figure 6.6 and Table 6.3. As one could expect, $P_{21}(k)$ alone is not able to constrain all the six cosmological parameters at once and some of them remain completely unconstrained. However, fixing τ to its fiducial cosmology value, resulted to be enough to reach numerical convergence and obtain broad constraints. Looking at the 2D contour in Figure 6.6, we can observe a clear positive correlation between $\Omega_c h^2$ and H_0. We anticipate that this feature will be pivotal when combining $P_{21}(k)$ with CMB data.

This correlation is almost completely removed when we combine $P_{21}(k)$ with the *background* likelihood, i.e. including the three more data points on $f\sigma_8$, H,
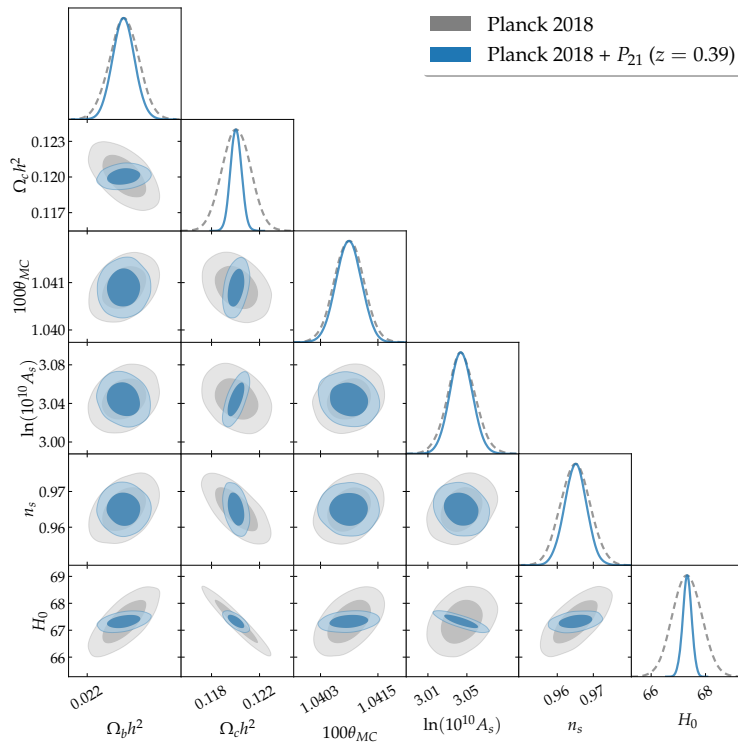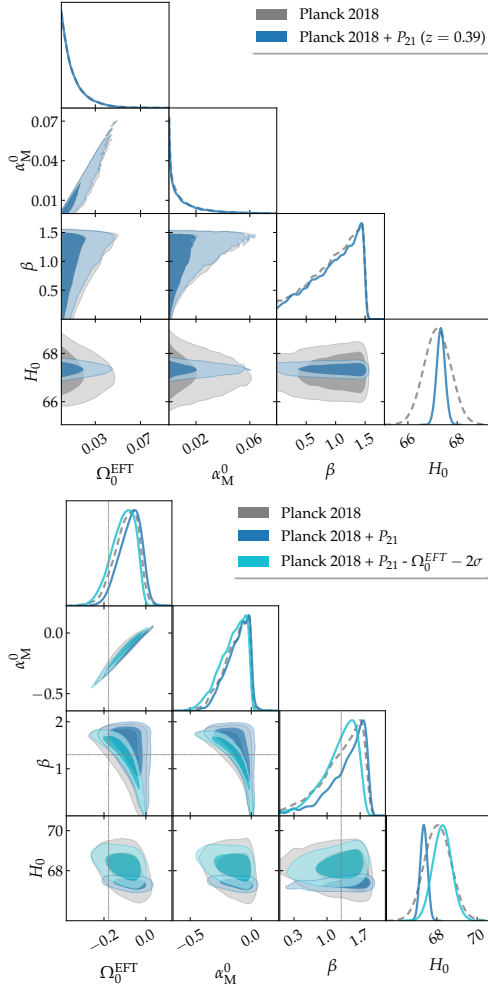
Figure 6.7: Joint constraints (68% and 95% confidence regions) and marginalized posterior distributions on cosmological parameters for a ΛCDM model. Here the label Planck 2018 stands for TT, TE, EE + lowE + lensing while the label $P_{21}(z = 0.39)$ stands for the 21cm power spectrum likelihood at redshift $z = 0.39$.

and D_A. In this case, we obtain significantly tighter and smoother posterior distributions, as shown in Figure 6.6 and we obtain a competitive error on the estimate of H_0, i.e.

$$H_0 = 67.1 \pm 1.3 \text{ km s}^{-1}\text{Mpc}^{-1}. \tag{6.11}$$

Thus, we observe that 21cm observables alone can constrain H_0 with an error comparable to measurements obtained from other probes [11]. E.g. early time probes constrain H_0 with an error of ~ 1.2 km s^{-1}Mpc^{-1}, from the Dark Energy Survey observations combined with BAO and BBN data [5]. Once the impact of $P_{21}(k)$ alone is established, we turn to combine $P_{21}(k)$ with Planck 2018 CMB data. Marginalized posterior distributions are shown in Figure 6.7, while constraints are listed in Table 6.3. We find that adding $P_{21}(k)$ significantly improves on the constraints produced by Planck data alone, reducing the error on cosmological parameters by at least $\sim 10\%$ to $\sim 70\%$. The maximum effect is obtained for $\Omega_c h^2$ and H_0. With Planck data we obtain $\sigma_{\Omega_c h^2} = 1.2 \times 10^{-3}$, and $\sigma_{H_0} = 0.53$, while adding the $P_{21}(k)$ likelihood the errors reduce to $\sigma_{\Omega_c h^2} = 4.6 \times 10^{-4}$ and $\sigma_{H_0} = 0.16$. The percentage reduction is of the 61% and the 69%, respectively.

Par.	Planck 2018	Planck 2018 + P_{21}	P_{21}	P_{21} + bg
$\Omega_b h^2$	0.02237 ± 0.00014	0.02236 ± 0.00011 $(-\mathbf{24}\%)$	0.038 ± 0.015	0.0226 ± 0.0035
$\Omega_c h^2$	0.1201 ± 0.0012	0.12004 ± 0.00046 $(-\mathbf{61}\%)$	$0.162^{+0.050}_{-0.033}$	0.1227 ± 0.0081
n_s	0.9650 ± 0.0041	0.9651 ± 0.0031 $(-\mathbf{25}\%)$	$< 1.10^\dagger$	$0.951^{+0.072}_{-0.085}$
H_0	67.32 ± 0.53	67.32 ± 0.16 $(-\mathbf{69}\%)$	$> 57.8^\dagger$	67.1 ± 1.3

Table 6.3: Marginalized constraints on cosmological parameters at the 68% confidence level for a ΛCDM model. 95% confidence levels are marked with †. Deviations in the error with respect to Planck 2018 results are shown in brackets. Here the label Planck 2018 stands for TT, TE, EE + lowE + lensing, while the label $P_{21}(z = 0.39)$ stands for the 21cm power spectrum likelihood at redshift $z = 0.39$. The label *bg* represents the additional *background* likelihood described in Section 6.1.2.2.

Comparing the 2D contour plots of figures Figure 6.6 and Figure 6.7, we observe that $\Omega_c h^2$ and H_0 are correlated both using $P_{21}(k)$ or Planck data alone. Nevertheless, the correlation appears to develop along two orthogonal directions for the two data sets. When using the data sets combined, the contour reduces to the intersection of these two regions, thus producing very tight constraints on $\Omega_c h^2$ and H_0. Therefore, the $P_{21}(k)$ likelihood performs as expected, i.e. it provides complementary correlations to that of CMB and remarkably improves on the constraints.

Although we do not show results here, we note that the effect of adding BAO data has also been tested. We observe no significant impact when we combine BAO both with $P_{21}(k)$ data alone and with Planck + $P_{21}(k)$.

6.2.2 *Pure EFT models on a ΛCDM background*

After having established the constraining power of the 21cm signal, we study its impact on beyond ΛCDM theories. We consider the *pure EFT* models on a ΛCDM background, which are described in Section 6.1.3.2. We test three different scenarios: *i*) the *pure* linear EFT model, *ii*) the *pure* exponential EFT model, *iii*) a *pure* exponential EFT model for which we allow a negative running of the Planck mass. Results are shown in figures Figure 6.8, Figure 6.9 and Table 6.4.

As a first check, we compute constraints from $P_{21}(k)$ alone. As before, in this analysis, τ is kept fixed to its fiducial cosmology value. We observe that the state-of-the-art mock uncertainties still provide a weak constraining power for these models and the EFT parameters appear to be loosely constrained. As displayed in Table 6.4, for both the *pure* linear and exponential EFT models we find Ω_0^{EFT} to be unconstrained. The best result is achieved on the parameter β describing the exponential EFT models. $P_{21}(k)$ alone is able to constrain β with a slightly broader error with respect to the one we obtain from Planck data. Moreover, we observe that adding the background data slightly improves the results on the EFT parameters, although with no significant impact. This is consistent with the fact that we assume a designer approach, where we parametrize independently the background and the EFT functions. Consequently, adding information on the background does not have a direct impact on EFT parameter constraints. We conclude that the mock data set we constructed for the redshift bin $z = 0.39$ exhibits a limited constraining power on the EFT parameters. How-
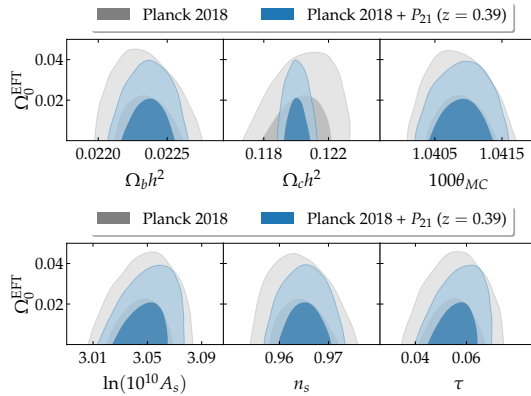
Figure 6.8: Joint constraints (68% and 95% confidence regions) on cosmological and EFT parameters for a *pure* linear EFT model on a ΛCDM background. Here the label Planck 2018 stands for TT, TE, EE + lowE + lensing while the label $P_{21}(z = 0.39)$ stands for the 21cm power spectrum likelihood at redshift $z = 0.39$.

ever, we anticipate that future tomographic observations at multiple redshifts could significantly help to increase the constraining power of this observable alone on EFT parameters. We further discuss this claim in Section 6.2.5.

We proceed by combining $P_{21}(k)$ with the latest Planck 2018 CMB observations. Overall, we observe that constraints on cosmological parameters remain unaffected compared to the ΛCDM case. Furthermore, adding $P_{21}(k)$ produces an improvement in the EFT parameters at the level of $1 - 18\%$. In the following, we discuss results for each *pure* EFT model individually.

First, for the linear model from Planck data alone, we constrain Ω_0^{EFT} to be

$$\Omega_0^{\text{EFT}} < 0.035 \quad (95\% \text{ CL}), \tag{6.12}$$

as we can see in Table 6.4. This upper limit improves on previous results in the literature ($\Omega_0^{\text{EFT}} < 0.043$), which were produced using Planck 2015 data sets and an older version of the code EFTCAMB (see Section 6.1.3.2). When we add the $P_{21}(k)$ likelihood, we get

$$\Omega_0^{\text{EFT}} < 0.031 \quad (95\% \text{ CL}), \tag{6.13}$$

which improves the constraint from Planck alone at the level of 11%. Contour plots are shown in Figure 6.8. We can observe that adding $P_{21}(k)$ has a mild effect on removing the correlation between Ω_0^{EFT} and some of the cosmological parameters, e.g. $\Omega_c h^2$.

Second, as shown in Table 6.4 for the *pure* exponential EFT model we obtain constraints from Planck 2018 data alone which are compatible with previous results in the literature, produced with Planck 2015 data as before (see Sec-

Par.	Planck 2018	Planck 2018 + P_{21}	P_{21}	$P_{21} + bg$
Linear EFT				
Ω_0^{EFT}	$< 0.035^\dagger$	$< 0.031^\dagger$ ($-\mathbf{11}\%$)	—	—
H_0	67.21 ± 0.55	67.33 ± 0.17 ($-\mathbf{70}\%$)	$> 57.7^\dagger$	67.0 ± 1.3
Exponential EFT				
Ω_0^{EFT}	$< 0.036^\dagger$	$< 0.034^\dagger$ ($-\mathbf{5}\%$)	—	—
β	$0.96^{+0.54}_{-0.19}$	$0.97^{+0.53}_{-0.19}$ ($-\mathbf{1}\%$)	1.30 ± 0.57	$1.20^{+0.58}_{-0.47}$
α_M^0	$< 0.045^\dagger$	$< 0.044^\dagger$ ($-\mathbf{3}\%$)	$< 1.89^\dagger$	$< 1.72^\dagger$
H_0	67.20 ± 0.55	67.34 ± 0.17 ($-\mathbf{69}\%$)	$> 64.3^\dagger$	66.9 ± 1.3
Exponential EFT **negative running**				
Ω_0^{EFT}	$-0.094^{+0.071}_{-0.042}$	$-0.075^{+0.063}_{-0.042}$ ($-\mathbf{7}\%$)	—	$0.19^{+0.69}_{-0.34}$
β	$1.28^{+0.56}_{-0.21}$	$1.41^{+0.48}_{-0.15}$ ($-\mathbf{18}\%$)	$1.21^{+0.57}_{-0.70}$	1.38 ± 0.55
α_M^0	$-0.133^{+0.13}_{-0.048}$	$-0.117^{+0.12}_{-0.052}$ ($-\mathbf{3}\%$)	$0.31^{+0.84}_{-0.70}$	0.36 ± 0.80
H_0	68.03 ± 0.66	67.36 ± 0.18 ($-\mathbf{73}\%$)	$> 56.3^\dagger$	67.0 ± 1.3

Table 6.4: Marginalized constraints on cosmological parameters at the 68% confidence level for *pure* EFT models on a ΛCDM background. 95% confidence levels are marked with †, while the symbol — means that we do not find any constraint. Deviations in the error with respect to Planck 2018 results are shown in brackets. Here the label Planck 2018 stands for TT, TE, EE + lowE + lensing while the label P_{21} stands for the 21cm power spectrum likelihood at redshift $z = 0.39$. The label *bg* represents the additional *background* likelihood described in Section 6.1.2.2.

tion 6.1.3.2). Adding $P_{21}(k)$ provides similar effects as for the linear model. With $P_{21}(k)$ + Planck we obtain:

$$\Omega_0^{\text{EFT}} < 0.034 \quad (95\% \text{ CL}),$$
$$\beta = 0.97^{+0.53}_{-0.19} \quad (68\% \text{ CL}), \tag{6.14}$$
$$\alpha_M^0 < 0.044 \quad (95\% \text{ CL}),$$

Note a 5% reduction of the upper limit on Ω_0^{EFT}, and consequently on α_M^0, with respect to Planck data alone. Instead, constraints on the parameter β appear to be unaffected when we add $P_{21}(k)$[6]. Contour plots are shown in Figure 6.9 (left panel). As for the linear case, we notice a small reduction of the correlation between Ω_0^{EFT} and H_0. The characteristic shape of the $\beta - \alpha_M^0$ contour is mainly set by viability requirements, which sharply cut the samples at $\beta \sim 1.6$. For lower values of β, the MCMC samples converge towards $\Omega_0^{\text{EFT}} = 0$, resulting in an elongated shape of the contour. This is an attribute of the functional form of the EFT function $\Omega^{\text{EFT}}(a)$. According to Equation 6.9, when $\Omega_0^{\text{EFT}} = 0$, i.e. in the ΛCDM limit, also $\Omega^{\text{EFT}}(a) = 0$ for any value of β. Thus, near the ΛCDM limit, β is unconstrained and the MCMC samples populate all the values allowed by viability conditions. We can observe this property for all the exponential models, i.e. in both the left and the right panels of Figure 6.9.

---

[6]Notice that the posterior distribution of the parameter β is asymmetrical resulting in different confidence levels above and below the mean value. When we compute percentage deviations between different results, we compare the mean of the upper and lower errors. We do so for all asymmetrical constraints.

Lastly, we tested the case of a *pure* exponential EFT model where we allow negative values of the function Ω^{EFT}. This scenario corresponds to a negative running of the Planck mass. From Planck 2018 data we find

$$\Omega_0^{\text{EFT}} = -0.094^{+0.071}_{-0.042} \quad (68\% \text{ CL}),$$
$$\alpha_M^0 = -0.133^{+0.13}_{-0.048} \quad (68\% \text{ CL}), \tag{6.15}$$
$$\beta = 1.28^{+0.56}_{-0.21} \quad (68\% \text{ CL}).$$

Compared with state-of-the-art constraints for the same data sets reported in Section 6.1.3.2, our results present slightly different features, although we check that they carry the same statistical significance. χ^2 deviations with respect to the ΛCDM constraints are comparable. We find $\Delta\chi^2 = \chi^2_{\Lambda\text{CDM}} - \chi^2_{\text{EFT}} = -4.4$ to be compared with $\Delta\chi^2 = -4.3$ found in [4]. Moreover, the significance of the deviation from $\Omega_0^{\text{EFT}} = 0$, being 1.3σ, is the same for our results and results in the literature. The disparities that we find could be caused by a different choice of viability conditions. E.g., for Ω_0^{EFT} it may be that we allow to sample a larger portion of the parameter space resulting in different but statistically equivalent constraints.

As presented in Table 6.4, when we add $P_{21}(k)$ we find

$$\Omega_0^{\text{EFT}} = -0.075^{+0.063}_{-0.042} \quad (68\% \text{ CL}),$$
$$\alpha_M^0 = -0.117^{+0.12}_{-0.052} \quad (68\% \text{ CL}), \tag{6.16}$$
$$\beta = 1.41^{+0.48}_{-0.15} \quad (68\% \text{ CL}),$$

with a reduction on the errors at the level of 7% on Ω_0^{EFT} and 18% on β. In the contour plots of Figure 6.9 (right panel), we observe the full shape of the $\beta - \alpha_M^0$ confidence region.

Compared with the results in the left panel, the sharp cut-off at $\beta \sim 1.6$ here disappears, given that we relax some of the viability conditions. This allows us to reconstruct the full shape of the posterior distribution for higher values of β. For lower values of β, instead, we observe the clustering of the samples along the $\Omega_0^{\text{EFT}} = 0$ axis, as for the case with stronger viability conditions shown in the left panel. This feature impairs the contour on Ω_0^{EFT}, pushing it towards the ΛCDM limit. Knowing or fine-tuning β a priori would remove these artificial effects, and it could significantly help in better constraining Ω_0^{EFT}. We highlight that for the time being we do not introduce weak lensing data, which should move the constraints to the ΛCDM limit, as one can observe in [4].

The significance of the deviation from zero for the data sets Planck 2018 + $P_{21}(k)$ is 1.2σ, slightly lower than the value obtained with Planck data alone. From this, we may infer that the 21cm signal seems to bring back Ω_0^{EFT} to its ΛCDM limit. However, this feature is caused by the choice we made for the central points of the mock data set for $P_{21}(k)$, which we generate assuming a ΛCDM cosmology.

In order to test this statement, we conduct a further consistency check for our mock data set for the *pure* exponential EFT model with negative values of Ω_0^{EFT}. We consider a new mock data set with the same errors, but different central points. To generate such points we use the predicted $P_{21}(k)$ power spectrum for an exponential EFT model described by the parameter $\Omega_0^{\text{EFT}} = -0.178$, which is 2σ away from the mean value of the Planck constraint, taken from Table 6.4.

Figure 6.9: Joint constraints (68% and 95% confidence regions) and marginalized posterior distributions on cosmological and EFT parameters for a *pure* exponential EFT model on a ΛCDM background (left panel). We show also results for the same model for a negative running of the Planck mass (right panel). Here the label Planck 2018 stands for TT, TE, EE + lowE + lensing while the label $P_{21}(z = 0.39)$ stands for the 21cm power spectrum likelihood at redshift $z = 0.39$. $\Omega_0^{\text{EFT}} - 2\sigma$ mark the constraints obtained from a new mock data set constructed setting Ω_0^{EFT} 2σ away from the Planck estimate. I.e., we set $\Omega_0^{\text{EFT}} = -0.178$, 2σ away from the Planck constraints, and $\beta = 1.28$, its Planck constraint. These values are marked with gray lines in the right panel plots.

We set β and all the other cosmological parameters to their Planck constraint. Results are shown in the right panel of Figure 6.9. For Planck 2018 + $P_{21}(k)$ likelihood computed on this new data set, we find Ω_0^{EFT} constrained to be

$$\Omega_0^{\text{EFT}} = -0.109^{+0.071}_{-0.041} \quad (68\% \text{ CL}). \tag{6.17}$$

While the error on Ω_0^{EFT} remains unchanged, this estimate appears to be away from 0 at the level of 1.5σ, to be compared with the previous 1.3σ from Planck 2018 data. The contour in the $\beta - \alpha_M^0$ confidence region (Figure 6.9, right panel, cyan contour) is significantly reduced with respect to the previous case (blue contour). Assuming that one could place a prior or fix β and remove the artificial clustering around the $\Omega_0^{\text{EFT}} = 0$ axis, the significance of the deviation from the ΛCDM limit would increase remarkably. Thus, if $P_{21}(k)$ data would prefer an EFT Universe, we should be able to detect and distinguish it from ΛCDM. The constraints on the EFT parameters (Ω_0^{EFT}, β) appropriately decrease when using the EFT mock dataset, while the cosmological parameters ($\Omega_c h^2$, H_0) show only mild improvement, remaining equivalent to that of Planck constraints. Essentially, the $P_{21}(k)$ mock modeled around ΛCDM, aids to bring the constraints closer to Planck constraints for all the parameters. While the $P_{21}(k)$ modeled around the EFT, as expected, provides better agreement with the Planck constraints on the cosmological parameters and additionally shows improvement for the EFT parameters.

In conclusion, we notice that the conformal coupling characteristic of GBD models, explored here with the *pure* EFT approach, is sensitive to 21cm signal observations. However, the constraining power of a realistic mock data set is still limited by the capability of state-of-the-art instruments. When used without other probes like the CMB, the $P_{21}(k)$ likelihood shows a mild constraining power. When combined with CMB measurements, results are dominated by the more comprehensive Planck 2018 data sets. In this framework, the realistic, MeerKAT-like, single bin $P_{21}(k)$ likelihood improves the constraints on EFT parameters at the level of $\sim 10\%$. We expect that adding tomographic observations of $P_{21}(k)$ for multiple redshift bins would improve the constraining power of this new observable, as we examine in Section 6.2.5.

6.2.3 *Adding likelihood nuisance parameters*

When modeling $P_{21}(k)$ we keep both the bias b_{HI} and the amplitude of the brightness temperature a_{T_b} fixed to their ΛCDM limit, lacking a theoretical prediction of how these two quantities might change for beyond ΛCDM scenarios. See [160] for this type of computation. This assumption is accurate enough for our purposes since we expect to detect small variations from ΛCDM.

In this section, we relax this assumption and implement the bias and the brightness temperature as nuisance likelihood parameters and test their effects on the parameter constraints. Note that varying these two quantities correspond to altering the amplitude of the power spectrum. We compare four different case studies, where: *i*) we keep fixed both a_{T_b} and b_{HI}, *ii*) we vary only b_{HI}, *iii*) we vary only a_{T_b}, *iv*) we vary both a_{T_b} and b_{HI}. Confidence regions and marginalized posteriors are shown in Figure 6.10. We start studying the effect of nuisance parameters using Planck 2018 data + $P_{21}(k)$ assuming a ΛCDM universe.
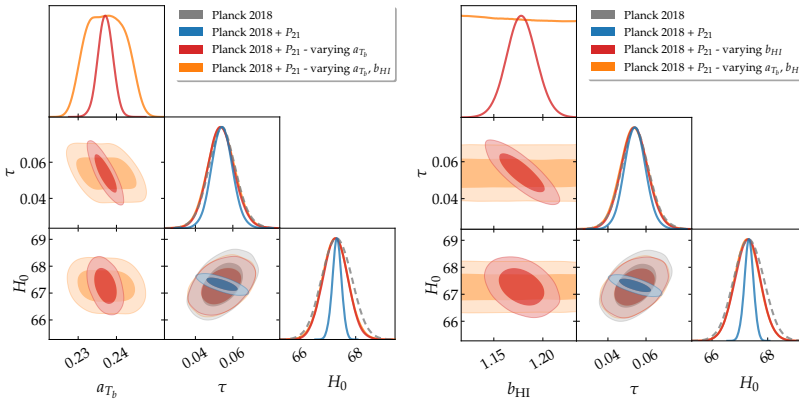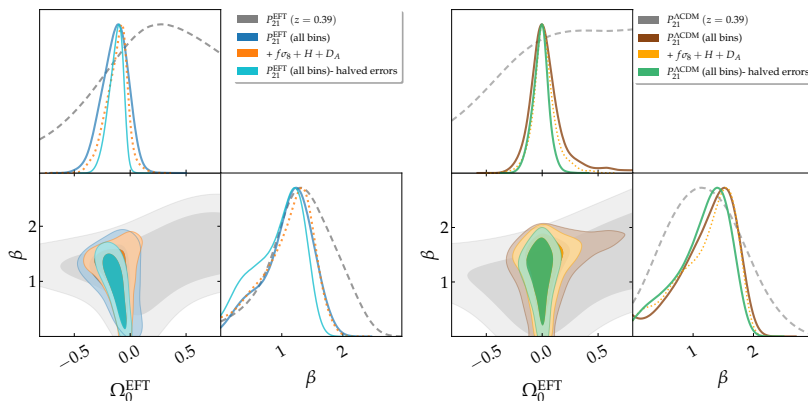
Figure 6.10: Joint constraints (68% and 95% confidence regions) and marginalized posterior distributions on cosmological parameters for a ΛCDM model. We open the parameter space to the two nuisance parameters a_{T_b} and b_{HI}, i.e. the amplitude of the brightness temperature and the HI bias. We study different configurations: both the parameters are fixed, one is free the other is fixed, they are both free. Here the label Planck 2018 stands for TT, TE, EE + lowE + lensing while the label P_{21} stands for the 21cm power spectrum likelihood at redshift $z = 0.39$.

We observe that adding separately b_{HI} or a_{T_b} (case ii) and iii)) produces comparable results. Red contours in Figure 6.10 represent this scenario. We notice that, as expected, the addition of one nuisance parameter reduces the constraining power of $P_{21}(k)$. With respect to Planck constraints, we observe a reduction of the error at the level of $\sim 15\%$, to be compared with the $\sim 65\%$ that we found with fixed a_{T_b} and b_{HI}.

When two nuisance parameters are varied (case iv)), we obtain a similar effect on cosmological parameters, while losing constraining power on a_{T_b} and b_{HI}. In Figure 6.10 (orange contours), we see that the brightness temperature a_{T_b} is loosely constrained while the bias b_{HI} remains completely unconstrained. In conclusion, although b_{HI} and a_{T_b} are two very different physical quantities, they have similar effects on the parameter constraints. In the following, we fix the bias b_{HI} and leave the brightness temperature a_{T_b} as a nuisance parameter.

We have tested the effect of varying a_{T_b} on EFT parameter constraints. We find that, as expected, adding a nuisance parameter reduces the constraining power on model parameters. When varying a_{T_b}, we observe it to be mildly correlated with EFT parameters.

6.2.4 *Results for a wCDM background*

We now turn our attention to EFT models on a *w*CDM background. We would like to test the impact of the $P_{21}(k)$ likelihood in a more complex framework, in which we open the parameter space to the DE equation of state parameter w_0. We highlight that throughout this analysis we always vary a_{T_b}, the amplitude of the brightness temperature along with the other cosmological parameters, as discussed in Section 6.2.3. Using $P_{21}(k)$ alone and with background data we find broad constraints, comparable with the ones described above in Section 6.2.2.
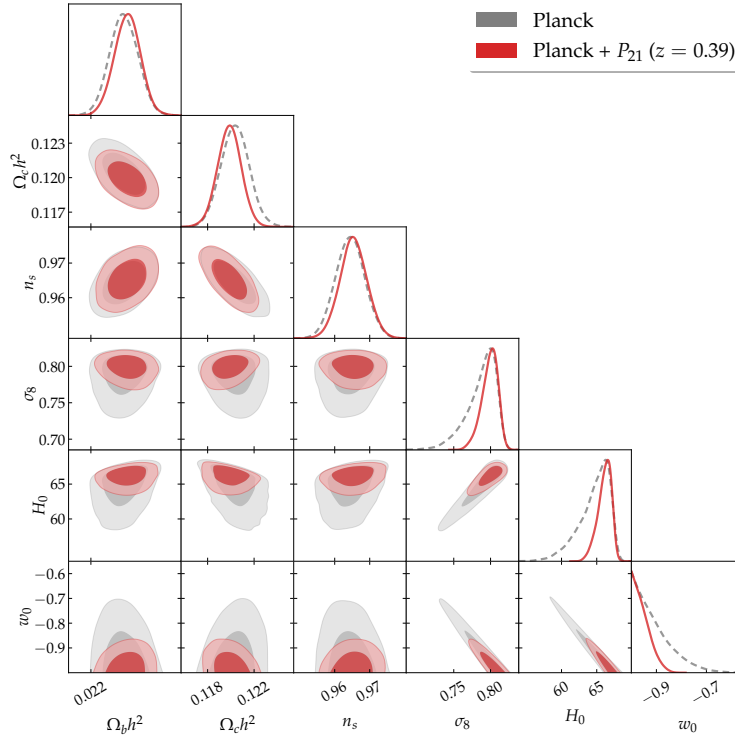
Figure 6.11: Joint constraints (68% and 95% confidence regions) and marginalized posterior distributions on cosmological parameters for a wCDM model. Here the label Planck 2018 stands for TT, TE, EE + lowE + lensing while the label $P_{21}(z = 0.39)$ stands for the 21cm power spectrum likelihood at redshift $z = 0.39$. We vary the nuisance parameter a_{T_b}, i.e. the amplitude of the brightness temperature, keeping fixed the HI bias b_{HI}.

In the following, we focus on constraints obtained by combining the $P_{21}(k)$ likelihood with CMB.

First, we test the effect of $P_{21}(k)$ for a simple wCDM model, i.e. we only add a constant w_0 to the parameter space. As shown in Figure 6.11 and Table 6.5, $P_{21}(k)$ data significantly reduces the error on w_0 and consequently on H_0 and σ_8. E.g., on w_0 we obtain an improvement of 53% on the upper limit found from Planck data alone. Given that w_0 is degenerate with both H_0 and σ_8, this translates into a reduction in the errors on these parameters at the level of 50% and 40% respectively. Adding $P_{21}(k)$ reduces the degeneracy between w_0 and the other parameters. Notice that, the improvement on cosmological parameter errors is compatible with the results we obtained for ΛCDM with a_{T_b} as a nuisance.

We show results for EFT models in Figure 6.12 and Table 6.5. We test the linear and the *pure* exponential EFT models. Overall, the improvement brought by $P_{21}(k)$ on w_0 and derived parameters is compatible with the results for the vanilla wCDM case. For the linear model, we obtain the upper limit:

$$\Omega_0^{\text{EFT}} < 0.034 \quad (95\% \text{ CL}), \tag{6.18}$$
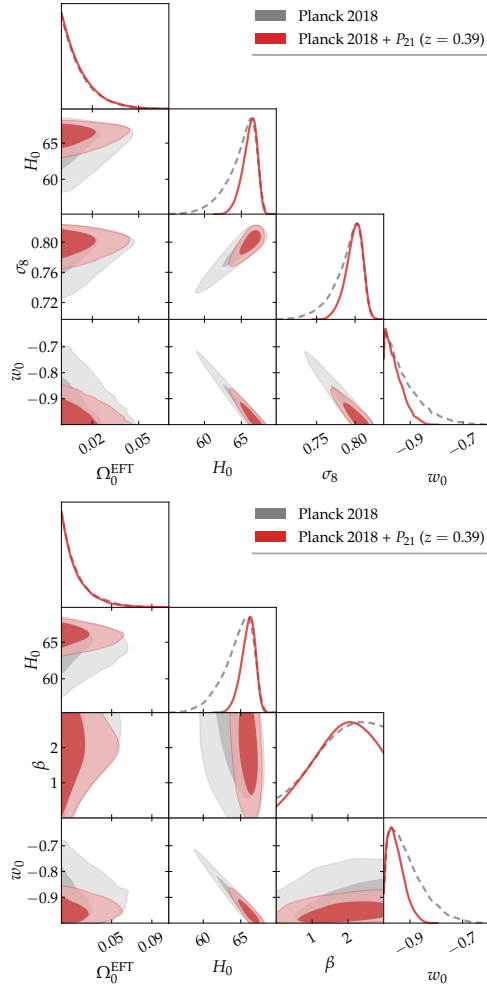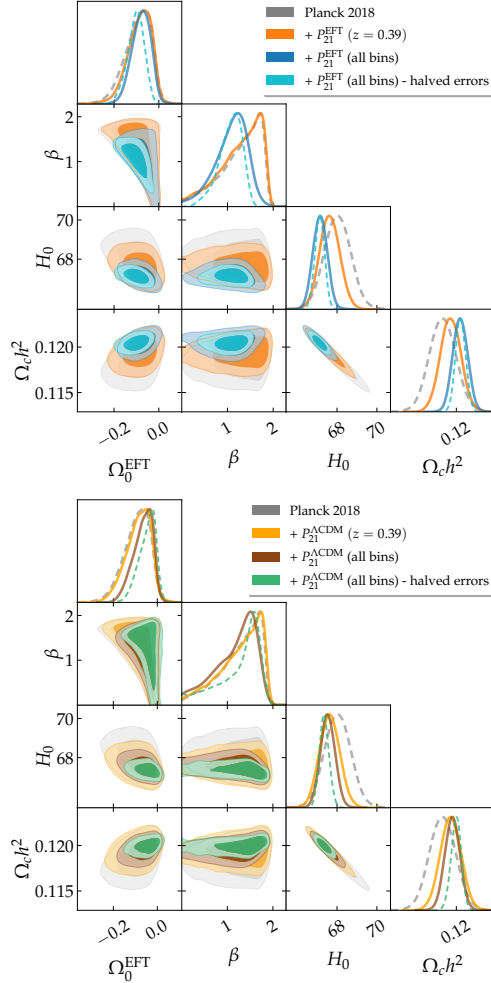
Figure 6.12: Joint constraints (68% and 95% confidence regions) and marginalized posterior distributions on cosmological and EFT parameters for a *pure* linear EFT model on a *w*CDM background (left panel). We show also results for a *pure* exponential EFT model (right panel). Here the label Planck 2018 stands for TT, TE, EE + lowE + lensing, while the label $P_{21}(z = 0.39)$ stands for the 21cm power spectrum likelihood at redshift $z = 0.39$. $f\sigma_8 + H + D_A$ represents the additional *background* likelihood described in Section 6.1.2.2 and computed at the same redshift $z = 0.39$. We vary the nuisance parameter a_{T_b}, i.e. the amplitude of the brightness temperature, keeping fixed the HI bias b_{HI}.

Par.	Planck 2018	Planck 2018 + P_{21}
*w*CDM		
w_0	$< -0.76^\dagger$	$< -0.89^\dagger$ $(-\mathbf{53}\%)$
H_0	$64.6^{+2.7}_{-1.1}$	$66.1^{+1.2}_{-0.69}$ $(-\mathbf{50}\%)$
σ_8	$0.787^{+0.025}_{-0.011}$	$0.799^{+0.013}_{-0.0085}$ $(-\mathbf{40}\%)$
Linear EFT		
w_0	$-0.925^{+0.020}_{-0.079}$	$-0.960^{+0.015}_{-0.043}$ $(-\mathbf{41}\%)$
Ω_0^{EFT}	$< 0.034^\dagger$	$< 0.034^\dagger$
H_0	$64.9^{+2.4}_{-0.97}$	$66.1^{+1.2}_{-0.70}$ $(-\mathbf{44}\%)$
Exponential EFT		
w_0	$-0.911^{+0.028}_{-0.084}$	$-0.953^{+0.018}_{-0.041}$ $(-\mathbf{47}\%)$
Ω_0^{EFT}	$< 0.051^\dagger$	$< 0.047^\dagger$ $(-\mathbf{7}\%)$
β	—	$1.79^{+1.1}_{-0.47}$ $(-\mathbf{5}\%)$
H_0	$64.6^{+2.5}_{-1.1}$	$66.0^{+1.1}_{-0.73}$ $(-\mathbf{49}\%)$

Table 6.5: Marginalized constraints on cosmological parameters at the 68% confidence level for *pure* EFT models on a *w*CDM background. For *w*CDM the equation of state parameter is $w_0 > -1$. 95% confidence levels are marked with †, while the symbol — means that we do not find any constraint. Deviations in the error with respect to Planck 2018 results are shown in brackets. Here the label Planck 2018 stands for TT, TE, EE + lowE + lensing while the label P_{21} stands for the P_{21} likelihood at redshift $z = 0.39$.

from both Planck 2018 data with or without the addition of $P_{21}(k)$ Note that this constraint significantly improves over previous results in the literature($\Omega_0^{\mathrm{EFT}} <$ 0.058), computed from Planck 2013 [137] and WMAP [345] data sets and without polarization data (see Section 6.1.3.2). Although adding $P_{21}(k)$ does not impact the upper limit on Ω_0^{EFT}, in the contours (left panel of Figure 6.12) we observe that it reduces the correlation between Ω_0^{EFT} and other parameters. For the exponential model, instead, adding $P_{21}(k)$ reduces the errors on EFT parameters at the level of $5 - 7\%$, as presented in Table 6.5. For Planck 2018 + $P_{21}(k)$ we find:

$$\Omega_0^{\mathrm{EFT}} < 0.047 \quad (95\% \text{ CL}),$$
$$\beta = 1.79^{+1.1}_{-0.47} \quad (68\% \text{ CL}). \tag{6.19}$$

In the 2D contours (right panel of Figure 6.12) again we notice that $P_{21}(k)$ helps remove the correlation between EFT and cosmological parameters. We highlight that the confidence regions in the plane $\Omega_0^{\mathrm{EFT}} - \beta$ here do not show the cut-off for $\beta \sim 1.6$, which we found for the same model on a ΛCDM background. This means that when we add w_0 to the parameter space, a wider region is allowed by viability conditions and we are able to reconstruct the contour for higher values of β. Note that viability conditions are responsible also for the skewed elongated posteriors that we observe in Figure 6.12. As before (see Figure 6.9), the samples are clustered along the $\Omega_0^{\mathrm{EFT}} = 0$, due to the modeling we consider.

On a *w*CDM background evolution, the major impact of the $P_{21}(k)$ likelihood is to reduce the estimate on the equation of state parameter w_0, and consequently on H_0 and σ_8. For EFT models, $P_{21}(k)$ produces results similar

PAR.	Planck 2018 + $P_{21}^{\text{EFT}}(z=0.39)$	Planck 2018 + $P_{21}^{\text{EFT}}(\text{bins})$	Planck 2018 + $P_{21}^{\text{EFT}}(\text{bins})$ – halved errors
$\Omega_c h^2$	$0.1194 \pm 0.0011\ (-22\%)$	$0.12042 \pm 0.00080\ (-43\%)$	$0.12046 \pm 0.00055\ (-61\%)$
Ω_0^{EFT}	$-0.086^{+0.064}_{-0.038}\ (-10\%)$	$-0.079^{+0.047}_{-0.036}\ (-26\%)$	$-0.103^{+0.042}_{-0.032}\ (-35\%)$
β	$1.28^{+0.58}_{-0.22}\ (+4\%)$	$1.08^{+0.42}_{-0.25}\ (-13\%)$	$1.06^{+0.30}_{-0.19}\ (-36\%)$
H_0	$67.63 \pm 0.50 (-24\%)$	$67.15 \pm 0.36\ (-46\%)$	$67.13 \pm 0.24\ (-65\%)$

PAR.	Planck 2018 + $P_{21}^{\Lambda\text{CDM}}(z=0.39)$	Planck 2018 + $P_{21}^{\Lambda\text{CDM}}(\text{bins})$	Planck 2018 + $P_{21}^{\Lambda\text{CDM}}(\text{bins})$ – halved errors
$\Omega_c h^2$	$0.1194 \pm 0.0011\ (-22\%)$	$0.11957 \pm 0.00082\ (-41\%)$	$0.11997 \pm 0.00055\ (-61\%)$
Ω_0^{EFT}	$-0.086^{+0.068}_{-0.039}\ (-10\%)$	$-0.066^{+0.055}_{-0.031}\ (-24\%)$	$-0.047^{+0.047}_{-0.027}\ (-35\%)$
β	$1.28^{+0.58}_{-0.22}\ (+4\%)$	$1.18^{+0.57}_{-0.26}\ (-8\%)$	$1.26^{+0.55}_{-0.18}\ (-5\%)$
H_0	$67.63 \pm 0.51\ (-23\%)$	$67.54 \pm 0.37\ (-44\%)$	$67.36 \pm 0.24\ (-65\%)$

PAR.	$P_{21}^{\Lambda\text{CDM}}(\text{bins})$	$P_{21}^{\text{EFT}}(\text{bins})$	$P_{21}^{\text{EFT}}(\text{bins})$ – halved errors
Ω_0^{EFT}	$0.053^{+0.075}_{-0.17}$	$-0.14^{+0.13}_{-0.10}$	$-0.131^{+0.074}_{-0.045}$
β	$1.26^{+0.55}_{-0.30}$	$1.10^{+0.49}_{-0.29}$	$0.94^{+0.48}_{-0.32}$
H_0	$74.1^{+8.1}_{-11}$	70 ± 9	$67.32^{+0.77}_{-1.6}$

Table 6.6: Marginalized constraints on cosmological parameters at the 68% confidence level. We test a *pure* exponential EFT model on a ΛCDM background, with negative running of the Planck mass. We test the effects of tomography by means of two new 21cm power spectrum mock data sets: P_{21}^{EFT}, constructed around an EFT theory described by $\Omega_0^{\text{EFT}} = -0.178$ and $\beta = 1.28$, and $P_{21}^{\Lambda\text{CDM}}$, constructed around our fiducial cosmology. We compare the constraining power of a single bin $(z = 0.39)$ with the five bins at $z = 0$, 0.39, 0.53, 0.67, 2.5 combined (bins) and this same set with halved error bars. We use the 21cm power spectrum likelihood combined with Planck observations. The label Planck 2018 stands for TT, TE, EE + lowE + lensing. Deviations in the error with respect to Planck 2018 results are shown in brackets.

to what we found for the ΛCDM background. I.e., the $P_{21}(k)$ likelihood has mild constraining power on the EFT parameters and it helps in reducing the degeneracy with the other model parameters.

6.2.5 Tomography

In the results above we explored the constraining power of a realistic $P_{21}(k)$ mock data set at the redshift $z = 0.39$, with conservative error bars. In this section, instead, we would like to test a more ideal case, by exploiting the tomographic nature of 21cm intensity mapping observations. To this end, we construct new mock data sets with multiple redshifts and we investigate how this improves on the constraints for beyond ΛCDM models.

We add to the mock data at $z = 0.39$ four new mock $P_{21}(k)$ measurements at redshifts $z = 0$, 0.53, 0.67, 2.5, that we add to the one at $z = 0.39$ in the likelihood. We consider observations in different redshift bins to be independent. The errors for the bins $z = 0$, $z = 0.53$, and $z = 0.67$ forecast plausible MeerKAT-like observations and they are constructed with the same technique of Section 6.1.2.1. For the bin at $z = 2.5$, we assume to have an observation

Figure 6.13: Joint constraints (68% and 95% confidence regions) and marginalized posterior distributions on cosmological and EFT parameters. We investigate a *pure* exponential EFT model on a ΛCDM background, with a negative running of the Planck mass. We test the effects of tomography by means of two new 21cm power spectrum mock data sets: P_{21}^{EFT}, constructed around an EFT theory described by $\Omega_0^{\mathrm{EFT}} = -0.178$ and $\beta = 1.28$ (left panel), and $P_{21}^{\Lambda\mathrm{CDM}}$, constructed around our fiducial cosmology (right panel). We compare the constraining power of a single bin ($z = 0.39$) with the five bins at $z = 0, 0.39, 0.53, 0.67, 2.5$ combined (all bins) and this same set with halved error bars. The label $f\sigma_8 + H + D_A$ represents the additional *background* likelihood described in Section 6.1.2.2. We vary the nuisance parameter a_{T_b}, i.e. the amplitude of the brightness temperature, keeping fixed the HI bias b_{HI}.

of $P_{21}(k)$ from the extended HIRAX experiment, as in [339]. For this bin, we use the errorbars adopted for the data set at redshift $z = 0.67$. For all bins, we consider also a more optimistic case, i.e. we halve the errors on each point.

Central points in the data sets are generated from theory predictions and then randomly displaced, as we did for the data set at $z = 0.39$ in Section 6.1.2.1. For all the five bins, we construct two data sets: $P_{21}^{\Lambda\mathrm{CDM}}$ and P_{21}^{EFT}. For $P_{21}^{\Lambda\mathrm{CDM}}$, the theory we use to generate central points is our ΛCDM fiducial cosmology. For P_{21}^{EFT}, instead, we consider an exponential *pure* EFT model, in which Ω_0^{EFT} is 2σ away form the Planck constraints, as in Section 6.2.2 and Figure 6.9. I.e., we fix the EFT parameters to $\beta = 1.28$ and $\Omega_0^{\mathrm{EFT}} = -0.178$, while we leave the cosmological parameters to their fiducial value.

We compute constraints from both the $P_{21}^{\Lambda\mathrm{CDM}}$ and the P_{21}^{EFT} likelihood, which we use alone and combined with Planck 2018 data. We compare results from the realistic single bin at $z = 0.39$ with an ideal tomographic data set constructed with all five bins combined and with halved errors. We test a *pure* exponential EFT model with the negative running of the Planck mass. The analysis conducted here is similar to the one of Section 6.2.2 and Figure 6.9. However, here we vary the amplitude of the brightness temperature a_{T_b} as a nuisance, while in Figure 6.9 a_{T_b} is kept fixed. Results are shown in figures Figure 6.13, Figure 6.15, Figure 6.14 and Table 6.6.

Most of the constraining power comes from the redshift bins at $z = 0, 0.39, 2.5$. This is because the mock data at the intermediate redshifts are constructed assuming a MeerKAT-like single dish experiment with large error bars due to the λ/D scaling of the primary beam. In Figure 6.13, the constraints from
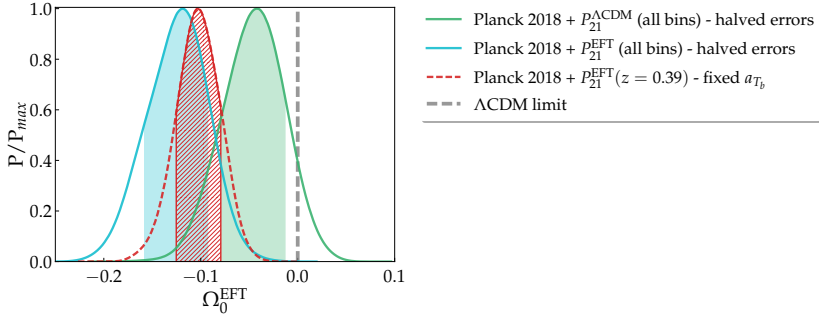
Figure 6.14: Marginalized posterior distributions for the EFT parameter Ω_0^{EFT}, describing a *pure* exponential EFT model on a ΛCDM background, with a negative running of the Planck mass. We test the effect of adding a stronger hard prior on the parameter β, which we choose to be $\beta \in [1.2, 1.4]$. We consider tomographic data set with five bins and half errors and compare results from P_{21}^{EFT}, constructed around an EFT theory described by $\Omega_0^{\mathrm{EFT}} = -0.178$ and $\beta = 1.28$ (blue line), and $P_{21}^{\Lambda\mathrm{CDM}}$, constructed around our fiducial cosmology (green line). We add also the result for the single bin with no nuisance parameters. The gray dashed line mark the ΛCDM limit for Ω_0^{EFT}, while the shaded regions correspond to the 1σ confidence limit. We use the 21cm power spectrum likelihood combined with Planck observations. The label Planck 2018 stands for TT, TE, EE + lowE + lensing.

the $P_{21}(k)$ likelihood alone are shown for both P_{21}^{EFT} (left panel) and $P_{21}^{\Lambda\mathrm{CDM}}$ (right panel). We observe that the largest improvement in the EFT constraints for the $P_{21}(k)$ likelihood is coming from tomography alone, while the inclusion of the *background* (orange dotted lines) has no significant impact on the EFT parameters posteriors. Compared with the very loose constraint from the single bin (gray dashed lines), with tomography, the Ω_0^{EFT} and β parameters are found to be more tightly constrained. The effect is more significant for Ω_0^{EFT} and it is maximized when we halve the error bars. Observe that tomography influences also cosmological parameters. E.g., estimates of H_0 and $\Omega_c h^2$ from all bins with halved errors are of the same order as the results found above for the single bin combined with Planck.

In Figure 6.15 constraints from tomographic measures of $P_{21}(k)$ combined with Planck are presented. As above, compared with the single bin, tomography significantly reduces the errors on both EFT and cosmological parameters (see Table 6.6). With tomography, deviations in the errors from Planck alone results for Ω_0^{EFT} and β increase up to the level of -35%, to be compared with the less than -10% found with the single bin only. The effect is even stronger for cosmological parameters. For H_0 and $\Omega_c h^2$ from Planck combined with tomography with halved error bars, we observe a reduction of the error with respect to Planck at the level of $\sim 65\%$. These improvements are comparable with the results from the analysis of sections Section 6.2.1 and Section 6.2.2, with no nuisance parameters, that, instead, are varied here. Looking at the 2D contours of Figure 6.15, we recognize the characteristic elongated shape in the plane $\beta - \Omega_0^{\mathrm{EFT}}$, that we discussed in Section 6.2.2. Here, we find a much broader confidence region, due to the fact that we vary the nuisance parameter a_{T_b}. Adding tomography further reduces the correlation between H_0 and $\Omega_c h^2$, resulting in the tight constraints described above.

Figure 6.15: Joint constraints (68% and 95% confidence regions) and marginalized posterior distributions on cosmological and EFT parameters. We investigate a *pure* exponential EFT model on a ΛCDM background, with a negative running of the Planck mass. We test the effects of tomography by means of two new 21cm power spectrum mock data sets: P_{21}^{EFT}, constructed around an EFT theory described by $\Omega_0^{\mathrm{EFT}} = -0.178$ and $\beta = 1.28$ (left panel), and $P_{21}^{\Lambda\mathrm{CDM}}$, constructed around our fiducial cosmology (right panel). We compare the constraining power of a single bin ($z = 0.39$) with the five bins at $z = 0, 0.39, 0.53, 0.67, 2.5$ combined (all bins) and this same set with halved error bars. We use the 21cm power spectrum likelihood combined with Planck observations. The label Planck 2018 stands for TT, TE, EE + lowE + lensing. We vary the nuisance parameter a_{T_b}, i.e. the amplitude of the brightness temperature, keeping fixed the HI bias b_{HI}.

Lastly, we observe that constraints from P_{21}^{EFT} (left panels) and $P_{21}^{\Lambda\text{CDM}}$ (right panels) are consistent. The two mock data sets produce similar errors with different mean values, as one would expect. By comparing results from the P_{21}^{EFT} and $P_{21}^{\Lambda\text{CDM}}$ data sets, we assess if with the $P_{21}(k)$ likelihood an EFT universe would be distinguishable from a ΛCDM one. We recall that the ΛCDM limit for the considered EFT model is $\Omega_0^{\text{EFT}} = 0$, while β is allowed to assume any value. This gives rise to the clustering of the samples along $\Omega_0^{\text{EFT}} = 0$ in the $\Omega_0^{\text{EFT}} - \beta$ confidence regions, which, in turn, drives all the contours to be compatible. However, we expect that placing a stronger prior on β could remove this effect, as discussed in Section 6.2.2. We test this hypothesis by placing a narrow hard prior on β, i.e. $\beta \in [1.2, 1.4]$, and looking at the modifications in the Ω_0^{EFT} marginalized posterior. Results are shown in Figure 6.14. The significance of the deviation from the ΛCDM limit (gray dashed line), is 1.4σ for $P_{21}^{\Lambda\text{CDM}}$ (green line) while it is 3.8σ for P_{21}^{EFT} (cyan line), where we considered the tomographic data sets with halved errors. The error on Ω_0^{EFT} is now the same for both the data sets and the two posteriors are 2.4σ away from each other. For the single bin $P_{21}^{\text{EFT}}(z = 0.39)$ with no nuisance parameter (red dashed line), that we presented in Figure 6.9, the deviation from $\Omega_0^{\text{EFT}} = 0$ is even more significant, being 4.5σ. This implies that the constraints on the EFT models obtained using realistic $P_{21}(k)$ data could greatly benefit from knowing the amplitude of the brightness temperature a priori, even in comparison to a more optimistic (halved errors) tomographic data set. This, in turn, reasserts the utility of the future, tomographic $P_{21}(k)$ data in detecting beyond ΛCDM models.

6.3 CONCLUSIONS

In this work, we construct a new likelihood function to compute constraints from observations of the 21cm signal power spectrum, measured through intensity mapping techniques. We extend the public available codes EFTCAMB and EFTCosmoMC [254, 255, 334] by implementing a new likelihood module fully integrated with the original codes.

As described in sections Section 6.1.1 and Section 6.1.2, we model the power spectrum of the 21cm signal $P_{21}(z, k)$ as in [57, 153, 158]. Then, we build a realistic mock data set of forecasted $P_{21}(z, k)$ measures at redshift $z = 0.39$. We model such data set mimicking the MeerKAT [37, 58, 59] telescope observations, for which real data will be available in the near future.

We complement our mock $P_{21}(k)$ with an additional likelihood function to include external 21cm intensity mapping forecasts on background quantities. We use results in [339], where forecasts on $f\sigma_8$, H, and D_A are given for a hypothetical HIRAX measure in the redshift range $2.5 < z < 5$, as outlined in section Section 6.1.2.2. We refer to this likelihood as *background* likelihood. We further expand the $P_{21}(k)$ likelihood to include observations in multiple redshift bins.

We test the effect of the $P_{21}(k)$ likelihood first in a ΛCDM framework, then on several beyond ΛCDM models that we study within the EFT formalism. Exploiting the strength of EFTCAMB/EFTCosmoMC, we analyze *pure* EFT models on a ΛCDM and a wCDM background. We consider two different parametrizations of the $\Omega^{\text{EFT}}(a)$ function, i.e. a linear and an exponential evolution in time.

We conduct an MCMC statistical analysis to obtain marginalized confidence levels and regions on cosmological and EFT parameters. Constraints are com-

puted from both $P_{21}(k)$ data set alone and combined with Planck 2018 CMB observations [4]. We test also the effect of adding to $P_{21}(k)$ alone the *background* likelihood.

Our main goal is to forecast the state-of-the-art constraining power of the $P_{21}(k)$ observable on beyond ΛCDM theories. This is why we mainly focus on the results obtained with the realistic mock data set at redshift $z = 0.39$. However, we believe that the tomographic nature of 21cm signal intensity mapping could be pivotal to constrain DE. Thus, to verify this claim, we complete our analysis by testing the effects of tomography and constructing an ideal mock data set of observations at five different redshift bins.

As discussed in section Section 6.2, we find that:

- the mock data set $P_{21}(k)$ at $z = 0.39$ alone displays a mild constraining power on the cosmological parameters, which is remarkably improved when we add the *background* data set, by forecast intensity mapping observations at intermediate redshift;

- in a ΛCDM scenario adding $P_{21}(k)$ to Planck 2018 CMB data significantly improve the constraints on $\Omega_c h^2$ and H_0, at the level of 61% and 69% respectively, for fixed nuisance parameters;

- for *pure* EFT models we observe a mild reduction in the constraints when combining CMB data with $P_{21}(k)$, in the range of $1 - 18\%$;

- state-of-the-art forecast data for $P_{21}(k)$ alone are still not able to significantly constrain *pure* EFT models. Forecasts in other redshift bins are expected to improve on the constraining power of $P_{21}(k)$ on such models;

- for the *pure* linear EFT model on a ΛCDM background we find Ω_0^{EFT} constrained to be $\Omega_0^{\text{EFT}} < 0.031$ (95% CL) for Planck 2018 + $P_{21}(k)$ data. This constraint improves on previous results in literature [243, 255];

- for the *pure* exponential EFT model on a ΛCDM background for Planck 2018 + $P_{21}(k)$ we obtain $\Omega_0^{\text{EFT}} < 0.034$ (95% CL), $\beta = 0.97^{+0.53}_{-0.19}$ and $\alpha_M^0 < 0.044$ (95% CL). As above, we improve on previous results in [243];

- for the *pure* exponential EFT model on a ΛCDM background with a negative running of the Planck mass we obtain from Planck 2018 + $P_{21}(k)$ the constraints $\Omega_0^{\text{EFT}} = 0.075^{+0.063}_{-0.042}$, $\beta = 1.41^{+0.48}_{-0.15}$ and $\alpha_M^0 = 0.117^{+0.12}_{-0.052}$;

- adding one nuisance parameter to the $P_{21}(k)$ likelihood, e.g. the amplitude of the brightness temperature a_{T_b}, reduces the constraining power compared with the case with no nuisances. Deviations with respect to Planck 2018 results for $\Omega_c h^2$ and H_0 are at the level of $\sim 15\%$, to be compared with the $\sim 65\%$ found with no nuisances;

- repeating the analysis on a wCDM background and with a nuisance parameter produces comparable results. The major effect is obtained on w_0, H_0, and σ_8 when $P_{21}(k)$ data are combined with Planck. We obtain an improvement on the errors of these parameters at the level of $40 - 50\%$. For the EFT models, we find that the $P_{21}(k)$ likelihood has mild constraining power on the EFT parameters when used both alone and combined with CMB data;

- tomography significantly improves the constraining power of the $P_{21}(k)$ likelihood on *pure* EFT models. With five bins combined in the redshift range from $z = 0$ to $z = 2.5$, we are able to constrain EFT parameters for a *pure* exponential EFT model with negative running of the Planck mass by means of the $P_{21}(k)$ likelihood alone;

- for the same model, when we combine the tomographic data sets with Planck 2018 CMB data, we find an improvement in the constraints on Ω_0^{EFT} and β with respect to Planck results at the level of the $\sim 25\%$ and $\sim 10\%$, respectively. In the ideal case of halved errors, these values both go up to the $\sim 35\%$, to be compared with the less than 10% found with only one redshift bin.

Overall, in our study, we find that, at the current state of observations, the 21cm signal power spectrum, measured at one redshift, shows a mild constraining power on the EFT functions that we tested. We expect, and we verified, that $P_{21}(k)$ is sensitive to EFT parameters. Nevertheless, the one realistic mock data set at redshift $z = 0.39$ is still too retained to be able to constrain EFT theories alone. When combined with CMB data, constraints provided by CMB on EFT parameters are too stringent and current $P_{21}(k)$ mock data do not have a substantial impact. On cosmological parameters, instead, the $P_{21}(k)$ likelihood proves to be effective in reducing the correlation between $\Omega_c h^2$ and H_0 when combined with CMB, thus significantly improving the constraints on cosmological parameters.

We find that the constraining power of $P_{21}(k)$ on the considered EFT functions is significantly improved by tomography. With five redshift bins, we are able to constrain the EFT functions, with $P_{21}(k)$ alone, and to improve Planck results, with $P_{21}(k)$ and CMB together. For tomographic observations of the 21cm signal, such as those that are modeled here, real observations will hopefully be available in the future. However, our test, although preliminary, seems to confirm that tomographic 21cm signal detections will help to expand our knowledge of DE.

In this work, we test simple EFT scenarios and validate the new $P_{21}(k)$ likelihood code. This analysis could be the starting point to study the constraining power of 21cm signal observations on more complex MG-DE models.

7

TESTING GRAVITY BY CROSS-CORRELATING SKAO OBERVATIONS WITH GRAVITATIONAL WAVES

I N A GENERAL RELATIVISTIC framework, gravitational waves (GW or GWs) and electromagnetic (EM) waves are expected to propagate in the same way to the effects of matter perturbations between the emitter and the observer. A different behavior might be a signature of alternative theories of gravity. In this work, we study the cross-correlation of resolved GW events and EM signals, considering weak lensing, angular clustering, and their cross-correlation as observable probes. We perform a Fisher matrix analysis to forecast the constraining power of future observations of the SKAO, for radio galaxy clustering and intensity mapping, and the Einstein telescope (ET), for GWs, on MG phenomenological functions $\{\mu_0, \eta_0, \Sigma_0\}$, either opening to or keeping fixed the background parameters $\{w_0, w_a\}$.

We find that, although lensing-only forecasts provide significantly unconstrained results, the combination with angular clustering and the combination of all three considered tracers, i.e. GW, 21cm IM, and resolved galaxies, leads to interesting and competitive constraints. This offers a novel and alternative path to multi-tracing opportunities for cosmology and the MG sector.

This chapter is structured as follows: in Section 7.1 we describe our methodology, presenting the treated probes (weak lensing, angular clustering, and their cross-term) in Section 7.1.1 and the adopted Fisher analysis formalism in Section 7.1.2; in Section 7.2 we introduce and characterize the considered tracers (GWs, IM and resolved galaxies); in Section 7.3 we introduce the tested MG parametrization; in Section 7.4 we present our forecasts on the relevant MG parameters and in Section 7.5 we draw our conclusions.

7.1 METHODOLOGY

In this section, we describe the observables considered and the adopted methodology. In Section 7.1.1 we characterize our observables: the angular power spectra for weak lensing, angular clustering, and their cross term. In Section 7.1.2 we describe the Fisher formalism on which we rely.

7.1.1 *Observables: angular power spectra*

The observables we consider are the angular power spectra C_ℓs for two different probes: weak lensing (denoted as L) and angular clustering (denoted as C), with the addition of the cross-term (L × C). Given two tracers {X,Y} (e.g. GW events, galaxies, IM) associated with two different redshift bins $\{z_i, z_j\}$, we define the power spectra of their cross-correlation as $C_{\Gamma\Theta}^{X_i, Y_j}(\ell)$, with Γ, Θ indicating the considered probe (e.g. L or C). We make use of the flat-sky and Limber approximations, which are accurate at 10% for $\ell = 4$, 1% for $\ell = 14$, and less

than 0.1% for $\ell > 45$ [346]. In the following, we characterize the power spectra for the considered probes.

- **Weak lensing (L)**. The characterization and physical meaning of this observable depends on the tracer that we take into account. For what concerns resolved galaxies, it describes the physical effect of distortion of their shape due to the inhomogeneous distribution of matter between the objects and the observer. It is often referred to as *cosmic shear* (see e.g. [347, 348]). It is given by the sum of three different terms: the proper cosmological signal ($\gamma\gamma$ term) and the two intrinsic alignment (IA) terms (γI and II terms). The latters consider that observed galaxies are usually already characterized by an intrinsic ellipticity, which should be taken into account when estimating the shear due to weak lensing only. The three terms can be written as (see e.g. [349]):

$$C_{\gamma\gamma}^{X_i Y_j}(\ell) = \int_0^\infty \frac{dz\, c}{H(z)} \frac{W_\gamma^{X_i}(z)\, W_\gamma^{Y_j}(z)}{\chi^2(z)}\, P_{\mathrm{mm}}\left(\frac{\ell}{\chi(z)}, z\right) \tag{7.1}$$

$$C_{\gamma I}^{X_i Y_j}(\ell) = \int_0^\infty \frac{dz\, c}{H(z)} \frac{W_\gamma^{X_i}(z)\, W_{\mathrm{IA}}^{Y_j}(z) + W_{\mathrm{IA}}^{X_i}(z)\, W_\gamma^{Y_j}(z)}{\chi^2(z)} \times$$
$$\times\, \mathcal{F}_{\mathrm{IA}}(z)\, P_{\mathrm{mm}}\left(\frac{\ell}{\chi(z)}, z\right) \tag{7.2}$$

$$C_{\mathrm{II}}^{X_i Y_j}(\ell) = \int_0^\infty \frac{dz\, c}{H(z)} \frac{W_{\mathrm{IA}}^{X_i}(z)\, W_{\mathrm{IA}}^{Y_j}(z)}{\chi^2(z)}\, \mathcal{F}_{\mathrm{IA}}^2(z) P_{\mathrm{mm}}\left(\frac{\ell}{\chi(z)}, z\right) \tag{7.3}$$

where c is the speed of light, $H(z)$ is the Hubble parameter, $\chi(z)$ is the comoving distance, P_m is the matter power spectrum, and the window functions are given by:

$$W_\gamma^{X_i}(z) = \frac{3}{2}\Omega_\mathrm{m} \frac{H_0^2}{c^2} \chi(z)(1+z) \int_z^\infty dx\, n_{X_i}(x) \frac{\chi(x) - \chi(z)}{\chi(x)} \tag{7.4}$$

$$W_{\mathrm{IA}}^{X_i}(z) = n_{X_i}(z) \frac{H(z)}{c}, \tag{7.5}$$

where n_{X_i} is the redshift distribution of the considered tracer and the intrinsic alignment kernel $\mathcal{F}_{\mathrm{IA}}$ is modeled through the extended non-linear alignment model:

$$\mathcal{F}_{\mathrm{IA}}(z) = -\frac{A_{\mathrm{IA}} \mathcal{C}_1 \Omega_\mathrm{m}}{D_1(z)}(1+z)^{\eta_{\mathrm{IA}}} \left(\frac{\langle L \rangle(z)}{L_*(z)}\right)^{\beta_{\mathrm{IA}}}, \tag{7.6}$$

with $\mathcal{C}_1 = 0.0134$, $D_1(z)$ is the linear growth factor and the intrinsic alignment parameters have fiducial values $\{A_{\mathrm{IA}}, \eta_{\mathrm{IA}}, \beta_{\mathrm{IA}}\} = \{1.72, -0.41, 2.17\}$. Finally, $\frac{\langle L \rangle(z)}{L_*(z)}$ is the mean luminosity of the sample in units of the typical luminosity at a given redshift. Here, we use the same specification used for Euclid [34], both for ease of comparison with similar studies and also under the assumption that the galaxies observed by SKAO will display a similar redshift evolution of their luminosity. However, we note that this assumption must be explicitly checked, by performing an analysis on actual observations, as in reference [350].

Equations Equation 7.1 - Equation 7.3 can be summed up to give the lensing power spectrum

$$C_{LL}^{X_i Y_j}(\ell) = \int_0^\infty \frac{dz\, c}{H(z)} \frac{W_L^{X_i}(z)\, W_L^{Y_j}(z)}{\chi^2(z)} P_{mm}\left(\frac{\ell}{\chi(z)}, z\right), \qquad (7.7)$$

where

$$W_L^{X_i}(z) = W_\gamma^{X_i}(z) + \mathcal{F}_{IA}(z)\, W_{IA}^{X_i}(k, z). \qquad (7.8)$$

In the case of GW events we do not have an intrinsic shape that undergoes cosmic shear, so the intrinsic alignment term is not present. Indeed, in this case, the propagation of the gravitational wave in the presence of a matter distribution leads to magnification in the strain signal $h(f)$:

$$h(f) = \mathcal{Q}(\alpha)\sqrt{\frac{5}{24}} \frac{G^{5/6}\mathcal{M}^2 (f\mathcal{M})^{-7/6}}{c^{3/2}\pi^{2/3}d_L} e^{i\phi}, \qquad (7.9)$$

where f is the frequency, $\mathcal{Q}(\alpha)$ is a function of the angles describing the position and orientation of the binary, $\mathcal{M}$ is the chirp mass of the binary system, d_L is the luminosity distance of the source and G is the gravitational constant. What one can measure is an alteration in the measured GW strain $\tilde{h}(\hat{r}, f) = h(f)[1 + \kappa(\hat{r})]$, where $\hat{r}$ describes the position of the source and $\kappa(\hat{r})$ is the lensing convergence, related to the angular power spectra as $C_{LL}(\ell) = \langle \kappa_{\ell m} \kappa_{\ell' m'} \rangle \delta_{\ell\ell'} \delta_{mm'}$. We refer the interested reader to e.g. references [81, 106, 109, 351–356] for further details.

Finally, although IM (by definition) is a probe that does not provide resolved galaxies, we can still describe the effects of weak lensing as a magnification received by the observer (see e.g. references [357, 358] for additional details). As one would expect, also in this case the IA term is not present ($\mathcal{F}_{IA}^{IM}(z) = 0$).

- **Angular clustering (C).** Our tracers can also be used to estimate the clustering as a function of the separation angle (or equivalently the multipoles):

$$C_{CC}^{X_i Y_j}(\ell) = \int_0^\infty \frac{dz\, c}{H(z)} \frac{W_C^{X_i}\left(\frac{\ell}{\chi(z)}, z\right) W_C^{Y_j}\left(\frac{\ell}{\chi(z)}, z\right)}{\chi^2(z)} P_{mm}\left(\frac{\ell}{\chi(z)}, z\right),$$
$$(7.10)$$

where the window function for clustering is given by

$$W_C^{X_i}(k, z) = b_X(k, z)\, n_{X_i}(z) \frac{H(z)}{c} \qquad (7.11)$$

and $b_X(k, z)$ is the bias parameter for tracer X, describing the relation between the tracer and the underlying matter distribution (see e.g. [317, 359–365]). We apply this formalism to all tracers considered in this work.

• **Lensing × Clustering (L × C)**. Finally, the cross-correlation L × C between weak lensing and angular clustering of two tracers can be expressed as

$$C_{CL}^{X_i Y_j}(\ell) = \int_0^\infty \frac{dz\, c}{H(z)} \frac{W_C^{X_i}\left(\frac{\ell}{\chi(z)}, z\right) W_L^{Y_j}(z)}{\chi^2(z)} P_{mm}\left(\frac{\ell}{\chi(z)}, z\right). \quad (7.12)$$

Essentially, it is given by the combination of a Lensing window function with a Clustering one.

7.1.2 *Fisher analysis*

In this work, we make use of the Fisher matrix analysis, which we briefly sketch in this section. Assuming again two tracers {X,Y} (e.g. GW events, galaxies, IM), we divide the total redshift interval surveyed in N_{bins}^X bins, with amplitude Δz^X for tracer X, and in N_{bins}^Y redshift bins with amplitude Δz^Y for tracer Y.

Considering the observed power spectra $\tilde{C}_\ell$s for a specific probe (L only, C only or L × C, which we do not make explicit throughout this section) and a generic set of parameters $\{\theta_n\}$ for the Fisher analysis, we can organize our data in the (symmetric) matrix $\mathcal{C}_\ell$ as

$$\mathcal{C}_\ell = \begin{bmatrix} \tilde{C}_\ell^{XX}(z_1^X, z_1^X) & \dots & \tilde{C}_\ell^{XX}(z_1^X, z_N^X) & \tilde{C}_\ell^{XY}(z_1^X, z_1^Y) & \dots & \tilde{C}_\ell^{XY}(z_1^X, z_N^Y) \\ & \dots & \tilde{C}_\ell^{XX}(z_2^X, z_N^X) & \tilde{C}_\ell^{XY}(z_2^X, z_1^Y) & \dots & \tilde{C}_\ell^{XY}(z_2^X, z_N^Y) \\ & \dots & \vdots & \vdots & \dots & \vdots \\ & & \tilde{C}_\ell^{XX}(z_N^X, z_N^X) & \tilde{C}_\ell^{XY}(z_N^X, z_1^Y) & \dots & \tilde{C}_\ell^{XY}(z_N^X, z_N^Y) \\ & & & \tilde{C}_\ell^{YY}(z_1^Y, z_1^Y) & \dots & \tilde{C}_\ell^{YY}(z_1^Y, z_N^Y) \\ & & & & \vdots \\ & & & & \dots \\ & & & & & \tilde{C}_\ell^{YY}(z_N^Y, z_N^Y) \end{bmatrix}, \quad (7.13)$$

The matrix $\mathcal{C}_\ell$ has dimensions of $(N_{bins}^X + N_{bins}^Y) \times (N_{bins}^X + N_{bins}^Y)$. Note that in general $z_i^X \neq z_i^Y$, since the two tracers may be distributed among different bins. We stress again that the tilde symbol stands for *observed* C_ℓs. It is trivial to expand the above matrix to the case in which a third tracer Z is considered at the same time. In this case, the matrix would be accordingly expanded with all XZ, YZ, and ZZ correlations and would have dimensions of $(N_{bins}^X + N_{bins}^Y + N_{bins}^Z) \times (N_{bins}^X + N_{bins}^Y + N_{bins}^Z)$. The three tracers case is also explored in this work (see sections Section 7.2 and Section 7.4). Equation 7.13 refers to the case in which just one probe is taken into account (L only, C only, or L × C). When all three probes are considered simultaneously for a forecast, the global $\mathcal{C}_\ell$ matrix will be made of 4 different sub-matrices like the one in Equation 7.13: one for L only, one for C only, and two for L × C. We provide in Figure 7.1 a sketch of the global $\mathcal{C}_\ell$ matrix in the case of all probes and three tracers (GW, IM, gal as described in Section 7.2). Its dimensions are $2(N_{bins}^{IM} + N_{bins}^{GW} + N_{bins}^{gal}) \times 2(N_{bins}^{IM} + N_{bins}^{GW} + N_{bins}^{gal})$.

The $\mathcal{C}_\ell$ matrix is then used to compute the Fisher matrix elements as

$$F_{\alpha\beta} = f_{sky} \sum_\ell \frac{2\ell+1}{2} \text{Tr}\left[\mathcal{C}_\ell^{-1}(\partial_\alpha \mathcal{C}_\ell)\mathcal{C}_\ell^{-1}(\partial_\beta \mathcal{C}_\ell)\right], \quad (7.14)$$
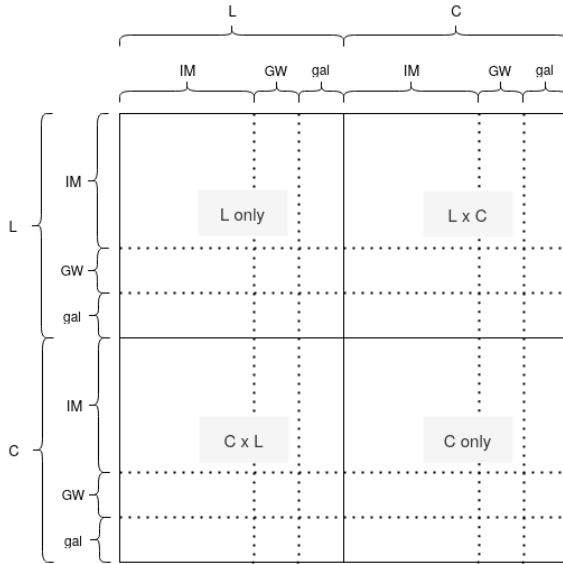
Figure 7.1: Sketch for the $\mathcal{C}_\ell$ matrix in the case of all probes (L only, C only, and L × C) and three tracers (GW, IM, gal) considered simultaneously.

where ∂_α indicates the partial derivative with respect to the parameter θ_α and f_{sky} is the fraction of the sky covered by the intersection of the considered surveys. The Fisher-estimated marginal error on the parameter θ_α is given by $\sqrt{(F^{-1})_{\alpha\alpha}}$. According to the Cramér-Rao bound, the quantity $\sqrt{(F^{-1})_{\alpha\alpha}}$ provides the smallest expectable error for a "real-life" experiment, setting a lower bound to its estimate (and having the equality only in the case of gaussian likelihood and errors). Fisher's approach may not always be the most accurate method to adopt since instrumental/observational systematic errors and/or the parameter posterior may not be Gaussian distributed. Still, it remains a simple and fast method to yield forecasts for designed experiments, providing reasonable results, especially for a first estimate. The novelty of this work allows us to adopt a Fisher formalism while considering its estimates informative enough to bring meaningful and reliable conclusions, although different techniques (such as MCMC, see Section 4.2.3) may be suggested for further investigation. We refer the interested reader to references [366, 367] for further discussion about Fisher analysis and the impact of several approximations therein and in the observables considered.

7.2 TRACERS

In this section, we characterize the considered tracers. In Table 7.1 we summarize their redshift-dependent specifics, such as binning, redshift range, and os on.

Tracer	GW^{bright} (ET)	GW^{dark} (ET) & gal (SKAO)	IM (SKAO)
z range	[0.5-2.5]	[0.5-3.5]	[0.5-3.5]
N$_{bins}$	8	3	30
Δz	0.25	1.0	0.1

Table 7.1: Specifics for the considered tracers: redshift range, number of redshift bins N_{bins} and bin width Δz.

7.2.1 *Gravitational Waves*

We consider GW events from compact objects resolved mergers (BHBH, BHNS, and NSNS) detected by the Einstein telescope (ET) experiment, as planned in [26]. We treat two categories of GW events, depending on whether they can be associated with an EM counterpart:

- **Dark sirens**: they are not accompanied by an EM follow-up. We treat BHBH and BHNS mergers as dark sirens and consider $N_{bins}^{GW^{dark}} = 3$ redshift bins with width $\Delta z^{GW^{dark}} = 1.0$ in the redshift range $[0.5 - 3.5]$. We choose large redshift bins to take into account the poor redshift localization of these kinds of sources. Given the lack of an EM counterpart, their angular resolution is limited by the capabilities of the considered GW instrument, which we set to $\ell_{max} = 100$ [26].

- **Bright sirens**: the GW emission is associated with an EM counterpart. This helps not only in improving the angular localization of the emitting source but provides also extra information in the MG context, due to the fact that GWs and EM waves might behave differently depending on the MG model under consideration (see Section 7.3 for further details). We treat NSNS mergers as bright sirens and consider $N_{bins}^{GW^{bright}} = 8$ redshift bins with width $\Delta z^{GW^{bright}} = 0.25$ in the redshift range $[0.5 - 2.5]$. This is motivated by the z-uncertainty behavior for NSNS binaries $\delta z/z \approx 0.1\, z$ [368], making our choice quite conservative at lower redshifts. Since the detection of an EM follow-up can help in significantly improving the angular localization of the sources, it allows us to push our analysis to a higher ℓ_{max}. We set $\ell_{max} = 300$ for bright sirens, which appears to be a conservative estimate for these types of experiments (see e.g. [81, 109, 369]), furthermore allowing us to avoid non-linearities in the power spectra modeling. We comment on the impact of the choice of ℓ_{max} in Section 7.4.

Prescriptions to describe the redshift evolution of the GW tracers and their bias parameter are taken from references [101, 370] and provided in Figure 7.2. These specifics predict a detection of $\sim 2.2 \cdot 10^4$ BHBH+BHNS mergers and $\sim 1.4 \cdot 10^4$ NSNS mergers in the corresponding redshift intervals (for $T_{obs}^{GW} = 1$yr and $f_{sky} = 0.5$). The GW events bias is evaluated through an abundance matching technique (see e.g. [371]), linking the luminosity/SFR of each host galaxy to the mass of the hosting dark matter halo, eventually matching the bias of the associated halo to a galaxy with given SFR. Lastly, characterizing COs mergers with the same bias of their host galaxies, the final bias expression is estimated
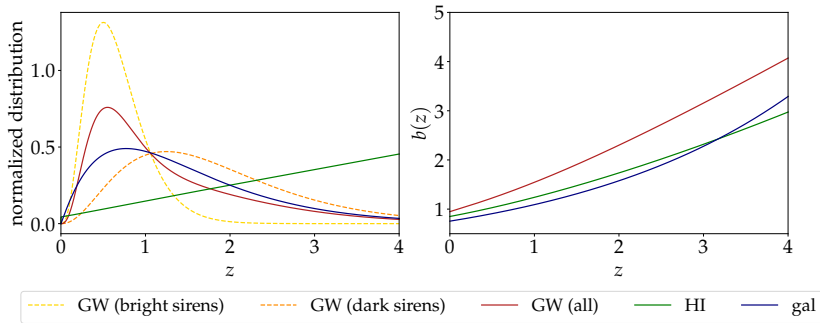
Figure 7.2: Specifics for the considered tracers: HI (green), resolved SKAO galaxies (blue), detected GW events from ET for dark sirens (orange), bright sirens (yellow), and both combined (dark red). Left panel: normalized redshift distributions (number counts for GWs and resolved galaxies, mean brightness temperature $T_b(z)$ for HI). Right panel: biases.

by taking into account which galaxy types give the biggest contribution to the observed merger rate proportionally. For further details on the GW bias estimate procedure, we refer the interested reader to [101, 370] and references therein.

Given a theoretical predicted value for the C_ℓs under study (computed with COLIBRI[1], which we modified to extend it to the multi-tracing case), the observed power spectra $\tilde{C}_\ell$s are characterized by the presence of extra noise terms: $\tilde{C}_\ell^{\mathrm{GW,X}}(z_i, z_j) = C_\ell^{\mathrm{GW,X}}(z_i, z_j) + C_\ell^{\mathrm{N,GW}}(z_i)$. In the case of GWs-related power spectra, following e.g. [109], we assume that:

$$C_\ell^{\mathrm{N,GW}}(z_i) = \frac{1}{n_{\mathrm{GW}}} e_{d_L}^2 \, \exp{\frac{\ell^2 \theta_{\min}^2}{8 \ln 2}}, \qquad (7.15)$$

where n_{GW} is the number density of sources in the considered redshift bin z_i, $\theta_{\min}$ is the sky localization area of the gravitational wave sources, and $e_{d_L} \sim 3/\mathrm{SNR}$ is the relative error on the luminosity distance estimation (see e.g. [105, 372]), where the average value of the Signal-to-Noise ratio (SNR) estimate for detected GWs events is derived by results from reference [101] and takes the values of SNR =8.4 (15.4) for bright (dark) sirens. We assume that this shot-noise/beam noise term affects all the probes considered in this work (i.e. L, C, L×C).

7.2.2 *Neutral hydrogen intensity mapping*

We consider the forecasted HI distribution given by the SKA-Mid intensity mapping survey [57, 373, 374] in the redshift range $[0.5 - 3.5]$, divided in bins of width $\Delta z^{\mathrm{IM}} = 0.1$, for a total of $N_{\mathrm{bins}}^{\mathrm{IM}} = 30$ redshift bins. This is expected to be around the optimal redshift range for the SKA-Mid survey [57]. The HI mean brightness temperature redshift evolution and the bias are taken from references [51, 307] and provided in Figure 7.2. The HI bias prescription derives from the outputs of a semi-analytical model for galaxy formation explicitly

---

[1]See https://github.com/GabrieleParimbelli/COLIBRI.

incorporating a treatment of neutral hydrogen and is in agreement with results of [158] based on Illustris TNG hydro-dynamical simulations.

Noise sources for IM are the result of contributions from different elements, described as follows:

- **Beam effects**: the relation between theoretical C_ℓ^{XY} and the observed $\tilde{C}_\ell^{XY}$ is:

$$\tilde{C}_\ell^{\mathrm{IM,IM}}(z_i, z_j) = \mathcal{B}(z_i)\mathcal{B}(z_j)C_\ell^{\mathrm{IM,IM}}(z_i, z_j) + C_\ell^{\mathrm{N,IM}} \tag{7.16}$$

and

$$\tilde{C}_\ell^{\mathrm{IM,X}}(z_i, z_j) = \mathcal{B}(z_i)C_\ell^{\mathrm{IM,X}}(z_i, z_j) \tag{7.17}$$

where the $\mathcal{B}^X(z_i)$ describes the suppression of the signal at scales smaller than the FWHM of the beam θ_B. In single-dish configuration $\theta_B \sim 1.22\lambda/D_d$, implying a stronger suppression of the signal at lower frequencies:

$$\mathcal{B}(z_i) = \exp[-\ell(\ell+1)(\theta_B(z_i)/\sqrt{16\ln 2})^2]. \tag{7.18}$$

The beam term affects all probes considered (L, C, L×C).

- **Foreground noise**: IM data analysis has to deal with the delicate cleaning procedure of the signal from the bright foreground emission (see e.g. references [44, 64, 65, 67, 335, 375, 376]). Although modeling the foregrounds is beyond the scope of this work, we need to take into account the residual error that could be expected after a foreground removal procedure. Following reference [108], we model the foreground-cleaning-related noise term as

$$C_\ell^{\mathrm{fg}} = K^{\mathrm{fg}} \cdot F(\ell), \tag{7.19}$$

where K^{fg} is an overall normalization constant determining the overall amplitude of the residual foregrounds-related errors and is given by an average value of all the $C_\ell^{\mathrm{IM,IM}}(z_i, z_j)$ components:

$$K^{\mathrm{fg}} = \left\langle C_\ell^{\mathrm{IM,IM}}(z_i, z_j) \right\rangle. \tag{7.20}$$

The function $F(\ell)$ encodes the scale-dependence, described by

$$F(\ell) = \frac{1}{f_{\mathrm{sky}}} A e^{b\ell^c}, \tag{7.21}$$

with a stronger error at larger scales. With the chosen numerical values ($A \sim 0.129$, $b \sim -0.081$, $c \sim 0.581$) the error is around 12% at $\ell \sim 2$ and 4% at $\ell \sim 100$ (for $f_{\mathrm{sky}} = 1.0$). This term affects all probes (L, C, L×C), but only IM × IM terms (for all redshift bins combinations).

- **Instrumental noise**: the noise angular power spectrum for the experiment setup under study (single dish mode [57, 58] with an ensemble of N_d dishes) writes as (see e.g. [58, 157, 377]):

$$C_\ell^{\mathrm{instr}}(z_i) = \sigma_T^2 \theta_B^2 \approx \left(\frac{T_{\mathrm{sys}}}{T_b(z_i)\sqrt{n_{\mathrm{pol}}Bt_{\mathrm{obs}}N_d}} \sqrt{\frac{S_{\mathrm{area}}}{\theta_B^2}} \frac{1}{T_b(z_i)} \right)^2 \theta_B^2, \tag{7.22}$$

where the single-dish root mean square noise temperature σ_T is given by

$$\sigma_T \approx \frac{T_{\text{sys}}}{\sqrt{n_{\text{pol}} B t_{\text{obs}}}} \frac{\lambda^2}{\theta_B^2 A_e} \sqrt{S_{\text{area}}/\theta_B^2} \sqrt{\frac{1}{N_d}} \tag{7.23}$$

and the other parameters involved are (according to SKA-Mid prescriptions): $T_{\text{sys}} = 28$ K for the system temperature, $B = 20 \cdot 10^6$ Hz for the bandwidth, $t_0 = 5000\, h = 1.8 \cdot 10^7$ s for the observation time, $N_d = 254$ for the total number of dishes, $S_{\text{area}} = 20000 deg^2$ for the total surveyed area, $A_e = 140$ m^2, $D_d = 15$ m and $S_{\text{area}} = 20000$ deg$^2 \sim f_{\text{sky}} = 0.5$ for the reference sky coverage [377]. $T_b(z_i)$ is the mean brightness temperature at the center of the redshift bin and it acts as a normalization factor to retrieve a dimensionless C_ℓ. This noise component affects all the probes considered in this work (L, C, L×C) but it is de-correlated among different bins, affecting only IM auto-correlations.

- **Lensing reconstruction error**: references such as [357, 358] model an extra scale independent noise contribution, due to inaccuracies in the reconstruction of the signal. Since it should affect scales smaller than our $\ell = \mathcal{O}(100)$ cut-off, we opt for not taking it into account. For the sake of completeness, we checked that artificially introducing a noise term overcoming the observed signal at around $2/3$ of the explored angular range, would worsen our forecasts by $\sim 15 - 20\%$ or less. Still, let us stress again that the actual scales at which this noise is supposed to dominate start from around $\ell \sim \mathcal{O}(100)$, safely allowing us to neglect this term.

7.2.3 Galaxies

We consider SKAO radio-galaxies distributed following the T-RECS catalog [378] for SKAO (radio continuum survey with $z < 5$). We consider $N^g_{\text{bins}} = 3$ redshift bins with width $\Delta z^g = 1.0$ in the redshift range $[0.5 - 3.5]$. Their redshift distribution and bias are provided in Figure 7.2 (see e.g. reference [100] for further details). The galaxy bias formulation relies on outputs from the S^3 simulation [379]. We model noise sources for SKAO radio galaxies as follows:

- **Shot noise**: the shot noise term affects only the Clustering probe and reads as

$$C_\ell^{N,g} = C_\ell^{\text{shot},g} = \frac{1}{n_g}, \tag{7.24}$$

where n_g is the source number density in the considered redshift bin. This term affects only $g(z_i) \times g(z_i)$ terms (same tracer and same z bin).

- **Shape noise**: this term affects only the Lensing probe and it encodes the intrinsic ellipticity of observed galaxies, which may bias results if not taken into account. It reads as

$$C_\ell^{N,g} = C_\ell^{\text{shape},g} = \frac{\gamma^2}{n_g} \tag{7.25}$$

where $\gamma = 0.3$ is the intrinsic shear term [380]. This term affects only $g(z_i) \times g(z_i)$ terms (same tracer and same z bin).

Parameter	$\ln 10^{10} A_s$	n_s	w_0	w_a	E_{11}	E_{22}
Fiducial value	3.098	0.9619	-1.00	0.00	0.18	0.80

Table 7.2: Assumed fiducial cosmology [4]. MG parameters are from Planck 2018 TT, TE, EE + lowE. Fiducial values for the E_{ii} parameters lead to fiducial values on $\{\mu_0, \eta_0, \Sigma_0\} = \{1.12, 1.55, 1.43\}$.

• **Shot × shape noise**: being the $L \times C$ probe term made of the contribution of both Lensing and Clustering, we model its noise contribution as a mixture of the shot and shape noises affecting Clustering and Lensing respectively. It reads as

$$C_\ell^{N,g} = \sqrt{(C_\ell^{shot,g})^2 + (C_\ell^{shape,g})^2} = \frac{\sqrt{1 + \gamma^2}}{n_g}. \tag{7.26}$$

7.3 TESTED MODELS

Future GWs observations are expected to contribute significantly to probing gravity [381]. Forecasts on the cross-correlation of the GWs signal with other probes suggest that the multi-messenger approach could be a powerful tool to exploit GWs observations to constrain models beyond ΛCDM [81, 109, 369]. The GWs luminosity distance, for bright events, could provide a new probe to test gravity. In this work, we discuss if future GWs observations combined with LSS probes could add new information on MG theories. We parametrize the effects of MG in a phenomenological way by adopting a general prescription suited to probe small departures from GR. In this section, we give a brief overview of the formalism we adopt and the models we investigate.

7.3.1 *Phenomenological parametrizations*

As discussed in Chapter 3, starting from the LSS sector, we focus on scalar perturbations to the metric in the conformal Newtonian gauges, with the line element given by

$$ds^2 = a^2 \left[-(1 + 2\Psi)d\tau^2 + (1 - 2\Phi)dx^2 \right], \tag{7.27}$$

where a is the scale factor, τ is the conformal time, and the time and scale-dependent functions Ψ and Φ describe the scalar perturbations of the metric: the Newtonian potential and spatial curvature inhomogeneities, respectively. Modifications of gravity impact the growth of structure and the evolution of the gravitational potentials, see e.g. [382, 383]. Interestingly, these effects, on linear scales, can be fully captured by two functions of time and scale (see e.g. [15–19] and Section 3.2.1)

$$k^2 \Psi \equiv -4\pi G a^2 \mu(k, z) \rho \Delta, \tag{7.28}$$

and

$$\Phi / \Psi \equiv \eta(k, z), \tag{7.29}$$
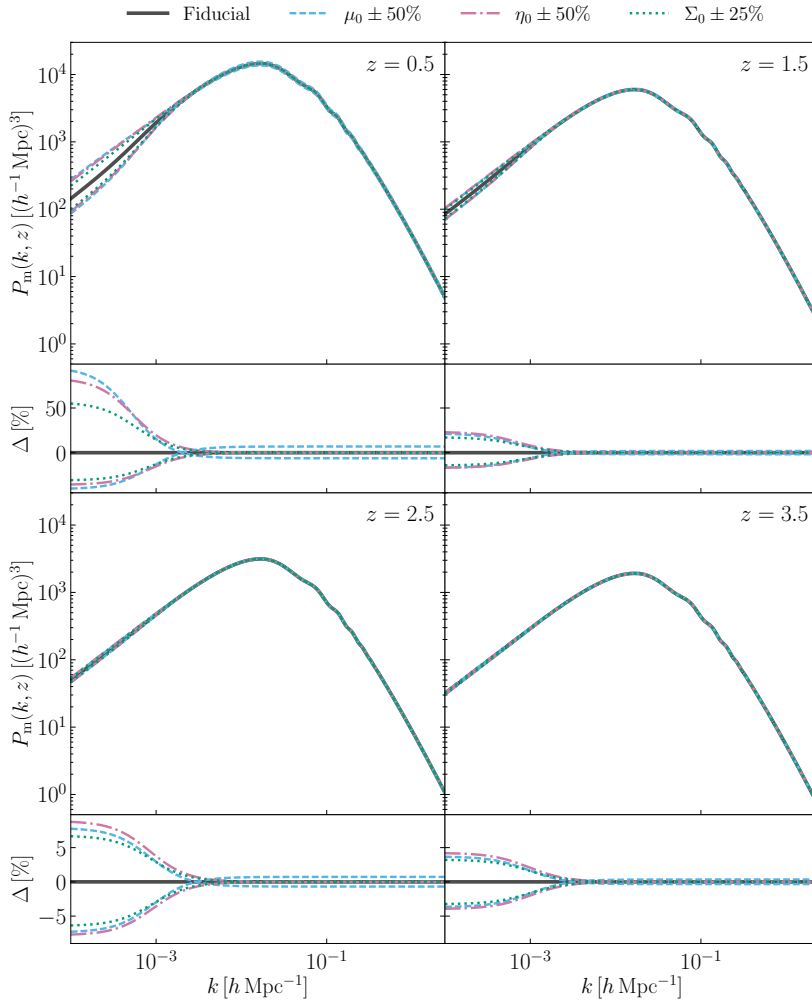
Figure 7.3: *Upper panels*: predicted matter power spectrum for different values of the MG parameters at redshifts $z = \{0.5, 1.5, 2.5, 3.5\}$. We show $P_{\mathrm{m}}(k, z)$ for the assumed fiducial cosmology (solid black lines, see table Table 7.2) and for variations of μ_0 (dashed light blue lines), η_0 (dashed-dotted pink lines) and Σ_0 (dotted green lines). When varying Σ_0, we keep μ_0 fixed. *Lower panels*: percentage variations with respect to the fiducial cosmology.

where $\rho\Delta = \rho_{\rm m}\Delta_{\rm m} + \rho_{\rm r}\Delta_{\rm r}$, i.e. the sum of the matter (m) and radiation (r) contributions. One can also define the function $\Sigma(k,z)$, that quantifies modifications to the lensing potential, as

$$k^2(\Phi + \Psi) \equiv -8\pi G a^2 \Sigma(k,z)\rho\Delta. \tag{7.30}$$

The three phenomenological functions $\mu(k,z)$, $\eta(k,z)$ and $\Sigma(k,z)$ are not independent. One should consider two of them at the time, e.g. the pair (μ, η) or (μ, Σ). It is possible to express $\Sigma(k,z)$ as a function of $\mu(k,z)$ and $\eta(k,z)$ as

$$\Sigma(k,z) = \frac{\mu(k,z)}{2}(1 + \eta(k,z)). \tag{7.31}$$

Deviations from ΛCDM are encoded in $(\mu(k,z), \eta(k,z))$ or $(\mu(k,z), \Sigma(k,z))$, with the ΛCDM case corresponding to $\mu(k,z) = 1$, $\eta(k,z) = 1$, $\Sigma(k,z) = 1$. To give a more intuitive interpretation of the physical meaning of the involved quantities, let us specify that the Σ function acts on relativistic particles, affecting mainly the lensing observable, whereas μ controls gravity effects on massive particles, controlling the growth of matter perturbations and affecting clustering. Finally, η, usually referred to as the gravitational slip parameter, cannot be directly connected to a constraining observable as the previous two functions. However, given that it quantifies differences between the two gravitational potentials, its behavior may be indicative of a breaking of the equivalence principle.

Several parametrizations of the phenomenological functions have been explored and constrained, see e.g. [13] for a review on recent results. In this work, we follow the approach of the Planck 2015 paper on dark energy and modified gravity [243]. We choose a time-dependent only parametrization for the evolution of $\mu(k,z)$ and $\eta(k,z)$, the so-called late-time parametrization

$$\begin{aligned} \mu(z) &= 1 + E_{11}\Omega_{\rm DE}(z) \\ \eta(z) &= 1 + E_{22}\Omega_{\rm DE}(z). \end{aligned} \tag{7.32}$$

The evolution is set by the value of the parameters E_{11} and E_{22}, while the background is kept fixed. This choice of parametrization simplifies the analysis and allows a direct comparison with the results of [243]. But there are also good reasons for not expecting any scale dependence of the model to show up within the range of scales covered by the data that we consider. In fact, in order to satisfy local tests of gravity, these theories need to have a working screening mechanism, which suppresses any deviation from GR through environmental effects. Well-known examples are the Chameleon and Vainshtein mechanism, see e.g. [384]. In both cases, the requirements for a successful screening effectively push the characteristic length scale of the model either into the small, non-linear scales (Chameleon case) or to very large, horizon-size scales (Vainshtein case). Let us point out that even while not working with a specific model, there are some assumptions that we make beyond the basis of our choice of parametrization. One such assumption is that modifications of gravity are relevant at late times; in this sense, we are linking them possibly to the source of cosmic acceleration, but more broadly to tests of gravity with large-scale structures. Or, said in other words, we aim for this parametrization to broadly represent Horndeski's models of gravity with a luminal speed of sound, which is the theoretical framework on which our analysis is built.

We consider both the $(\mu(z), \eta(z))$ and the $(\mu(z), \Sigma(z))$ pair. In the latter case, $\Sigma(z)$ as a function of E_{11} and E_{22} is computed using equation Equation 7.31. When performing the Fisher analysis, we vary E_{11} and E_{22} and derive the predicted constraints on the parameters (μ_0, η_0) and (μ_0, Σ_0), where $\mu_0 \equiv \mu(z=0)$, $\eta_0 \equiv \eta(z=0)$, $\Sigma_0 \equiv \Sigma(z=0)$.

We compute the theoretical matter power spectrum with the code MG-CAMB[2] [18, 238, 385], the modified version of the Einstein-Boltzmann solver CAMB[3] [173], extended to study modified gravity models within the phenomenological parametrization framework. In figure Figure 7.3, we show the linear matter spectrum for the assumed fiducial cosmology (see table Table 7.2) and for different values of the MG parameters (μ_0, η_0) and (μ_0, Σ_0). This is the power spectrum used to compute the C_ℓs introduced in Section 7.1.1. We observe that the most significant modifications occur at large scales. Varying the parameters η_0 or Σ_0 affects only the larger scales, while μ_0 has an impact on smaller scales too. The modifications become milder at higher redshifts, according to how the parametrization we chose performs.

The late-time parametrization has been studied in the literature in several contexts [4, 5, 239, 243, 386, 387] and current data sets do not show a significant preference for models beyond ΛCDM. Recently, a non-parametric Bayesian reconstruction of μ, Σ, along with the dark energy density, from all available LSS and CMB data was performed in [241, 242]; while the outcome is consistent with ΛCDM within 2σ, some interesting features in Σ were identified as an imprint of cosmological tensions.

The phenomenological functions μ, Σ and η parametrize modifications of the dynamics of perturbations within the scalar sector. When including GWs, one should consider that tensor perturbations are generally also affected by modifications of gravity. For the observables of interest in this work, the effects of modified gravity on GWs propagating on the FLRW background can be encoded in the difference between the electromagnetic luminosity distance $d_L^{EM}(z)$ and the GW one $d_L^{GW}(z)$. The phenomenological function $\Xi(z)$, defined as

$$\Xi(z) \equiv \frac{d_L^{GW}(z)}{d_L^{EM}(z)}, \tag{7.33}$$

quantifies the effect of bright sirens. The EM luminosity distance can be expressed as $d_L^{EM}(z) = \sqrt{L/4\pi S}$, where L and S are the bolometric luminosity and the bolometric flux for the observed object, respectively. This quantity can also be expressed as a function of the comoving distance χ as (for $\Omega_k = 0$): $d_L^{EM}(z) = (1+z)\chi = (1+z)d_H \int_0^z dz'/E(z')$, with $E(z) = \sqrt{\Omega_m(1+z)^3 + \Omega_k(1+z)^2 + \Omega_\Lambda}$ and $d_H = c/H_0$. The GW luminosity distance $d_L^{GW}(z)$ is estimated in a way not dependent on a distance ladder, and relies on the extraction of information enclosed in the GW waveform such as the strain and the frequency. A univocal analytic expression for the $d_L^{GW}(z)$ is nontrivial to obtain, as it is also highly dependent on the assumed gravity model. In [381], the authors performed an extensive study of Ξ both in terms of parametrizations and of the specific form it takes in given models of MG. In the latter case, Ξ is in general related to operators of the Lagrangian that affect also scalar perturbations; for instance, in Horndeski gravity it is a function

---

[2] See https://github.com/sfu-cosmo/MGCAMB.
[3] See https://camb.info/.

of the non-minimal coupling, which is a key contributor to μ and Σ as well. Therefore, in a theoretical embedding, Ξ is not completely independent of μ and Σ.

The expressions we used for GW lensing in the auto- and cross-correlation rely on calculations of the relativistic corrections to the luminosity distance of GW in Horndeski and DHOST theories with the speed of sound $c_T^2 = 1$ [388]. In this case, it is not straightforward to find an explicit expression for $\Xi(z)$ in terms of μ, Σ and/or η which is valid on all linear scales. For $c_T^2 = 1$, in the quasi-static regime and on scales above the mass scale of the model, the running of the Planck mass is the main contributor to both μ, implying that the relation between Ξ and μ tends towards the simple form

$$\Xi(z) = \sqrt{1 + \frac{1}{\mu(z)}}. \tag{7.34}$$

However, on smaller scales, the relation becomes more complicated, as discussed in [249], and the expression for Ξ would acquire another term, dependent on the other MG functions at play. For the parametrization of μ and η that we employ in this work, based on [243], the exact form of this additional term, which should depend on η, is complex to work out without losing generality. For this reason, we decide to parametrize the Ξ function as follows

$$\Xi(z) = \sqrt{1 + \frac{1}{\mu(z)} + \frac{a_1}{\eta(z)^{a_2}}}, \tag{7.35}$$

where a_1 and a_2 are varied along with the other parameters in the Fisher analysis and regarded as nuisances. With this parametrization of Ξ, we can reproduce the main features of the results found for several models [381]. We fix the fiducial values of a_1 and a_2 in order to obtain a variation of Ξ in redshift comparable to the results for DHOST models in [381].

Let us stress that our method for GW lensing builds on the expressions for the luminosity distance of GWs and its relativistic corrections; the latter are explicitly known only for the class of Horndeski models with a luminal speed of tensors. This is therefore the context in which we perform our analysis. In this framework, the Ξ function is not independent of the μ, η or μ, Σ functions. In other words, they all depend, solely or partially, on the non-minimal coupling of the theory. A more general framework may not encode this dependence; forecasts in such cases would be expected to be less constraining. In order to correctly quantify the degrading, we would need to go beyond the theoretical framework on which we have built our analysis; this is certainly an interesting direction for future work.

In the following section, we discuss how the observables that we consider in this work are modified in light of the MG phenomenological functions.

7.3.2 *Modified angular power spectra and MG parameters*

Above, we commented on how the MG parameters affect the linear matter power spectrum (see figure Figure 7.3). In this section, we outline their impact on the observables that we consider in this work, presented in section Section 7.1.1.

On the one hand, all the angular power spectra are computed with the linear matter power spectrum $P_{\rm m}(k,z)$. In our analysis the modified $P_{\rm m}(k,z)$ is computed numerically by means of the code MGCAMB, as discussed above. As can be noticed in Figure 7.3, the MG functions affect the matter power spectrum $P_{\rm m}(k)$. The effect of μ is quite direct and the most notable, given that μ changes the rate of clustering of matter. The functions η and Σ have a less direct impact on $P_{\rm m}(k)$, but still affect it. In particular, Σ impacts the C spectrum via the magnification bias. On the other hand, the MG models we consider modify the lensing potential. In the scalar sector, modifications to the lensing potential are encoded by the MG function $\Sigma(z)$, through equation Equation 7.30. This means that an extra factor $\Sigma(z)$ appears each time the term $(\Phi + \Psi)$ appears. Thus, the lensing angular power spectra of equation Equation 7.7 become [239]

$$C_{\rm LL}^{X_i Y_j}(\ell) = \int_0^\infty \frac{dz\, c}{H(z)} \frac{W_{\rm L}^{X_i}(z)\, W_{\rm L}^{Y_j}(z)}{\chi^2(z)}\, \Sigma^2(z)\, P_{\rm mm}\left(\frac{\ell}{\chi(z)}, z\right), \qquad (7.36)$$

while the cross-correlation spectra between lensing and clustering will be

$$C_{\rm CL}^{X_i Y_j}(\ell) = \int_0^\infty \frac{dz\, c}{H(z)} \frac{W_{\rm C}^{X_i}\left(\frac{\ell}{\chi(z)}, z\right)\, W_{\rm L}^{Y_j}(z)}{\chi^2(z)}\, \Sigma(z) P_{\rm mm}\left(\frac{\ell}{\chi(z)}, z\right). \qquad (7.37)$$

Following [369], the $\Xi(z)$ function is going to appear in the Lensing observables related to bright GW sirens. This is because for bright sirens the estimator of the convergence depends on the ratio $d_{\rm L}^{\rm GW}/d_{\rm L}^{\rm EM}$. Explicitly, this results into

$$C_{\rm LL}^{GW_i^{bright} GW_j^{bright}}(\ell) \simeq \Xi^2(z) \int_0^\infty \frac{dz'\, c}{H(z')} \frac{W_{\rm L}^{X_i}(z')\, W_{\rm L}^{Y_j}(z')}{\chi^2(z')}\, \Sigma^2(z')\, P_{\rm mm}\left(\frac{\ell}{\chi(z')}, z'\right), \quad (7.38)$$

while the cross-correlation spectra between lensing and clustering will be

$$C_{\rm L\Theta}^{GW_i^{bright} Y_j}(\ell) \simeq \Xi(z) \int_0^\infty \frac{dz'\, c}{H(z')} \frac{W_{\rm L}^{GW_i^{bright} Y_j}\left(\frac{\ell}{\chi(z')}, z'\right)\, W_{\rm L}^{Y_j}(z')}{\chi^2(z')}\, \Sigma(z') P_{\rm mm}\left(\frac{\ell}{\chi(z')}, z'\right). \quad (7.39)$$

Following reference [369], it is worth clarifying that the approximately equal symbol in the above two equations is due to the linearization at first order of the convergence estimator, in the parameters describing it which are introduced in equation (3.8) of [369]. We refer the interested reader to reference [369] for further details.

7.4 FORECASTS

In accordance to what described in Section 7.1.2, we perform a Fisher analysis on the following parameters: $\{E_{11}, E_{22}, w_0, w_a, \ln 10^{10} A_s, n_s, K^{\rm fg}, a_1, a_2\}$ (for a total of 9 parameters). The fiducial values we use in this pipeline (mainly taken from Planck results [4]) are summarized in table Table 7.2.[4] Where explicitly stated, the $\{w_0, w_a\}$ parameters are kept fixed instead. Given errors

---

[4]The fiducial value of $K^{\rm fg}$ depends on the case considered (z binning and probe): we adopt $K^{\rm fg} = 5.72 \cdot 10^{-8}$ $(9.64 \cdot 10^{-6})$ for the redshift binning chosen in the dark sirens case for the Lensing (Clustering) probe and $K^{\rm fg} = 4.49 \cdot 10^{-8}$ $(1.05 \cdot 10^{-5})$ for the redshift binning chosen in the bright sirens case for the Lensing (Clustering) probe. The fiducial values for $\{a_1, a_2\}$ are respectively -0.95 and 0.14. We omit these values from table Table 7.2 for the sake of simplicity.

PROBE	σ_{μ_0}	σ_{η_0}	σ_{Σ_0}	σ_{w_0}	σ_{w_a}	σ_{μ_0}	σ_{η_0}	σ_{Σ_0}	σ_{w_0}	σ_{w_a}
	darkGW×IM					brightGW×IM				
Lensing	15.62	38.92	2.09	2.78	8.66	24.45	61.86	3.73	4.59	16.18
C	1.20	1.84	0.99	0.53	1.43	1.12	1.84	1.00	0.47	1.34
L + C	0.10	0.24	0.04	0.11	0.23	0.08	0.20	0.06	0.05	0.15
	darkGW×IM×gal					brightGW×IM×gal				
Lensing	1.96	4.48	0.09	0.45	1.41	2.78	6.66	0.24	0.96	3.62
Clustering	0.80	1.39	0.82	0.32	0.92	0.30	1.25	0.68	0.12	0.35
L + C	0.05	0.11	0.01	0.04	0.08	0.06	0.10	0.02	0.03	0.09

Table 7.3: Fisher estimated errors on the $\mu_0, \eta_0, \Sigma_0, w_0, w_a$ parameters for different tracers and probes combinations.

PROBE	σ_{μ_0}	σ_{η_0}	σ_{Σ_0}	σ_{μ_0}	σ_{η_0}	σ_{Σ_0}
	darkGW×IM			brightGW×IM		
Lensing	10.46	25.46	1.06	16.38	40.61	2.06
Clustering	0.18	1.10	0.62	0.19	1.23	0.68
L + C	0.09	0.20	0.02	0.03	0.09	0.03
	darkGW×IM×gal			brightGW×IM×gal		
Lensing	1.13	2.60	0.06	1.63	3.93	0.14
Clustering	0.17	1.08	0.61	0.09	0.50	0.29
L + C	0.08	0.17	0.02	0.03	0.06	0.01

Table 7.4: Fisher estimated errors on the μ_0, η_0, Σ_0 parameters for different tracers and probes combinations. The parameters w_0, w_a are kept fixed.

on $\{E_{11}, E_{22}\}$, we derive constraints on the $\{\mu_0, \eta_0, \Sigma_0\}$ parameters. We perform Fisher analysis for the following different cases:

- Different probes: L only, C only, and L + C;

- Different tracers combinations: GW × IM and GW × IM × gal;

- GW are either treated as dark (BHBH and BHNS mergers) or bright (NSNS) sirens.

The next section provides results on $\{\mu_0, \Sigma_0\}$ for all the cases listed above.

7.4.1 *Results*

We provide Fisher estimated constraints on the $\{\mu_0, \eta_0, \Sigma_0\}$ parameters (and w_0, w_a where relevant) in Table 7.3 and Table 7.4. All results refer to $f_{\text{sky}} = 0.5$ and $T_{\text{obs}}^{\text{GW}} = 15$yr.   In Figure 7.4, Figure 7.5 we provide $1-2\sigma$ contour ellipses on the $\{\mu_0, \Sigma_0\}$ parameters (for $f_{\text{sky}} = 0.5$ and $T_{\text{obs}}^{\text{GW}} = 15$yr). In Figure 7.7, Figure 7.8 we provide forecasts on $\{\mu_0, \Sigma_0\}$ for different values of f_{sky}, fixing
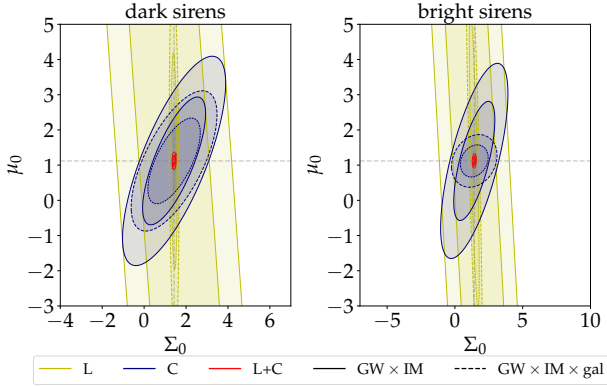
Figure 7.4: Contours for $\{\mu_0, \Sigma_0\}$ in the GW×IM (solid line) and GW×IM×gal (dashed line) cases, all probes considered (colors according to legend). The left panels refer to dark sirens (BHBH+BHNS), right panels refer to bright sirens (NSNS). w_0, w_a are among the Fisher parameters considered. $T_{\mathrm{obs}}^{\mathrm{GW}}$=15 yr and $f_{\mathrm{sky}} = 0.5$.
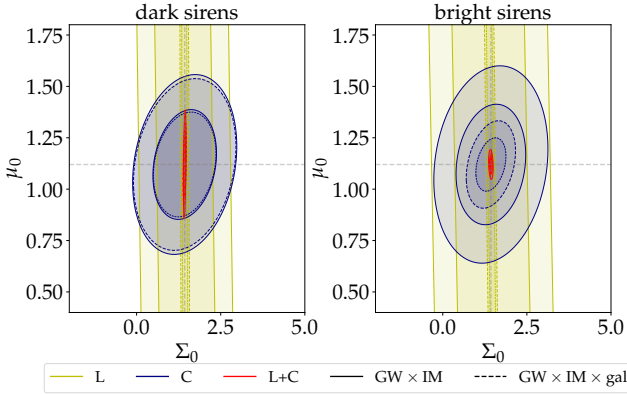
Figure 7.5: Contours for $\{\mu_0, \Sigma_0\}$ in the GW×IM (solid line) and GW×IM×gal (dashed line) cases, all probes considered (colors according to legend). The left panels refer to dark sirens (BHBH+BHNS), right panels refer to bright sirens (NSNS). w_0, w_a are fixed to fiducial values. $T_{\mathrm{obs}}^{\mathrm{GW}}$=15 yr and $f_{\mathrm{sky}} = 0.5$.
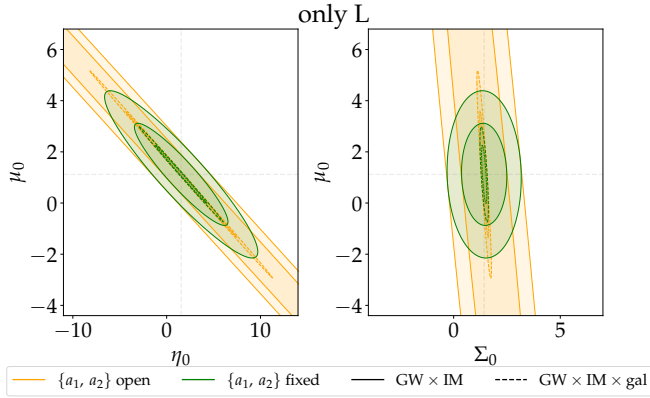
Figure 7.6: Contours for $\{\mu_0, \eta_0\}$ and (μ_0, Σ_0) in the GW×IM (solid line) and GW×IM×gal (dashed line) cases, for the only-L case. Comparison between forecasts fixing or opening the $\{a_1, a_2\}$ parameters describing the Ξ function according to Equation 7.35. w_0, w_a are fixed to fiducial values. $T_{\rm obs}^{\rm GW}$=15 yr and $f_{\rm sky} = 0.5$.

w_0, w_a. The same plots for the $\{\mu_0, \eta_0\}$ parameters are provided in the appendix of [118]. In light of these results, we can express the following statements.

Lensing-only case

Focusing on the Lensing-only case, we find that both bright and dark sirens cases are not good at constraining the parameters of interest, although some differences in the constraining power between the two cases can be found. Indeed, considering bright sources brings both advantages and disadvantages, with the resulting outcome depending on which of the two dominates. Specifically, the advantage of having an EM counterpart is enclosed in the presence of the MG function Ξ defined in Section 7.3 (not present for dark sirens), which introduces a severely stronger dependence of the C_ℓs on the μ_0, η_0, Σ_0 parameters. On the other side, detectable bright sources cover a lower redshift range (since NSNS binaries are less massive than BHBH or BHNS they can be detected up to lower redshifts). This might give a disadvantage, both concerning the number of detected sources (i.e. worse shot noise) and the possibility to perform a less deep tomography (fewer redshift bins available, i.e. less information). Overall, bright sirens may give better/worse results with respect to the dark case depending on the balance between these two effects and on which probe we are considering.

Generally, in the L-only case, the advantages of considering bright sirens are not able to dominate on the downsides (or at least significantly), with constraints comparable between the two cases (see e.g. Table 7.3 and Table 7.4). This is even more evident in e.g. Figure 7.4, Figure 7.5: the L-only contour ellipses (in yellow) show an extremely wide extension in all dark sirens panels (left side), leaving especially μ_0 and η_0 barely constrained. Unfortunately, a similar trend can be found for bright sirens L-only ellipses (right panels of both figures). The same insight can be drawn from Figure 7.7, Figure 7.8.
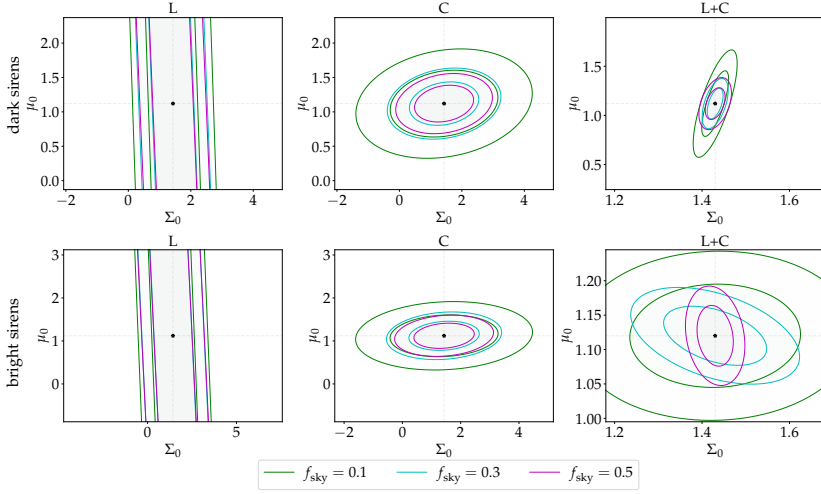
Figure 7.7: Contours for $\{\mu_0, \Sigma_0\}$ parameters for the GW×IM case, all probes considered (only Lensing: left panels; only Clustering: center panels; Lensing + Clustering: right panels), for dark (top panels) and bright (bottom panels) sirens and for different values of f_{sky} (color-coded according to legend). w_0, w_a are fixed to fiducial values. $T_{\text{obs}}^{\text{GW}}$=15 yr.
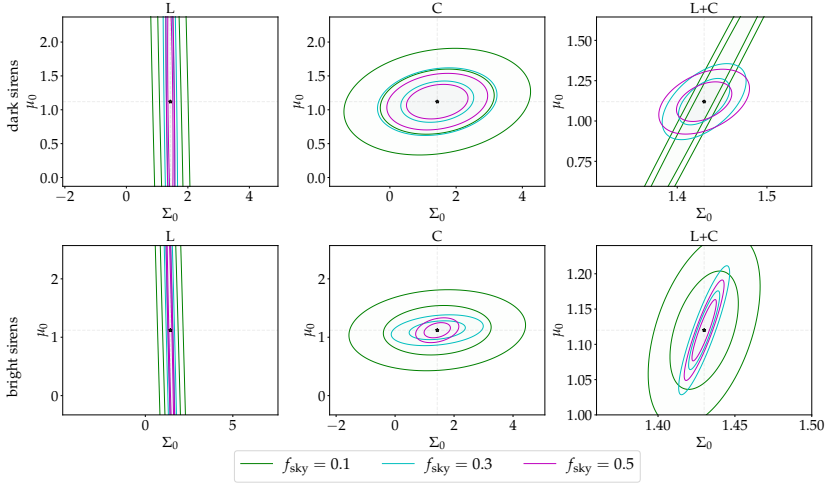
Figure 7.8: Contours for $\{\mu_0, \Sigma_0\}$ parameters for the GW×IM×gal case, all probes considered (only Lensing: left panels; only Clustering: center panels; Lensing + Clustering: right panels), for dark (top panels) and bright (bottom panels) sirens and for different values of f_{sky} (color-coded according to legend). w_0, w_a are fixed to fiducial values. $T_{\text{obs}}^{\text{GW}}$=15 yr.
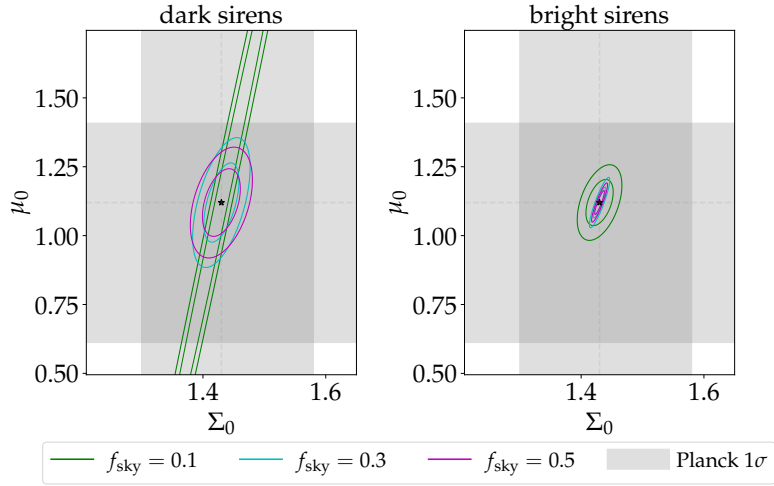
Figure 7.9: Contours for the most stringent constraints we find on $\{\mu_0, \Sigma_0\}$: GW×IM×gal, Lensing + Clustering case, for dark (left) and bright (right) sirens and for different values of f_{sky} (color-coded according to legend). w_0, w_a are fixed to fiducial values. T_{obs}^{GW}=15 yr. The gray area shows $1\sigma = 68\%$ confidence regions from Planck TT,TE,EE+lowE without CMB lensing (see table 7 of [4]).

Furthermore, we can see that adding galaxies in addition to the GW × IM cross-correlation significantly improves the results, especially in the dark sirens case: dashed lines (GW×IM×gal) in Figure 7.4 and Figure 7.5 tend to mark tighter ellipses than solid lines (GW×IM).

Overall, Lensing-only forecasts are non-competitive with Planck constraints [4], showing nonetheless the advantage of taking into account the information coming from a higher number of tracers (GW×IM×gal vs. GW×IM).

L+C case

Adding the angular Clustering probe to Lensing data (L+C case) significantly improves the results in any case considered (bright/dark sirens, with/without adding resolved galaxies), providing constraints tighter up to two orders of magnitude (see e.g. Table 7.4). This shows that not only cross-correlating different tracers but especially combining together different probes is a remarkably powerful tool to exploit, that provides significant extra information. This is especially evident in Figure 7.4: the C-only (in blue) and especially the L+C (in red) contours are firmly more constraining than the (yellow) L-only ones, often breaking down degeneracies between parameters.

The best results we obtain in the L+C case are very competitive with Planck results [4], highlighting the power of cross-combining observables of different tracers and probes. Results concerning the Σ_0 parameter are especially promising. This is reasonable since Σ_0 is the parameter describing deviations from GR for Lensing effects, as explained in Section 7.3. To highlight the competitiveness of our best constraints with those from Planck, in Figure 7.9 we compare our L+C forecasts (GW×IM×gal case) with the 68% confidence regions from Planck TT,TE,EE+lowE (without CMB lensing, see table 7 of [127]). Planck results are

compatible with ΛCDM and Planck data alone do not show a significant preference for beyond ΛCDM values of μ_0, η_0 and Σ_0: indeed, their results are less than 1σ away from the ΛCDM limit for μ_0 and η_0, and $\sim 2\sigma$ for Σ_0. Our best results are highly competitive and severely reduce Planck errors: assuming a Planck best fit as fiducial value our measurements show a mild preference for non-ΛCDM values of μ_0 and η_0 (respectively $\sim 4\sigma$ and $\sim 9\sigma$), and a clearly stronger preference for Σ_0 (at more than 20σ) since our lensing observable is strongly affected by it. This means that if experimental data will confirm beyond ΛCDM central values, we would be able to confirm a preference for MG models with a high confidence level.

Comparing the bright/dark sirens cases, we see no univocal pattern among the two (see e.g. red L+C contours in Figure 7.4 and Figure 7.5). This can be motivated by the explanation laid in the previous point: taking bright sirens has both pros (extra information contained in the Ξ parameter for Lensing) and cons (shallower tomography in both L and C). Given the addition of Clustering, which is independent of Ξ, we can not naturally expect a striking difference as for the L-only case, but a competition between these two opposite effects, with not clearly predictable outcomes. We also note that generally adding galaxies improves the constraining power, which is an expected outcome as more information is being fed to the pipeline (as for the L-only case).

Fixing $\{a_1, a_2\}$ parameters

In Section 7.3 we have introduced the $\Xi(z)$ function, which is parametrized by $\{a_1, a_2\}$ according to Equation 7.35. In order to take into account possible uncertainties to the modeling of this function, we opted to allow $\{a_1, a_2\}$ to vary, introducing them among the Fisher parameters considered in the analysis (as described in Section 7.3). Nonetheless, this inevitably introduces an extra source of uncertainty, disadvantaging predictions for the bright sources case and leading to forecasts in the Lensing-only case for bright sirens usually no better than those for dark sirens, as highlighted in the "Lensing-only case" subsection above. Nonetheless, one may wonder what the advantage of considering bright sources would be if the behavior of $\Xi(z)$ was assumed fixed, getting rid of this extra source of uncertainty. Figure 7.6 provides constraints on μ_0, η_0, Σ_0 (for $f_{\rm sky} = 0.5$ and $T^{\rm GW}_{\rm obs} = 15{\rm yr}$) for the Lensing-only case, comparing the cases of $\{a_1, a_2\}$ open and $\{a_1, a_2\}$ fixed to fiducial values (with w_0, w_a fixed). It shows a significant improvement in the constraining power of the experiments, with contour ellipses covering more reasonable ranges, highlighting a severe degradation in the constraining power due to the uncertainty on the modeling of the parameters describing $\Xi(z)$.

Indeed, Fisher estimated errors on $\{\mu_0, \eta_0, \Sigma_0\}$ when keeping $\{a_1, a_2\}$ fixed are the following: $\{1.32, 3.29, 0.70\}$ for the GW $\times$ IM case and $\{0.75, 1.80, 0.08\}$ when adding galaxies. When comparing these numerical values to those in the "LENSING" rows of Table 7.4, we can see an improvement of up to one order of magnitude (for the GW $\times$ IM case).

These results show that if the behavior of $\Xi(z)$ was to be known, being able to detect an EM counterpart would be of crucial importance for experiments based only on the Weak Lensing observable, allowing to constrain $\{\mu_0, \eta_0, \Sigma_0\}$ with good accuracy, and significantly better than a case in which only dark sirens would be available. Nonetheless, an approach taking into account the

uncertainty on the modeling of $\Xi(z)$ is safer and more realistic, although provides more pessimistic forecasts.

$\{w_0, w_a\}$ effects

Since we are studying theories with fixed background, it is natural to wonder about the impact of keeping the $\{w_0, w_a\}$ parameters fixed (results provided in Table 7.4 and Figure 7.5) or open, as extra Fisher parameters (Table 7.3 and Figure 7.4). When fixing w_0, w_a at their fiducial values results are in general either comparable or significantly more optimistic (up to a few factors unity), with smaller contour ellipses. As one would expect, the higher number of free parameters usually leads to less tight constraints.

f_{sky} effects

Improving the surveyed area of the sky logically improves the constraining power, sometimes significantly. It can be seen in Figure 7.7, Figure 7.8, that the contours related to higher values of f_{sky} (in magenta) are tighter than those for low $f_{sky} = 0.1$ values (in green), sometimes reducing parameters degeneracies. This is valid for all considered probes: L, C, and L+C (left, middle and right panels). We also report, not shown explicitly, a very mild dependence on the values of T_{obs}^{GW}, showing that in this framework the GW shot noise does not provide the bulk of the weight to the error budget.

Role of the EM counterpart for bright sirens

As described over the course of this manuscript, the bright sirens case relies on the assumption that NSNS mergers are associated with an EM counterpart. This is an optimistic starting point, which is why we accompany these results to the BHBH+BHNS dark case. For completeness (although not explicitly reported here for the sake of brevity) we have also computed forecasts labeling all GW sources (BHBH, BHNS, and NSNS mergers) as dark sirens. We found that results are generally comparable to the BHBH+BHNS dark case up to a few percentages. For this reason, results in this latter case can also be seen as a proxy for forecasts in a scenario characterized by a complete lack of EM counterparts.

Impact of ℓ_{max} for bright sirens

Throughout this section, we have provided results with a choice of $\ell_{max} = 300$ for detected bright sirens. As described in Section 7.2.1, we are allowed to push our angular resolution limit beyond the intrinsic instrument limitation thanks to the detectability of EM counterparts. Nonetheless, we explored a set-up with an $\ell_{max} = 100$ even for bright sirens. This way, we are testing the extreme case in which EM counterparts would not be exploited for improving the angular resolution. Forecasts obtained this way are less optimistic than the $\ell_{max} = 300$ ones, with relative differences from just a few percentages (mainly for the Lensing-only case) up to a factor ~ 5 for the Clustering-only and L+C cases. Nonetheless, we note that this would not lead to orders of magnitude of difference among the forecasts, providing us fairly robust results to the specific ℓ_{max} choice.

7.5 CONCLUSIONS

Cross-correlations between different tracers of the LSS and different observable probes can richly enhance the amount of physical information that can be extracted by present and forthcoming experiments. In this work we considered three different tracers: 1) resolved GW signals from compact object mergers as observed by ET, both assuming the detection of EM counterparts (for NSNS, bright sirens) or not (for BHBH and BHNS, dark sirens); 2) the Intensity Mapping of the neutral hydrogen distribution as observed by the SKA-Mid survey; 3) resolved radio-galaxies as mapped by SKAO. This allows us to correlate and compare both GW and EM signals, testing the possible imprints of beyond-GR behaviors, as these two observables are supposed to respond in the same way to matter perturbations effects such as lensing. For this reason, the primary observational probe we took into account is the weak lensing power spectrum, both in auto and cross-tracers correlation. In order to gauge the effects of combining together different probes, we also introduced the angular clustering power spectra and their L×C cross-term. We performed a Fisher matrix analysis in order to test a late-time parametrization scenario, forecasting the constraining power on the MG parameters $\{\mu_0, \eta_0, \Sigma_0\}$.

Our findings show that combining together different observational probes has a strikingly positive effect on the constraining power, with an improvement of up to an order of magnitude and results which are even competitive with constraints from Planck. We also find that, generally, cross-correlating together more tracers provides better constraints, as the combination of more information from different sources is more powerful than auto-correlation-only experiments.

In addition, we also show that when considering probes that describe physical effects that would be different between GW and EM sources (i.e. Lensing), the detection of an EM counterpart might be of crucial importance, allowing us to actively test the presence of different behaviors between these two observables and confirm or rule out GR alternatives to the description of gravity.

This work extends the efforts of the scientific community in the field of multi-tracing and multi-probes astrophysics and cosmology, showing that in an era rich in surveys and data (both from the present time and near-future experiments) the interconnection of different sources is able to yield results and constraints which are significantly more powerful than auto-correlation or single-probe results.

WEIGHING NEUTRINOS WITH 21CM INTENSITY MAPPING

F**UTURE** 21CM intensity mapping observations, tracing the large-scale distribution of matter in the Universe, are expected to be an important cosmological probe to investigate the effect of massive neutrinos on the evolution of structures. The large volumes probed with IM will allow to sample the neutrino free-streaming over a wide range of scales. In this work, we make use of the pipeline developed in Chapter 4 and Chapter 5 to test the constraining power of future SKAO observations on the total neutrino mass.

We find an upper limit on the total neutrino mass of 0.478 eV (95% confidence level) from 21cm multipole observations alone. When combined with CMB observations, intensity mapping data reduces the upper limit to 0.129 eV. The results from our analysis are consistent with other works in the literature further validating the validity of our pipeline. In this chapter, we give an overview of preliminary results that we plan to expand in the future.

We summarize the modifications to the mock datasets and the likelihood we implement for massive neutrinos in Section 8.1. The results we obtain for the 21cm multipoles alone and combined with CMB and BAO data are discussed in Section 8.2. A summary of our conclusions can be found in Section 8.3.

This chapter is based on «Latest perspectives on weighing the neutrinos with the SKAO 21cm Intensity Mapping.», by M. B**ERTI**, *M. Spinelli, B.S. Haridasu, and M. Viel, in preparation [119].*

8.1 METHODS

To forecast the constraining power of 21cm observations on the neutrino mass we make use of the formalism and technical tools developed in Chapter 4 and Chapter 5. In the following, we discuss how the theoretical predictions for the power spectrum are modified for massive neutrinos (Section 8.1.1) and present the constructed mock data set of SKAOobservations (Section 8.1.2).

8.1.1 *The 21cm power spectrum model for massive neutrinos*

The 21cm power spectrum is a biased tracer of the cold and baryonic matter distribution. When dealing with massive neutrinos one has to modify the 21cm power spectrum, in order to consider properly the neutrino contributions. The current picture shows that, although a fraction of massive neutrinos clusters inside the halos, they do not contribute significantly to CDM halo mass (see e.g. [389, 390]). Therefore, following e.g. [339], we redefine the non-linear 21cm power spectrum for massive neutrinos as

$$P_{21}(z, k, \mu) = \bar{T}_{\mathrm{b}}^2(z) \left[b_{\mathrm{HI}}(z) + f_{\mathrm{CDM+b}}(z) \, \mu^2 \right]^2 P_{\mathrm{CDM+b}}(z, k) + P_{\mathrm{SN}}, \quad (8.1)$$

where both the matter power spectrum and the growth rate are computed with the Einstein-Boltzmann solver CAMB[1] [173] for the CDM and baryon matter only.

[1]See https://camb.info/.
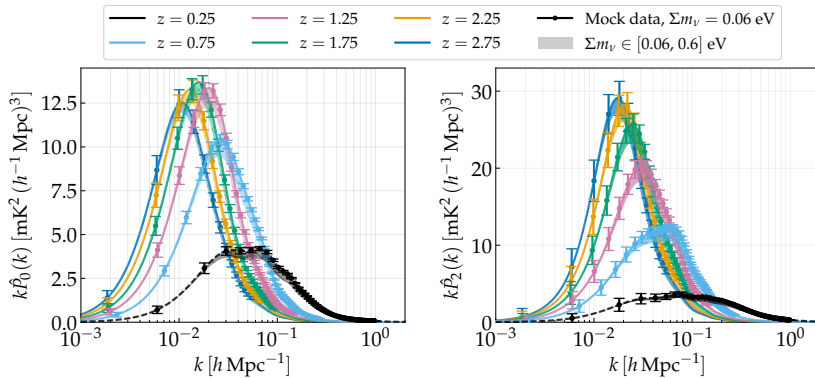
Figure 8.1: Tomographic mock data set for 21cm linear power spectrum monopole (upper panel) and quadrupole (lower panel) observations with massive neutrinos. The considered six redshift bins are centered at redshifts {0.25, 0.75, 1.25, 1.75, 2.25, 2.75}. For the first redshift bin (black dashed line) we assume a SKA-Mid Band 2 survey. The data sets for the other five bins, instead, assume a SKA-Mid Band 1 survey (see Table 4.1). Shaded areas show how theoretical predictions for the multiples are modified for different values of the total neutrino mass.

The other quantities appearing in Equation 8.1 are defined in Chapter 4. Non-linear corrections to the power spectrum are obtained with the latest version of the HMcode2020 [391], which include accurate computations for massive neutrinos that were found to be in agreement with a variety of theoretical tools [392].

Taking into account the AP distortions (see Equation 5.2-Equation 5.5) and the telescope beam effects, the observed non-linear 21cm power spectrum is

$$\hat{P}_{21}(z, k, \mu) = \frac{1}{\alpha_\perp^2 \alpha_\parallel} \tilde{B}^2(z, q, \nu) P_{21}(z, q, \nu).$$ (8.2)

Expanding in Legendre's polynomials, we compute the power spectrum multipoles as

$$\hat{P}_\ell(z, k) = \frac{(2\ell + 1)}{2} \int_{-1}^{1} d\mu \, \mathcal{L}_\ell(\mu) \hat{P}_{21}(z, k, \mu).$$ (8.3)

In the following, we consider measurements of the 21cm power spectrum monopole ($\ell = 0$) and quadrupole ($\ell = 2$).

Modifications to the 21cm) power spectrum induced by the neutrino free-streaming are clearly visible as the shaded areas in Figure 8.1. This is the effect we aim at constraining in the following analysis.

8.1.2   *Forecasted SKAO observations and analysis settings*

We construct mock observations of the 21cm power spectrum multipoles consistently with the planned cosmological surveys of the SKAO [57]. We forecast observations for six equi-spaced, non-overlapping redshift bins, in the range $z = 0 - 3$ with $\Delta z = 0.5$. The six bins are centered at redshifts $z = \{0.25, 0.75, 1.25, 1.75, 2.25, 2.75\}$. For a comprehensive discussion on the assumed telescope specifications and the modeling of the errors we refer to

Chapter 4.[2] Figure 8.1 shows the mock data set we construct for the monopole and the quadrupole. We observe that increasing the total neutrino mass suppresses the power at small scales, as expected from the neutrino free-streaming effect.

To perform the MCMC analysis we use an expanded version of the sampler CosmoMC[3] [136, 212], modified in order to include the computation of the theoretical expectations for the power spectrum multipoles and of the likelihood function. We vary the complete set of cosmological parameters along with the total neutrino mass Σm_ν and the nuisance parameters, including the shot noise. The assumed fiducial cosmology is Planck 2018 [4], with $\Sigma m_\nu = 0.06$ eV. On each parameter, we assume a flat prior. For the neutrino mass, we consider $\Sigma m_\nu \in [0.06, 1]$ eV, as suggested by the state-of-the-art constraints from particle physics.

8.1.2.1 *BAO data sets*

Measurements of the BAO scale at different redshifts provide an important geometrical test for cosmology, independent from CMB observations. Due to the fact that BAO observations are a probe for the expansion, they are particularly useful to constrain the background evolution. In this work, we analyze the complementarity of the constraining power of 21cm intensity mapping with CMB and BAO data. With the label "BAO" we refer to the set of following observations: the Sloan Digital Sky Survey (SDSS)[4] six-degree-Field Galaxy Survey (6dFGS) at an effective redshift $z_{eff} = 0.106$ [319]; the SDSS Main Galaxy Sample (MGS) at $z_{eff} = 0.15$ [320]; the SDSS Baryon Oscillation Spectroscopic Survey (BOSS); we use data sets from both the 11th and 12th data release, in particular from DR11 we adopt the LOWZ sample at $z_{eff} = 0.32$ and CMASS sample at $z_{eff} = 0.57$ [393]; from DR12 we adopt measurements at $z_{eff} = 0.38, 0.51, 0.61$ [266].

8.2   RESULTS

We present here the result of our forecast analysis. First, we assess the constraining power of 21cm observations alone and with BAO data (Section 8.2.1). Then we investigate how future 21cm multiples measurements impact the results on the cosmological parameters from Planck alone (Section 8.2.2). We show the marginalized 1D and 2D contours for the studied set of parameters and the 95% confidence levels. We recall that with the label "Planck 2018" we refer to the combination TT, TE, EE + low-ℓ + lowE + lensing (see Section 2.2.1).

8.2.1   *Forecasted constraints on the neutrino mass from the SKAO*

As shown in Figure 8.2, SKAO observations are expected to have good constraining power on the neutrino mass (see also [309, 339, 380, 394–396]). From 21cm multipoles alone we find a constraint on the total neutrino mass comparable

---

[2]The analysis in this chapter differs from the one of Chapter 4 in the addition of the AP effects, as modeled in Chapter 5, and the assumption of the dependence on the CDM and baryon power spectrum in order the correctly model massive neutrinos.

[3]See https://cosmologist.info/cosmomc.

[4]https://www.sdss.org/

Likelihoods		$\Sigma m_\nu^{\rm fid} = 0.1$
$\hat{P}_0 + \hat{P}_2$	< 0.216	< 0.227
+ nuisance	< 0.478	< 0.535
$\hat{P}_0 + \hat{P}_2$ + BAO	< 0.227	
+ nuisance	< 0.413	
Planck 2018	< 0.259	
+ $\hat{P}_0 + \hat{P}_2$	< 0.101	< 0.117
+ nuisance	< 0.129	< 0.127
Planck 2018 + BAO	< 0.149	
+ $\hat{P}_0 + \hat{P}_2$	< 0.101	
+ nuisance	< 0.130	

Table 8.1: Marginalized constraints on cosmological parameters at the 95% confidence level. Here, the label "$\hat{P}_0 + \hat{P}_2$" stands for the baseline tomographic data set for the monopole and the quadrupole combined and with multipole covariance taken into account. The label "nuisance" indicates that we vary the nuisance parameters along with the cosmological ones.

with the one from Planck, as displayed in Table 8.1. In a more realistic scenario, in which we take into account the astrophysical nuisances, we observe that the constraining power on Σm_ν as well as on the other cosmological parameters is reduced. In addition, Figure 8.2 shows how the correlations among the parameters are modified with the addition of the nuisances. We note that the widened constraint on Σm_ν obtained for $\hat{P}_0 + \hat{P}_2$ + nuisances is compatible with other forecast analysis for the SKAO in the literature (see e.g. [309, 339]).

Combining the forecasted 21cm multipole data sets with BAO observations do not improve significantly on the constraints from 21cm observations alone. Indeed, as discussed below, our analysis seems to indicate that BAO and 21cm intensity mapping data carry comparable information on the neutrino mass. This is expected due to the fact that full-shape analysis, such as the one we conduct here, provide more rich, scale-dependent information with respect to the BAO alone.

In order to explore how different scenarios could induce variations in the 21cm intensity mapping constraining power, we mimic recent constraints that favor higher neutrino masses (see e.g. [397]) and we construct an additional mock data set with a different fiducial for the total neutrino mass, i.e. we consider $\Sigma m_\nu^{\rm fid} = 0.1$ eV. The results, that we show in Table 8.1, consistently provide higher upper limits on the neutrino mass.

8.2.2 *Improvement from combining CMB observations with 21cm intensity mapping*

In Figure 8.3 we present the results we obtain by combining Planck 2018 data with the forecasted 21cm multipole data sets. We observe that the constraints on the neutrino mass are significantly improved by the addition of the 21cm likelihood. The improvement is stronger than what is found with Planck 2018 + BAO, for fixed nuisances, or comparable, for varying nuisances. As noted
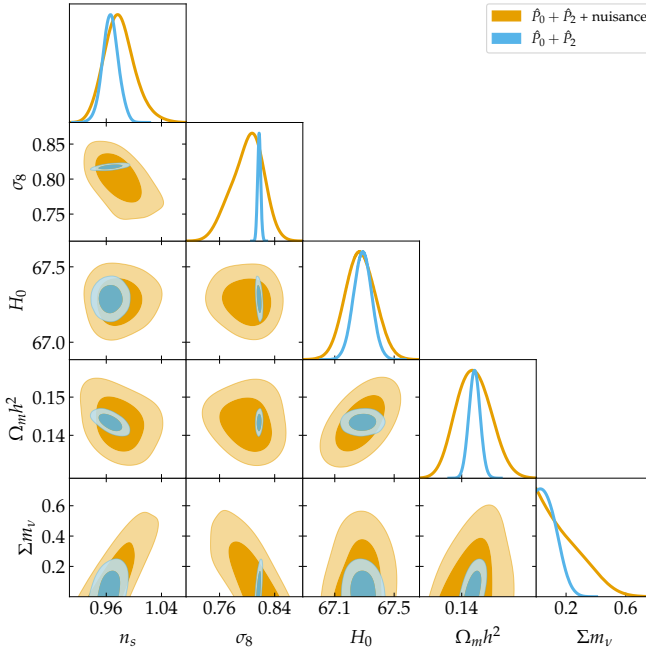
Figure 8.2: Joint constraints (68% and 95% confidence regions) and marginalized posterior distributions on cosmological parameters. The label "$\hat{P}_0 + \hat{P}_2$" stands for the baseline tomographic data set for the monopole and the quadrupole combined and with multipole covariance taken into account. The label "nuisance" indicates that we vary the nuisances parameters along with the cosmological ones.

before, BAO measurements do not add information to the Planck 2018 + $\hat{P}_0 + \hat{P}_2$ combination, as can be seen in Table 8.1.

8.3 CONCLUSIONS

In this work, we present preliminary results on the neutrino mass constraints produced by adapting the pipeline we develop in Chapter 4 and Chapter 5. We forecast the constraining power on Σm_ν of 21cm monopole and quadrupole mock SKAO observations alone and combined with BAO and CMB data.

We find upper limits consistent with other results in the literature. This further validates our modeling of the 21cm power spectrum signal and our likelihood implementation. In particular, we find a constraint of $\Sigma m_\nu < 0.478$ eV (95% confidence level) from 21cm observations alone. Combining this probe with CMB observations provide significantly tighter constraints with respect to Planck alone results, i.e. $\Sigma m_\nu < 0.129$ eV. Additional BAO likelihoods do not carry information complementary to the 21cm power spectrum multipoles.

We plan on finalizing the work presented in this chapter as follows. The number of effective neutrinos N_{eff} and the A_L parameter are strictly intertwined with Σm_ν. Opening the parameter space to N_{eff} and the A_L could provide interesting results for 21cm observations, offering a natural extension of this work.
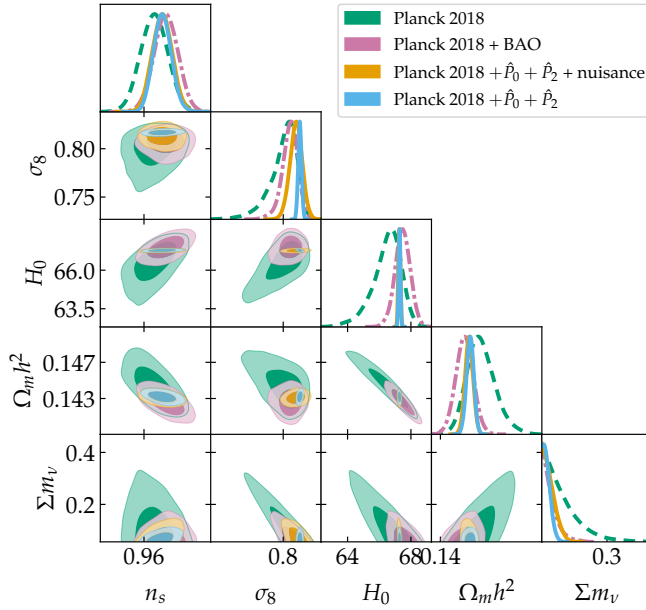
Figure 8.3: Joint constraints (68% and 95% confidence regions) and marginalized posterior distributions on cosmological parameters. The label "Planck 2018" stands for TT, TE, EE + lowE + lensing, while the label "$\hat{P}_0 + \hat{P}_2$" stands for the baseline tomographic data set for the monopole and the quadrupole combined and with multipole covariance taken into account. The label "nuisance" indicates that we vary the nuisances parameters along with the cosmological ones.

Insights on cosmological neutrinos can come also from the interplay between 21cm intensity mapping and other cosmological probes. The likelihood we implement in Chapter 5 to test cross-correlations between 21cm observations and galaxy clustering could be straightforwardly applied to neutrino mass testing. This would provide a forecast on Σm_ν from the cross-correlations between the SKAO and Euclid or DESI. We further discuss these extensions in the section Overview of ongoing and future projects.

CONCLUSIONS

COMPENDIUM OF THIS THESIS

Rationale

C osmology is entering an exciting new phase, where upcoming high-precision observations hold the promise of shedding light on the dark Universe and beyond. At this pivotal moment, it is essential to prepare for the vast wealth of upcoming data.

The goal of this thesis has been to actively contribute to the scientific community's efforts in this regard. Grounded on a theoretical background, this work lies at the intersection between theory and observations. Indeed, the focus of this study was twofold: 1) by building on noteworthy results in the literature, we developed and made use of advanced statistical and numerical tools to assess the constraining power of ongoing and future cosmological observations, including innovative probes such as the neutral hydrogen intensity mapping (IM); 2) we explored and studied a broad set of cosmological models, with a particular emphasis on dark energy (DE) and modified gravity (MG) alternative theories. In the following, we give an overview of the analysis performed in this thesis and summarize the most remarkable results.

Forecasts for 21cm intensity mapping

Although we explored synergies between a variety of cosmological probes, the core of this thesis has been to generate mock data sets of the large-scale distribution of neutral hydrogen in the post-reionization Universe, as they will be measured by cutting-edge experiments targeting the 21cm line. To this end, we defined a procedure to construct mock data sets mimicking measurements from several planned surveys of the SKA Observatory (SKAO) and its precursor MeerKAT, already in operation. We then developed a likelihood code to conduct Bayesian analyses with different 21cm probes. This resulted in a versatile pipeline, that can be easily interfaced with both forecasted IM measurements and available data.

We modeled and forecasted several 21cm observables: the auto power spectrum signal, its first two detectable multipoles, i.e. the monopole and the quadrupole, and the 21cm and galaxy clustering cross-correlation power spectrum. In order to assess the constraining power of near-future, realistic observations, we forecasted single-bin MeerKAT measurements of the auto power spectrum, at the effective redshift $z = 0.39$, which is currently being targeted by MeerKAT observations. To exploit the tomographic nature of future SKAO surveys, such as the planned SKA-Mid survey, we considered 21cm power spectrum monopole and quadrupole observations within 6 redshift bins in the range $z = 0 - 3$. For this mock data set, we also explored the effects of extending the forecasted detections to smaller, fully non-linear scales. To study the interplay between 21cm intensity mapping and galaxy clustering, we built mock data sets for the cross-correlation power spectrum monopole, choosing to focus on the SKAO for IM and the planned DESI and Euclid galaxy surveys. We considered measurements at multiple bins in the redshift ranges probed by DESI and Euclid, i.e. $z = 0.7 - 1.8$.

A part of this thesis was also devoted to forecasting the constraining power of 21cm observations in cross-correlation with gravitational waves (GWs). In this case, we considered resolved GW signals from compact object mergers as

observed by the Einstein telescope (ET), with and without the assumption of detecting electromagnetic counterparts, combined with the SKAO 21cm intensity mapping and resolved radio-galaxies.

Testing the ΛCDM Universe and beyond

The theoretical focus of this thesis has been to study the impact of future key cosmological observations on a variety of cosmological models. We explored the ΛCDM model along with a subset of MG-DE alternative theories and neutrino extensions.

We investigated several models within the MG-DE scenario. We chose to work with a model-independent approach and focused on parametrized frameworks of gravity, both in the EFT and phenomenological formulation. The EFT of cosmic acceleration is a versatile formalism that allows sampling a large number of different theoretical scenarios of increasing complexity. For a first thorough forecast of 21cm intensity mapping constraints on MG-DE, we started from the subset representing Generalized Brans Dicke theories, which includes $f(R)$ and, more generally, chameleon type theories. In the designer approach, this class of theories can be easily explored by varying two functions of time, which determine both the background and linear perturbation dynamics. We chose the Hubble parameter, $H(a)$, and the conformal coupling $\Omega^{\mathrm{EFT}}(a)$, which implies a running of the Planck mass corresponding to $\alpha_M = H^{-1}\mathrm{d}\ln\left(1 + \Omega^{\mathrm{EFT}}\right)/\mathrm{d}t$. In our analysis, we fixed the background evolution to ΛCDM or wCDM and studied the effects on the observables of different parametrizations of the $\Omega^{\mathrm{EFT}}(a)$ function.

In the phenomenological approach, the impact of modifications of gravity on the growth of structures and the evolution of the gravitational potentials can be cast into two functions of time and scale. Following analogous studies in the literature, we provide constraints on widely used parameterizations of the $\mu(z)$ and $\Sigma(z)$ functions, which capture modifications to the Poisson equation and gravitational lensing, respectively. In the context of GW observables, an additional function must be introduced. The parameter $\Xi(z)$ quantifies differences in the electromagnetic and GW luminosity distance and it modifies the lensing for bright sirens. From the $\mu(z)$ and $\Sigma(z)$ evolution, we derived a parametrization for $\Xi(z)$ to correctly model the lensing observables.

Lastly, we conducted a preliminary analysis to weigh neutrinos with 21cm probes. We considered the extension to ΛCDM in which we allowed for different values of the total neutrino mass Σm_ν, within the range left available from particle physics detections. When varying Σm_ν, we took into account modification to the modeling of the 21cm power spectra.

Numerical analysis tools

In our analysis we constrained the full set of cosmological parameters from forecasted measurements of the 21cm probes alone and in combination with state-of-the-art cosmological observations, such as the cosmic microwave background (CMB) and baryon acoustic oscillations (BAO) measurements. To describe a ΛCDM cosmology, we considered the following six independent parameters: $\Omega_b h^2$ and $\Omega_c h^2$, the density of the baryonic and cold dark matter, respectively, the scalar spectral index n_s, the normalization of the primordial power spectrum A_s, the Thomson scattering optical depth due to reionization τ, and θ_{MC}, a measure of the angular scale of the sound horizon at decoupling. Constraints on other key parameters, such as H_0 and σ_8, were derived from this set. Along with the standard cosmology parameters, we also constrained specific parameters describing alternative theories and the nuisances relative to the selected cosmological probe.

To explore such a high-dimensional parameter space, we performed a Bayesian analysis sampling the posterior distribution through Monte Carlo Markov chain (MCMC) techniques. We developed original numerical tools to work with a variety of 21cm probes. We expanded the CAMB/CosmoMC suite, including the extensions EFTCAMB/EFTCosmoMC, by implementing the numerical computation of the forecasted 21cm power spectra and likelihoods. The Bayesian analysis and marginalization have been performed with the GetDist code. The likelihood function we developed is operational and ready to be used to test a variety of theoretical models with future real 21cm observations. Indeed, in light of the recent measurements of the MeerKAT power spectrum in cross-correlation with WiggleZ galaxy clustering [61], we tested our analysis pipeline on measured data providing interesting preliminary results.

We found promising results confirming the value of 21cm intensity mapping observations as a key cosmological probe. In what follows, we summarize the main outcomes of this thesis. *Results*

· *The forecasted SKAO constraining power on ΛCDM and the impact of combining 21cm observations with CMB.* Our analysis revealed that mock SKAO 21cm multipole observations exhibit a good constraining power on the cosmological parameters, comparable to other probes. For instance, combining the 21cm monopole and quadrupole measurements resulted in both H_0 and σ_8 being constrained at approximately the 7% level. Notably, the 2D contours showed pronounced degeneracies between parameters, particularly in the $\Omega_c h^2$ - H_0 and $\ln(10^{10} A_s)$ - σ_8 planes. Combining 21cm observations with Planck 2018 CMB data significantly narrowed the parameter constraints compared to the Planck results alone. The most substantial improvements have been observed for $\Omega_c h^2$ and H_0, with errors reduced by a factor of four. The joint analysis yielded precise estimates of $\Omega_c h^2$ and H_0, which we constrained at the 0.25% and 0.16% level, to be compared with Planck estimates of 0.99% and 0.79%, respectively. The errors for $\ln(10^{10} A_s)$ and σ_8 were reduced by more than a factor of two, leading to 0.17% and 0.26% constraints respectively, in light of Planck estimates of 0.46% and 0.73%. Expanding the 21cm data set to non-linear scales led to increased constraining power. The most significant outcome has been the improvement in the constraints of A_s and σ_8. This is ascribable to the information acquired from lower scales, that facilitate a more accurate determination of the power spectrum amplitude. We concluded that 21cm SKAO observations will provide a competitive cosmological probe, complementary to CMB and, thus, pivotal for gaining statistical significance on the cosmological parameters constraints.

· *The impact of adding astrophysical nuisances.* In our analysis, we accounted for the uncertainty regarding the brightness temperature T_b, which relies on the total HI density Ω_{HI}, and the HI bias b_{HI}. To address this, we introduced nuisance parameters into our study. Specifically, we considered the combinations $\bar{T}_b b_{\mathrm{HI}} \sigma_8$ and $\bar{T}_b f \sigma_8$. With the inclusion of these nuisance parameters, the constraining power of 21cm multipoles on A_s and, consequently, on σ_8, is significantly reduced. However, this did not extend to the results obtained for $\Omega_c h^2$ and H_0, both for the 21cm data set alone and when combined with Planck data, possibly due to the tomographic nature of the observations that help fix the expansion. This confirmed the

strength of 21cm tomographic measurements, further endorsing ongoing observational efforts in the field.

· *Improvements on ΛCDM from 21cm cross-correlations with galaxy clustering.*
We found that, although less constraining, forecasted SKAO power spectrum measurements in cross-correlation with galaxy clustering showed a constraining power compatible with the 21cm auto-power spectrum one. The constructed SKAO×DESI and SKAO×Euclid data sets constrained the cosmological parameters at the sub-percent level. As for the auto-power spectrum, the strongest result has been on H_0, with constraints from 21cm and galaxy clustering cross-correlation alone ranging from 0.49% to 1.96%. The tightest error on H_0 was achieved when combining 21cm power spectrum multipoles with cross-correlation mock observations, reaching a value of 0.33%, competitive with Planck results. Combining the forecasted cross-correlation measurements with CMB data proved to be instrumental in reducing errors on cosmological parameters. For $\Omega_c h^2$ and H_0, these were reduced by factors ranging from 2.5 to 1.8 and 3.8 to 2, respectively. The best results were obtained by combining all 21cm probes, leading to a reduction by factors of 3.2 for $\Omega_c h^2$ and 5.6 for H_0, even accounting for nuisance parameters. We concluded that 21cm SKAO observations in cross-correlation with galaxy clustering will provide a competitive cosmological probe, less constraining that 21cm auto-power spectrum measurements, but equally complementary to CMB and, therefore, extremely important in strengthening the statistical significance of the constraints on cosmological parameters.

· *State-of-the-art cosmological parameters constraints from the MeerKAT detection in cross-correlation with WiggleZ.* We validated our analysis pipeline by testing it on the recent MeerKAT measurements of the power spectrum in cross-correlation with WiggleZ galaxy clustering, published in [61]. The procedure we used to construct mock data yields observations that align with measured data. While state-of-the-art observations may have limited constraining power on the complete set of cosmological parameters, the results we found are in line with the forecasted analysis outcome. Thus, the working pipeline presented in this work was found to be compatible and ready to deal with measured data sets.

· *A realistic MeerKAT forecast on EFT models of DE.* The constructed MeerKAT single-bin, auto-power spectrum mock data set revealed a mild constraining power on the considered EFT models of DE. When combining the 21cm power spectrum with CMB data, we observed a reduction in the EFT parameters constraints, in the range of $1 - 18\%$. Nevertheless, our results improved upon previous findings in the literature, enabling us to establish a stringent upper limit of $\Omega_0^{\text{EFT}} \leq 0.035$, at the 95% confidence level. Allowing for a negative running of the Planck mass, we found instead the constraint $\Omega_0^{\text{EFT}} = 0.075^{+0.063}_{-0.042}$. As for ΛCDM, the inclusion of nuisance parameters resulted in a decrease in constraining power. However, the use of tomography significantly enhanced the constraining power of the 21cm likelihood on EFT models. Combining a 21cm five bin power spectrum data sets with Planck 2018 CMB data, led to a constraint on Ω_0^{EFT} reduced by the 25% compared to Planck results, i.e.

$\Omega_0^{\text{EFT}} = -0.066^{+0.055}_{-0.031}$. Changing the background evolution from ΛCDM to wCDM yielded equivalent results.

· *Testing the MG-DE phenomenological functions with cross-correlations between 21cm intensity mapping and GWs.* We observed that the combination of observational probes of distinct nature has a remarkably positive impact on the MG phenomenological functions $\mu(z)$ and $\Sigma(z)$. We observed that cross-correlating multiple tracers generally leads to stronger constraints, as the synergy of diverse information from various sources enhances the overall statistical power compared to relying solely on auto-correlation experiments. Moreover, considering probes that exhibit distinct physical effects between GW and electromagnetic sources, such as lensing, makes the detection of an electromagnetic counterpart crucial. This enabled us to actively examine potential deviations between these observables and test for alternative theories of gravity. Combining 21cm intensity mapping with GWs provided an improvement of up to an order of magnitude and results that rival the constraints obtained from Planck data alone. The tightest errors on the MG parameters we have found are 0.03 on $\mu(z)$ and 0.01 on $\Sigma(z)$.

· *Constraints on the total neutrino mass as measured by the SKAO.* Using the pipeline developed to forecast the SKAO power spectrum multipole constraining power, we have provided an upper limit on the total neutrino mass. We have found a constraint of $\Sigma m_\nu < 0.478$ eV (95% confidence level) from 21cm observations alone. Combining this probe with CMB observations provides significantly tighter constraints with respect to Planck alone results, i.e. $\Sigma m_\nu < 0.129$ eV. We have observed that 21cm power spectrum multipoles carry information comparable to widely tested probes, such as the BAO data.

Final remarks

This thesis encompassed a comprehensive analysis spanning a wide range of topics in cosmology, enabling the author to deepen their understanding of theoretical aspects and parameter constraining and forecast analysis techniques. Noteworthy novelty aspects with respect to other works in the literature include the use of MCMC and Bayesian analysis techniques, taking into account the full set of cosmological parameters, the joint analysis between 21cm intensity mapping and CMB observation, and a discussion on the effects of the astrophysical nuisances.

The results of this thesis are in broad agreement with similar works in the literature and confirm the key role of future late-time 21cm intensity mapping observations. In particular, combining 21cm power spectrum measurement to CMB leads to a substantial improvement of the constraints on $\Omega_c h^2$ and H_0, offering a potential new element in the H_0 value discussion. Although present-day surveys have a mild constraining power over beyond ΛCDM extensions, our study suggests that more ideal tomographic 21cm signal observations could potentially improve the knowledge of DE-MG theories. We conclude that 21cm intensity mapping measurements provide a new interesting cosmological probe, that carries rich information complementary to other high-precision measurements.

The work presented in this thesis is suitable for further extensions. In the following, we outline some of the projects we have planned or that are currently underway.

IN THIS THESIS, we explored the constraining power of several 21cm signal probes. Although our analysis encompassed various theoretical and observational scenarios, we are actively planning or have already initiated extensions of this work with the pursuit of the following projects.

Forecasted constraints on the neutrino mass with the SKAO. The results on the neutrino mass constraints presented in Chapter 8 are currently under further study. Our focus involves an evaluation of the impact of cross-correlation between 21cm intensity mapping and galaxy clustering, using the mock data sets discussed in Chapter 5. In the analysis of Chapter 8, we found that BAO and 21 cm probes carried comparable information. However, this could not be the case for full-shape analyses of the galaxy clustering power spectrum, that provide 3D measurements form an independent tracer. We aim to expand the analysis by adding measurements of the galaxy power spectrum multipoles (see e.g. [398]). In addition, we plan on exploring the effect of combining 21cm observations with the newest CMB data from the Atacama Cosmology Telescope (ACT)[5] and the South Pole Telescope (SPT),[6] and on opening the parameter space to parameters that were proved to be strictly intertwined with Σm_ν, such as A_L. A paper to report our findings is currently in preparation [119]. This work is being carried out in collaboration with Dr S.B. Haridasu (SISSA).

Testing EFT of DE with SKAO intensity mapping. The analysis for the MeerKAT telescope of Chapter 6, suggests that the tomographic nature of 21cm observations could be pivotal to constrain DE. It is thus interesting to confirm these results by exploiting the full SKAO potential. We plan to use the formalism from Chapter 4 and Chapter 5 to forecast constraints on a broad class of EFT models. Preliminary tests seem to show that 21cm observations may have a good constraining power on more complex EFT models, involving EFT functions beyond first order. Indeed, current observations leave unconstrained the γ_1 parameter [399].

Easing the A_L tension with EFT models. It is well-known in the literature that MG-DE model can help easing the A_L tension [400]. In [401], we study the interplay between the EFT models considered in Chapter 6 and A_L. Figure 8.4 shows how EFT models can mimic the global rescaling of the lensing potential angular power spectrum introduced by A_L. By constraining the cosmological parameters using Planck CMB data, we observe a strong correlation between the parameters $\{S_8, \Omega_0^{\mathrm{EFT}}, A_L\}$. From Figure 8.5, it is clear that while lower negative values of Ω_0^{EFT} allow for reduced lensing amplitudes, this also implies an increase in the S_8 values, mediated via the larger gravitational constant. Although we tested several models with a variety of cosmological observations, such as DES-Y1 [5] weak lensing data, we are now interested in the role played by newer CMB and weak lensing measurements such as ACT and DES-Y3 [387]. We are currently working in this regard. This work is being carried out in

---

[5]See https://act.princeton.edu/.
[6]See https://pole.uchicago.edu/public/Home.html.
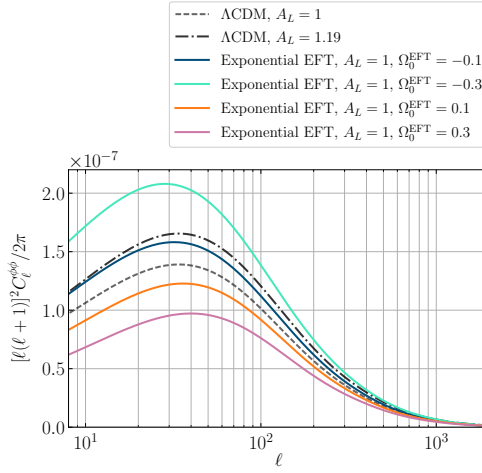
Figure 8.4: Predicted lensing potential power spectra for different values of A_L and EFT parameters.
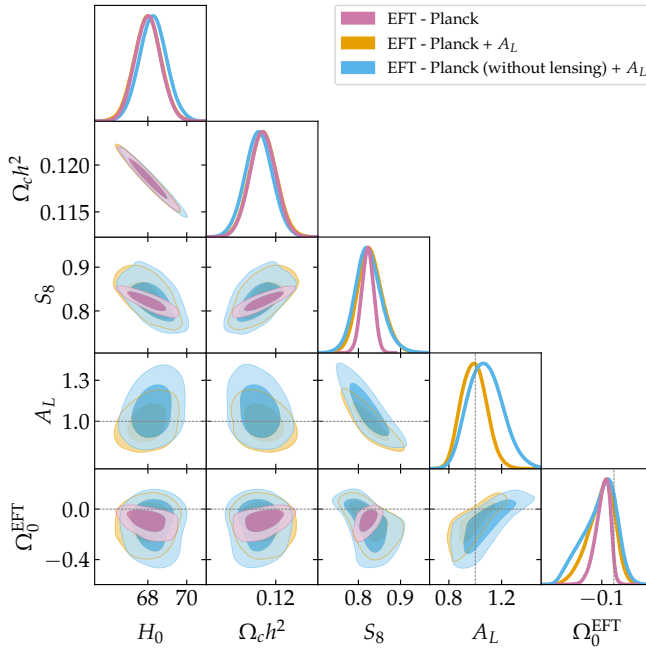
Figure 8.5: Joint constraints (68% and 95% confidence regions) and marginalized posterior distributions on cosmological parameters, for different beyond ΛCDM scenarios.

collaboration with Dr S.B. Haridasu (SISSA).

Reconstructing gravity. An interesting alternative to the parametrized frameworks of gravity, is gravity reconstruction [241, 242]. The fundamental idea is to follow a maximal model-independent approach, allowing the data to lead the reconstruction of MG-DE functions evolution. Via a parametrized redshift binning, one can perform complex MCMC analysis, whose outcome is to constrain the value of the MG-DE functions at each redshift bin. Our goal is to expand on the results in the literature, which focus on the $\mu(z)$ and $\Sigma(z)$ reconstruction relying on the EFT formalism, to reconstruct more complex functions of time and scale. I.e., we aim to explore current data constraints on the Horndeski functions in the α-basis [256]. At the moment, we are finalizing technical aspects to develop the necessary numerical tools and reproduce results in the literature. This study is being carried out in collaboration with Dr E. Bellini (INFN).

The quest for new physics beyond ΛCDM is an exciting research path that should be tackled by using different methodologies and data. In this context, 21cm observations present a unique and pivotal opportunity to constrain cosmological scales and redshifts that remain poorly probed by other observables.

ACKNOWLEDGEMENTS

APPENDIX

ANALYTICAL COMPUTATION OF THE MONOPOLE AND THE QUADRUPOLE

As part of the work in Chapter 4, following other results in the literature (see e.g. [402]) we analytically compute the first two coefficients of the Legendre polynomial expansion of $P_{21}(k)$. We start from Equation 4.8, i.e.

$$\hat{P}_\ell(z,k) = \frac{(2\ell+1)}{2} \int_{-1}^{1} \mathrm{d}\mu\, \mathcal{L}_\ell(\mu) \hat{P}_{21}(z,k,\mu) \tag{a.1}$$

that, substituting Equation 6.1, becomes

$$
\begin{aligned}
\hat{P}_\ell(z,k) &= \frac{(2\ell+1)}{2} \bar{T}_\mathrm{b}^2(z) P_\mathrm{m}(z,k) \int_{-1}^{1} \mathrm{d}\mu\, \mathcal{L}_\ell(\mu) \tilde{B}^2(z,k,\mu) \cdot \\
&\quad \cdot \left[b_\mathrm{HI}(z) + f(z)\,\mu^2 \right]^2 \\
&= \frac{(2\ell+1)}{2} \bar{T}_\mathrm{b}^2 P_\mathrm{m} \int_{-1}^{1} \mathrm{d}\mu\, \mathcal{L}_\ell(\mu)\, e^{-k^2 R_\mathrm{beam}^2 (1-\mu^2)} \cdot \\
&\quad \cdot \left[b_\mathrm{HI} + f\,\mu^2 \right]^2 \\
&= \frac{(2\ell+1)}{2} \bar{T}_\mathrm{b}^2 P_\mathrm{m}\, e^{-A} \int_{-1}^{1} \mathrm{d}\mu\, \mathcal{L}_\ell(\mu)\, e^{A\mu^2} \left[b_\mathrm{HI} + f\,\mu^2 \right]^2
\end{aligned}
\tag{a.2}
$$

where we defined $A = k^2 R_\mathrm{beam}^2$ and dropped the explicit dependencies on z and k for the sake of notation easiness.

Computing the monopole $\hat{P}_0$

Using $\mathcal{L}_0(\mu) = 1$ we obtain

$$\hat{P}_0 = \frac{\bar{T}_\mathrm{b}^2 P_\mathrm{m}}{2} e^{-A} \int_{-1}^{1} \mathrm{d}\mu\, e^{A\mu^2} \left(b_\mathrm{HI}^2 + 2 b_\mathrm{HI} f \mu^2 + f^2 \mu^4 \right). \tag{a.3}$$

The computation reduces to the following integrals

$$
\begin{aligned}
\int_{-1}^{1} \mathrm{d}\mu\, e^{A\mu^2} &= \frac{\sqrt{\pi}\, \mathrm{erfi}(\sqrt{A})}{\sqrt{A}}, \\
\int_{-1}^{1} \mathrm{d}\mu\, e^{A\mu^2} \mu^2 &= \frac{e^A}{A} - \frac{\sqrt{\pi}\, \mathrm{erfi}(\sqrt{A})}{2 A^{3/2}}, \\
\int_{-1}^{1} \mathrm{d}\mu\, e^{A\mu^2} \mu^4 &= \frac{3\sqrt{\pi}\, \mathrm{erfi}(\sqrt{A})}{4 A^{5/2}} + \frac{e^A (2A - 3)}{2 A^2},
\end{aligned}
\tag{a.4}
$$

where $\mathrm{erfi}(x)$ is the imaginary error function. Thus, we get the following final expression for $\hat{P}_0$

$$
\begin{aligned}
\hat{P}_0 = \frac{\bar{T}_b^2 \, P_m}{2} e^{-A} \Bigg[& b_{\mathrm{HI}}^2 \frac{\sqrt{\pi}\, \mathrm{erfi}(\sqrt{A})}{\sqrt{A}} + 2b_{\mathrm{HI}}f \left(\frac{e^A}{A} - \frac{\sqrt{\pi}\, \mathrm{erfi}(\sqrt{A})}{2A^{3/2}} \right) + \\
& + f^2 \left(\frac{3\sqrt{\pi}\, \mathrm{erfi}(\sqrt{A})}{4A^{5/2}} + \frac{e^A(2A-3)}{2A^2} \right) \Bigg].
\end{aligned}
$$
(a.5)

Computing the quadrupole $\hat{P}_2$

Using $\mathcal{L}_2(\mu) = \frac{3\mu^2}{2} - \frac{1}{2}$ we obtain

$$
\begin{aligned}
\hat{P}_2 &= \frac{5}{2} \bar{T}_b^2 \, P_m \, e^{-A} \int_{-1}^{1} d\mu \left(\frac{3\mu^2}{2} - \frac{1}{2} \right) e^{A\mu^2} \left[b_{\mathrm{HI}} + f\mu^2 \right]^2 \\
&= \frac{5}{2} \bar{T}_b^2 \, P_m \, e^{-A} \int_{-1}^{1} d\mu \, \frac{3\mu^2}{2} \, e^{A\mu^2} \left[b_{\mathrm{HI}} + f\mu^2 \right]^2 - \frac{5}{2} \hat{P}_0.
\end{aligned}
$$
(a.6)

Adding to the set of Equation a.4 the integral

$$
\int_{-1}^{1} d\mu \, e^{A\mu^2} \mu^6 = -\frac{15\sqrt{\pi}\, \mathrm{erfi}(\sqrt{A})}{8A^{7/2}} + \frac{e^A(15 - 10A + 4A^2)}{4A^3},
$$
(a.7)

we can compute the final expression

$$
\begin{aligned}
\hat{P}_2 = \frac{15\bar{T}_b^2 \, P_m}{4} e^{-A} \Bigg[& b_{\mathrm{HI}}^2 \left(\frac{e^A}{A} - \frac{\sqrt{\pi}\, \mathrm{erfi}(\sqrt{A})}{2A^{3/2}} \right) + 2b_{\mathrm{HI}}f \cdot \\
& \cdot \left(\frac{3\sqrt{\pi}\, \mathrm{erfi}(\sqrt{A})}{4A^{5/2}} + \frac{e^A(2A-3)}{2A^2} \right) + f^2 \left(-\frac{15\sqrt{\pi}\, \mathrm{erfi}(\sqrt{A})}{8A^{7/2}} + \right. \\
& \left. + \frac{e^A(15 - 10A + 4A^2)}{4A^3} \right) \Bigg] - \frac{5}{2} \hat{P}_0.
\end{aligned}
$$
(a.8)

The analytical expressions computed above are used in this thesis to compute numerical expectations for the 21cm power spectrum monopole and quadrupole in the codes CAMB/CosmoMC.

CONSTRAINTS ON THE NUISANCE PARAMETERS

In this appendix we present and comment on the constraints for the nuisance parameters, discussed in Chapter 4 and Chapter 6, where we investigated different implementations.

In Figure b.1 we test the effects of varying the nuisance parameter a_{T_b}, i.e. the amplitude of the brightness temperature, keeping fixed the HI bias b_{HI}. We observe that a_{T_b} is mildly correlated with the EFT parameters.

Figure b.2 shows the 1D and 2D marginalized posterior distributions of the nuisance parameters $[\bar{T}_b b_{\mathrm{HI}} \sigma_8]_i$ and $[\bar{T}_b f \sigma_8]_i$ ($i = \{a, b, c, d\}$), which describe the redshift evolution of $\bar{T}_b b_{\mathrm{HI}} \sigma_8(z)$ and $\bar{T}_b f \sigma_8(z)$. We consider $\hat{P}_{21}$ multipoles observations alone and combined with CMB. We find that the nuisances are constrained. The 2D contours show a clear degeneracy with the cosmological parameters, which is eased when we open the parameter space to the shot noise. As discussed above, adding the nuisance parameters we lose all the constraining power on A_s, but we recover it when we extend the data set to non-linear scales.

Figure b.3, instead, shows the marginalized posteriors for the shot noise value $P_{\mathrm{SN},i}$ at each redshift bin $i = \{1, \ldots, 6\}$. We obtain good constraints at low redshift ($i = \{1, 2\}$), where we have more data points, while in the highest bins ($i = \{3, 4, 5\}$), the shot noise results are unconstrained. $P_{\mathrm{SN},1}$ and $P_{\mathrm{SN},2}$ present a very mild degeneracy with the cosmological parameters. The shot noise and the other nuisances $\bar{T}_b b_{\mathrm{HI}} \sigma_8$ and $\bar{T}_b f \sigma_8$ are, instead, uncorrelated.
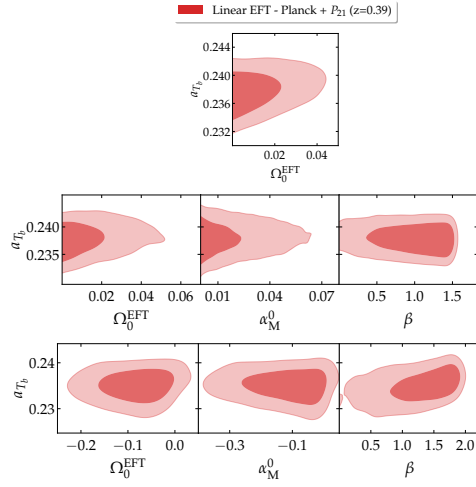
Figure b.1: Joint constraints (68% and 95% confidence regions) on EFT and nuisance parameters for a *pure* linear (upper row), an exponential (second row) and an exponential with negative running of the Planck mass (third row) EFT model, on a ΛCDM background. Here the label Planck 2018 stands for TT, TE, EE + lowE + lensing while the label $P_{21}(z = 0.39)$ stands for the 21cm power spectrum likelihood at redshift $z = 0.39$. Results relative to the analysis in Chapter 6.
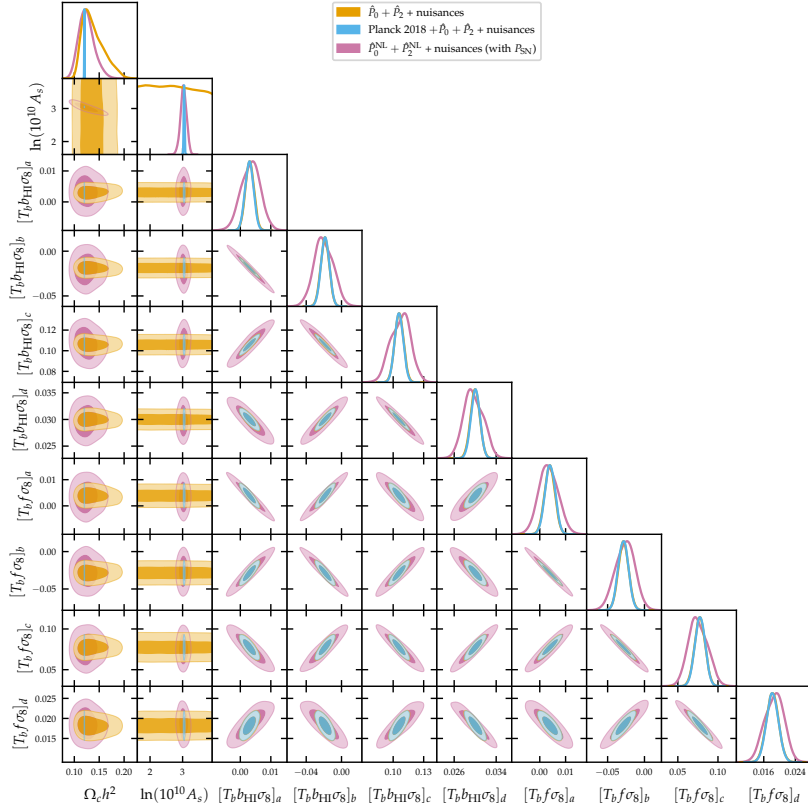
Figure b.2: Joint constraints (68% and 95% confidence regions) and marginalized posterior distributions on cosmological and nuisance parameters. Here, the label "Planck 2018" stands for TT, TE, EE + lowE + lensing, while the label "$\hat{P}_0 + \hat{P}_2$" stands for the baseline tomographic data set for the monopole and the quadrupole combined and with multipole covariance taken into account. The label "$\hat{P}_0^{\mathrm{NL}} + \hat{P}_2^{\mathrm{NL}}$" indicates that the full non-linear data set has been used. The label "nuisances" indicates that we vary the nuisance parameters along with the cosmological ones. Results relative to the analysis in Chapter 4.
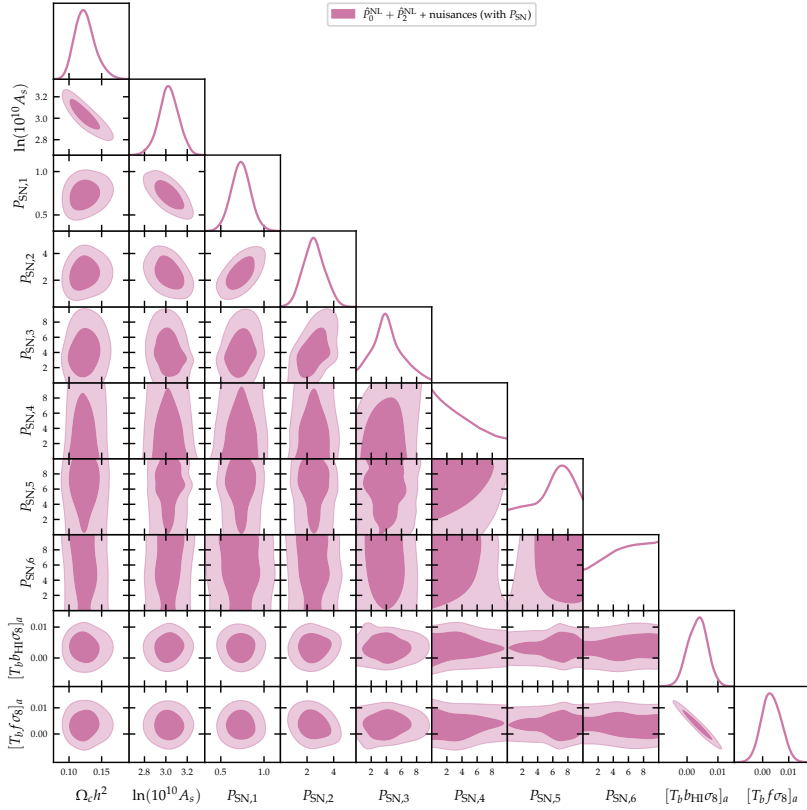
Figure b.3: Joint constraints (68% and 95% confidence regions) and marginalized posterior distributions on cosmological parameters and the shot noise at different redshifts. Here, the label "$\hat{P}_0^{\mathrm{NL}} + \hat{P}_2^{\mathrm{NL}}$" indicates that the full non-linear data set has been used. The label "nuisances" indicates that we vary the nuisance parameters along with the cosmological ones. Results relative to the analysis in Chapter 4.

C

ON THE IMPACT OF INCLUDING THE ALCOCK-PACZYNSKI EFFECTS

With respect to the analysis in Chapter 4, in Chapter 5 we extended our likelihood code to include the Alcock-Paczynski distortions, which are used in other works (e.g. [68, 156, 286]). We neglected AP effects in the first approximation because we assumed to know the true cosmology, given that it is the one we input when constructing the mock data set. In this section, we give an overview of how the cosmological parameter constraints are affected by the addition of AP effects.

Contrary to what we naively expected, implementing the AP modifications significantly improves the constraints. In the upper panel of Figure c.1, we compare the effects of different mock data sets. Our reference (orange lines and contours) is the 21cm power spectrum monopole ($\hat{P}_0$) and quadrupole ($\hat{P}_2$) mock data set that we construct in Chapter 4. This data set forecasts SKAO observations in multipole redshift bins in the range 0 - 3, i.e. for six bins centered at $\{0.25, 0.75, 1.25, 1.75, 2.25, 2.75\}$ and with a width of $\Delta z = 0.5$. The nuisances parameters for this data set are $\bar{T}_b b_{HI} \sigma_8$, $\bar{T}_b f \sigma_8$, and the HI shot noise, for the non-linear 21cm power spectrum.

Using the exact same framework, but implementing also the AP distortions of the amplitude and of the wave vectors as described in Section 5.1.1 (light blue contours), we find a crucially improved constraining power. E.g., for $\Omega_c h^2$ with only 21cm observations, we recover the Planck constraint (dashed green lines and contours). On H_0, instead, we find even better constraints than Planck. When adding the nuisances (pink contours), the improvement is reduced, although still significantly better than the no AP case. We believe that the extra dependence on $H(z)$ that is introduced in the observable with the AP modifications is the cause of the improved constraining power.

Dealing with mock observations fabricated by ourselves, we have the advantage of knowing the true cosmology. We, thus, further test the impact of AP by creating a data set with a different value of $\Omega_c h^2 = 0.13$. We, however, do not change the fiducial cosmology, for which $\Omega_c h^2 = 0.12011$. Running the MCMC analysis on this data set we find consistent results. The $\Omega_c h^2$ constraint is pushed towards the true value, resulting in a constraint in between the true value and the assumed fiducial one. The errors, instead, are left unchanged, although the 2D contours are rigidly shifted. Thus, it seems that assuming the wrong cosmology impacts only the mean marginalized values of the parameters.

However, the smoking gun of having assumed the wrong cosmology is the probability distribution of the AP parameters themselves. Although we do not show the results here, we implemented the time-dependent $\alpha_\perp$ and $\alpha_\parallel$ as derived parameters and computed the marginalized constraints. We find that when the true cosmology matches the fiducial one, the $\alpha_\perp$, and $\alpha_\parallel$ marginalized posteriors are centered around one. When, instead, the true cosmology is not the assumed one, although still compatible with one the constraints, both 1D
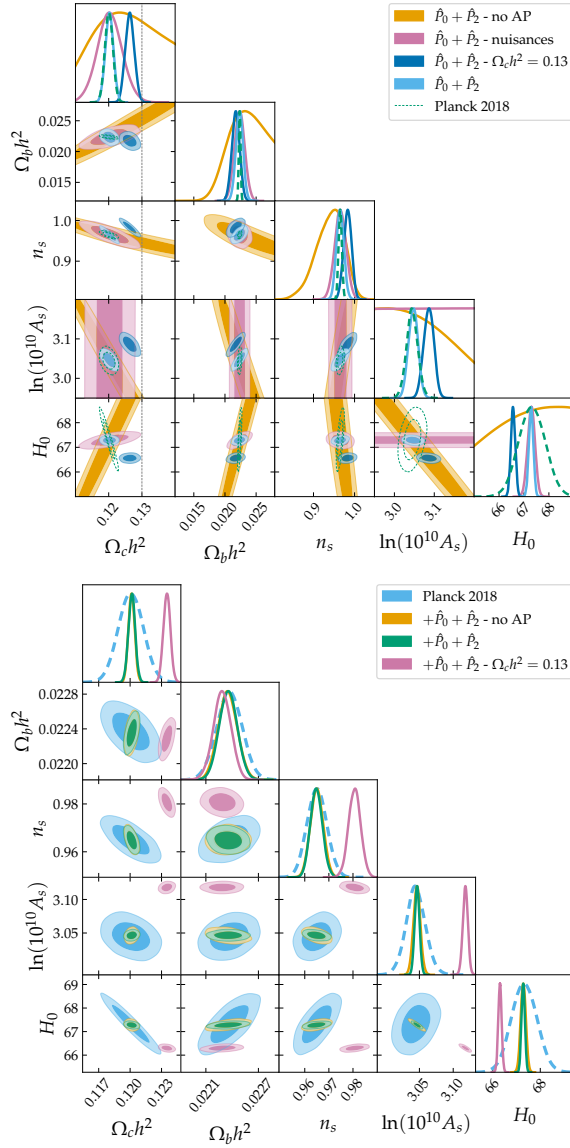
Figure c.1: Joint constraints (68% and 95% confidence regions) and marginalized posterior distributions on a subset of the cosmological parameters. We show results for the 21cm multipoles alone (upper panel) and combined with CMB observations (lower panel). The label "Planck 2018" (dashed lines) stands for TT, TE, EE + lowE + lensing, while the label "$\hat{P}_0 + \hat{P}_2$" stands for the forecasted 21cm non-linear power spectrum monopole and quadrupole observations, with and without ("no AP") AP effects taken into account. "$\hat{P}_0 + \hat{P}_2 - \Omega_c h^2 = 0.13$" labels the results obtained for a mock data set with a value of $\Omega_c h^2$ different from the assumed fiducial cosmology. The label "nuis." indicates that we vary the nuisance parameters along with the cosmological ones.

and 2D, are clearly shifted. Thus, one can test their assumptions by looking at the AP parameters constraints.

The lower panel of Figure c.1 shows the results for the same exercise, but combining 21cm observations with Planck data.

We conclude that even when the whole set of cosmological parameters is used, the AP distortions are crucial not only to take into account our lack of knowledge of the true underlying cosmology but also to increase the constraining power on the cosmological parameters in matter power spectrum dependent probes as the 21cm IM one.

d

To test the procedure we follow to construct the mock data sets in Chapter 4 and Chapter 5, we compare our predictions to the measured cross-correlation data published in [61].

As in Section 5.3.3, we adjust the parameters of our formalism to mimic MeerKAT observations in the redshift bin centered at $z = 0.43$ and with $\Delta z = 0.059$. We find that with our pipeline we predict fewer k-bin in a wider scale range and a slightly different value for the brightness temperature, due to different Ω_{HI}. Correcting for the brightness temperature results in cross-correlation power spectrum values more in agreement with observations (Figure d.1). However, this is not enough to reproduce the observed signal-to-noise ratio. Indeed, we find that varying the brightness temperature changes the power spectrum and the errors consistently, not impacting the signal-to-noise. Instead, adjusting the k-bin width to match the one in [61] is enough to better reproduce the observed signal-to-noise ratio, as shown in Figure d.2.

We conclude that, compared to the state of the art, the pipeline we adopt in this work is consistent with real observational data. We are, however, more optimistic about the accessible scales and bin widths. Differences in the predicted power spectrum amplitude, i.e. the brightness temperature, are taken into account when opening the parameter space to the nuisance parameters.
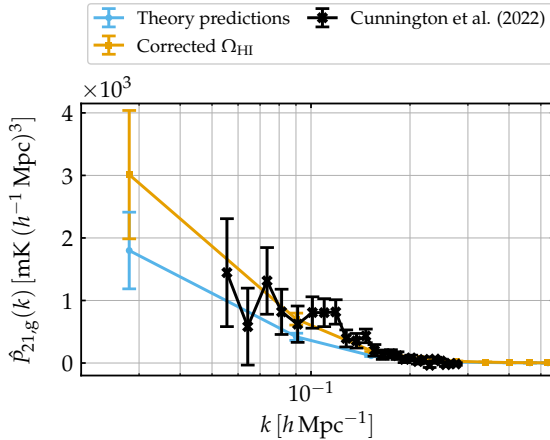
Figure d.1: Observed and predicted 21cm MeerKAT observations in cross-correlation with WiggleZ galaxy clustering.
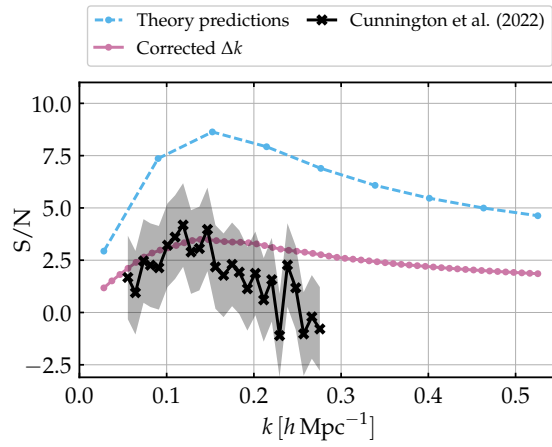
Figure d.2: Signal-to-noise ratio as a function of k. We compare real data observations ("Cunnington et al. (2022)"), with the signal-to-noise predicted by the formalism adopted in this work. The gray shaded area shows the 2σ region for the observed signal-to-noise.

BIBLIOGRAPHY

[1] Adam G. Riess et al. «Observational Evidence from Supernovae for an Accelerating Universe and a Cosmological Constant.» In: AJ 116.3 (Sept. 1998), pp. 1009–1038. DOI: 10.1086/300499. arXiv: astro-ph/9805201 [astro-ph].

[2] S. Perlmutter et al. «Measurements of Ω and Λ from 42 High-Redshift Supernovae.» In: ApJ 517.2 (June 1999), pp. 565–586. DOI: 10.1086/307221. arXiv: astro-ph/9812133 [astro-ph].

[3] Steven Weinberg. «The cosmological constant problem.» In: *Reviews of Modern Physics* 61.1 (Jan. 1989). Ed. by Jong-Ping Hsu and D. Fine, pp. 1–23. DOI: 10.1103/RevModPhys.61.1.

[4] "" Planck Collaboration VI. «VI - Cosmological parameters.» In: A&A 641, A6 (Sept. 2020), A6. DOI: 10.1051/0004-6361/201833910. arXiv: 1807.06209 [astro-ph.CO].

[5] T. M. C. Abbott et al. «Dark Energy Survey Year 1 Results: Constraints on Extended Cosmological Models from Galaxy Clustering and Weak Lensing.» In: *Phys. Rev. D* 99.12, 123505 (June 2019), p. 123505. DOI: 10.1103/PhysRevD.99.123505. arXiv: 1810.02499 [astro-ph.CO].

[6] H. Hildebrandt et al. «KiDS-450: Cosmological parameter constraints from tomographic weak gravitational lensing.» In: *Mon. Not. Roy. Astron. Soc.* 465 (2017), p. 1454. DOI: 10.1093/mnras/stw2805. arXiv: 1606.05338 [astro-ph.CO].

[7] Adam G. Riess et al. «Milky Way Cepheid Standards for Measuring Cosmic Distances and Application to Gaia DR2: Implications for the Hubble Constant.» In: *Astrophys. J.* 861.2 (2018), p. 126. DOI: 10.3847/1538-4357/aac82e. arXiv: 1804.10655 [astro-ph.CO].

[8] Adam G. Riess, Stefano Casertano, Wenlong Yuan, Lucas M. Macri, and Dan Scolnic. «Large Magellanic Cloud Cepheid Standards Provide a 1% Foundation for the Determination of the Hubble Constant and Stronger Evidence for Physics beyond ΛCDM.» In: ApJ 876.1, 85 (May 2019), p. 85. DOI: 10.3847/1538-4357/ab1422. arXiv: 1903.07603 [astro-ph.CO].

[9] Kenneth C. Wong et al. «HoLiCOW XIII. A 2.4% measurement of H_0 from lensed quasars: 5.3σ tension between early and late-Universe probes.» In: *arXiv e-prints*, arXiv:1907.04869 (July 2019). arXiv: 1907.04869 [astro-ph.CO].

[10] Wendy L. Freedman et al. «The Carnegie-Chicago Hubble Program. VIII. An Independent Determination of the Hubble Constant Based on the Tip of the Red Giant Branch.» In: *arXiv e-prints*, arXiv:1907.05922 (July 2019). arXiv: 1907.05922 [astro-ph.CO].

[11] L. Verde, T. Treu, and A. G. Riess. «Tensions between the Early and the Late Universe.» In: *Nature Astron.* 3 (July 2019), p. 891. DOI: 10.1038/s41550-019-0902-0. arXiv: 1907.10625 [astro-ph.CO].

[12]   Pedro G. Ferreira. «Cosmological Tests of Gravity.» In: *Ann. Rev. Astron. Astrophys.* 57 (2019), pp. 335–374. DOI: 10.1146/annurev-astro-091918-104423. arXiv: 1902.10503 [astro-ph.CO].

[13]   Mustapha Ishak. «Testing General Relativity in Cosmology.» In: *Living Rev. Rel.* 22.1 (2019), p. 1. DOI: 10.1007/s41114-018-0017-4. arXiv: 1806.10122 [astro-ph.CO].

[14]   Jiamin Hou, Julian Bautista, Maria Berti, Carolina Cuesta-Lazaro, César Hernández-Aguayo, Tilman Tröster, and Jinglan Zheng. «Cosmological Probes of Structure Growth and Tests of Gravity.» In: *Universe* 9.7 (2023). ISSN: 2218-1997. DOI: 10.3390/universe9070302. URL: https://www.mdpi.com/2218-1997/9/7/302.

[15]   Edmund Bertschinger. «On the Growth of Perturbations as a Test of Dark Energy.» In: *Astrophys. J.* 648 (2006), pp. 797–806. DOI: 10.1086/506021. arXiv: astro-ph/0604485.

[16]   Luca Amendola, Martin Kunz, and Domenico Sapone. «Measuring the dark side (with weak lensing).» In: *JCAP* 04 (2008), p. 013. DOI: 10.1088/1475-7516/2008/04/013. arXiv: 0704.2421 [astro-ph].

[17]   Levon Pogosian and Alessandra Silvestri. «The pattern of growth in viable f(R) cosmologies.» In: *Phys. Rev. D* 77 (2008). [Erratum: Phys.Rev.D 81, 049901 (2010)], p. 023503. DOI: 10.1103/PhysRevD.77.023503. arXiv: 0709.0296 [astro-ph].

[18]   Gong-Bo Zhao, Levon Pogosian, Alessandra Silvestri, and Joel Zylberberg. «Searching for modified growth patterns with tomographic surveys.» In: Phys. Rev. D 79.8, 083513 (2009), p. 083513. DOI: 10.1103/PhysRevD.79.083513. arXiv: 0809.3791 [astro-ph].

[19]   Pengjie Zhang, Michele Liguori, Rachel Bean, and Scott Dodelson. «Probing Gravity at Cosmological Scales by Measurements which Test the Relationship between Gravitational Lensing and Matter Overdensity.» In: *Phys. Rev. Lett.* 99 (2007), p. 141302. DOI: 10.1103/PhysRevLett.99.141302. arXiv: 0704.1932 [astro-ph].

[20]   Giulia Gubitosi, Federico Piazza, and Filippo Vernizzi. «The effective field theory of dark energy.» In: *Journal of Cosmology and Astro-Particle Physics* 2013.2, 032 (Feb. 2013), p. 032. DOI: 10.1088/1475-7516/2013/02/032. arXiv: 1210.0201 [hep-th].

[21]   Jolyon Bloomfield, Éanna É. Flanagan, Minjoon Park, and Scott Watson. «Dark energy or modified gravity? An effective field theory approach.» In: *Journal of Cosmology and Astro-Particle Physics* 2013.8, 010 (Aug. 2013), p. 010. DOI: 10.1088/1475-7516/2013/08/010. arXiv: 1211.7054 [astro-ph.CO].

[22]   B. P. Abbott et al. «Observation of Gravitational Waves from a Binary Black Hole Merger.» In: *Phys. Rev. Lett.* 116 (6 Feb. 2016), p. 061102. DOI: 10.1103/PhysRevLett.116.061102. arXiv: 1602.03837.

[23]   B. P. Abbott et al. «Properties of the Binary Black Hole Merger GW150914.» In: *Phys. Rev. Lett.* 116 (24 June 2016), p. 241102. DOI: 10.1103/PhysRevLett.116.241102. arXiv: 1602.03840.

[24] B. P. Abbott et al. «GWTC-1: A Gravitational-Wave Transient Catalog of Compact Binary Mergers Observed by LIGO and Virgo during the First and Second Observing Runs.» In: *Phys. Rev. X* 9 (3 Sept. 2019), p. 031040. DOI: 10.1103/PhysRevX.9.031040.

[25] R. Abbott et al. «GWTC-2: Compact Binary Coalescences Observed by LIGO and Virgo during the First Half of the Third Observing Run.» In: *Phys. Rev. X* 11 (2 June 2021), p. 021053. DOI: 10.1103/PhysRevX.11.021053.

[26] B. Sathyaprakash et al. «Scientific objectives of Einstein Telescope.» In: *Classical and Quantum Gravity* 29.12 (2012), p. 124013. DOI: 10.1088/0264-9381/29/12/124013. arXiv: 1206.0331.

[27] David Reitze, Rana X Adhikari, Stefan Ballmer, Barry Barish, Lisa Barsotti, GariLynn Billingsley, Duncan A Brown, Yanbei Chen, Dennis Coyne, Robert Eisenstein, et al. «Cosmic explorer: the US contribution to gravitational-wave astronomy beyond LIGO.» In: *arXiv preprint arXiv:1907.04833* (2019).

[28] Pau Amaro-Seoane, Heather Audley, Stanislav Babak, John Baker, Enrico Barausse, Peter Bender, Emanuele Berti, Pierre Binetruy, Michael Born, Daniele Bortoluzzi, et al. «Laser interferometer space antenna.» In: *arXiv preprint arXiv:1702.00786* (2017). DOI: https://doi.org/10.48550/arXiv.1702.00786.

[29] Kentaro Somiya. «Detector configuration of KAGRA - the Japanese cryogenic gravitational-wave detector.» In: *Classical and Quantum Gravity* 29.12 (2012), p. 124007. DOI: 10.1088/0264-9381/29/12/124007. arXiv: 1111.7185.

[30] C. S. Unnikrishnan. «IndIGO and LIGO-India: Scope and Plans for Gravitational Wave Research and Precision Metrology in India.» In: *International Journal of Modern Physics D* 22.01 (2013), p. 1341010. DOI: 10.1142/S0218271813410101. arXiv: 1510.06059.

[31] Mariana Vargas-Magaña, David D. Brooks, Michael M. Levi, and Gregory G. Tarle. «Unraveling the Universe with DESI.» In: *53rd Rencontres de Moriond on Cosmology*. 2018, pp. 11–18. arXiv: 1901.01581 [astro-ph.IM].

[32] Amir Aghamousa et al. *The DESI Experiment Part II: Instrument Design*. Oct. 2016. arXiv: 1611.00037 [astro-ph.IM].

[33] Luca Amendola et al. «Cosmology and fundamental physics with the Euclid satellite.» In: *Living Rev. Rel.* 21.1 (2018), p. 2. DOI: 10.1007/s41114-017-0010-3. arXiv: 1606.00180 [astro-ph.CO].

[34] A. Blanchard et al. «Euclid preparation: VII. Forecast validation for Euclid cosmological probes.» In: *Astron. Astrophys.* 642 (2020), A191. DOI: 10.1051/0004-6361/202038071. arXiv: 1910.09273 [astro-ph.CO].

[35] Jonathan R. Pritchard and Abraham Loeb. «21 cm cosmology in the 21st century.» In: *Reports on Progress in Physics* 75.8, 086901 (Aug. 2012), p. 086901. DOI: 10.1088/0034-4885/75/8/086901. arXiv: 1109.6012 [astro-ph.CO].

[36] R. Ansari, J. E. Campagne, P. Colom, J. M. Le Goff, C. Magneville, J. M. Martin, M. Moniez, J. Rich, and C. Yèche. «21 cm observation of large-scale structures at z ~1. Instrument sensitivity and foreground subtraction.» In: A&A 540, A129 (Apr. 2012), A129. DOI: 10.1051/0004-6361/201117837. arXiv: 1108.1474 [astro-ph.CO].

[37] Mario G. Santos et al. «Cosmology from a SKA HI intensity mapping survey.» In: *PoS* AASKA14 (2015). Ed. by Tyler L. Bourke et al., p. 019. DOI: 10.22323/1.215.0019. arXiv: 1501.03989 [astro-ph.CO].

[38] Philip Bull et al. «Beyond Λ CDM: Problems, solutions, and the road ahead.» In: *Physics of the Dark Universe* 12 (June 2016), pp. 56–99. DOI: 10.1016/j.dark.2016.02.001. arXiv: 1512.05356 [astro-ph.CO].

[39] Steven Furlanetto, S. Peng Oh, and Frank Briggs. «Cosmology at Low Frequencies: The 21 cm Transition and the High-Redshift Universe.» In: *Phys. Rept.* 433 (2006), pp. 181–301. DOI: 10.1016/j.physrep.2006.08.002. arXiv: astro-ph/0608032.

[40] Kevin Bandura et al. «Canadian Hydrogen Intensity Mapping Experiment (CHIME) Pathfinder.» In: *Proc. SPIE Int. Soc. Opt. Eng.* Society of Photo-Optical Instrumentation Engineers (SPIE) Conference Series 9145, 914522 (July 2014). Ed. by Larry M. Stepp, Roberto Gilmozzi, and Helen J. Hall, p. 22. DOI: 10.1117/12.2054950. arXiv: 1406.2288 [astro-ph.IM].

[41] CHIME Collaboration et al. «Detection of Cosmological 21 cm Emission with the Canadian Hydrogen Intensity Mapping Experiment.» In: *arXiv e-prints*, arXiv:2202.01242 (Feb. 2022), arXiv:2202.01242. arXiv: 2202.01242 [astro-ph.CO].

[42] L. B. Newburgh et al. «HIRAX: A Probe of Dark Energy and Radio Transients.» In: *Proc. SPIE Int. Soc. Opt. Eng.* Society of Photo-Optical Instrumentation Engineers (SPIE) Conference Series 9906, 99065X (Aug. 2016). Ed. by Helen J. Hall, Roberto Gilmozzi, and Heather K. Marshall, p. 99065X. DOI: 10.1117/12.2234286. arXiv: 1607.02059 [astro-ph.IM].

[43] K. W. Masui et al. «Measurement of 21 cm brightness fluctuations at z ~ 0.8 in cross-correlation.» In: *Astrophys. J. Lett.* 763 (2013), p. L20. DOI: 10.1088/2041-8205/763/1/L20. arXiv: 1208.0331 [astro-ph.CO].

[44] Laura Wolz et al. «H I constraints from the cross-correlation of eBOSS galaxies and Green Bank Telescope intensity maps.» In: MNRAS 510.3 (Mar. 2022), pp. 3495–3511. ISSN: 0035-8711. DOI: 10.1093/mnras/stab3621. arXiv: 2102.04946 [astro-ph.CO].

[45] Wenkai Hu, Xin Wang, Fengquan Wu, Yougang Wang, Pengjie Zhang, and Xuelei Chen. «Forecast for FAST: from Galaxies Survey to Intensity Mapping.» In: *Mon. Not. Roy. Astron. Soc.* 493.4 (Apr. 2020), pp. 5854–5870. DOI: 10.1093/mnras/staa650. arXiv: 1909.10946 [astro-ph.CO].

[46] Somnath Bharadwaj, B. B. Nath, Biman B. Nath, and Shiv K. Sethi. «Using HI to probe large scale structures at z ~ 3.» In: *J. Astrophys. Astron.* 22 (2001), p. 21. DOI: 10.1007/BF02933588. arXiv: astro-ph/0003200.

[47] Richard A. Battye, Rod D. Davies, and Jochen Weller. «Neutral hydrogen surveys for high redshift galaxy clusters and proto-clusters.» In: *Mon. Not. Roy. Astron. Soc.* 355 (2004), pp. 1339–1347. DOI: 10.1111/j.1365-2966.2004.08416.x. arXiv: astro-ph/0401340.

[48] Matthew McQuinn, Oliver Zahn, Matias Zaldarriaga, Lars Hernquist, and Steven R. Furlanetto. «Cosmological parameter estimation using 21 cm radiation from the epoch of reionization.» In: *Astrophys. J.* 653 (2006), pp. 815–830. DOI: 10.1086/505167. arXiv: astro-ph/0512263.

[49] Tzu-Ching Chang, Ue-Li Pen, Jeffrey B. Peterson, and Patrick Mc-Donald. «Baryon Acoustic Oscillation Intensity Mapping as a Test of Dark Energy.» In: *Phys. Rev. Lett.* 100 (2008), p. 091303. DOI: 10.1103/PhysRevLett.100.091303. arXiv: 0709.3672 [astro-ph].

[50] Hee-Jong Seo, Scott Dodelson, John Marriner, Dave Mcginnis, Albert Stebbins, Chris Stoughton, and Alberto Vallinotto. «A ground-based 21cm Baryon acoustic oscillation survey.» In: *Astrophys. J.* 721 (2010), pp. 164–173. DOI: 10.1088/0004-637X/721/1/164. arXiv: 0910.5007 [astro-ph.CO].

[51] R. A. Battye, I. W. A. Browne, C. Dickinson, G. Heron, B. Maffei, and A. Pourtsidou. «HI intensity mapping : a single dish approach.» In: *Mon. Not. Roy. Astron. Soc.* 434.2 (July 2013), pp. 1239–1256. ISSN: 0035-8711. DOI: 10.1093/mnras/stt1082. arXiv: 1209.0343 [astro-ph.CO].

[52] Ely D. Kovetz et al. *Line-Intensity Mapping: 2017 Status Report*. Sept. 2017. arXiv: 1709.09066 [astro-ph.CO].

[53] Tzu-Ching Chang, Ue-Li Pen, Kevin Bandura, and Jeffrey B. Peterson. «An intensity map of hydrogen 21-cm emission at redshift z~0.8.» In: Nature 466.7305 (July 2010), pp. 463–465. DOI: 10.1038/nature09187.

[54] C. J. Anderson et al. «Low-amplitude clustering in low-redshift 21-cm intensity maps cross-correlated with 2dF galaxy densities.» In: MNRAS 476.3 (May 2018), pp. 3382–3392. DOI: 10.1093/mnras/sty346. arXiv: 1710.00424 [astro-ph.CO].

[55] Steven Cunnington. «Detecting the power spectrum turnover with H I intensity mapping.» In: MNRAS 512.2 (May 2022), pp. 2408–2425. DOI: 10.1093/mnras/stac576. arXiv: 2202.13828 [astro-ph.CO].

[56] Sourabh Paul, Mario G. Santos, Zhaoting Chen, and Laura Wolz. *A first detection of neutral hydrogen intensity mapping on Mpc scales at $z \approx 0.32$ and $z \approx 0.44$*. Jan. 2023. DOI: 10.48550/ARXIV.2301.11943. arXiv: 2301.11943 [astro-ph.CO]. URL: https://arxiv.org/abs/2301.11943.

[57] "" SKA Cosmology SWG. «Cosmology with Phase 1 of the Square Kilometre Array: Red Book 2018: Technical specifications and performance forecasts.» In: *Publ. Astron. Soc. Austral.* 37 (2020), e007. DOI: 10.1017/pasa.2019.51. arXiv: 1811.02743 [astro-ph.CO].

[58] Mario G. Santos et al. «MeerKLASS: MeerKAT Large Area Synoptic Survey.» In: *MeerKAT Science: On the Pathway to the SKA*. Sept. 2017. arXiv: 1709.06099 [astro-ph.CO].

[59]   Jingying Wang et al. «HI intensity mapping with MeerKAT: Calibration pipeline for multi-dish autocorrelation observations.» In: *arXiv preprint arXiv:2011.13789* (Nov. 2020). DOI: 10.1093/mnras/stab1365. arXiv: 2011.13789 [astro-ph.CO].

[60]   Melis O. Irfan, Philip Bull, Mario G. Santos, Jingying Wang, Keith Grainge, Yichao Li, Isabella P. Carucci, Marta Spinelli, and Steven Cunnington. «Measurements of the diffuse Galactic synchrotron spectral index and curvature from MeerKLASS pilot data.» In: MNRAS 509.4 (Feb. 2022), pp. 4923–4939. DOI: 10.1093/mnras/stab3346. arXiv: 2111.08517 [astro-ph.GA].

[61]   Steven Cunnington et al. *HI intensity mapping with MeerKAT: power spectrum detection in cross-correlation with WiggleZ galaxies*. June 2022. arXiv: 2206.01579 [astro-ph.CO].

[62]   David Alonso, Philip Bull, Pedro G. Ferreira, Roy Maartens, and M. Santos. «Ultra large-scale cosmology in next-generation experiments with single tracers.» In: *Astrophys. J.* 814.2 (2015), p. 145. DOI: 10.1088/0004-637X/814/2/145. arXiv: 1505.07596 [astro-ph.CO].

[63]   L. Wolz, C. Tonini, C. Blake, and J. S. B. Wyithe. «Intensity Mapping Cross-Correlations: Connecting the Largest Scales to Galaxy Evolution.» In: *Mon. Not. Roy. Astron. Soc.* 458.3 (Mar. 2016), pp. 3399–3410. ISSN: 0035-8711. DOI: 10.1093/mnras/stw535. arXiv: 1512.04189 [astro-ph.CO].

[64]   Isabella P. Carucci, Melis O. Irfan, and Jérôme Bobin. «Recovery of 21 cm intensity maps with sparse component separation.» In: *Mon. Not. Roy. Astron. Soc.* 499.1 (Sept. 2020), pp. 304–319. DOI: 10.1093/mnras/staa2854. arXiv: 2006.05996 [astro-ph.CO].

[65]   Siyambonga D. Matshawule, Marta Spinelli, Mario G. Santos, and Sibonelo Ngobese. «Hi intensity mapping with MeerKAT: Primary beam effects on foreground cleaning.» In: *Monthly Notices of the Royal Astronomical Society* 506.4 (Nov. 2020), pp. 5075–5092. DOI: 10.1093/mnras/stab1688. arXiv: 2011.10815 [astro-ph.CO].

[66]   Melis O. Irfan and Philip Bull. «Cleaning foregrounds from single-dish 21 cm intensity maps with Kernel principal component analysis.» In: *Mon. Not. Roy. Astron. Soc.* 508.3 (2021), pp. 3551–3568. DOI: 10.1093/mnras/stab2855. arXiv: 2107.02267 [astro-ph.CO].

[67]   Steven Cunnington, Melis O. Irfan, Isabella P. Carucci, Alkistis Pourtsidou, and Jérôme Bobin. «21-cm foregrounds and polarization leakage: cleaning and mitigation strategies.» In: *Mon. Not. Roy. Astron. Soc.* 504.1 (June 2021), pp. 208–227. DOI: 10.1093/mnras/stab856. arXiv: 2010.02907 [astro-ph.CO].

[68]   Paula S. Soares, Steven Cunnington, Alkistis Pourtsidou, and Chris Blake. «Power spectrum multipole expansion for HI intensity mapping experiments: unbiased parameter estimation.» In: *Mon. Not. Roy. Astron. Soc.* 502.2 (2021), pp. 2549–2564. DOI: 10.1093/mnras/stab027. arXiv: 2008.12102 [astro-ph.CO].

[69] Paula S. Soares, Catherine A. Watkinson, Steven Cunnington, and Alkistis Pourtsidou. «Gaussian Process Regression for foreground removal in H i Intensity Mapping experiments.» In: *Mon. Not. Roy. Astron. Soc.* 510.4 (2022), pp. 5872–5890. DOI: 10.1093/mnras/stab2594. arXiv: 2105.12665 [astro-ph.CO].

[70] Marta Spinelli, Isabella P. Carucci, Steven Cunnington, Stuart E. Harper, Melis O. Irfan, José Fonseca, Alkistis Pourtsidou, and Laura Wolz. «SKAO H I intensity mapping: blind foreground subtraction challenge.» In: MNRAS 509.2 (Jan. 2022), pp. 2048–2074. DOI: 10.1093/mnras/stab3064. arXiv: 2107.10814 [astro-ph.CO].

[71] Alkistis Pourtsidou. *Interferometric HI intensity mapping: perturbation theory predictions and foreground removal effects*. June 2022. arXiv: 2206.14727 [astro-ph.CO].

[72] Michael R Nolta, EL Wright, L Page, CL Bennett, M Halpern, G Hinshaw, N Jarosik, A Kogut, M Limon, SS Meyer, et al. «First year Wilkinson microwave anisotropy probe observations: dark energy induced correlation with radio sources.» In: *The Astrophysical Journal* 608.1 (2004), p. 10. DOI: 10.1086/386536.

[73] Shirley Ho, Christopher Hirata, Nikhil Padmanabhan, Uros Seljak, and Neta Bahcall. «Correlation of CMB with large-scale structure. I. Integrated Sachs-Wolfe tomography and cosmological implications.» In: *Physical Review D* 78.4 (2008), p. 043519.

[74] Christopher M Hirata, Shirley Ho, Nikhil Padmanabhan, Uroš Seljak, and Neta A Bahcall. «Correlation of CMB with large-scale structure. II. Weak lensing.» In: *Physical Review D* 78.4 (2008), p. 043520.

[75] A. Raccanelli, A. Bonaldi, M. Negrello, S. Matarrese, G. Tormen, and G. De Zotti. «A reassessment of the evidence of the Integrated Sachs-Wolfe effect through the WMAP-NVSS correlation.» In: *Monthly Notices of the Royal Astronomical Society* 386.4 (2008), pp. 2161–2166. DOI: 10.1111/j.1365-2966.2008.13189.x. arXiv: 0802.0084.

[76] Alvise Raccanelli et al. «Cosmological measurements with forthcoming radio continuum surveys.» In: *Monthly Notices of the Royal Astronomical Society* 424.2 (Aug. 2012), pp. 801–819. DOI: 10.1111/j.1365-2966.2012.20634.x. arXiv: 1108.0930 [astro-ph.CO].

[77] Alvise Raccanelli et al. «Probing primordial non-Gaussianity via iSW measurements with SKA continuum surveys.» In: *Journal of Cosmology and Astroparticle Physics* 2015.1, 042 (Jan. 2015), p. 042. DOI: 10.1088/1475-7516/2015/01/042. arXiv: 1406.0010 [astro-ph.CO].

[78] F. Bianchini et al. «Cross-correlation between the CMB lensing potential measured by Planck and high-z sub-mm galaxies detected by the Herschel-ATLAS survey.» In: *Astrophys. J.* 802.1 (2015), p. 64. DOI: 10.1088/0004-637X/802/1/64. arXiv: 1410.4502 [astro-ph.CO].

[79] Federico Bianchini and Andrea Lapi. «Cross-correlation between cosmological and astrophysical datasets: the Planck and Herschel case.» In: *IAU Symp.* 306 (2014), pp. 202–205. DOI: 10.1017/S1743921314013647.

[80] Federico Bianchini et al. «Toward a tomographic analysis of the cross-correlation between Planck CMB lensing and H-ATLAS galaxies.» In: *Astrophys. J.* 825.1 (2016), p. 24. DOI: 10.3847/0004-637X/825/1/24. arXiv: 1511.05116 [astro-ph.CO].

[81] Suvodip Mukherjee, Benjamin D. Wandelt, and Joseph Silk. «Multi-messenger tests of gravity with weakly lensed gravitational waves.» In: *Phys. Rev. D* 101 (10 May 2020), p. 103509. DOI: 10.1103/PhysRevD.101.103509.

[82] Ke Fang, Arka Banerjee, Eric Charles, and Yuuki Omori. «A Cross-Correlation Study of High-energy Neutrinos and Tracers of Large-Scale Structure.» In: *The Astrophysical Journal* 894.2 (2020), p. 112.

[83] Héctor J Martínez, Manuel E Merchán, Carlos A Valotto, and Diego G Lambas. «Quasar-galaxy and AGN-galaxy cross-correlations.» In: *The Astrophysical Journal* 514.2 (1999), p. 558.

[84] Bhuvnesh Jain, Ryan Scranton, and Ravi K. Sheth. «Quasar—galaxy and galaxy—galaxy cross-correlations: model predictions with realistic galaxies.» In: *Monthly Notices of the Royal Astronomical Society* 345.1 (Oct. 2003), pp. 62–70. ISSN: 0035-8711. DOI: 10.1046/j.1365-8711.2003.06965.x.

[85] Xiaohu Yang, H. J. Mo, Frank C. van den Bosch, Simone M. Weinmann, Cheng Li, and Y. P. Jing. «The cross-correlation between galaxies and groups: probing the galaxy distribution in and around dark matter haloes.» In: *Monthly Notices of the Royal Astronomical Society* 362.2 (Sept. 2005), pp. 711–726. ISSN: 0035-8711. DOI: 10.1111/j.1365-2966.2005.09351.x.

[86] Kerstin Paech, Nico Hamaus, Ben Hoyle, Matteo Costanzi, Tommaso Giannantonio, Steffen Hagstotz, Georg Sauerwein, and Jochen Weller. «Cross-correlation of galaxies and galaxy clusters in the Sloan Digital Sky Survey and the importance of non-Poissonian shot noise.» In: *Monthly Notices of the Royal Astronomical Society* 470.3 (June 2017), pp. 2566–2577. ISSN: 0035-8711. DOI: 10.1093/mnras/stx1354.

[87] Samuel J. Schmidt, Brice Ménard, Ryan Scranton, Christopher Morrison, and Cameron K. McBride. «Recovering redshift distributions with cross-correlations: pushing the boundaries.» In: *Monthly Notices of the Royal Astronomical Society* 431.4 (Apr. 2013), pp. 3307–3318. ISSN: 0035-8711. DOI: 10.1093/mnras/stt410.

[88] D. Alonso and P. G. Ferreira. «Constraining ultralarge-scale cosmology with multiple tracers in optical and radio surveys.» In: *Phys. Rev. D* 92 (6 Sept. 2015), p. 063525. DOI: 10.1103/PhysRevD.92.063525.

[89] Ely D. Kovetz, Alvise Raccanelli, and Mubdi Rahman. «Cosmological constraints with clustering-based redshifts.» In: *Monthly Notices of the Royal Astronomical Society* 468.3 (Mar. 2017), pp. 3650–3656. ISSN: 0035-8711. DOI: 10.1093/mnras/stx691.

[90] A. Pourtsidou, D. Bacon, R. Crittenden, and R. B. Metcalf. «Prospects for clustering and lensing measurements with forthcoming intensity mapping and optical surveys.» In: *Monthly Notices of the Royal Astronomical Society* 459.1 (Mar. 2016), pp. 863–870. ISSN: 0035-8711. DOI: 10.1093/mnras/stw658.

[91] Alkistis Pourtsidou. «Testing gravity at large scales with H*I* intensity mapping.» In: *Mon. Not. Roy. Astron. Soc.* 461.2 (June 2016), pp. 1457–1464. ISSN: 0035-8711. DOI: 10.1093/mnras/stw1406. arXiv: 1511.05927 [astro-ph.CO].

[92] Alvise Raccanelli, Ely Kovetz, Liang Dai, and Marc Kamionkowski. «Detecting the integrated Sachs-Wolfe effect with high-redshift 21-cm surveys.» In: *Phys. Rev. D* 93 (8 Apr. 2016), p. 083512. DOI: 10.1103/PhysRevD.93.083512. URL: https://link.aps.org/doi/10.1103/PhysRevD.93.083512.

[93] Alkistis Pourtsidou, David Bacon, and Robert Crittenden. «HI and cosmological constraints from intensity mapping, optical and CMB surveys.» In: *Mon. Not. Roy. Astron. Soc.* 470.4 (June 2017), pp. 4251–4260. ISSN: 0035-8711. DOI: 10.1093/mnras/stx1479. arXiv: 1610.04189 [astro-ph.CO].

[94] L. Wolz, C. Blake, and J. S. B. Wyithe. «Determining the HI content of galaxies via intensity mapping cross-correlations.» In: *Monthly Notices of the Royal Astronomical Society* 470.3 (June 2017), pp. 3220–3226. ISSN: 0035-8711. DOI: 10.1093/mnras/stx1388.

[95] David Alonso, Pedro G. Ferreira, Matt J. Jarvis, and Kavilan Moodley. «Calibrating photometric redshifts with intensity mapping observations.» In: *Phys. Rev. D* 96 (4 Aug. 2017), p. 043515. DOI: 10.1103/PhysRevD.96.043515.

[96] L Wolz, S G Murray, C Blake, and J S Wyithe. «Intensity mapping cross-correlations II: HI halo models including shot noise.» In: *Monthly Notices of the Royal Astronomical Society* 484.1 (Nov. 2018), pp. 1007–1020. ISSN: 0035-8711. DOI: 10.1093/mnras/sty3142.

[97] Steven Cunnington, Ian Harrison, Alkistis Pourtsidou, and David Bacon. «HI intensity mapping for clustering-based redshift estimation.» In: *Monthly Notices of the Royal Astronomical Society* 482.3 (Oct. 2018), pp. 3341–3355. ISSN: 0035-8711. DOI: 10.1093/mnras/sty2928.

[98] Masamune Oguri. «Measuring the distance-redshift relation with the cross-correlation of gravitational wave standard sirens and galaxies.» In: *Physical Review D* 93.8, 083511 (Apr. 2016), p. 083511. DOI: 10.1103/PhysRevD.93.083511. arXiv: 1603.02356 [astro-ph.CO].

[99] Alvise Raccanelli, Ely D. Kovetz, Simeon Bird, Ilias Cholis, and Julian B. Muñoz. «Determining the progenitors of merging black-hole binaries.» In: *Phys. Rev. D* 94 (2 July 2016), p. 023516. DOI: 10.1103/PhysRevD.94.023516. arXiv: 1605.01405.

[100] Giulio Scelfo, Nicola Bellomo, Alvise Raccanelli, Sabino Matarrese, and Licia Verde. «GW×LSS: chasing the progenitors of merging binary black holes.» In: *JCAP* 2018.09 (Sept. 2018), pp. 039–039. DOI: 10.1088/1475-7516/2018/09/039. arXiv: 1809.03528v1.

[101]   Giulio Scelfo, Lumen Boco, Andrea Lapi, and Matteo Viel. «Exploring galaxies-gravitational waves cross-correlations as an astrophysical probe.» In: *Journal of Cosmology and Astroparticle Physics* 2020.10 (Oct. 2020), pp. 045–045. DOI: 10.1088/1475-7516/2020/10/045.

[102]   Toshiya Namikawa, Atsushi Nishizawa, and Atsushi Taruya. «Anisotropies of gravitational-wave standard sirens as a new cosmological probe without redshift information.» In: *Physical review letters* 116.12 (2016), p. 121302.

[103]   David Alonso, Giulia Cusin, Pedro G. Ferreira, and Cyril Pitrou. «Detecting the anisotropic astrophysical gravitational wave background in the presence of shot noise through cross-correlations.» In: (Feb. 2020). arXiv: 2002.02888.

[104]   Guadalupe Cañas Herrera, Omar Contigiani, and Valeri Vardanyan. «Cross-correlation of the astrophysical gravitational-wave background with galaxy clustering.» In: *Phys. Rev. D* 102 (4 Aug. 2020), p. 043513. DOI: 10.1103/PhysRevD.102.043513.

[105]   Francesca Calore, Alessandro Cuoco, Tania Regimbau, Surabhi Sachdev, and Pasquale Dario Serpico. «Cross-correlating galaxy catalogs and gravitational waves: a tomographic approach.» In: *Physical Review Research* 2.2 (2020), p. 023314. DOI: 10.1103/PhysRevResearch.2.023314.

[106]   Stefano Camera and Atsushi Nishizawa. «Beyond Concordance Cosmology with Magnification of Gravitational-Wave Standard Sirens.» In: *Phys. Rev. Lett.* 110 (15 Apr. 2013), p. 151103. DOI: 10.1103/PhysRevLett.110.151103. arXiv: 1303.5446.

[107]   S. Libanore, M. C. Artale, D. Karagiannis, M. Liguori, N. Bartolo, Y. Bouffanais, N. Giacobbo, M. Mapelli, and S. Matarrese. «Gravitational Wave mergers as tracers of Large Scale Structures.» In: *Journal of Cosmology and Astroparticle Physics* 2021.02 (Feb. 2021), pp. 035–035. DOI: 10.1088/1475-7516/2021/02/035. URL: https://doi.org/10.1088/1475-7516/2021/02/035.

[108]   Giulio Scelfo, Marta Spinelli, Alvise Raccanelli, Lumen Boco, Andrea Lapi, and Matteo Viel. «Gravitational waves × HI intensity mapping: cosmological and astrophysical applications.» In: *Journal of Cosmology and Astroparticle Physics* 2022.01 (Jan. 2022), p. 004. DOI: 10.1088/1475-7516/2022/01/004.

[109]   Suvodip Mukherjee, Benjamin D Wandelt, and Joseph Silk. «Probing the theory of gravity with gravitational lensing of gravitational waves and galaxy surveys.» In: *Monthly Notices of the Royal Astronomical Society* 494.2 (Mar. 2020), pp. 1956–1970. ISSN: 0035-8711. DOI: 10.1093/mnras/staa827.

[110]   Suvodip Mukherjee, Benjamin D. Wandelt, Samaya M. Nissanke, and Alessandra Silvestri. «Accurate precision cosmology with redshift unknown gravitational wave sources.» In: *Phys. Rev. D* 103 (4 Feb. 2021), p. 043520. DOI: 10.1103/PhysRevD.103.043520.

[111]   Suvodip Mukherjee and Joseph Silk. «Time dependence of the astrophysical stochastic gravitational wave background.» In: *Monthly Notices of the Royal Astronomical Society* 491.4 (Nov. 2019), pp. 4690–4701. ISSN: 0035-8711. DOI: 10.1093/mnras/stz3226.

[112]   Guadalupe Cañas-Herrera, Omar Contigiani, and Valeri Vardanyan. «Learning How to Surf: Reconstructing the Propagation and Origin of Gravitational Waves with Gaussian Processes.» In: *The Astrophysical Journal* 918.1 (Aug. 2021), p. 20. DOI: 10.3847/1538-4357/ac09e3.

[113]   Suvodip Mukherjee, Alex Krolewski, Benjamin D Wandelt, and Joseph Silk. «Cross-correlating dark sirens and galaxies: measurement of H0 from GWTC-3 of LIGO-Virgo-KAGRA.» In: *arXiv preprint arXiv:2203.03643* (2022).

[114]   Cristina Cigarrán Díaz and Suvodip Mukherjee. «Mapping the cosmic expansion history from LIGO-Virgo-KAGRA in synergy with DESI and SPHEREx.» In: *Monthly Notices of the Royal Astronomical Society* 511.2 (Jan. 2022), pp. 2782–2795. ISSN: 0035-8711. DOI: 10.1093/mnras/stac208.

[115]   Maria Berti, Marta Spinelli, and Matteo Viel. «Multipole expansion for 21 cm intensity mapping power spectrum: Forecasted cosmological parameters estimation for the SKA Observatory.» In: *Mon. Not. Roy. Astron. Soc.* 521.3 (2023), pp. 3221–3236. DOI: 10.1093/mnras/stad685. arXiv: 2209.07595 [astro-ph.CO].

[116]   Maria Berti, Marta Spinelli, and Matteo Viel. «21cm Intensity Mapping cross-correlation with galaxy surveys: current cosmological parameters estimation for MeerKAT and forecasts for the SKA Observatory.» In: 2023.

[117]   Maria Berti, Marta Spinelli, Balakrishna S. Haridasu, Matteo Viel, and Alessandra Silvestri. «Constraining beyond ΛCDM models with 21cm intensity mapping forecasted observations combined with latest CMB data.» In: *JCAP* 01.01 (2022), p. 018. DOI: 10.1088/1475-7516/2022/01/018. arXiv: 2109.03256 [astro-ph.CO].

[118]   Giulio Scelfo, Maria Berti, Alessandra Silvestri, and Matteo Viel. «Testing gravity with gravitational waves × electromagnetic probes cross-correlations.» In: *JCAP* 02 (2023), p. 010. DOI: 10.1088/1475-7516/2023/02/010. arXiv: 2210.02460 [astro-ph.CO].

[119]   Maria Berti, Marta Spinelli, Balakrishna S. Haridasu, and Matteo Viel. «Latest perspectives on weighing the neutrinos with the SKAO 21cm Intensity Mapping.» In: 2023.

[120]   S. Dodelson and Academic Press (Londyn ; 1941-1969). *Modern Cosmology*. Elsevier Science, 2003. ISBN: 9780122191411. URL: https://books.google.it/books?id=3oPRxdXJexcC.

[121]   S. Weinberg. *Cosmology*. OUP Oxford, 2008. ISBN: 9780198526827. URL: https://books.google.it/books?id=rswTDAAAQBAJ.

[122]   H. Mo, F. van den Bosch, and S. White. *Galaxy Formation and Evolution*. Galaxy Formation and Evolution. Cambridge University Press, 2010. ISBN: 9780521857932. URL: https://books.google.it/books?id=Zj7fDU3Z4wsC.

[123]   John A Peacock. *Cosmological physics*. Cambridge university press, 1999.

[124]   S. Carroll, S.M. Carroll, and Addison-Wesley. *Spacetime and Geometry: An Introduction to General Relativity*. Addison Wesley, 2004. ISBN: 9780805387322. URL: https://books.google.it/books?id=1SKFQgAACAAJ.

[125]   Edwin Hubble. «A Relation between Distance and Radial Velocity among Extra-Galactic Nebulae.» In: *Contributions from the Mount Wilson Observatory* 3 (Jan. 1929), pp. 23–28.

[126]   Mikhail Denissenya, Eric V. Linder, and Arman Shafieloo. «Cosmic curvature tested directly from observations.» In: J. Cosmology Astropart. Phys. 2018.3, 041 (Mar. 2018), p. 041. DOI: 10.1088/1475-7516/2018/03/041. arXiv: 1802.04816 [astro-ph.CO].

[127]   Eleonora Di Valentino et al. «Snowmass2021 - Letter of interest cosmology intertwined IV: The age of the universe and its curvature.» In: *Astropart. Phys.* 131 (2021), p. 102607. DOI: 10.1016/j.astropartphys.2021.102607. arXiv: 2008.11286 [astro-ph.CO].

[128]   R. L. Workman et al. «Review of Particle Physics.» In: *PTEP* 2022 (2022), p. 083C01. DOI: 10.1093/ptep/ptac097.

[129]   Volker Springel et al. «Simulating the joint evolution of quasars, galaxies and their large-scale distribution.» In: *Nature* 435 (2005), pp. 629–636. DOI: 10.1038/nature03597. arXiv: astro-ph/0504097.

[130]   Daniel Baumann. «Inflation.» In: *Theoretical Advanced Study Institute in Elementary Particle Physics: Physics of the Large and the Small*. 2011, pp. 523–686. DOI: 10.1142/9789814327183_0010. arXiv: 0907.5424 [hep-th].

[131]   Roman Scoccimarro, H. M. P. Couchman, and Joshua A. Frieman. «The Bispectrum as a Signature of Gravitational Instability in Redshift-Space.» In: *Astrophys. J.* 517 (1999), pp. 531–540. DOI: 10.1086/307220. arXiv: astro-ph/9808305.

[132]   Xingang Chen, Min-xin Huang, Shamit Kachru, and Gary Shiu. «Observational signatures and non-Gaussianities of general single field inflation.» In: *JCAP* 01 (2007), p. 002. DOI: 10.1088/1475-7516/2007/01/002. arXiv: hep-th/0605045.

[133]   Solène Chabanier, Marius Millea, and Nathalie Palanque-Delabrouille. «Matter power spectrum: from Lyα forest to CMB scales.» In: *Mon. Not. Roy. Astron. Soc.* 489.2 (2019), pp. 2247–2253. DOI: 10.1093/mnras/stz2310. arXiv: 1905.08103 [astro-ph.CO].

[134]   Guido D'Amico, Jérôme Gleyzes, Nickolas Kokron, Katarina Markovic, Leonardo Senatore, Pierre Zhang, Florian Beutler, and Héctor Gil-Marín. «The Cosmological Analysis of the SDSS/BOSS data from the Effective Field Theory of Large-Scale Structure.» In: *JCAP* 05 (2020), p. 005. DOI: 10.1088/1475-7516/2020/05/005. arXiv: 1909.05271 [astro-ph.CO].

[135]   Wayne Hu and Naoshi Sugiyama. «Small scale cosmological perturbations: An Analytic approach.» In: *Astrophys. J.* 471 (1996), pp. 542–570. DOI: 10.1086/177989. arXiv: astro-ph/9510117.

[136] Antony Lewis and Sarah Bridle. «Cosmological parameters from CMB and other data: A Monte Carlo approach.» In: Phys. Rev. D 66.10, 103511 (Nov. 2002). DOI: 10.1103/PhysRevD.66.103511. arXiv: astro-ph/0205436 [astro-ph].

[137] Planck Collaboration et al. «Planck 2013 results. XVI. Cosmological parameters.» In: A&A 571, A16 (Nov. 2014), A16. DOI: 10.1051/0004-6361/201321591. arXiv: 1303.5076 [astro-ph.CO].

[138] Elcio Abdalla et al. «Cosmology intertwined: A review of the particle physics, astrophysics, and cosmology associated with the cosmological tensions and anomalies.» In: *Journal of High Energy Astrophysics* 34 (June 2022), pp. 49–211. DOI: 10.1016/j.jheap.2022.04.002. arXiv: 2203.06142 [astro-ph.CO].

[139] A. Arbey and F. Mahmoudi. «Dark matter and the early Universe: a review.» In: *Prog. Part. Nucl. Phys.* 119 (2021), p. 103865. DOI: 10.1016/j.ppnp.2021.103865. arXiv: 2104.11488 [hep-ph].

[140] Michel Chevallier and David Polarski. «Accelerating Universes with Scaling Dark Matter.» In: *International Journal of Modern Physics D* 10.2 (Jan. 2001), pp. 213–223. DOI: 10.1142/S0218271801000822. arXiv: gr-qc/0009008 [gr-qc].

[141] Erminia Calabrese, Anze Slosar, Alessandro Melchiorri, George F. Smoot, and Oliver Zahn. «Cosmic Microwave Weak lensing data as a test for the dark universe.» In: *Phys. Rev. D* 77 (2008), p. 123531. DOI: 10.1103/PhysRevD.77.123531. arXiv: 0803.2309 [astro-ph].

[142] Julien Lesgourgues and Sergio Pastor. «Massive neutrinos and cosmology.» In: Phys. Rep. 429.6 (July 2006), pp. 307–379. DOI: 10.1016/j.physrep.2006.04.001. arXiv: astro-ph/0603494 [astro-ph].

[143] P. F. De Salas, S. Gariazzo, O. Mena, C. A. Ternes, and M. Tórtola. «Neutrino Mass Ordering from Oscillations and Beyond: 2018 Status and Future Prospects.» In: *Front. Astron. Space Sci.* 5 (2018), p. 36. DOI: 10.3389/fspas.2018.00036. arXiv: 1806.11051 [hep-ph].

[144] M. Aker et al. «Direct neutrino-mass measurement with sub-electronvolt sensitivity.» In: *Nature Phys.* 18.2 (2022), pp. 160–166. DOI: 10.1038/s41567-021-01463-1. arXiv: 2105.08533 [hep-ex].

[145] A. A. Penzias and R. W. Wilson. «A Measurement of Excess Antenna Temperature at 4080 Mc/s.» In: ApJ 142 (July 1965), pp. 419–421. DOI: 10.1086/148307.

[146] D. J. Fixsen, E. S. Cheng, J. M. Gales, John C. Mather, R. A. Shafer, and E. L. Wright. «The Cosmic Microwave Background spectrum from the full COBE FIRAS data set.» In: *Astrophys. J.* 473 (1996), p. 576. DOI: 10.1086/178173. arXiv: astro-ph/9605054.

[147] G. F. Smoot et al. «Structure in the COBE Differential Microwave Radiometer First-Year Maps.» In: ApJ 396 (Sept. 1992), p. L1. DOI: 10.1086/186504.

[148] D. N. Spergel et al. «First-Year Wilkinson Microwave Anisotropy Probe (WMAP) Observations: Determination of Cosmological Parameters.» In: ApJS 148.1 (Sept. 2003), pp. 175–194. DOI: 10.1086/377226. arXiv: astro-ph/0302209 [astro-ph].

[149] Wayne Hu. «Lecture Notes on CMB Theory: From Nucleosynthesis to Recombination.» In: (Feb. 2008). arXiv: 0802.3688 [astro-ph].

[150] Planck Collaboration et al. «Planck 2015 results. XIII. Cosmological parameters.» In: A&A 594, A13 (Sept. 2016), A13. DOI: 10.1051/0004-6361/201525830. arXiv: 1502.01589 [astro-ph.CO].

[151] R. K. Sachs and A. M. Wolfe. «Perturbations of a Cosmological Model and Angular Variations of the Microwave Background.» In: ApJ 147 (Jan. 1967), p. 73. DOI: 10.1086/148982.

[152] N. Aghanim et al. «Planck 2018 results. VIII. Gravitational lensing.» In: *Astron. Astrophys.* 641 (2020), A8. DOI: 10.1051/0004-6361/201833886. arXiv: 1807.06210 [astro-ph.CO].

[153] N. Kaiser. «Clustering in real space and in redshift space.» In: *Mon. Not. Roy. Astron. Soc.* 227 (1987), pp. 1–27.

[154] J. C. Jackson. «Fingers of God: A critique of Rees' theory of primoridal gravitational radiation.» In: *Mon. Not. Roy. Astron. Soc.* 156 (1972), 1P–5P. DOI: 10.1093/mnras/156.1.1P. arXiv: 0810.3908 [astro-ph].

[155] Daniel J. Eisenstein et al. «Detection of the Baryon Acoustic Peak in the Large-Scale Correlation Function of SDSS Luminous Red Galaxies.» In: ApJ 633.2 (Nov. 2005), pp. 560–574. DOI: 10.1086/466512. arXiv: astro-ph/0501171 [astro-ph].

[156] José Luis Bernal, Patrick C. Breysse, Héctor Gil-Marín, and Ely D. Kovetz. «User's guide to extracting cosmological information from line-intensity maps.» In: *Phys. Rev. D* 100.12 (2019), p. 123522. DOI: 10.1103/PhysRevD.100.123522. arXiv: 1907.10067 [astro-ph.CO].

[157] Philip Bull, Pedro G. Ferreira, Prina Patel, and Mario G. Santos. «Late-time cosmology with 21cm intensity mapping experiments.» In: *Astrophys. J.* 803.1 (2015), p. 21. DOI: 10.1088/0004-637X/803/1/21. arXiv: 1405.1452 [astro-ph.CO].

[158] Francisco Villaescusa-Navarro et al. «Ingredients for 21 cm Intensity Mapping.» In: *Astrophys. J.* 866.2 (2018), p. 135. DOI: 10.3847/1538-4357/aadba0. arXiv: 1804.09180 [astro-ph.CO].

[159] Philippe Brax, Sebastien Clesse, and Anne-Christine Davis. «Signatures of Modified Gravity on the 21-cm Power Spectrum at Reionisation.» In: *JCAP* 01 (2013), p. 003. DOI: 10.1088/1475-7516/2013/01/003. arXiv: 1207.1273 [astro-ph.CO].

[160] Alex Hall, Camille Bonvin, and Anthony Challinor. «Testing General Relativity with 21-cm intensity mapping.» In: *Phys. Rev. D* 87.6 (2013), p. 064026. DOI: 10.1103/PhysRevD.87.064026. arXiv: 1212.0728 [astro-ph.CO].

[161] Aditya Chowdhury, Nissim Kanekar, Jayaram N. Chengalur, Shiv Sethi, and K. S. Dwarakanath. «H I 21-centimetre emission from an ensemble of galaxies at an average redshift of one.» In: Nature 586.7829 (Oct. 2020), pp. 369–372. DOI: 10.1038/s41586-020-2794-710.48550/arXiv.2010.06617. arXiv: 2010.06617 [astro-ph.GA].

[162] Adam Lidz, Steven R. Furlanetto, S. Peng Oh, James Aguirre, Tzu-Ching Chang, Olivier Doré, and Jonathan R. Pritchard. «Intensity Mapping with Carbon Monoxide Emission Lines and the Redshifted 21 cm Line.» In: ApJ 741.2, 70 (Nov. 2011), p. 70. DOI: `10.1088/0004-637X/741/2/7010.48550/arXiv.1104.4800`. arXiv: `1104.4800 [astro-ph.CO]`.

[163] Patrick C. Breysse, Ely D. Kovetz, and Marc Kamionkowski. «Carbon monoxide intensity mapping at moderate redshifts.» In: MNRAS 443.4 (Oct. 2014), pp. 3506–3512. DOI: `10.1093/mnras/stu131210.48550/arXiv.1405.0489`. arXiv: `1405.0489 [astro-ph.CO]`.

[164] Tony Y. Li, Risa H. Wechsler, Kiruthika Devaraj, and Sarah E. Church. «Connecting CO Intensity Mapping to Molecular Gas and Star Formation in the Epoch of Galaxy Assembly.» In: ApJ 817.2, 169 (Feb. 2016), p. 169. DOI: `10.3847/0004-637X/817/2/16910.48550/arXiv.1503.08833`. arXiv: `1503.08833 [astro-ph.CO]`.

[165] Marta Silva, Mario G. Santos, Asantha Cooray, and Yan Gong. «Prospects for Detecting C II Emission during the Epoch of Reionization.» In: ApJ 806.2, 209 (June 2015), p. 209. DOI: `10.1088/0004-637X/806/2/20910.48550/arXiv.1410.4808`. arXiv: `1410.4808 [astro-ph.GA]`.

[166] Anthony R. Pullen, Paolo Serra, Tzu-Ching Chang, Olivier Doré, and Shirley Ho. «Search for C II emission on cosmological scales at redshift Z ∼ 2.6.» In: MNRAS 478.2 (Aug. 2018), pp. 1911–1924. DOI: `10.1093/mnras/sty1243`. arXiv: `1707.06172 [astro-ph.CO]`.

[167] Marta B. Silva, Mario G. Santos, Yan Gong, Asantha Cooray, and James Bock. «Intensity Mapping of Lyα Emission during the Epoch of Reionization.» In: ApJ 763.2, 132 (Feb. 2013), p. 132. DOI: `10.1088/0004-637X/763/2/13210.48550/arXiv.1205.1493`. arXiv: `1205.1493 [astro-ph.CO]`.

[168] Anthony R. Pullen, Olivier Doré, and Jamie Bock. «Intensity Mapping across Cosmic Times with the Lyα Line.» In: ApJ 786.2, 111 (May 2014), p. 111. DOI: `10.1088/0004-637X/786/2/11110.48550/arXiv.1309.2295`. arXiv: `1309.2295 [astro-ph.CO]`.

[169] Yan Gong, Asantha Cooray, Marta B. Silva, Michael Zemcov, Chang Feng, Mario G. Santos, Olivier Dore, and Xuelei Chen. «Intensity Mapping of Hα, Hβ, [OII], and [OIII] Lines at z < 5.» In: ApJ 835.2, 273 (Feb. 2017), p. 273. DOI: `10.3847/1538-4357/835/2/273`. arXiv: `1610.09060 [astro-ph.GA]`.

[170] B. Marta Silva, Saleem Zaroubi, Robin Kooistra, and Asantha Cooray. «Tomographic intensity mapping versus galaxy surveys: observing the Universe in H α emission with new generation instruments.» In: MNRAS 475.2 (Apr. 2018), pp. 1587–1608. DOI: `10.1093/mnras/stx3265`. arXiv: `1711.09902 [astro-ph.GA]`.

[171] J. R. Bond and G. Efstathiou. «Cosmic background radiation anisotropies in universes dominated by nonbaryonic dark matter.» In: ApJ 285 (Oct. 1984), pp. L45–L48. DOI: `10.1086/184362`.

[172] Chung-Pei Ma and Edmund Bertschinger. «Cosmological Perturbation Theory in the Synchronous and Conformal Newtonian Gauges.» In: ApJ 455 (Dec. 1995), p. 7. DOI: 10.1086/176550. arXiv: astro-ph/9506072 [astro-ph].

[173] Antony Lewis, Anthony Challinor, and Anthony Lasenby. «Efficient computation of CMB anisotropies in closed FRW models.» In: *Astrophys. J.* 538 (2000), pp. 473–476. DOI: 10.1086/309179. arXiv: astro-ph/9911177.

[174] Julien Lesgourgues. «The Cosmic Linear Anisotropy Solving System (CLASS) I: Overview.» In: *arXiv e-prints*, arXiv:1104.2932 (2011). arXiv: 1104.2932 [astro-ph.IM].

[175] Manoj Kaplinghat, Lloyd Knox, and Constantinos Skordis. «Rapid Calculation of Theoretical Cosmic Microwave Background Angular Power Spectra.» In: ApJ 578.2 (Oct. 2002), pp. 665–674. DOI: 10.1086/342656. arXiv: astro-ph/0203413 [astro-ph].

[176] Michael Doran. «CMBEASY: an object oriented code for the cosmic microwave background.» In: J. Cosmology Astropart. Phys. 2005.10, 011 (Oct. 2005). DOI: 10.1088/1475-7516/2005/10/011. arXiv: astro-ph/0302138 [astro-ph].

[177] N. W. Boggess et al. «The COBE Mission: Its Design and Performance Two Years after Launch.» In: ApJ 397 (Oct. 1992), p. 420. DOI: 10.1086/171797.

[178] C. L. Bennett et al. «Nine-year Wilkinson Microwave Anisotropy Probe (WMAP) Observations: Final Maps and Results.» In: ApJS 208.2, 20 (Oct. 2013), p. 20. DOI: 10.1088/0067-0049/208/2/20. arXiv: 1212.5225 [astro-ph.CO].

[179] F. De Bernardis et al. «Survey strategy optimization for the Atacama Cosmology Telescope.» In: *Observatory Operations: Strategies, Processes, and Systems VI*. Ed. by Alison B. Peck, Robert L. Seaman, and Chris R. Benn. Vol. 9910. Society of Photo-Optical Instrumentation Engineers (SPIE) Conference Series. July 2016, 991014, p. 991014. DOI: 10.1117/12.2232824. arXiv: 1607.02120 [astro-ph.IM].

[180] Thibaut Louis et al. «The Atacama Cosmology Telescope: two-season ACTPol spectra and parameters.» In: J. Cosmology Astropart. Phys. 2017.6, 031 (June 2017), p. 031. DOI: 10.1088/1475-7516/2017/06/031. arXiv: 1610.02360 [astro-ph.CO].

[181] B. A. Benson et al. «SPT-3G: a next-generation cosmic microwave background polarization experiment on the South Pole telescope.» In: *Millimeter, Submillimeter, and Far-Infrared Detectors and Instrumentation for Astronomy VII*. Ed. by Wayne S. Holland and Jonas Zmuidzinas. Vol. 9153. Society of Photo-Optical Instrumentation Engineers (SPIE) Conference Series. July 2014, 91531P, 91531P. DOI: 10.1117/12.2057305. arXiv: 1407.2973 [astro-ph.IM].

[182] J. W. Henning et al. «Measurements of the Temperature and E-mode Polarization of the CMB from 500 Square Degrees of SPTpol Data.» In: ApJ 852.2, 97 (Jan. 2018), p. 97. DOI: 10.3847/1538-4357/aa9ff4. arXiv: 1707.09353 [astro-ph.CO].

[183]   Brian G. Keating, Peter A. R. Ade, James J. Bock, Eric Hivon, William L. Holzapfel, Andrew E. Lange, Hien Nguyen, and Ki Won Yoon. «BICEP: a large angular scale CMB polarimeter.» In: *Polarimetry in Astronomy*. Ed. by Silvano Fineschi. Vol. 4843. Society of Photo-Optical Instrumentation Engineers (SPIE) Conference Series. Feb. 2003, pp. 284–295. DOI: 10.1117/12.459274.

[184]   Thomas Essinger-Hileman et al. «CLASS: the cosmology large angular scale surveyor.» In: *Millimeter, Submillimeter, and Far-Infrared Detectors and Instrumentation for Astronomy VII*. Ed. by Wayne S. Holland and Jonas Zmuidzinas. Vol. 9153. Society of Photo-Optical Instrumentation Engineers (SPIE) Conference Series. July 2014, 91531I, p. 91531I. DOI: 10.1117/12.2056701. arXiv: 1408.4788 [astro-ph.IM].

[185]   Kevork N. Abazajian et al. «CMB-S4 Science Book, First Edition.» In: *arXiv e-prints*, arXiv:1610.02743 (Oct. 2016), arXiv:1610.02743. arXiv: 1610.02743 [astro-ph.CO].

[186]   Peter Ade et al. «The Simons Observatory: science goals and forecasts.» In: J. Cosmology Astropart. Phys. 2019.2, 056 (Feb. 2019), p. 056. DOI: 10.1088/1475-7516/2019/02/056. arXiv: 1808.07445 [astro-ph.CO].

[187]   Planck 2018 results. «V. CMB power spectra and likelihoods.» In: *Astron. Astrophys.* 641 (2020), A5. DOI: 10.1051/0004-6361/201936386. arXiv: 1907.12875 [astro-ph.CO].

[188]   Planck 2018 results. «III. High Frequency Instrument data processing and frequency maps.» In: *Astron. Astrophys.* 641 (2020), A3. DOI: 10.1051/0004-6361/201832909. arXiv: 1807.06207 [astro-ph.CO].

[189]   Jeffrey A. Newman and Daniel Gruen. «Photometric Redshifts for Next-Generation Surveys.» In: *Annual Review of Astronomy and Astrophysics* 60.1 (2022), pp. 363–414. DOI: 10.1146/annurev-astro-032122-014611. eprint: https://doi.org/10.1146/annurev-astro-032122-014611. URL: https://doi.org/10.1146/annurev-astro-032122-014611.

[190]   Rene Laureijs, J Amiaux, S Arduini, J-L Augueres, J Brinchmann, R Cole, M Cropper, C Dabin, L Duvet, A Ealet, et al. «Euclid definition study report.» In: *arXiv preprint arXiv:1110.3193* (2011). DOI: https://doi.org/10.48550/arXiv.1110.3193.

[191]   M. Colless. «First results from the 2dF Galaxy Redshift Survey.» In: *Philosophical Transactions of the Royal Society of London Series A* 357.1750 (Jan. 1999), p. 105. DOI: 10.1098/rsta.1999.0317. arXiv: astro-ph/9804079 [astro-ph].

[192]   D. Heath Jones et al. «The 6dF Galaxy Survey: samples, observational techniques and the first data release.» In: MNRAS 355.3 (Dec. 2004), pp. 747–763. DOI: 10.1111/j.1365-2966.2004.08353.x. arXiv: astro-ph/0403501 [astro-ph].

[193]   Michael J. Drinkwater et al. «The WiggleZ Dark Energy Survey: survey design and first data release.» In: MNRAS 401.3 (Jan. 2010), pp. 1429–1452. DOI: 10.1111/j.1365-2966.2009.15754.x. arXiv: 0911.4246 [astro-ph.CO].

[194] Daniel J. Eisenstein et al. «SDSS-III: Massive Spectroscopic Surveys of the Distant Universe, the Milky Way, and Extra-Solar Planetary Systems.» In: AJ 142.3, 72 (Sept. 2011), p. 72. DOI: 10.1088/0004-6256/142/3/72. arXiv: 1101.1529 [astro-ph.IM].

[195] Michael R. Blanton et al. «Sloan Digital Sky Survey IV: Mapping the Milky Way, Nearby Galaxies, and the Distant Universe.» In: AJ 154.1, 28 (July 2017), p. 28. DOI: 10.3847/1538-3881/aa7567. arXiv: 1703.00052 [astro-ph.GA].

[196] Kyle S. Dawson et al. «The Baryon Oscillation Spectroscopic Survey of SDSS-III.» In: AJ 145.1, 10 (Jan. 2013), p. 10. DOI: 10.1088/0004-6256/145/1/10. arXiv: 1208.0022 [astro-ph.CO].

[197] Kyle S. Dawson et al. «The SDSS-IV Extended Baryon Oscillation Spectroscopic Survey: Overview and Early Data.» In: AJ 151.2, 44 (Feb. 2016), p. 44. DOI: 10.3847/0004-6256/151/2/44. arXiv: 1508.04473 [astro-ph.CO].

[198] DESI Collaboration et al. «The DESI Experiment Part I: Science,Targeting, and Survey Design.» In: *arXiv e-prints*, arXiv:1611.00036 (Oct. 2016), arXiv:1611.00036. arXiv: 1611.00036 [astro-ph.IM].

[199] M. P. van Haarlem et al. «LOFAR: The LOw-Frequency ARray.» In: A&A 556, A2 (Aug. 2013), A2. DOI: 10.1051/0004-6361/201220873. arXiv: 1305.3550 [astro-ph.IM].

[200] Andre A. Costa et al. «The BINGO project - VII. Cosmological forecasts from 21 cm intensity mapping.» In: *Astron. Astrophys.* 664 (2022), A20. DOI: 10.1051/0004-6361/202140888. arXiv: 2107.01639 [astro-ph.CO].

[201] Carlos A. Wuensche et al. «The BINGO project - II. Instrument description.» In: *Astron. Astrophys.* 664 (2022), A15. DOI: 10.1051/0004-6361/202039962. arXiv: 2107.01634 [astro-ph.IM].

[202] Keith Vanderlinde et al. «The Canadian Hydrogen Observatory and Radio-transient Detector (CHORD).» en. In: (2019). DOI: 10.5281/ZENODO.3765414. URL: https://zenodo.org/record/3765414.

[203] Fengquan Wu et al. «The Tianlai dish pathfinder array: design, operation, and performance of a prototype transit radio interferometer.» In: *Mon. Not. Roy. Astron. Soc.* 506.3 (2021), pp. 3455–3482. DOI: 10.1093/mnras/stab1802. arXiv: 2011.05946 [astro-ph.IM].

[204] Olivier Perdereau et al. «The Tianlai dish array low-z surveys forecasts.» In: *Mon. Not. Roy. Astron. Soc.* 517.3 (2022), pp. 4637–4655. DOI: 10.1093/mnras/stac2832. arXiv: 2205.06086 [astro-ph.CO].

[205] L. Wolz, F. B. Abdalla, C. Blake, J. R. Shaw, E. Chapman, and S. Rawlings. «The effect of foreground subtraction on cosmological measurements from Intensity Mapping.» In: *Mon. Not. Roy. Astron. Soc.* 441.4 (2014), pp. 3271–3283. DOI: 10.1093/mnras/stu792. arXiv: 1310.8144 [astro-ph.CO].

[206] Steven Cunnington, Laura Wolz, Alkistis Pourtsidou, and David Bacon. «Impact of foregrounds on HI intensity mapping cross-correlations with optical surveys.» In: *Mon. Not. Roy. Astron. Soc.* 488.4 (2019), pp. 5452–5472. DOI: 10.1093/mnras/stz1916. arXiv: 1904.01479 [astro-ph.CO].

[207] Licia Verde. «A practical guide to Basic Statistical Techniques for Data Analysis in Cosmology.» In: *arXiv e-prints*, arXiv:0712.3028 (Dec. 2007). arXiv: 0712.3028 [astro-ph].

[208] J. V. Wall and C. R. Jenkins. *Practical Statistics for Astronomers*. Vol. 3. 2003.

[209] W.R. Gilks, S. Richardson, and D. Spiegelhalter. *Markov Chain Monte Carlo in Practice*. Chapman & Hall/CRC Interdisciplinary Statistics. Taylor & Francis, 1995. ISBN: 9780412055515. URL: https://books.google.it/books?id=TRXrMWY_i2IC.

[210] D. Gamerman. *Markov Chain Monte Carlo: Stochastic Simulation for Bayesian Inference*. Chapman & Hall/CRC Texts in Statistical Science. Taylor & Francis, 1997. ISBN: 9780412818202. URL: https://books.google.it/books?id=JJsFxSkE_WsC.

[211] Nicholas Metropolis, Arianna W. Rosenbluth, Marshall N. Rosenbluth, Augusta H. Teller, and Edward Teller. «Equation of State Calculations by Fast Computing Machines.» In: J. Chem. Phys. 21.6 (June 1953), pp. 1087–1092. DOI: 10.1063/1.1699114.

[212] Antony Lewis. «Efficient sampling of fast and slow cosmological parameters.» In: Phys. Rev. D 87.10, 103529 (May 2013). DOI: 10.1103/PhysRevD.87.103529. arXiv: 1304.4473 [astro-ph.CO].

[213] Andrew Gelman and Donald B. Rubin. «Inference from Iterative Simulation Using Multiple Sequences.» In: *Statistical Science* 7 (Jan. 1992), pp. 457–472. DOI: 10.1214/ss/1177011136.

[214] Austin Joyce, Lucas Lombriser, and Fabian Schmidt. «Dark Energy Versus Modified Gravity.» In: *Annual Review of Nuclear and Particle Science* 66.1 (Oct. 2016), pp. 95–122. DOI: 10.1146/annurev-nucl-102115-044553. arXiv: 1601.06133 [astro-ph.CO].

[215] C. Brans and R. H. Dicke. «Mach's Principle and a Relativistic Theory of Gravitation.» In: *Physical Review* 124.3 (Nov. 1961), pp. 925–935. DOI: 10.1103/PhysRev.124.925.

[216] Gregory Walter Horndeski. «Second-Order Scalar-Tensor Field Equations in a Four-Dimensional Space.» In: *International Journal of Theoretical Physics* 10.6 (Sept. 1974), pp. 363–384. DOI: 10.1007/BF01807638.

[217] Thomas P. Sotiriou and Valerio Faraoni. «f(R) Theories Of Gravity.» In: *Rev. Mod. Phys.* 82 (2010), pp. 451–497. DOI: 10.1103/RevModPhys.82.451. arXiv: 0805.1726 [gr-qc].

[218] Antonio De Felice and Shinji Tsujikawa. «f(R) theories.» In: *Living Rev. Rel.* 13 (2010), p. 3. DOI: 10.12942/lrr-2010-3. arXiv: 1002.4928 [gr-qc].

[219] Salvatore Capozziello and L. Z. Fang. «Curvature Quintessence.» In: *International Journal of Modern Physics D* 11.4 (Jan. 2002), pp. 483–491. DOI: 10.1142/S0218271802002025. arXiv: gr-qc/0201033 [gr-qc].

[220] S. Capozziello, S. Carloni, and A. Troisi. «Quintessence without scalar fields.» In: *arXiv e-prints*, astro-ph/0303041 (Mar. 2003), astro–ph/0303041. arXiv: astro-ph/0303041 [astro-ph].

[221]   Sean M. Carroll, Vikram Duvvuri, Mark Trodden, and Michael S. Turner. «Is cosmic speed-up due to new gravitational physics?» In: Phys. Rev. D 70.4, 043528 (Aug. 2004), p. 043528. DOI: 10.1103/PhysRevD.70.043528. arXiv: astro-ph/0306438 [astro-ph].

[222]   Takeshi Chiba. «1/R gravity and scalar-tensor gravity.» In: *Physics Letters B* 575.1-2 (Nov. 2003), pp. 1–3. DOI: 10.1016/j.physletb.2003.09.033. arXiv: astro-ph/0307338 [astro-ph].

[223]   Adrienne L. Erickcek, Tristan L. Smith, and Marc Kamionkowski. «Solar system tests do rule out 1/R gravity.» In: Phys. Rev. D 74.12, 121501 (Dec. 2006), p. 121501. DOI: 10.1103/PhysRevD.74.121501. arXiv: astro-ph/0610483 [astro-ph].

[224]   Wayne Hu and Ignacy Sawicki. «Models of f(R) Cosmic Acceleration that Evade Solar-System Tests.» In: *Phys. Rev. D* 76 (2007), p. 064004. DOI: 10.1103/PhysRevD.76.064004. arXiv: 0705.1158 [astro-ph].

[225]   John D. Barrow and S. Cotsakis. «Inflation and the Conformal Structure of Higher Order Gravity Theories.» In: *Phys. Lett. B* 214 (1988), pp. 515–518. DOI: 10.1016/0370-2693(88)90110-4.

[226]   Tessa Baker et al. «The Novel Probes Project – Tests of Gravity on Astrophysical Scales.» In: *arXiv e-prints*, arXiv:1908.03430 (Aug. 2019), arXiv:1908.03430. arXiv: 1908.03430 [astro-ph.CO].

[227]   G. R. Dvali, Gregory Gabadadze, and Massimo Porrati. «4-D gravity on a brane in 5-D Minkowski space.» In: *Phys. Lett. B* 485 (2000), pp. 208–214. DOI: 10.1016/S0370-2693(00)00669-9. arXiv: hep-th/0005016.

[228]   C. Deffayet. «Cosmology on a brane in Minkowski bulk.» In: *Physics Letters B* 502.1-4 (Mar. 2001), pp. 199–208. DOI: 10.1016/S0370-2693(01)00160-5. arXiv: hep-th/0010186 [hep-th].

[229]   Markus A. Luty, Massimo Porrati, and Riccardo Rattazzi. «Strong interactions and stability in the DGP model.» In: *Journal of High Energy Physics* 2003.9, 029 (Sept. 2003), p. 029. DOI: 10.1088/1126-6708/2003/09/029. arXiv: hep-th/0303116 [hep-th].

[230]   Wenjuan Fang, Sheng Wang, Wayne Hu, Zoltán Haiman, Lam Hui, and Morgan May. «Challenges to the DGP model from horizon-scale growth and geometry.» In: Phys. Rev. D 78.10, 103509 (Nov. 2008), p. 103509. DOI: 10.1103/PhysRevD.78.103509. arXiv: 0808.2208 [astro-ph].

[231]   Varun Sahni and Yuri Shtanov. «Braneworld models of dark energy.» In: J. Cosmology Astropart. Phys. 2003.11, 014 (Nov. 2003), p. 014. DOI: 10.1088/1475-7516/2003/11/014. arXiv: astro-ph/0202346 [astro-ph].

[232]   Fabian Schmidt. «Cosmological simulations of normal-branch braneworld gravity.» In: Phys. Rev. D 80.12, 123003 (Dec. 2009), p. 123003. DOI: 10.1103/PhysRevD.80.123003. arXiv: 0910.0235 [astro-ph.CO].

[233]   Kazuya Koyama and Fabio P. Silva. «Non-linear interactions in a cosmological background in the DGP braneworld.» In: *Phys. Rev. D* 75 (2007), p. 084040. DOI: 10.1103/PhysRevD.75.084040. arXiv: hep-th/0702169.

[234] Alberto Nicolis, Riccardo Rattazzi, and Enrico Trincherini. «Galileon as a local modification of gravity.» In: Phys. Rev. D 79.6, 064036 (Mar. 2009), p. 064036. DOI: 10.1103/PhysRevD.79.064036. arXiv: 0811.2197 [hep-th].

[235] C. Deffayet, Xian Gao, D. A. Steer, and G. Zahariade. «From k-essence to generalized Galileons.» In: Phys. Rev. D 84.6, 064039 (Sept. 2011), p. 064039. DOI: 10.1103/PhysRevD.84.064039. arXiv: 1103.3260 [hep-th].

[236] T. Kobayashi, M. Yamaguchi, and J. Yokoyama. «Generalized G-Inflation — Inflation with the Most General Second-Order Field Equations —.» In: *Progress of Theoretical Physics* 126.3 (Sept. 2011), pp. 511–529. DOI: 10.1143/PTP.126.511. arXiv: 1105.5723 [hep-th].

[237] Gong-Bo Zhao, Tommaso Giannantonio, Levon Pogosian, Alessandra Silvestri, David J. Bacon, Kazuya Koyama, Robert C. Nichol, and Yong-Seon Song. «Probing modifications of General Relativity using current cosmological observations.» In: *Phys. Rev. D* 81 (2010), p. 103510. DOI: 10.1103/PhysRevD.81.103510. arXiv: 1003.0001 [astro-ph.CO].

[238] Alireza Hojjati, Levon Pogosian, and Gong-Bo Zhao. «Testing gravity with CAMB and CosmoMC.» In: *JCAP* 08 (2011), p. 005. DOI: 10.1088/1475-7516/2011/08/005. arXiv: 1106.4543 [astro-ph.CO].

[239] Santiago Casas, Martin Kunz, Matteo Martinelli, and Valeria Pettorino. «Linear and non-linear Modified Gravity forecasts with future surveys.» In: *Phys. Dark Univ.* 18 (2017), pp. 73–104. DOI: 10.1016/j.dark.2017.09.009. arXiv: 1703.01271 [astro-ph.CO].

[240] Marco Raveri. «Reconstructing Gravity on Cosmological Scales.» In: *Phys. Rev. D* 101.8 (2020), p. 083524. DOI: 10.1103/PhysRevD.101.083524. arXiv: 1902.01366 [astro-ph.CO].

[241] Marco Raveri, Levon Pogosian, Kazuya Koyama, Matteo Martinelli, Alessandra Silvestri, Gong-Bo Zhao, Jian Li, Simone Peirone, and Alex Zucca. «A joint reconstruction of dark energy and modified growth evolution.» In: (July 2021). arXiv: 2107.12990 [astro-ph.CO].

[242] Levon Pogosian, Marco Raveri, Kazuya Koyama, Matteo Martinelli, Alessandra Silvestri, Gong-Bo Zhao, Jian Li, Simone Peirone, and Alex Zucca. «Imprints of cosmological tensions in reconstructed gravity.» In: *Nature Astron.* 6.12 (2022), pp. 1484–1490. DOI: 10.1038/s41550-022-01808-7. arXiv: 2107.12992 [astro-ph.CO].

[243] P. A. R. Ade et al. «Planck 2015 results. XIV. Dark energy and modified gravity.» In: *Astron. Astrophys.* 594 (2016), A14. DOI: 10.1051/0004-6361/201525814. arXiv: 1502.01590 [astro-ph.CO].

[244] C. Armendariz-Picon, V. Mukhanov, and Paul J. Steinhardt. «Dynamical Solution to the Problem of a Small Cosmological Constant and Late-Time Cosmic Acceleration.» In: Phys. Rev. Lett. 85.21 (Nov. 2000), pp. 4438–4441. DOI: 10.1103/PhysRevLett.85.4438. arXiv: astro-ph/0004134 [astro-ph].

[245] C. Armendariz-Picon, V. Mukhanov, and Paul J. Steinhardt. «Essentials of k-essence.» In: Phys. Rev. D 63.10, 103510 (May 2001), p. 103510. DOI: 10.1103/PhysRevD.63.103510. arXiv: astro-ph/0006373 [astro-ph].

[246] Emiliano Sefusatti and Filippo Vernizzi. «Cosmological structure formation with clustering quintessence.» In: J. Cosmology Astropart. Phys. 2011.3, 047 (Mar. 2011), p. 047. DOI: 10.1088/1475-7516/2011/03/047. arXiv: 1101.1026 [astro-ph.CO].

[247] Farbod Hassani, Benjamin L'Huillier, Arman Shafieloo, Martin Kunz, and Julian Adamek. «Parametrising non-linear dark energy perturbations.» In: J. Cosmology Astropart. Phys. 2020.4, 039 (Apr. 2020), p. 039. DOI: 10.1088/1475-7516/2020/04/039. arXiv: 1910.01105 [astro-ph.CO].

[248] Noemi Frusciante, Simone Peirone, Luís Atayde, and Antonio De Felice. «Phenomenology of the generalized cubic covariant Galileon model and cosmological bounds.» In: Phys. Rev. D 101.6, 064001 (Mar. 2020), p. 064001. DOI: 10.1103/PhysRevD.101.064001. arXiv: 1912.07586 [astro-ph.CO].

[249] Levon Pogosian and Alessandra Silvestri. «What can cosmology tell us about gravity? Constraining Horndeski gravity with Σ and μ.» In: Phys. Rev. D 94.10 (2016), p. 104014. DOI: 10.1103/PhysRevD.94.104014. arXiv: 1606.05339 [astro-ph.CO].

[250] Noemi Frusciante and Louis Perenon. «Effective field theory of dark energy: A review.» In: Phys. Rept. 857 (2020), pp. 1–63. DOI: 10.1016/j.physrep.2020.02.004. arXiv: 1907.03150 [astro-ph.CO].

[251] Paolo Creminelli, Markus A. Luty, Alberto Nicolis, and Leonardo Senatore. «Starting the Universe: stable violation of the null energy condition and non-standard cosmologies.» In: Journal of High Energy Physics 2006.12, 080 (Dec. 2006), p. 080. DOI: 10.1088/1126-6708/2006/12/080. arXiv: hep-th/0606090 [hep-th].

[252] Clifford Cheung, A. Liam Fitzpatrick, Jared Kaplan, Leonardo Senatore, and Paolo Creminelli. «The effective field theory of inflation.» In: Journal of High Energy Physics 2008.3, 014-014 (Mar. 2008), pp. 014–014. DOI: 10.1088/1126-6708/2008/03/014. arXiv: 0709.0293 [hep-th].

[253] Steven Weinberg. «Effective field theory for inflation.» In: Phys. Rev. D 77.12, 123541 (June 2008). DOI: 10.1103/PhysRevD.77.123541. arXiv: 0804.4291 [hep-th].

[254] Bin Hu, Marco Raveri, Noemi Frusciante, and Alessandra Silvestri. «Effective field theory of cosmic acceleration: An implementation in CAMB.» In: Phys. Rev. D 89.10, 103530 (May 2014). DOI: 10.1103/PhysRevD.89.103530. arXiv: 1312.5742 [astro-ph.CO].

[255] Marco Raveri, Bin Hu, Noemi Frusciante, and Alessandra Silvestri. «Effective Field Theory of Cosmic Acceleration: constraining dark energy with CMB data.» In: Phys. Rev. D 90.4 (2014), p. 043513. DOI: 10.1103/PhysRevD.90.043513. arXiv: 1405.1022 [astro-ph.CO].

[256] Emilio Bellini and Ignacy Sawicki. «Maximal freedom at minimum cost: linear large-scale structure in general modifications of gravity.» In: J. Cosmology Astropart. Phys. 2014.7, 050 (July 2014), p. 050. DOI: 10.1088/1475-7516/2014/07/050. arXiv: 1404.3713 [astro-ph.CO].

[257] Miguel Zumalacarregui and Uros Seljak. «Limits on stellar-mass compact objects as dark matter from gravitational lensing of type Ia supernovae.» In: *Phys. Rev. Lett.* 121.14 (2018), p. 141101. DOI: 10.1103/PhysRevLett.121.141101.

[258] E. Bellini et al. «Comparison of Einstein-Boltzmann solvers for testing general relativity.» In: Phys. Rev. D 97.2, 023520 (Jan. 2018). DOI: 10.1103/PhysRevD.97.023520. arXiv: 1709.09135 [astro-ph.CO].

[259] Lucas Lombriser and Andy Taylor. «Breaking a dark degeneracy with gravitational waves.» In: J. Cosmology Astropart. Phys. 2016.3, 031 (Mar. 2016), p. 031. DOI: 10.1088/1475-7516/2016/03/031. arXiv: 1509.08458 [astro-ph.CO].

[260] Lucas Lombriser and Nelson A. Lima. «Challenges to self-acceleration in modified gravity from gravitational waves and large-scale structure.» In: *Physics Letters B* 765 (Feb. 2017), pp. 382–385. DOI: 10.1016/j.physletb.2016.12.048. arXiv: 1602.07670 [astro-ph.CO].

[261] B. P. Abbott, R. Abbott, T. D. Abbott, F. Acernese, K. Ackley, C. Adams, T. Adams, P. Addesso, R. X. Adhikari, and V. B. Adya. «GW170817: Observation of Gravitational Waves from a Binary Neutron Star Inspiral.» In: Phys. Rev. Lett. 119.16, 161101 (Oct. 2017). DOI: 10.1103/PhysRevLett.119.161101. arXiv: 1710.05832 [gr-qc].

[262] Rafael C. Nunes, Márcio E. S. Alves, and José C. N. de Araujo. «Primordial gravitational waves in Horndeski gravity.» In: Phys. Rev. D 99.8, 084022 (Apr. 2019), p. 084022. DOI: 10.1103/PhysRevD.99.084022. arXiv: 1811.12760 [gr-qc].

[263] Valeria Pettorino and Luca Amendola. «Friction in gravitational waves: A test for early-time modified gravity.» In: *Physics Letters B* 742 (Mar. 2015), pp. 353–357. DOI: 10.1016/j.physletb.2015.02.007. arXiv: 1408.2224 [astro-ph.CO].

[264] Isabela S. Matos, Maurício O. Calvão, and Ioav Waga. «Gravitational wave propagation in f (R) models: New parametrizations and observational constraints.» In: Phys. Rev. D 103.10, 104059 (May 2021), p. 104059. DOI: 10.1103/PhysRevD.103.104059. arXiv: 2104.10305 [gr-qc].

[265] Kris Pardo, Maya Fishbach, Daniel E. Holz, and David N. Spergel. «Limits on the number of spacetime dimensions from GW170817.» In: J. Cosmology Astropart. Phys. 2018.7, 048 (July 2018), p. 048. DOI: 10.1088/1475-7516/2018/07/048. arXiv: 1801.08160 [gr-qc].

[266] Shadab Alam, Metin Ata, Stephen Bailey, Florian Beutler, Dmitry Bizyaev, Jonathan A. Blazek, Adam S. Bolton, Joel R. Brownstein, Angela Burden, and Chia-Hsun Chuang. «The clustering of galaxies in the completed SDSS-III Baryon Oscillation Spectroscopic Survey: cosmological analysis of the DR12 galaxy sample.» In: MNRAS 470.3 (Sept. 2017), pp. 2617–2652. ISSN: 0035-8711. DOI: 10.1093/mnras/stx721. arXiv: 1607.03155 [astro-ph.CO].

[267] Eleonora Di Valentino and Sarah Bridle. «Exploring the Tension between Current Cosmic Microwave Background and Cosmic Shear Data.» In: *Symmetry* 10.11 (Nov. 2018), p. 585. DOI: 10.3390/sym10110585.

[268] Planck Collaboration et al. «Planck intermediate results. XLVI. Reduction of large-scale systematic effects in HFI polarization maps and estimation of the reionization optical depth.» In: A&A 596, A107 (Dec. 2016), A107. DOI: 10.1051/0004-6361/201628890. arXiv: 1605.02985 [astro-ph.CO].

[269] Planck Collaboration et al. «Planck 2015 results. XV. Gravitational lensing.» In: A&A 594, A15 (Sept. 2016), A15. DOI: 10.1051/0004-6361/201525941. arXiv: 1502.01591 [astro-ph.CO].

[270] Simone Aiola et al. «The Atacama Cosmology Telescope: DR4 maps and cosmological parameters.» In: J. Cosmology Astropart. Phys. 2020.12, 047 (Dec. 2020), p. 047. DOI: 10.1088/1475-7516/2020/12/047. arXiv: 2007.07288 [astro-ph.CO].

[271] Eva Silverstein and Alexander Westphal. «Monodromy in the CMB: Gravity waves and string inflation.» In: Phys. Rev. D 78.10, 106003 (Nov. 2008), p. 106003. DOI: 10.1103/PhysRevD.78.106003. arXiv: 0803.3085 [hep-th].

[272] Liam McAllister, Eva Silverstein, and Alexander Westphal. «Gravity waves and linear inflation from axion monodromy.» In: Phys. Rev. D 82.4, 046003 (Aug. 2010), p. 046003. DOI: 10.1103/PhysRevD.82.046003. arXiv: 0808.0706 [hep-th].

[273] P. Daniel Meerburg. «Alleviating the tension at low ℓ through axion monodromy.» In: Phys. Rev. D 90.6, 063529 (Sept. 2014), p. 063529. DOI: 10.1103/PhysRevD.90.063529. arXiv: 1406.3243 [astro-ph.CO].

[274] Richard A. Battye and Adam Moss. «Evidence for Massive Neutrinos from Cosmic Microwave Background and Lensing Observations.» In: Phys. Rev. Lett. 112.5, 051303 (Feb. 2014), p. 051303. DOI: 10.1103/PhysRevLett.112.051303. arXiv: 1308.5870 [astro-ph.CO].

[275] Hans Böhringer and Gayoung Chon. «Constraints on neutrino masses from the study of the nearby large-scale structure and galaxy cluster counts.» In: *Modern Physics Letters A* 31.21, 1640008 (July 2016), p. 1640008. DOI: 10.1142/S0217732316400083. arXiv: 1610.02855 [astro-ph.CO].

[276] Eleonora Di Valentino, Alessandro Melchiorri, Olga Mena, and Sunny Vagnozzi. «Nonminimal dark sector physics and cosmological tensions.» In: Phys. Rev. D 101.6, 063502 (Mar. 2020), p. 063502. DOI: 10.1103/PhysRevD.101.063502. arXiv: 1910.09853 [astro-ph.CO].

[277] Eleonora Di Valentino, Alessandro Melchiorri, Olga Mena, and Sunny Vagnozzi. «Interacting dark energy in the early 2020s: A promising solution to the H_0 and cosmic shear tensions.» In: *Physics of the Dark Universe* 30, 100666 (Dec. 2020), p. 100666. DOI: 10.1016/j.dark.2020.100666. arXiv: 1908.04281 [astro-ph.CO].

[278] Stefano Camera, Matteo Martinelli, and Daniele Bertacca. «Does quartessence ease cosmic tensions?» In: *Physics of the Dark Universe* 23, 100247 (Jan. 2019), p. 100247. DOI: 10.1016/j.dark.2018.11.008. arXiv: 1704.06277 [astro-ph.CO].

[279] Zahra Davari, Valerio Marra, and Mohammad Malekjani. «Cosmological constrains on minimally and non-minimally coupled scalar field models.» In: MNRAS 491.2 (Jan. 2020), pp. 1920–1933. DOI: 10.1093/mnras/stz3096. arXiv: 1911.00209 [gr-qc].

[280] Eleonora Di Valentino, Alessandro Melchiorri, and Joseph Silk. «Cosmological hints of modified gravity?» In: Phys. Rev. D 93.2, 023513 (Jan. 2016), p. 023513. DOI: 10.1103/PhysRevD.93.023513. arXiv: 1509.07501 [astro-ph.CO].

[281] Joan Solà Peracaula, Adrià Gómez-Valent, Javier de Cruz Pérez, and Cristian Moreno-Pulido. «Brans-Dicke Gravity with a Cosmological Constant Smoothes Out ΛCDM Tensions.» In: ApJ 886.1, L6 (Nov. 2019), p. L6. DOI: 10.3847/2041-8213/ab53e9. arXiv: 1909.02554 [astro-ph.CO].

[282] Joan Sola, Adria Gomez-Valent, Javier de Cruz Perez, and Cristian Moreno-Pulido. «Brans-Dicke cosmology with a Λ- term: a possible solution to ΛCDM tensions.» In: *arXiv e-prints*, arXiv:2006.04273 (June 2020), arXiv:2006.04273. arXiv: 2006.04273 [astro-ph.CO].

[283] Fergus Simpson et al. «CFHTLenS: testing the laws of gravity with tomographic weak lensing and redshift-space distortions.» In: MNRAS 429.3 (Mar. 2013), pp. 2249–2263. DOI: 10.1093/mnras/sts493. arXiv: 1212.3339 [astro-ph.CO].

[284] eBOSS collaboration et al. «Completed SDSS-IV extended Baryon Oscillation Spectroscopic Survey: Cosmological implications from two decades of spectroscopic surveys at the Apache Point Observatory.» In: Phys. Rev. D 103.8, 083533 (Apr. 2021), p. 083533. DOI: 10.1103/PhysRevD.103.083533. arXiv: 2007.08991 [astro-ph.CO].

[285] Gongbo Zhao, David Bacon, Roy Maartens, Mario Santos, and Alvise Raccanelli. «Model-independent constraints on dark energy and modified gravity with the SKA.» In: *PoS* AASKA14 (2015). Ed. by Tyler L. Bourke et al., p. 165. DOI: 10.22323/1.215.0165.

[286] Santiago Casas, Isabella P. Carucci, Valeria Pettorino, Stefano Camera, and Matteo Martinelli. «Constraining gravity with synergies between radio and optical cosmological surveys.» In: (Oct. 2022). arXiv: 2210.05705 [astro-ph.CO].

[287] Marius Cautun, Enrique Paillas, Yan-Chuan Cai, Sownak Bose, Joaquin Armijo, Baojiu Li, and Nelson Padilla. «The Santiago-Harvard-Edinburgh-Durham void comparison - I. SHEDding light on chameleon gravity tests.» In: MNRAS 476.3 (May 2018), pp. 3195–3217. DOI: 10.1093/mnras/sty463. arXiv: 1710.01730 [astro-ph.CO].

[288] Tilman Tröster et al. «Joint constraints on cosmology and the impact of baryon feedback: Combining KiDS-1000 lensing with the thermal Sunyaev-Zeldovich effect from Planck and ACT.» In: A&A 660, A27 (Apr. 2022), A27. DOI: 10.1051/0004-6361/202142197. arXiv: 2109.04458 [astro-ph.CO].

[289]   Stuart Wyithe, Abraham Loeb, and Paul Geil. «Baryonic Acoustic Oscillations in 21cm Emission: A Probe of Dark Energy out to High Redshifts.» In: *Mon. Not. Roy. Astron. Soc.* 383 (2008), p. 1195. DOI: 10.1111/j.1365-2966.2007.12631.x. arXiv: 0709.2955 [astro-ph].

[290]   Stuart Wyithe and Abraham Loeb. «The 21cm Power Spectrum After Reionization.» In: *Mon. Not. Roy. Astron. Soc.* 397 (2009), p. 1926. DOI: 10.1111/j.1365-2966.2009.15019.x. arXiv: 0808.2323 [astro-ph].

[291]   C. Heneka and L. Amendola. «General Modified Gravity With 21cm Intensity Mapping: Simulations and Forecast.» In: *JCAP* 10 (2018), p. 004. DOI: 10.1088/1475-7516/2018/10/004. arXiv: 1805.03629 [astro-ph.CO].

[292]   Bikash R. Dinda, Anjan A Sen, and Tirthankar Roy Choudhury. «Dark energy constraints from the 21 cm intensity mapping surveys with SKA1.» In: *arXiv e-prints*, arXiv:1804.11137 (Apr. 2018), arXiv:1804.11137. arXiv: 1804.11137 [astro-ph.CO].

[293]   Peng-Ju Wu and Xin Zhang. «Prospects for measuring dark energy with 21 cm intensity mapping experiments.» In: *JCAP* 01.01 (2022), p. 060. DOI: 10.1088/1475-7516/2022/01/060. arXiv: 2108.03552 [astro-ph.CO].

[294]   Peng-Ju Wu, Yichao Li, Jing-Fei Zhang, and Xin Zhang. «Prospects for measuring dark energy with 21 cm intensity mapping experiments: A joint survey strategy.» In: (Dec. 2022). arXiv: 2212.07681 [astro-ph.CO].

[295]   Kiyoshi Wesley Masui, Fabian Schmidt, Ue-Li Pen, and Patrick McDonald. «Projected Constraints on Modified Gravity Cosmologies from 21cm Intensity Mapping.» In: *Phys. Rev. D* 81 (2010), p. 062001. DOI: 10.1103/PhysRevD.81.062001. arXiv: 0911.3552 [astro-ph.CO].

[296]   Philip Bull, Martin White, and Anže Slosar. «Searching for dark energy in the matter-dominated era.» In: *Mon. Not. Roy. Astron. Soc.* 505.2 (2021), pp. 2285–2299. DOI: 10.1093/mnras/stab1338. arXiv: 2007.02865 [astro-ph.CO].

[297]   Réza Ansari et al. «Inflation and Early Dark Energy with a Stage II Hydrogen Intensity Mapping experiment.» In: (Oct. 2018). arXiv: 1810.09572 [astro-ph.CO].

[298]   Kirit S. Karkare and Simeon Bird. «Constraining the Expansion History and Early Dark Energy with Line Intensity Mapping.» In: *Phys. Rev. D* 98.4 (2018), p. 043529. DOI: 10.1103/PhysRevD.98.043529. arXiv: 1806.09625 [astro-ph.CO].

[299]   Xiaodong Xu, Yin-Zhe Ma, and Amanda Weltman. «Constraining the interaction between dark sectors with future HI intensity mapping observations.» In: *Phys. Rev. D* 97.8 (2018), p. 083504. DOI: 10.1103/PhysRevD.97.083504. arXiv: 1710.03643 [astro-ph.CO].

[300]   Ming Zhang, Bo Wang, Peng-Ju Wu, Jing-Zhao Qi, Yidong Xu, Jing-Fei Zhang, and Xin Zhang. «Prospects for Constraining Interacting Dark Energy Models with 21 cm Intensity Mapping Experiments.» In: *Astrophys. J.* 918.2 (2021), p. 56. DOI: 10.3847/1538-4357/ac0ef5. arXiv: 2102.03979 [astro-ph.CO].

[301] Isabella P. Carucci, Pier-Stefano Corasaniti, and Matteo Viel. «Imprints of non-standard dark energy and dark matter models on the 21cm intensity map power spectrum.» In: J. Cosmology Astropart. Phys. 2017.12, 018 (Dec. 2017), p. 018. DOI: 10.1088/1475-7516/2017/12/018. arXiv: 1706.09462 [astro-ph.CO].

[302] Chandrachud B. V. Dash and Tapomoy Guha Sarkar. «Constraining dark energy using the cross correlations of weak lensing with post-reionization probes of neutral hydrogen.» In: *JCAP* 02 (2021), p. 016. DOI: 10.1088/1475-7516/2021/02/016. arXiv: 2010.05816 [astro-ph.CO].

[303] Muntazir M. Abidi, Camille Bonvin, Mona Jalilvand, and Martin Kunz. «Model-Independent Test for Gravity using Intensity Mapping and Galaxy Clustering.» In: (Aug. 2022). arXiv: 2208.10419 [astro-ph.CO].

[304] Bryan R. Scott, Kirit S. Karkare, and Simeon Bird. «A Forecast for Large Scale Structure Constraints on Horndeski Gravity with Line Intensity Mapping.» In: (Sept. 2022). arXiv: 2209.13029 [astro-ph.CO].

[305] Azadeh Moradinezhad Dizgah, Emilio Bellini, and Garrett K. Keating. «Probing Dark Energy and Modifications of Gravity with Ground-Based Millimeter-Wavelength Line Intensity Mapping.» In: (Apr. 2023). arXiv: 2304.08471 [astro-ph.CO].

[306] Francisco Villaescusa-Navarro, Matteo Viel, Kanan K. Datta, and T. Roy Choudhury. «Modeling the neutral hydrogen distribution in the post-reionization Universe: intensity mapping.» In: J. Cosmology Astropart. Phys. 2014.9 (Sept. 2014), pp. 050–050. DOI: 10.1088/1475-7516/2014/09/050. arXiv: 1405.6713 [astro-ph.CO].

[307] Marta Spinelli, Anna Zoldan, Gabriella De Lucia, Lizhi Xie, and Matteo Viel. «The atomic Hydrogen content of the post-reionization Universe.» In: *Mon. Not. Roy. Astron. Soc.* 493.4 (Mar. 2020), pp. 5434–5455. ISSN: 0035-8711. DOI: 10.1093/mnras/staa604. arXiv: 1909.02242 [astro-ph.CO].

[308] Neil H. M. Crighton et al. «The neutral hydrogen cosmological mass density at z = 5.» In: *Mon. Not. Roy. Astron. Soc.* 452.1 (July 2015), pp. 217–234. ISSN: 0035-8711. DOI: 10.1093/mnras/stv1182. arXiv: 1506.02037 [astro-ph.CO].

[309] Francisco Villaescusa-Navarro, Philip Bull, and Matteo Viel. «Weighing Neutrinos with Cosmic Neutral Hydrogen.» In: ApJ 814.2, 146 (Dec. 2015), p. 146. DOI: 10.1088/0004-637X/814/2/146. arXiv: 1507.05102 [astro-ph.CO].

[310] Francisco Villaescusa-Navarro, David Alonso, and Matteo Viel. «Baryonic acoustic oscillations from 21 cm intensity mapping: the Square Kilometre Array case.» In: *Mon. Not. Roy. Astron. Soc.* 466.3 (2017), pp. 2736–2751. DOI: 10.1093/mnras/stw3224. arXiv: 1609.00019 [astro-ph.CO].

[311] Steven Cunnington, Alkistis Pourtsidou, Paula S. Soares, Chris Blake, and David Bacon. «Multipole expansion for H i intensity mapping experiments: simulations and modelling.» In: *Mon. Not. Roy. Astron. Soc.* 496.1 (2020), pp. 415–433. DOI: 10.1093/mnras/staa1524. arXiv: 2002.05626 [astro-ph.CO].

[312]   Atsushi Taruya, Takahiro Nishimichi, and Shun Saito. «Baryon Acoustic Oscillations in 2D: Modeling Redshift-space Power Spectrum from Perturbation Theory.» In: *Phys. Rev. D* 82 (2010), p. 063522. DOI: 10. 1103/PhysRevD.82.063522. arXiv: 1006.0699 [astro-ph.CO].

[313]   Jan Niklas Grieb, Ariel G. Sánchez, Salvador Salazar-Albornoz, and Claudio Dalla Vecchia. «Gaussian covariance matrices for anisotropic galaxy clustering measurements.» In: *Mon. Not. Roy. Astron. Soc.* 457.2 (2016), pp. 1577–1592. DOI: 10.1093/mnras/stw065. arXiv: 1509.04293 [astro-ph.CO].

[314]   Chris Blake. «Power spectrum modelling of galaxy and radio intensity maps including observational effects.» In: *Mon. Not. Roy. Astron. Soc.* 489.1 (2019), pp. 153–167. DOI: 10.1093/mnras/stz2145. arXiv: 1902. 07439 [astro-ph.CO].

[315]   Antony Lewis. *GetDist: a Python package for analysing Monte Carlo samples.* 2019. arXiv: 1910.13970 [astro-ph.IM]. URL: https://getdist. readthedocs.io.

[316]   Nils Schöneberg, Guillermo Franco Abellán, Andrea Pérez Sánchez, Samuel J. Witte, Vivian Poulin, and Julien Lesgourgues. *The H_0 Olympics: A fair ranking of proposed models.* July 2021. arXiv: 2107.10291 [astro-ph.CO].

[317]   James M. Bardeen, J. R. Bond, Nick Kaiser, and A. S. Szalay. «The Statistics of Peaks of Gaussian Random Fields.» In: *Astrophys. J.* 304 (1986), pp. 15–61. DOI: 10.1086/164143.

[318]   Will J. Percival et al. «Parameter constraints for flat cosmologies from CMB and 2dFGRS power spectra.» In: *Mon. Not. Roy. Astron. Soc.* 337 (2002), p. 1068. DOI: 10.1046/j.1365-8711.2002.06001.x. arXiv: astro-ph/0206256.

[319]   Florian Beutler, Chris Blake, Matthew Colless, D. Heath Jones, Lister Staveley-Smith, Lachlan Campbell, Quentin Parker, Will Saunders, and Fred Watson. «The 6dF Galaxy Survey: Baryon Acoustic Oscillations and the Local Hubble Constant.» In: *Mon. Not. Roy. Astron. Soc.* 416 (2011), pp. 3017–3032. DOI: 10.1111/j.1365-2966.2011.19250.x. arXiv: 1106.3366 [astro-ph.CO].

[320]   Ashley J. Ross, Lado Samushia, Cullan Howlett, Will J. Percival, Angela Burden, and Marc Manera. «The clustering of the SDSS DR7 main Galaxy sample - I. A 4 per cent distance measure at z = 0.15.» In: MNRAS 449.1 (May 2015), pp. 835–847. DOI: 10.1093/mnras/stv154. arXiv: 1409.3242 [astro-ph.CO].

[321]   Anna Zoldan, Gabriella De Lucia, Lizhi Xie, Fabio Fontanot, and Michaela Hirschmann. «HI-selected Galaxies in Hierarchical Models of Galaxy Formation and Evolution.» In: *Monthly Notices of the Royal Astronomical Society* (2016), stw2901.

[322]   Hong Guo, Cheng Li, Zheng Zheng, H. J. Mo, Y. P. Jing, Ying Zu, S. H. Lim, and Haojie Xu. «Constraining the H i–Halo Mass Relation from Galaxy Clustering.» In: *Astrophys. J.* 846.1 (2017), p. 61. DOI: 10.3847/ 1538-4357/aa85e7. arXiv: 1707.01999 [astro-ph.GA].

[323]   R. E. Smith, J. A. Peacock, A. Jenkins, S. D. M. White, C. S. Frenk, F. R. Pearce, P. A. Thomas, G. Efstathiou, and H. M. P. Couchmann. «Stable clustering, the halo model and nonlinear cosmological power spectra.» In: *Mon. Not. Roy. Astron. Soc.* 341 (2003), p. 1311. DOI: `10.1046/j.1365-8711.2003.06503.x`. arXiv: `astro-ph/0207664`.

[324]   Alexander Mead, Catherine Heymans, Lucas Lombriser, John Peacock, Olivia Steele, and Hans Winther. «Accurate halo-model matter power spectra with dark energy, massive neutrinos and modified gravitational forces.» In: *Mon. Not. Roy. Astron. Soc.* 459.2 (2016), pp. 1468–1488. DOI: `10.1093/mnras/stw681`. arXiv: `1602.02154 [astro-ph.CO]`.

[325]   C. Alcock and B. Paczynski. «An evolution free test for non-zero cosmological constant.» In: *Nature* 281 (1979), pp. 358–359. DOI: `10.1038/281358a0`.

[326]   Héctor Gil-Marín, Will J. Percival, Licia Verde, Joel R. Brownstein, Chia-Hsun Chuang, Francisco-Shu Kitaura, Sergio A. Rodríguez-Torres, and Matthew D. Olmstead. «The clustering of galaxies in the SDSS-III Baryon Oscillation Spectroscopic Survey: RSD measurement from the power spectrum and bispectrum of the DR12 BOSS galaxies.» In: *Mon. Not. Roy. Astron. Soc.* 465.2 (2017), pp. 1757–1788. DOI: `10.1093/mnras/stw2679`. arXiv: `1606.00439 [astro-ph.CO]`.

[327]   Nick Hand, Uros Seljak, Florian Beutler, and Zvonimir Vlah. «Extending the modeling of the anisotropic galaxy power spectrum to $k = 0.4$ hMpc^{-1}.» In: *JCAP* 10 (2017), p. 009. DOI: `10.1088/1475-7516/2017/10/009`. arXiv: `1706.02362 [astro-ph.CO]`.

[328]   Emanuele Castorina and Francisco Villaescusa-Navarro. «On the spatial distribution of neutral hydrogen in the Universe: bias and shot-noise of the HI power spectrum.» In: *Monthly Notices of the Royal Astronomical Society* 471.2 (June 2017), pp. 1788–1796. ISSN: 0035-8711. DOI: `10.1093/mnras/stx1599`. arXiv: `1609.05157 [astro-ph.CO]`.

[329]   Robert E. Smith. «Covariance of cross-correlations: towards efficient measures for large-scale structure.» In: MNRAS 400.2 (Dec. 2009), pp. 851–865. DOI: `10.1111/j.1365-2966.2009.15490.x`. arXiv: `0810.1960 [astro-ph]`.

[330]   Michael J. Drinkwater et al. «The WiggleZ Dark Energy Survey: final data release and the metallicity of UV-luminous galaxies.» In: *Mon. Not. Roy. Astron. Soc.* 474.3 (2018), pp. 4151–4168. DOI: `10.1093/mnras/stx2963`. arXiv: `1910.08284 [astro-ph.GA]`.

[331]   Chris Blake et al. «The WiggleZ Dark Energy Survey: the growth rate of cosmic structure since redshift z=0.9.» In: *Mon. Not. Roy. Astron. Soc.* 415 (2011), p. 2876. DOI: `10.1111/j.1365-2966.2011.18903.x`. arXiv: `1104.2948 [astro-ph.CO]`.

[332]   Nishikanta Khandai, Shiv K. Sethi, Tiziana Di Matteo, Rupert A. C. Croft, Volker Springel, Anirban Jana, and Jeffrey P. Gardner. «Detecting neutral hydrogen in emission at redshift z ~ 1.» In: *Mon. Not. Roy. Astron. Soc.* 415 (2011), p. 2580. DOI: `10.1111/j.1365-2966.2011.18881.x`. arXiv: `1012.1880 [astro-ph.CO]`.

[333]   A. Raichoor et al. «Target Selection and Validation of DESI Emission Line Galaxies.» In: AJ 165.3, 126 (Mar. 2023), p. 126. DOI: 10.3847/1538-3881/acb213. arXiv: 2208.08513 [astro-ph.CO].

[334]   Bin Hu, Marco Raveri, Noemi Frusciante, and Alessandra Silvestri. «EFTCAMB/EFTCosmoMC: Numerical Notes v3.0.» In: (May 2014). arXiv: 1405.3590 [astro-ph.IM].

[335]   E. R. Switzer et al. «Determination of $z \sim 0.8$ neutral hydrogen fluctuations using the 21cm intensity mapping autocorrelation.» In: *Monthly Notices of the Royal Astronomical Society: Letters* 434.1 (June 2013), pp. L46–L50. ISSN: 1745-3925. DOI: 10.1093/mnrasl/slt074. eprint: https://academic.oup.com/mnrasl/article-pdf/434/1/L46/9420415/slt074.pdf. URL: https://doi.org/10.1093/mnrasl/slt074.

[336]   K M B Asad et al. «Primary beam effects of radio astronomy antennas – II. Modelling MeerKAT L-band beams.» In: *Monthly Notices of the Royal Astronomical Society* 502.2 (2021), 2970–2983. ISSN: 1365-2966. DOI: 10.1093/mnras/stab104. URL: http://dx.doi.org/10.1093/mnras/stab104.

[337]   Stuart Harper, Clive Dickinson, Richard Battye, Sambit Roychowdhury, Ian Browne, Yin-Zhe Ma, Lucas Olivari, and Tianyue Chen. «Impact of Simulated 1/f Noise for HI Intensity Mapping Experiments.» In: *Mon. Not. Roy. Astron. Soc.* 478.2 (2018), pp. 2416–2437. DOI: 10.1093/mnras/sty1238. arXiv: 1711.07843 [astro-ph.CO].

[338]   Yichao Li, Mario G. Santos, Keith Grainge, Stuart Harper, and Jingying Wang. «HI intensity mapping with MeerKAT: 1/f noise analysis.» In: *Mon. Not. Roy. Astron. Soc.* 501.3 (2021), pp. 4344–4358. DOI: 10.1093/mnras/staa3856. arXiv: 2007.01767 [astro-ph.CO].

[339]   Andrej Obuljen, Emanuele Castorina, Francisco Villaescusa-Navarro, and Matteo Viel. «High-redshift post-reionization cosmology with 21cm intensity mapping.» In: *JCAP* 05 (2018), p. 004. DOI: 10.1088/1475-7516/2018/05/004. arXiv: 1709.07893 [astro-ph.CO].

[340]   Paolo Creminelli, Guido D'Amico, Jorge Noreña, and Filippo Vernizzi. «The effective theory of quintessence: the w < -1 side unveiled.» In: *Journal of Cosmology and Astro-Particle Physics* 2009.2, 018 (Feb. 2009), p. 018. DOI: 10.1088/1475-7516/2009/02/018. arXiv: 0811.0827 [astro-ph].

[341]   Noemi Frusciante, Georgios Papadomanolakis, and Alessandra Silvestri. «An extended action for the effective field theory of dark energy: a stability analysis and a complete guide to the mapping at the basis of EFTCAMB.» In: J. Cosmology Astropart. Phys. 2016.7, 018 (July 2016), p. 018. DOI: 10.1088/1475-7516/2016/07/018. arXiv: 1601.04064 [gr-qc].

[342]   Juan Espejo, Simone Peirone, Marco Raveri, Kazuya Koyama, Levon Pogosian, and Alessandra Silvestri. «Phenomenology of Large Scale Structure in scalar-tensor theories: joint prior covariance of w_{DE}, Σ and μ in Horndeski.» In: *Phys. Rev. D* 99.2 (2019), p. 023512. DOI: 10.1103/PhysRevD.99.023512. arXiv: 1809.01121 [astro-ph.CO].

[343] Valentina Salvatelli, Federico Piazza, and Christian Marinoni. «Constraints on modified gravity from Planck 2015: when the health of your theory makes the difference.» In: *JCAP* 09 (2016), p. 027. DOI: 10.1088/1475-7516/2016/09/027. arXiv: 1602.08283 [astro-ph.CO].

[344] Simone Peirone, Matteo Martinelli, Marco Raveri, and Alessandra Silvestri. «Impact of theoretical priors in cosmological analyses: The case of single field quintessence.» In: *Physical Review D* 96.6, 063524 (Sept. 2017). DOI: 10.1103/PhysRevD.96.063524. arXiv: 1702.06526 [astro-ph.CO].

[345] G. Hinshaw et al. «Nine-year Wilkinson Microwave Anisotropy Probe (WMAP) Observations: Cosmological Parameter Results.» In: ApJS 208.2, 19 (Oct. 2013), p. 19. DOI: 10.1088/0067-0049/208/2/19. arXiv: 1212.5226 [astro-ph.CO].

[346] Martin Kilbinger et al. «Precision calculations of the cosmic shear power spectrum projection.» In: *Monthly Notices of the Royal Astronomical Society* 472.2 (Dec. 2017), pp. 2126–2141. DOI: 10.1093/mnras/stx2082.

[347] Matthias Bartelmann and Peter Schneider. «Weak gravitational lensing.» In: *Physics Reports* 340.4 (2001), pp. 291–472. ISSN: 0370-1573. DOI: https://doi.org/10.1016/S0370-1573(00)00082-X.

[348] Henk Hoekstra and Bhuvnesh Jain. «Weak Gravitational Lensing and Its Cosmological Applications.» In: *Annual Review of Nuclear and Particle Science* 58.1 (2008), pp. 99–123. DOI: 10.1146/annurev.nucl.58.110707.171151.

[349] Benjamin Joachimi, Marcello Cacciato, Thomas D Kitching, Adrienne Leonard, Rachel Mandelbaum, Björn Malte Schäfer, Cristóbal Sifón, Henk Hoekstra, Alina Kiessling, Donnacha Kirk, et al. «Galaxy alignments: An overview.» In: *Space Science Reviews* 193.1 (2015), pp. 1–65. DOI: https://doi.org/10.1007/s11214-015-0177-4.

[350] B. Joachimi, R. Mandelbaum, F. B. Abdalla, and S. L. Bridle. «Constraints on intrinsic alignment contamination of weak lensing surveys using the MegaZ-LRG sample.» In: *Astronomy & Astrophysics* 527, A26 (Mar. 2011), A26. DOI: 10.1051/0004-6361/201015621. arXiv: 1008.3491 [astro-ph.CO].

[351] Ryuichi Takahashi. «Amplitude and Phase Fluctuations for Gravitational Waves Propagating through Inhomogeneous Mass Distribution in the Universe.» In: *The Astrophysical Journal* 644.1 (June 2006), pp. 80–85. DOI: 10.1086/503323.

[352] Pablo Laguna, Shane L. Larson, David Spergel, and Nicolás Yunes. «INTEGRATED SACHS–WOLFE EFFECT FOR GRAVITATIONAL RADIATION.» In: *The Astrophysical Journal* 715.1 (Apr. 2010), pp. L12–L15. DOI: 10.1088/2041-8205/715/1/l12.

[353] Curt Cutler and Daniel E. Holz. «Ultrahigh precision cosmology from gravitational waves.» In: *Phys. Rev. D* 80 (10 Nov. 2009), p. 104009. DOI: 10.1103/PhysRevD.80.104009.

[354] Giuseppe Congedo and Andy Taylor. «Joint cosmological inference of standard sirens and gravitational wave weak lensing.» In: *Phys. Rev. D* 99 (8 Apr. 2019), p. 083526. DOI: 10.1103/PhysRevD.99.083526.

[355] Daniele Bertacca, Alvise Raccanelli, Nicola Bartolo, and Sabino Matarrese. «Cosmological perturbation effects on gravitational-wave luminosity distance estimates.» In: *Physics of the Dark Universe* 20 (2018), pp. 32–40. ISSN: 2212-6864. DOI: https://doi.org/10.1016/j.dark.2018.03.001.

[356] Charlie T Mpetha, Giuseppe Congedo, and Andy Taylor. «Future prospects on testing extensions to ΛCDM through the weak lensing of gravitational waves.» In: *arXiv preprint arXiv:2208.05959* (2022).

[357] A. Pourtsidou and R. Benton Metcalf. «Weak lensing with 21 cm intensity mapping at z 2–3.» In: *Monthly Notices of the Royal Astronomical Society: Letters* 439.1 (Jan. 2014), pp. L36–L40. ISSN: 1745-3925. DOI: 10.1093/mnrasl/slt175.

[358] A. Pourtsidou and R. Benton Metcalf. «Gravitational lensing of cosmological 21 cm emission.» In: *Monthly Notices of the Royal Astronomical Society* 448.3 (Feb. 2015), pp. 2368–2383. ISSN: 0035-8711. DOI: 10.1093/mnras/stv102.

[359] Nick Kaiser. «On the spatial correlations of Abell clusters.» In: *The Astrophysical Journal* 284 (1984), pp. L9–L12. DOI: 10.1086/184341.

[360] H. J. Mo and S. D. M. White. «An analytic model for the spatial clustering of dark matter haloes.» In: *Monthly Notices of the Royal Astronomical Society* 282.2 (1996), pp. 347–361. DOI: 10.1093/mnras/282.2.347. arXiv: astro-ph/9512127.

[361] Sabino Matarrese, Peter Coles, Francesco Lucchin, and Lauro Moscardini. «Redshift evolution of clustering.» In: *Monthly Notices of the Royal Astronomical Society* 286.1 (Mar. 1997), pp. 115–132. DOI: 10.1093/mnras/286.1.115. arXiv: astro-ph/9608004.

[362] Avishai Dekel and Ofer Lahav. «Stochastic Nonlinear Galaxy Biasing.» In: *The Astrophysical Journal* 520.1 (July 1999), pp. 24–34. DOI: 10.1086/307428. arXiv: astro-ph/9806193.

[363] A. J. Benson, S. Cole, C. S. Frenk, C. M. Baugh, and C. G. Lacey. «The nature of galaxy bias and clustering.» In: *Monthly Notices of the Royal Astronomical Society* 311.4 (Feb. 2000), pp. 793–808. DOI: 10.1046/j.1365-8711.2000.03101.x. arXiv: astro-ph/9903343.

[364] J. A. Peacock and R. E. Smith. «Halo occupation numbers and galaxy bias.» In: *Monthly Notices of the Royal Astronomical Society* 318.4 (Nov. 2000), pp. 1144–1156. DOI: 10.1046/j.1365-8711.2000.03779.x. arXiv: astro-ph/0005010.

[365] Vincent Desjacques, Donghui Jeong, and Fabian Schmidt. «Large-scale galaxy bias.» In: *Physics Reports* 733 (2018), pp. 1–193. ISSN: 0370-1573. DOI: https://doi.org/10.1016/j.physrep.2017.12.002.

[366] Nicola Bellomo, José Luis Bernal, Giulio Scelfo, Alvise Raccanelli, and Licia Verde. «Beware of commonly used approximations. Part I. Errors in forecasts.» In: *Journal of Cosmology and Astroparticle Physics* 2020.10 (Oct. 2020), pp. 016–016. DOI: 10.1088/1475-7516/2020/10/016.

[367] José Luis Bernal, Nicola Bellomo, Alvise Raccanelli, and Licia Verde. «Beware of commonly used approximations. Part II. Estimating systematic biases in the best-fit parameters.» In: *Journal of Cosmology and Astroparticle Physics* 2020.10 (Oct. 2020), pp. 017–017. DOI: 10.1088/1475-7516/2020/10/017.

[368] Mohammadtaher Safarzadeh, Edo Berger, Ken KY Ng, Hsin-Yu Chen, Salvatore Vitale, Chris Whittle, and Evan Scannapieco. «Measuring the Delay Time Distribution of Binary Neutron Stars. II. Using the Redshift Distribution from Third-generation Gravitational-wave Detectors Network.» In: *The Astrophysical Journal Letters* 878.1 (2019), p. L13. DOI: 10.3847/2041-8213/ab22be.

[369] Anna Balaudo, Alice Garoffolo, Matteo Martinelli, Suvodip Mukherjee, and Alessandra Silvestri. «Prospects of testing late-time cosmology with weak lensing of gravitational waves and galaxy surveys.» In: *arXiv preprint arXiv:2210.06398* (2022). DOI: https://doi.org/10.48550/arXiv.2210.06398.

[370] L. Boco, A. Lapi, S. Goswami, F. Perrotta, C. Baccigalupi, and L. Danese. «Merging Rates of Compact Binaries in Galaxies: Perspectives for Gravitational Wave Detections.» In: *The Astrophysical Journal* 881.2, 157 (Aug. 2019), p. 157. DOI: 10.3847/1538-4357/ab328e. arXiv: 1907.06841 [astro-ph.GA].

[371] R. Aversa, A. Lapi, G. de Zotti, F. Shankar, and L. Danese. «Black Hole and Galaxy Coevolution from Continuity Equation and Abundance Matching.» In: *The Astrophysical Journal* 810.1, 74 (Sept. 2015), p. 74. DOI: 10.1088/0004-637X/810/1/74. arXiv: 1507.07318 [astro-ph.GA].

[372] W Del Pozzo. «Measuring the Hubble constant using gravitational waves.» In: *Journal of Physics: Conference Series* 484 (Mar. 2014), p. 012030. DOI: 10.1088/1742-6596/484/1/012030.

[373] P. E. Dewdney, P. J. Hall, R. T. Schilizzi, and T. J. L. W. Lazio. «The Square Kilometre Array.» In: *Proceedings of the IEEE* 97.8 (2009), pp. 1482–1496. DOI: 10.1109/JPROC.2009.2021005.

[374] Roy Maartens, Filipe B. Abdalla, Matt Jarvis, and Mario G. Santos. *Cosmology with the SKA – overview.* 2015. arXiv: 1501.04076 [astro-ph.CO].

[375] David Alonso, Philip Bull, Pedro G. Ferreira, and Mário G. Santos. «Blind foreground subtraction for intensity mapping experiments.» In: *Monthly Notices of the Royal Astronomical Society* 447.1 (Dec. 2014), pp. 400–416. ISSN: 0035-8711. DOI: 10.1093/mnras/stu2474.

[376] Paula S. Soares, Catherine A. Watkinson, Steven Cunnington, and Alkistis Pourtsidou. «Gaussian Process Regression for foreground removal in HI intensity mapping experiments.» In: *arXiv e-prints*, arXiv:2105.12665 (May 2021), arXiv:2105.12665. arXiv: 2105.12665 [astro-ph.CO].

[377] Mario G Santos, Philip Bull, David Alonso, Stefano Camera, Pedro G Ferreira, Gianni Bernardi, Roy Maartens, Matteo Viel, Francisco Villaescusa-Navarro, Filipe B Abdalla, et al. «Cosmology with a SKA HI intensity mapping survey.» In: *arXiv preprint arXiv:1501.03989* (2015).

[378] Anna Bonaldi, Matteo Bonato, Vincenzo Galluzzi, Ian Harrison, Marcella Massardi, Scott Kay, Gianfranco De Zotti, and Michael L Brown. «The Tiered Radio Extragalactic Continuum Simulation (T-RECS).» In: *Monthly Notices of the Royal Astronomical Society* 482.1 (Sept. 2018), pp. 2–19. ISSN: 0035-8711. DOI: 10.1093/mnras/sty2603.

[379] RJ Wilman, L Miller, MJ Jarvis, T Mauch, F Levrier, FB Abdalla, S Rawlings, H-R Klöckner, Danail Obreschkow, D Olteanu, et al. «A semi-empirical simulation of the extragalactic radio continuum sky for next generation radio telescopes.» In: *Monthly Notices of the Royal Astronomical Society* 388.3 (2008), pp. 1335–1348. DOI: 10.1111/j.1365-2966.2008.13486.x.

[380] Tim Sprenger, Maria Archidiacono, Thejs Brinckmann, Sébastien Clesse, and Julien Lesgourgues. «Cosmology in the era of Euclid and the Square Kilometre Array.» In: *Journal of Cosmology and Astroparticle Physics* 2019.02 (Feb. 2019), pp. 047–047. DOI: 10.1088/1475-7516/2019/02/047. arXiv: 1801.08331 [astro-ph.CO].

[381] Enis Belgacem et al. «Testing modified gravity at cosmological distances with LISA standard sirens.» In: *JCAP* 07 (2019), p. 024. DOI: 10.1088/1475-7516/2019/07/024. arXiv: 1906.01593 [astro-ph.CO].

[382] Alessandra Silvestri and Mark Trodden. «Approaches to Understanding Cosmic Acceleration.» In: *Rept. Prog. Phys.* 72 (2009), p. 096901. DOI: 10.1088/0034-4885/72/9/096901. arXiv: 0904.0024 [astro-ph.CO].

[383] Austin Joyce, Bhuvnesh Jain, Justin Khoury, and Mark Trodden. «Beyond the cosmological standard model.» In: Phys. Rep. 568 (Mar. 2015), pp. 1–98. DOI: 10.1016/j.physrep.2014.12.002. arXiv: 1407.0059 [astro-ph.CO].

[384] Philippe Brax. «Screening Mechanisms.» In: 2021. DOI: 10.1007/978-3-030-83715-0_20.

[385] Alex Zucca, Levon Pogosian, Alessandra Silvestri, and Gong-Bo Zhao. «MGCAMB with massive neutrinos and dynamical dark energy.» In: *JCAP* 05 (2019), p. 001. DOI: 10.1088/1475-7516/2019/05/001. arXiv: 1901.05956 [astro-ph.CO].

[386] S. Lee et al. «Probing gravity with the DES-CMASS sample and BOSS spectroscopy.» In: *Mon. Not. Roy. Astron. Soc.* 509.4 (2021), pp. 4982–4996. DOI: 10.1093/mnras/stab3129. arXiv: 2104.14515 [astro-ph.CO].

[387] T. M. C. Abbott et al. «Dark Energy Survey Year 3 Results: Constraints on extensions to ΛCDM with weak lensing and galaxy clustering.» In: (July 2022). arXiv: 2207.05766 [astro-ph.CO].

[388] Gianmassimo Tasinato, Alice Garoffolo, Daniele Bertacca, and Sabino Matarrese. «Gravitational-wave cosmological distances in scalar-tensor theories of gravity.» In: *JCAP* 06 (2021), p. 050. DOI: 10.1088/1475-7516/2021/06/050. arXiv: 2103.00155 [gr-qc].

[389] Francisco Villaescusa-Navarro, Federico Marulli, Matteo Viel, Enzo Branchini, Emanuele Castorina, Emiliano Sefusatti, and Shun Saito. «Cosmology with massive neutrinos I: towards a realistic modeling of the relation between matter, haloes and galaxies.» In: *JCAP* 03 (2014), p. 011. DOI: 10 . 1088 / 1475 - 7516 / 2014 / 03 / 011. arXiv: 1311 . 0866 [astro-ph.CO].

[390] Emanuele Castorina, Emiliano Sefusatti, Ravi K. Sheth, Francisco Villaescusa-Navarro, and Matteo Viel. «Cosmology with massive neutrinos II: on the universality of the halo mass function and bias.» In: *JCAP* 02 (2014), p. 049. DOI: 10 . 1088 / 1475 - 7516 / 2014 / 02 / 049. arXiv: 1311 . 1212 [astro-ph.CO].

[391] Alexander Mead, Samuel Brieden, Tilman Tröster, and Catherine Heymans. «HMcode-2020: Improved modelling of non-linear cosmological power spectra with baryonic feedback.» In: (Sept. 2020). DOI: 10.1093/ mnras/stab082. arXiv: 2009.01858 [astro-ph.CO].

[392] G. Parimbelli, C. Carbone, J. Bel, B. Bose, M. Calabrese, E. Carella, and M. Zennaro. «DEMNUni: comparing nonlinear power spectra prescriptions in the presence of massive neutrinos and dynamical dark energy.» In: *JCAP* 11 (2022), p. 041. DOI: 10.1088/1475-7516/2022/11/041. arXiv: 2207.13677 [astro-ph.CO].

[393] Lauren Anderson, Éric Aubourg, Stephen Bailey, Florian Beutler, Vaishali Bhardwaj, Michael Blanton, Adam S. Bolton, J. Brinkmann, Joel R. Brownstein, and Angela Burden. «The clustering of galaxies in the SDSS-III Baryon Oscillation Spectroscopic Survey: baryon acoustic oscillations in the Data Releases 10 and 11 Galaxy samples.» In: MNRAS 441.1 (June 2014), pp. 24–62. DOI: 10.1093/mnras/stu523. arXiv: 1312.4877 [astro-ph.CO].

[394] Jonathan R. Pritchard and Elena Pierpaoli. «Constraining massive neutrinos using cosmological 21 cm observations.» In: *Phys. Rev. D* 78 (2008), p. 065009. DOI: 10.1103/PhysRevD.78.065009. arXiv: 0805.1920 [astro-ph].

[395] Abraham Loeb and Stuart Wyithe. «Precise Measurement of the Cosmological Power Spectrum With a Dedicated 21cm Survey After Reionization.» In: *Phys. Rev. Lett.* 100 (2008), p. 161301. DOI: 10.1103/PhysRevLett. 100.161301. arXiv: 0801.1677 [astro-ph].

[396] K. N. Abazajian et al. «Cosmological and Astrophysical Neutrino Mass Measurements.» In: *Astropart. Phys.* 35 (2011), pp. 177–184. DOI: 10.1016/ j.astropartphys.2011.07.002. arXiv: 1103.5083 [astro-ph.CO].

[397] Eleonora Di Valentino and Alessandro Melchiorri. «Neutrino Mass Bounds in the Era of Tension Cosmology.» In: *Astrophys. J. Lett.* 931.2 (2022), p. L18. DOI: 10 . 3847 / 2041 - 8213 / ac6ef5. arXiv: 2112 . 02993 [astro-ph.CO].

[398] Oliver H. E. Philcox and Mikhail M. Ivanov. «BOSS DR12 full-shape cosmology: Λ CDM constraints from the large-scale galaxy power spectrum and bispectrum monopole.» In: Phys. Rev. D 105.4, 043517 (Feb. 2022), p. 043517. DOI: 10 . 1103 / PhysRevD . 105 . 043517. arXiv: 2112 . 04515 [astro-ph.CO].

[399]   Noemi Frusciante, Simone Peirone, Santiago Casas, and Nelson A. Lima. «Cosmology of surviving Horndeski theory: The road ahead.» In: *Phys. Rev. D* 99.6 (2019), p. 063538. DOI: 10.1103/PhysRevD.99.063538. arXiv: 1810.10521 [astro-ph.CO].

[400]   Bin Hu and Marco Raveri. «Can modified gravity models reconcile the tension between the CMB anisotropy and lensing maps in Planck-like observations?» In: *Phys. Rev. D* 91.12 (2015), p. 123515. DOI: 10.1103/PhysRevD.91.123515. arXiv: 1502.06599 [astro-ph.CO].

[401]   Balakrishna S. Haridasu, Maria Berti, and Matteo Viel. «Easing the CMB tension with Effective Field Theory models of Dark Energy.» In: 2023.

[402]   Dongwoo T. Chung. «A partial inventory of observational anisotropies in single-dish line-intensity mapping.» In: *Astrophys. J.* 881.2 (2019). [Erratum: Astrophys.J. 908, 115 (2021)], p. 149. DOI: 10.3847/1538-4357/ab3040. arXiv: 1905.00209 [astro-ph.CO].